EUROPEAN ORGANIZATION FOR NUCLEAR RESEARCH
CERN - AB DEPARTMENT

CERN–AB–2006–084 ABP/RF

Linac4 Technical Design Report

L. Arnaudon, P. Baudrenghien, M. Baylac (LPSC) , G. Bellodi, Y. Body, J. Borburgh, P. Bourquin, J. Broere, O. Brunner, L. Bruno, C. Carli, F. Caspers, S. Cousineau (ORNL), Y. Cuvet, C. De Almeida Martins, T. Dobers, T. Fowler, R. Garoby, F. Gerigk, B. Goddard, K. Hanke, M. Hori, M. Jones, K. Kahle, W. Kalbreier, T. Kroyer, D. Küchler, A.M. Lombardi, L.A. Lopez-Hernandez, M. Magistris, E. Mahner, M. Martini, S. Maury, T.K. Meinschad, E. Page, M. Paoluzzi, M. Pasini, U. Raich, C. Rossi, J.-P. Royer, E. Sargsyan, J. Serrano, R. Scrivens, M. Silari, M. Timmins, W. Venturini Delsolaro, M. Vretenar, R. Wegner, W. Weterings, T. Zickler

Editors: F. Gerigk, M. Vretenar

11th December 2006
Geneva, Switzerland

Abstract

Linac4 is an H^- linear accelerator, intended to replace Linac2 as injector to the PS Booster (PSB). By delivering to the PSB a beam at 160 MeV energy, Linac4 will provide the conditions to double the brightness and intensity of the beam from the PSB, thus removing the first bottleneck towards higher brightness for the LHC and simplifying operation. Moreover, this new linac constitutes an essential component of any of the envisaged LHC upgrade scenarios and could open the way to future extensions of the CERN accelerator complex towards higher performance. This Technical Design Report presents a detailed technical overview of the Linac4 design as it stands at end 2006.

Contents

List of tables **vii**

Acronyms and abbreviations **ix**

1 Introduction **1**
1.1 Linear accelerators at CERN . . . 1
1.2 From SPL to Linac4 . . . 2
1.3 Performance of the CERN accelerator complex with Linac4 . . . 2
1.4 Choice of parameters and linac layout . . . 6

2 Design overview **8**
2.1 Source and low-energy beam transport . . . 8
2.2 Radio-frequency quadrupole . . . 11
2.3 Chopper line . . . 14
2.4 Drift tube linac . . . 23
2.5 Cell-coupled drift tube linac . . . 29
2.6 Side-coupled linac . . . 33
2.7 Measurement line and dump . . . 36
2.8 Transfer line . . . 36
2.9 Booster injection . . . 39

3 Beam dynamics **47**
3.1 Front-end: LEBT, RFQ, and chopper line . . . 47
3.2 Main linac and transfer line . . . 50
3.3 End-to-end beam dynamics and error studies . . . 51
3.4 Loss management . . . 55
3.5 Beam dynamics in the PS booster . . . 57

4 General services and systems **63**
4.1 Radio frequency . . . 63
4.2 Beam instrumentation . . . 68
4.3 Magnets . . . 73
4.4 Booster injection equipment . . . 81
4.5 Controls . . . 86
4.6 Power converters . . . 87
4.7 Vacuum . . . 97
4.8 Survey . . . 97

5 Radiation protection and safety **101**
5.1 Radiation protection . . . 101
5.2 Access control . . . 107

5.3 General safety 108
5.4 Machine and personnel protection 108

6 Civil engineering and infrastructure **109**
6.1 Layout 109
6.2 Electrical infrastructure 114
6.3 Cooling and ventilation 116

7 Commissioning and planning **118**
7.1 The 3 MeV test stand 118
7.2 Commissioning strategy 120
7.3 Tentative project schedule 121

Acknowledgements **122**

References **123**

Appendix: Linac4 parameter list **128**

List of Tables

1.1 Beam intensities to be delivered by the PSB 5
1.2 Linac4 beam parameters 6
2.1 Twiss parameters and emittance growth for different LEBT setups 10
2.2 Main RFQ parameters 14
2.3 Magnetic elements in the chopper line 17
2.4 Main buncher parameters 17
2.5 Parameters of the three DTL tanks 25
2.6 Main CCDTL parameters 31
2.7 Main SCL parameters 36
2.8 Beam size at the diagnostic tool for nominal optics 36
2.9 Main transfer line parameters 37
2.10 Geometrical and RF parameters of the debunching cavities 39
2.11 Physical lengths, apertures and strengths of KSW and BS injection bumper magnets . . 44
3.1 Emittance increase between 3 and 160 MeV for a uniform and Gaussian beam 51
3.2 Total error amplitudes used for sensitivity studies 52
3.3 Sensitivity of Linac4 to RF errors 54
3.4 Sensitivity of Linac4 to transverse errors 54
3.5 Comparison between TraceWin and IMPACT results 55
3.6 Beam loss due to misalignment and gradient errors assuming correction with steerers . . 56
3.7 Beam loss due to rest-gas stripping assuming an average current of 40 mA and 0.1% duty cycle 57
4.1 Main parameters of the LEP-type klystrons 64
4.2 Main Parameters of the LEP-type circulators 64
4.3 Main parameters of the 704 MHz klystrons 65
4.4 Summary of the diagnostics instrumentation foreseen for Linac4 72
4.5 CCDTL and SCL quadrupole characteristics 75
4.6 Linac steering magnet characteristics 76
4.7 Quadrupole characteristics (transfer line) 76
4.8 Characteristics of the bending magnets in the transfer line 77
4.9 Characteristics of magnets installed in the actual LT, LTB and BI line to be reused for Linac4 80
4.10 Main parameters of the PMQ's for the Linac4 DTL 81
4.11 Main BI.DIS kicker system parameters 82
4.12 Main BI.SMV magnet parameters 83
4.13 Proposed nominal BI.DIS generator parameters 84
4.14 Assumed PFN sizes using a single PFN line 85
4.15 Operational characteristics of pulsed solid state modulators for klystrons 89
4.16 Operational characteristics of HV-DC power converters with output crowbar for RF amplifier tubes 89

4.17 Operational characteristics of pulsed MaxiDiscap power converters for CCDTL and SCL quadrupoles . . . 91
4.18 Operational characteristics of pulsed MiniDiscap power converters for steerers . . . 92
4.19 Operational characteristics of pulsed MaxiDiscap power converters for TL quadrupoles . 92
4.20 Operational characteristics of switch-mode current-regulated power converters for bending magnets . . . 93
4.21 Operational characteristics of high-current pulsed power converters for BI septa . . . 94
4.22 Power converter maximum ratings . . . 95
4.23 Full list of power converters for the 3 MeV test stand . . . 96
4.24 Overview of vacuum equipment needed for each part of Linac4 . . . 97
4.25 Errors associated with the alignment of the DTL tanks . . . 98
4.26 Errors associated with the alignment of the CCDTL& SCL modules . . . 98
5.1 Designation of radiation areas . . . 101
5.2 Source terms for 10 W proton losses, attenuation length in concrete and shielding required to obtain a dose equivalent rate of 0.5 μSv/h, 3 μSv/h or 10 μSv/h at 4 m distance from the beam line, corresponding to a non-designated, supervised or controlled area, respectively . . . 103
5.3 Dose rates outside the proposed shielding at selected energies for a full beam loss . . . 104
5.4 Dimensions and attenuation factors of the five legs of the waveguide labyrinth at the high-energy end of Linac4 . . . 105
5.5 Thickness of the concrete shield required around the beam transfer line for different loss scenarios . . . 106
6.1 Water cooling needs for Linac4 . . . 116
6.2 Cooling needs for RFQ . . . 116
6.3 Indoor conditions and internal loads . . . 117

Acronyms and abbreviations

ADC	Analog Digital Converter
BINP	Budker Institute of Nuclear Physics, Russia
BLM	Beam Line Monitor
BLVD	Bunch Length and Velocity Detector
BSM	Beam Shape Monitor
BSHM	Beam Shape and Halo Monitor
CARE	Coordinated Accelerator Research in Europe
CCDTL	Cell-Coupled Drift Tube Linac
CCL	Coupled-Cavity Linac
CEA	Commissariat pour l'Energie Atomique, France
CMW	Controls MiddleWare
CPU	Central Processing Unit
CW	Continuous Wave (operation)
DC	Direct Current
DESY	Deutsches Elektronen SYnchrotron, Germany
DSP	Digital Signal Processor
DTL	Drift Tube Linac
ECL	Emitter Coupled Logic
EMC	Electro-Magnetic Compatibility
EMQ	Electro-Magnetic Quadrupole
EU	European Union
FE	Finite Elements
FESA	Front-End Software Architecture
FPGA	Field Programmable Gate Array
GMT	General Machine Timing
GPS	Global Positioning System
HEBT	High-Energy Beam Transport
HIPPI	High Intensity Pulsed Proton Injectors
HLS	Hydrostatic Levelling System
HVAC	Heating Ventilation and Air Conditioning
IGBT	Insulated Gate Bipolar Transistor
IN2P3	Institut Nationale de Physique Nucléaire et de Physique des Particules, France
INR	Institut for Nuclear Research, Russia
IPHI	Injecteur de Protons de Haute Intensité, France
ISOL	Isotope Separator On-Line
ISOLDE	Isotope Separator On Line Experiment at CERN
ISTC	International Science and Technology Center, Russia
ITEP	Institute for Theoretical and Experimental Physics, Russia
JPARC	Japan Proton Accelerator Research Complex, Japan
JRA	Joint Research Activity
JTAG	Joint Test Action Group
LEBT	Low-Energy Beam Transport
LEIR	Low-Energy Ion Ring at CERN
LEP	Large Electron–Positron collider at CERN
LHC	Large Hadron Collider at CERN

LIBO	LInac BOoster
Linac	Linear accelerator
LLRF	Low-Level RF
LPSC	Laboratoire de Physique Subatomique et de Cosmologie, France
MEBT	Medium Energy Beam Transport
MOSFET	Metal Oxide Semiconductor Field Effect Transistor
NAOS	New Analog Observation System
TOF	Time Of Flight
OASIS	Open Analog Signals Information System
OFE	Oxygen Free Electronic
PCI	Peripheral Component Interconnect
PCM	PCI Mezzanine Card
PFC	Power Factor Correction
PFN	Pulse Forming Network
PFW	Pole Face Winding
PLC	Programmable Logic Controller
PMQ	Permanent Magnet Quadrupole
ppb	protons per bunch
PS	Proton Synchrotron at CERN
PSB	PS Booster at CERN
PVSS	ProzessVisualisierungs und Steuerungs-System
RF	Radio Frequency
RFQ	Radio Frequency Quadrupole
r.m.s.	root mean square
SCADA	Supervisory Control and Data Acquisition
SCL	Side-Coupled Linac
SEM	Secondary Electron emission Monitor
SNS	Spallation Neutron Source, USA
SPL	Superconducting Proton Linac study at CERN
SPS	Super Proton Synchrotron at CERN
TCU	Temperature Control Units
TL	Transfer Line
TTL	Transistor–Transistor Logic
UPS	Un-interruptible Power Supply
UTC	Coordinated Universal Time
VME	Virtual Machine Environment
VNIIEF	All-Russian Scientific Research Institute of Experimental Physics, Russia
VNIITF	All-Russian Scientific Research Institute of Technical Physics, Russia
WPS	Wire Positioning System

Chapter 1

Introduction

1.1 Linear accelerators at CERN

The linear accelerator is the first vital stage of any hadron accelerator complex. The linac generates the initial transverse and longitudinal beam emittances and thereby defines the beam quality for the next stages of acceleration. Moreover, the reliability of the linac injector has to be the highest of the entire accelerator complex, a fault of the linac shutting down all other machines.

The history of CERN accelerators illustrates the importance of having a modern linear accelerator, capable to fulfil the ever increasing needs of a versatile accelerator complex. The pioneering 50 MeV Linac1 started operation in 1959, injecting into the PS a beam of a few mA. Soon after commissioning, the PS required continuous increases in the linac current, which was eventually raised to 50 mA by the mid-70s, after several hardware upgrades. The commissioning of the PS Booster in 1972 further increased the strain on Linac1, now at the limit of its capabilities. The increasing demands on the linac together with the need to modernise the injectors in preparation for the SPS construction led to the decision to build Linac2, designed for a proton current as high as 150 mA, but bound to the PSB injection energy of 50 MeV [1].

Since its commissioning in 1978, Linac2 is the workhorse of the CERN accelerator complex. It went through some upgrades, the most notable being the replacement in 1993 of the 750 keV Cockroft-Walton pre-injector with a Radio Frequency Quadrupole (RFQ) that pushed the current up to 180 mA. Apart from the front-end the basic hardware is the same as at the time of commissioning. Even if the Linac2 reliability has been steadily improving during the 80's and 90's, reaching the remarkable availability of 98.5% averaged over the last 10 years, important vacuum leaks have been progressively appearing on the large 202 MHz accelerating tanks, requiring important repair interventions during the shut-down periods and being a constant cause of concern for future operation. Moreover, the RF tubes used in the Linac2 RF system will soon go out of production because of their obsolete design, dating back to the times of Linac1. The consequence is that, to keep Linac2 running, CERN will have to decide between buying and stocking a large amount of RF tubes or rebuilding the RF system with more modern devices.

It is also worth mentioning that, since Linac2 was designed 30 years ago, the technology of linear accelerators has significantly progressed, the most notable advance being the widening use of H^- acceleration and injection. Charge-exchange injection of H^- in a ring through a stripping foil allows accumulating protons over many turns without blowing up the emittance. In the linac, the total beam current can be distributed over longer pulses with lower peak current than for protons, which translates into substantial savings in the cost of the RF systems, usually dimensioned for peak power and peak current. At the moment of Linac2 construction the H^- technology was at its early beginning, and the choice was made to keep the conservative proton acceleration for the new CERN linac. However, during the last 20 years, most laboratories having proton synchrotrons with a linac injector have adopted H^-, the only ones left with proton injection being CERN and IHEP (Protvino).

Other recent advances in the linac technology are the use of higher frequencies, allowing for more compact accelerating structures with higher efficiency, and newer approaches to beam dynamics design. The latter are made possible by modern simulation codes and by a better understanding of halo formation phenomena, a particular concern in high space-charge systems like linear accelerators. Another modern technology applied in many laboratories is the chopping of the linac beam at low energy by dedicated chopping sections, with the goal of removing at low energy the bunches that would fall outside the buckets in the synchrotron. It should be stressed that both beam dynamics studies and chopping schemes are aimed at the reduction of beam loss and of the induced radioactivity in the linac and in the ring, well

in line with the general trend of reducing activation around particle accelerators.

Considering the cost to maintain a reliable operation of Linac2 today and in the future, and the many advantages of a new up-to-date H^- linac, it became clear after the successful running in of the heavy-ion Linac3 in 1994, that the next priority for the linac team was to analyse the option of building a new linac injector for protons at CERN.

1.2 From SPL to Linac4

The preparation of the CERN injectors for the LHC, which took place in the years 1995-2000 [2], allowed reaching the LHC goals but at the same time showed clearly that the present injectors are at the limit of their capabilities in terms of both brightness (for LHC) and intensity (for other users).

During the same years, the foreseen decommissioning of the LEP collider with its powerful 352 MHz RF system triggered the proposal to build a modern high-energy high-intensity linear accelerator at 352 MHz based on the LEP RF technology. The first designs were addressed at energy production applications [3], but soon came a proposal to build a 2 GeV linac at CERN to inject directly into the PS ring [4]. After some studies, this idea materialised into the conceptual design of a 2.2 GeV H^- linac called the Superconducting Proton Linac (SPL) published in 2000 [5]. This machine was meant to produce a low-intensity and high-brightness beam in the PS for LHC, but at the same time to generate high-intensity beams for other potential users, like a neutrino factory or a radioactive ion beam facility. In its original design as well as in the recent design update [6], the SPL is a modern H^- linac, equipped with a chopping section and with a sophisticated beam dynamics design. The starting RF frequency of 352 MHz is almost ideal for a linear accelerator of protons (or H^-), providing a good compromise between size, maximum gradient and focalisation in the first stages of acceleration.

The low-energy front-end of the SPL uses normal-conducting accelerating structures up to an energy of 180 MeV. The initial part up to 160 MeV energy is now proposed as the successor of Linac2, with the name of Linac4 [7]. The length of Linac4 is compatible with the space available in the PS South Hall, making possible an effective reuse of existing building, water and electricity infrastructure. In case of SPL approval, the entire Linac4 could be reused, although in a different location defined by future needs.

During the past few years R&D activity has been focused on Linac4 with important participations from external laboratories. The main contribution is the collaboration on the IPHI RFQ with CEA and IN2P3, whose outcome will be the delivery of the IPHI RFQ at CERN, to be used in the front-end of Linac4. The R&D on other subjects like chopping, beam dynamics and accelerating structures has been integrated in the HIPPI (High Intensity Pulsed Proton Injectors) Joint Research Activity (JRA) partially funded by the EU inside the CARE initiative. Other collaborations have been launched with Russia for the construction of prototype accelerating structures with the support of the International Science and Technology Center (ISTC) in Moscow. Promising contacts have been established with India, China and recently with Pakistan.

The conceptual design of Linac4 has been published in several papers [7,8]. The present technical design report represents at the same time the outcome of a 5-year R&D effort and a further step in the definition of the project, coming for the first time to a detailed definition of the different linac sub-systems and to the integration between the linac design and the modifications required for H^- injection into the PS Booster.

1.3 Performance of the CERN accelerator complex with Linac4

While it has been demonstrated that the nominal LHC luminosity ($1.0 \times 10^{34}\,\mathrm{cm}^{-2}\mathrm{s}^{-1}$) can be reached and slightly exceeded with the present LHC injector chain (Linac2, PSB, PS and SPS) [2], it is now clear that attaining and possibly exceeding the ultimate luminosity of $2.3 \times 10^{34}\,\mathrm{cm}^{-2}\mathrm{s}^{-1}$ will require higher beam brightness (intensity/emittance) from the injector chain, which can be obtained only after a

major upgrade of the LHC injectors [9]. Using double-batch injection from the PSB, the PS can currently deliver the LHC beam with a maximum population of about 1.4×10^{11} ppb (protons per bunch), sufficient to obtain the nominal beam characteristics at 450 GeV in the SPS (1.15×10^{11} ppb within a normalised emittance $\varepsilon_{\rm n} = 3.5\,\mu$m). Although the systematic on-going investigations are expected to improve transmission in the cascade of accelerators, the PSB with Linac2 will never allow to reliably operate at the ultimate performance level of 1.7×10^{11} ppb in the LHC.

Different schemes for increasing the brightness out of the PS have been considered and several limitations to higher beam brightness have been identified [9]. The first bottleneck is the space-charge dominated injection into the PS Booster. Removing this restriction with the construction of a new higher energy linac replacing the 50 MeV Linac2 appears as the scenario offering most advantages in terms of reliability and flexibility. A basic requirement for the new linac injector is the ability to make the LHC beam in a single PSB batch instead of the present double batch, which requires doubling the bunch population in the PSB within constant normalised transverse emittances. Delivering to the PS 4.1×10^{12} protons/ring, the brightness out of the PSB will be doubled and the single-batch operation for LHC will considerably simplify operation and reduce the filling time, with a beneficial effect on integrated luminosity. If the transfer efficiency is finally brought up to $\approx 100\%$, the ultimate bunch population of 1.7×10^{11} ppb in the LHC could be obtained with single-batch filling of the PS by the PSB. Alternatively, double-batch operation of the PSB could still be used to "comfortably" provide and probably significantly exceed the ultimate beam characteristics. Another possibility would be to use all 4 rings of the PSB instead of 3 as presently foreseen. This would, however, involve new splitting schemes and hardware modifications in the PSB which have not been studied in detail so far.

The fundamental parameter to consider at PSB injection is the incoherent space-charge tune shift, which can be estimated for lattices with "smooth" behaviour of the lattice functions and no strong changes of the ratio between horizontal and vertical betatron functions, by:

$$\Delta Q_{\rm x,y} \propto \frac{I_{\rm p}}{\varepsilon^*_{\rm x,y}\beta\gamma^2} \tag{1.1}$$

where $\Delta Q_{\rm x,y}$ is the incoherent (self field) detuning in the horizontal (x) and vertical (y) planes, $I_{\rm p}$ is the bunch peak current, $\varepsilon^*_{\rm x,y}$ are the normalised emittances (the ratio $I_{\rm p}/\varepsilon^*_{\rm x,y}$ is the beam brightness), and β and γ are the usual relativistic factors. Keeping the present tune shift in the PSB while doubling the brightness is possible by increasing by a factor of 2 the relativistic factor $\beta\gamma^2$ at injection; this corresponds to an increase in the injection energy to 160 MeV from the present 50 MeV. The flexibility given by the charge-exchange H^- injection mechanism for painting in the PSB acceptance should allow preserving the higher brightness during the acceleration process. Simulation results of the injection and acceleration of the Linac4 beam in the PSB are presented in Section 3.5.

The ISOLDE experiment, the only direct user of the PSB, will also benefit from Linac4. The present intensity for ISOLDE is limited by space-charge tune shift to some 3.2×10^{13} protons/pulse. In principle, twice the intensity could be achieved for the same tune shift. However, with the present injection at 50 MeV the vertical space-charge tune spread exceeds 0.5 and, thus, the vertical tune has to be shifted above the vertical half-integer resonance to $Q_{\rm V} \approx 4.55$. In preliminary simulations of H^- injection at 160 MeV beam into the PSB, no feasible scheme with such a high working point has been found up to now and if further studies do not succeed in finding such a scheme, the assumption that the intensity can be doubled should be considered slightly optimistic. However, even with a working point just below the vertical half-integer resonance, a substantial increase in the average current, compensating at the same time for the reduced number of pulses that will be available for ISOLDE once LHC is in operation, can be expected.

In terms of expected performance, the typical impact of Linac4 (accompanied by proper modifications to the LHC injectors, like the reduction of the PSB-PS repetition period to 0.9 s and some upgrades to PS and SPS for higher intensity), is summarised in Table 1.1 [9]. Thanks to smaller trans-

verse emittances, high-intensity beams should be more efficiently transmitted between accelerators. The improvement for neutrino experiments could ultimately reach a factor 1.7 (flux increase to CNGS from 4.5×10^{19} to 7.5×10^{19} pr./year), provided that the CNGS experiment is given priority over the other fixed-target experiments like COMPASS. For radioactive ions, a maximum factor 3.5 can be achieved (from 1.9 to 6.4 μA) assuming a doubled intensity per pulse and more pulses available for ISOLDE. The bunch population out of the PS could reach the LHC ultimate figure of 1.7×10^{11} protons in a 72 bunch train with single-batch injection from the PSB, if beam transmission from PSB to PS ejection is brought up to $\approx 100\%$.

The replacement of the ageing Linac2 with the new Linac4 is an important contribution to the general consolidation of the CERN accelerators which will reduce the "turn-around time" for LHC (time between physics coasts) and hence increase its integrated luminosity. It is also a fundamental component of all scenarios for upgrading the luminosity in the LHC and for increasing the flux of protons available to all experiments. Finally, Linac4 can also become the front end of a superconducting proton linac (the SPL), which can replace the PSB and open the way for a future extension of the CERN accelerator complex towards higher performance and for addressing the needs of new physics experiments on neutrinos and/or radio-active ions.

Table 1.1: Beam intensities to be delivered by the PSB assuming 100% transmission to the LHC and, where applicable, beam intensities in the PS after injection. Also quoted are the intensities required if the transmission efficiency from PSB to LHC at 7 TeV is 85% for the nominal beam and 80% for the ultimate.

Beam	**PSB intensity per ring for loss-free / lossy transmission to LHC** [10^{12} particles]	**PSB tr. emittances r.m.s. normalised normalised** [μm]	**PS intensity after injection loss-free / lossy** [10^{12} particles]
LHC nominal			
Linac2 [1)] (double batch)	$1.38/1.62$ (1 bunch per ring)	2.5 (H) 2.5 (V)	$8.3/9.7$ (6 bunches)
Linac4 [3)] (single batch)	$2.76/3.25$ (2 bunches per ring)	2.5 (H) 2.5 (V)	$8.3/9.7$ (6 bunches)
LHC ultimate			
Linac2 [1,2)] (double batch)	$2.04/2.55$* (1 bunch per ring)	2.5 (H) 2.5 (V)	$12.2/15.3$ (6 bunches)
Linac4 [3)] (single batch)	$4.08/5.1$* (2 bunches per ring)	2.5 (H) 2.5 (V)	$12.2/15.3$ (6 bunches)
Linac4 [3)] (double batch)	$4.08/5.1$ (1 bunch per ring)	2.5 (H) 2.5 (V)	$12.2/15.3$ (6 bunches)
CNGS			
Linac2 (double batch)	6.25 (1 bunch per ring)	11.5 (H) [4)] 4.6 (V) [4)]	50 (8 bunches)
Linac4 (single batch)	12.5 (2 bunches per ring)	11.5 (H) [4)] 4.6 (V) [4)]	50 (8 bunches)
ISOLDE			
Linac2 (single batch)	8.0 (1 bunch per ring)	12 (H) [4)] 7 (V) [4)]	–
Linac4 (single batch)	16.0 (1 bunch per ring)	12 (H) [4)] 7 (V) [4)]	–

1) Standard double-batch scheme with Linac2: the PSB provides a total of 6 bunches from 6 rings, filling six out of seven PS buckets. Gymnastics in the PS are used to split every PSB bunch in 12 LHC bunches.

2) Request can be satisfied at present by 3 PSB rings only (1, 2 and 4).

3) Standard single-batch scheme with Linac4: the PSB provides a total of 6 bunches from 3 ring (2 bunches/ring), filling six out of seven PS buckets. The spacing between bunches at ejection from the PSB is adjusted with RF on the first harmonic. The same gymnastics are used in the PS to split every PSB bunch in 12 LHC bunches.

4) Maximum acceptable emittances estimated from the acceptances of the PS machine (60 μm (H) and 20 μm (V)), assuming (pessimistically) Gaussian beams and allowing maximum losses of 1%; resulting maximum physical rms emittances are about 5 μm (H) and 2 μm (H).

*) Not feasible.

1.4 Choice of parameters and linac layout

The main Linac4 parameters are based on the requirements for PSB injection. Emittances are defined by the stringent needs of LHC while the maximum number of ions per pulse is defined by ISOLDE which should expect up to 6.4×10^{13} protons per cycle. Adding a safety margin to this figure, it has been decided to design Linac4 for a maximum of 1×10^{14} particles per pulse. The maximum repetition frequency for Linac4 is given by the limiting frequency of the PSB of 2 Hz. The average beam current required out of Linac4 is then 2×10^{14} protons/s, or 32 μA, corresponding to a beam power of 5.1 kW at the linac final energy of 160 MeV.

Considering the limits of present source technology and the overall RF requirements, the average current during pulse has been fixed to 40 mA, corresponding to a pulse length of 0.4 ms. The beam duty cycle of Linac4 is then 0.08%. Considering an RF pulse length of 0.5 ms, the corresponding RF duty cycle is 0.1%.

The chopping scheme, described in Section 2.3, allows removing some of the linac bunches, thus avoiding beam loss during longitudinal capture in the PSB. With the selected parameters, the pulse current before chopping has to be as high as 64 mA. Taking reasonable margins for beam loss in the low-energy transfer line between ion source and RFQ and in the chopping line, the RFQ output current is nominally set at 70 mA and the source current, at 80 mA. The target value for the transverse emittance out of the source has been set to 0.2 π mm mrad, a value compatible with present source technology that will allow for about a factor 2 reduction in the emittance at PSB entrance with respect to the present Linac2. The overall Linac4 beam parameters are summarised in Table 1.2.

Table 1.2: Linac4 beam parameters

Ion species	H^-
Output energy	160 MeV
Bunch frequency	352.2 MHz
Max. rep.-rate	2 Hz
Beam pulse length	400 μs
Max. beam duty cycle	0.08%
Chopper beam-on factor	62%
Chopping scheme	222/133 full/empty buckets
Source current	80 mA
RFQ output current	70 mA
Linac current	40 mA
Average current	0.032 mA
Beam power	5.1 kW
No. particles per pulse	1.00×10^{14}
No. particles per bunch	1.14×10^{9}
Source transverse emittance	0.2 π mm mrad
Linac transverse emittance	0.4 π mm mrad

The operating frequency of Linac4 is dictated by the availability of klystrons, circulators and waveguides at 352.2 MHz from the LEP RF system and by the use of the RFQ from the IPHI project. This frequency is particularly suited for a linear accelerator because it offers a good compromise between the large dimensions and relaxed fabrication tolerances of structures at low frequency and the high gradients and efficiencies allowed by higher frequencies. It is foreseen to double the RF frequency to 704.4 MHz in the latter sections of Linac4, in order to increase efficiency and gradient when the cell length, proportional to the particle β, becomes large enough to allow for more comfortable construction tolerances.

The overall architecture of Linac4 is shown in Fig. 1.1. The chosen sequence of accelerating sections is quite standard for modern pulsed linac designs. The ion source is followed by a Radio Frequency Quadrupole (RFQ), a chopping line and the accelerating structures. Three types of accelerating structures bring the energy up to 160 MeV: a Drift Tube Linac (DTL) up to 40 MeV, a Cell-Coupled Drift Tube Linac (CCDTL) up to 90 MeV and finally a Side Coupled Linac (SCL) to the final energy. A long transfer line equipped with debunching and collimation sections connects Linac4 to the existing Linac2 transfer line.

As part of the Linac4 project, the transfer line between Linac and PSB needs to be upgraded for operating at 160 MeV and charge-exchange injection has to be implemented in the PSB.

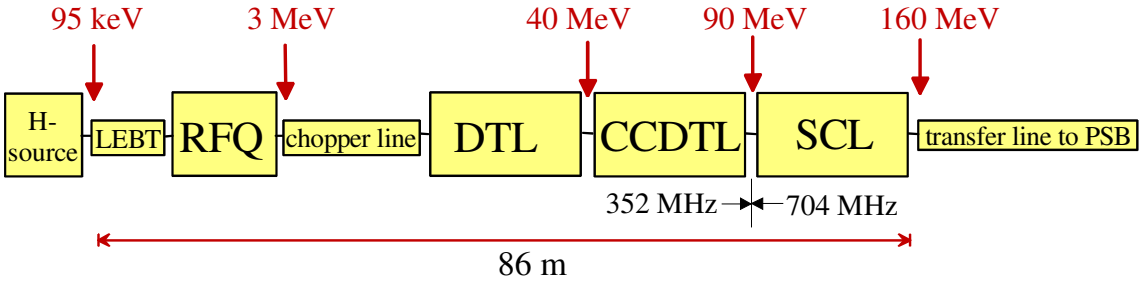

Figure 1.1: Scheme of Linac4

The transition energies between the different linac sections have been carefully optimised. While the extraction energy from the source (95 keV) is imposed by the input energy of the IPHI RFQ under construction, the energy of the chopper line, at the transition between RFQ and DTL has been analysed in more detail. While the voltage limitation of the chopper deflector suggests chopping at low energy, space-charge effects and the difficulty in the construction of the first drift tubes of the DTL pushes for a higher energy and a longer DTL period, which is proportional to beam velocity. However, the main concern for chopping at high energy is radiation generated by the dumped part of the beam and by the collimation section required before injection into the DTL. For this reason, the compromise energy of 3 MeV has been selected, at the limit for nuclear reactions inside copper. The first nuclear reaction can take place by tunnelling of the Coulomb barrier at energies above 2 MeV, though the cross section at 3 MeV is still small so that no appreciable radiation levels are expected around the chopper line.

The transition energies between the different accelerating sections (DTL, CCDTL and SCL) are related to RF consideration and discussed in Chapter 2.

It must be mentioned that, although the duty cycle of Linac4 is only 0.1%, the accelerating structures and the focusing system have been designed for a maximum duty cycle of 10%, to keep a margin for future operation of Linac4 as first part of the high-energy high-intensity SPL. As a general principle, all the hardware (accelerating structures, magnets, diagnostics, RF high-power components, etc.) of the linac will be built for high-duty operation, but the electronics (power supplies, etc.) and the infrastructure will be dimensioned only for the low duty cycle required for the PSB. The rationale behind this choice is that for structures and RF components there is only a limited increase in price for integrating from the beginning the option to run at high duty cycle, while for components like power supplies and for the electrical and cooling infrastructure the cost is often proportional to the duty cycle. Moreover, electronic components and power supplies could already be obsolete at the moment when the SPL is built.

Chapter 2

Design overview

2.1 Source and low-energy beam transport

Today there are two major types of H^- sources, surface and volume sources. A review of their technical principles, advantages and disadvantages is given in [10]. Not all of these ion sources are well suited for accelerator operation where intensity, short- and long-term stability, reliability and easy maintenance are of major importance. Reference [11] gives an overview of operational sources and source developments for high-intensity accelerators.

The technology of existing sources raises a number of questions. In many cases caesium is used to produce high H^- currents, but caesium pollution of the beam channel can give rise to voltage holding problems in the following accelerator structures. And the caesium injection lines can be clogged by caesium hydride, leading to lifetime limitations. The source emittance is defined mainly by the source structure and the principle of the H^- creation and can only be influenced to a small extent. For a fully optimised source there is a lower limit of the emittance that can be only overcome by cutting the beam intensity at the same time. It is also important to note, that the beam is in real space not necessarily round and homogeneous, influencing the beam dynamics in the following structures. The lifetime of filaments, cathodes or antennas inside the plasma chamber is a limiting factor for the reliability.

The requirements of 80 mA H^- current, 0.4 ms beam pulse, 2 Hz repetition rate, 0.25 π mm mrad normalised r.m.s. emittance for Linac4 cannot be met by one of the existing sources. The design and construction of a new source requires a long development time, and it cannot be guaranteed to reach the required parameters, thus the conservative approach for Linac4 is to copy an existing successful source design close to our specifications and try to improve it. After comparing the existing sources in terms of performance, long-term stability and reliability, the choice went to the DESY RF source (Fig. 2.1) [12, 13].

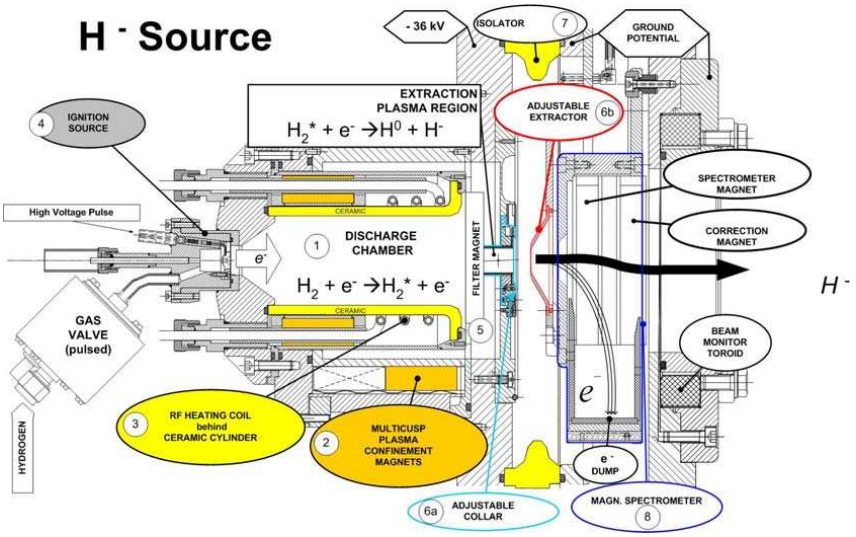

Figure 2.1: The DESY volume H^- source [13]

This source is an RF volume source, which delivers routinely 40 mA of H^- at an extraction voltage of 35 kV. The pulse length is 100 μs, the repetition rate 5 Hz and the emittance 0.25 π mm mrad (r.m.s., normalised). The source runs without caesium and has up to now a lifetime of 25,000 hours. Experiments with the source showed already currents up to 54 mA [12]. The pulse length is limited presently by the

available RF generator but a short test with a borrowed generator showed that the source can run with a pulse length of up to 3 ms. A collaboration with DESY was set up to exchange information and knowledge about the source. Development work of other groups with similar source types (e.g., at SNS) will also supply a valuable input. A test source will be assembled soon, retaining the DESY design and aiming at increasing the output current up to the Linac4 value by using a new RF generator with higher power output developed at CERN.

Due to the fact that the extraction voltage of the DESY source is lower than the 95 kV necessary for the injection into the RFQ, a post-acceleration from 35 kV to 95 kV needs to be included in the CERN design. The basic idea is to put the DESY RF source including the electronics (except the 2 MHz RF generator) on a 60 kV high voltage (HV) platform housed in a cage. In this way the source itself does not need to be modified. The outer DESY bucket (basically the right part behind the insulation ring in Fig. 2.2) is kept on a 60 kV HV platform. The inner DESY bucket (left part in Fig. 2.2) is kept at -35 kV and placed on a 35 kV HV platform with respect to the 60 kV platform. The two high voltage parts of the source are interlinked by a two electrode post-acceleration system. A simulation of the extracted beam showing the shape of the post-acceleration system is presented in Fig. 2.3.

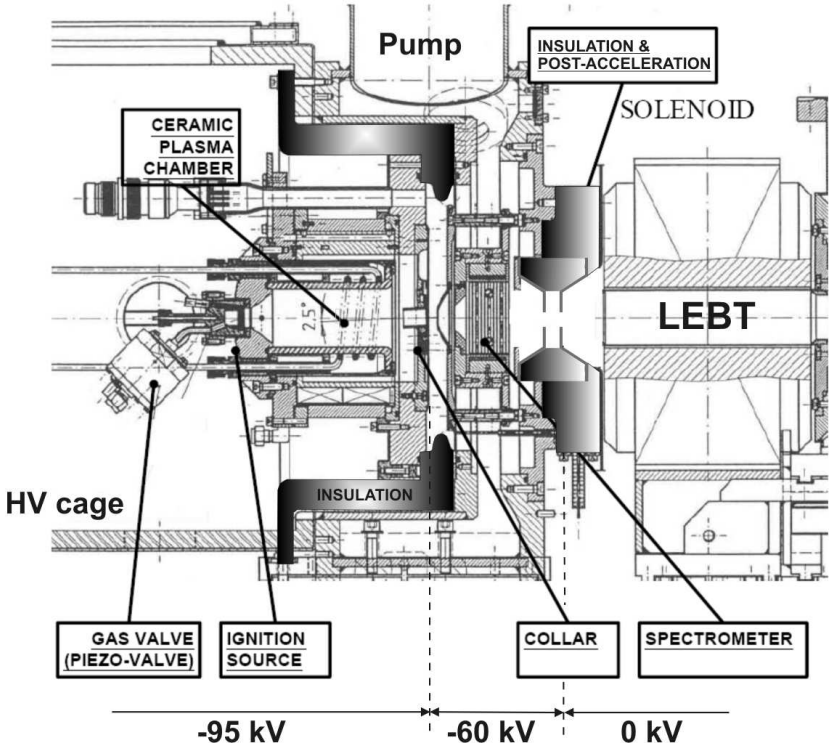

Figure 2.2: Schematic view of the post-acceleration system

The Low-Energy Beam Transport (LEBT) line provides the beam matching from the source to the RFQ and contains the diagnostics to monitor the source. The scheme of the LEBT for Linac4 is given in Fig. 2.4. The beam emerging from the source post-acceleration system will be more than 30 mm in diameter, and with a total divergence of approximately 100 mrad. Therefore, large diameter solenoids are required for the focusing. The same design as the DC solenoids of Linac3 [14] could be adopted, also allowing tests of longer pulse beams. The space-charge of long-pulse, unbunched beams can be suppressed by the capture of positive ions into the potential well of the beam [15], and simulations of beam transport have been made assuming that 10% of the beam current is not compensated. These show that the beam from the post-acceleration can be transported to the RFQ with less than 10% emittance growth using the Linac3 type solenoids, assuming a uniform particle distribution in horizontal-vertical space.

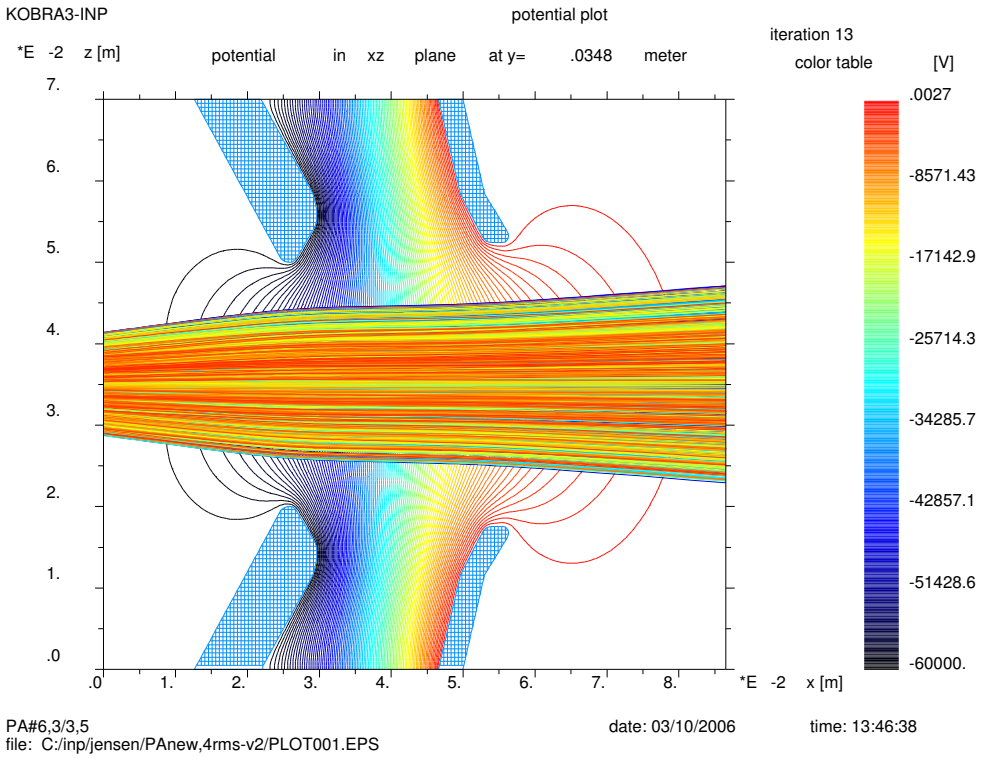

Figure 2.3: Beam simulation plot (program KOBRA) showing the post-acceleration system with shaping lens (left) at 60 kV and ground lens (right) with field levels and particle trajectories

A comparison of different solenoid types (the Linac2 pulsed design with a 60 mm aperture, the Linac3 solenoids and the LEP Injector Linac DC solenoid with 180 mm aperture), is shown in Table 2.1. The small emittance growth with the Linac3 solenoids confirms that they are a suitable choice for the LEBT. There is slightly smaller emittance growth using the LIL-SNS solenoids; however they would need to be pushed to considerably higher currents than their design value and would require significantly more expensive power supplies.

Table 2.1: Twiss parameters and emittance growth for different LEBT setups

	α	β [mm/mrad]	ε (r.m.s., unnormalised) [mm mrad]	$\Delta\varepsilon/\varepsilon$ (LEBT) (LEBT) [%]	$\Delta\varepsilon/\varepsilon$ (LEBT+ post-acc.) [%]
Linac2 type (L2)	1.5	0.076	23.7	20	35
Linac3 type (L3)	1.4	0.067	21.0	6.6	20
LIL-SNS	1.4	0.060	20.8	5.6	19

Beam space-charge compensation requires a time τ for the production of sufficient ions through beam impact ionization, given by $\tau = 1/n\sigma\nu$ where n, σ and ν are the residual gas density, the beam-molecule ionization cross-section and the beam velocity respectively. Typical cross-sections for H_2 ionisation by 100 keV protons are 2×10^{-16} cm^{-2} [16], leading to a compensation time of approximately 8 μs at 5×10^{-5} mbar. The pressure in the line will be regulated by gas injection, and the first measurements will be made with hydrogen, followed by other gases. At such a pressure pumping requires a turbo-molecular pumping group.

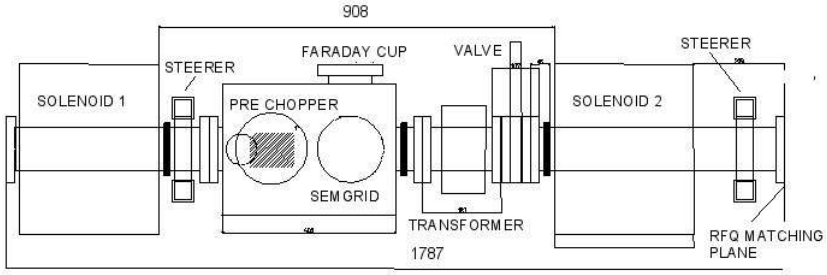

Figure 2.4: Schematic layout of the LEBT line

These relatively high vacuum pressures will cause negative ion stripping in the line, which will lead to losses in the range of 5 to 15% depending on the pressure and the gas used. Beam steering to the RFQ acceptance is made with 2 sets of horizontal and vertical steerers. Simulations have shown that within reasonable limits, there is little additional emittance growth caused by entering the solenoids with a small displacement or angle. The beam from an RF source will typically require 100 μs to stabilise. This beam can be prevented from entering the RFQ by using a pre-chopper, deflecting the beam away from the RFQ input. The fall-time of the pre-chopper need not be faster than 5 μs, as additional time will be required for the re-stabilisation of the space-charge compensation. The pre-chopper location will have to be carefully selected, because the beam has to be dumped close to the RFQ input aperture.

2.2 Radio-frequency quadrupole

After the ion source and the LEBT, a Radio-Frequency Quadrupole (RFQ) will perform the beam capture and bunching and will accelerate to the energy of 3 MeV. In order to avoid the development of a dedicated RFQ for Linac4 and SPL, in 2001 CERN has signed a collaboration agreement with the French IPHI (Injecteur de Protons de Haute Intensité) project, a CEA and IN2P3 joint effort to realise a high-intensity, CW RFQ [17]. The IPHI RFQ has been designed as a 100 mA proton CW accelerator, operating at 352.2 MHz, to explore the injector issues of high-intensity linacs for transmutation and other applications. The original IPHI design output energy of 5 MeV has been reduced to 3,MeV after the agreement with CERN, in order to make the RFQ compatible with the SPL/Linac4 design. After a CW test scheduled for the second half of 2007 in a dedicated test stand being prepared at CEA Saclay, the IPHI RFQ will be delivered to CERN in 2008 to be integrated into the new 3 MeV test stand, where it will operate at the much lower duty cycle of Linac4.

The IPHI RFQ is 6 m long and is made of three segments that are resonantly coupled to each other by means of two coupling cells. Each segment is composed of two modules, 1 metre each, mechanically coupled to each other. The end of the third segment, at the RFQ output, houses a fringe field cell. Figure 2.5 shows the module 1 of the IPHI RFQ after brazing, while Fig. 2.6 shows a 3D plot of the assembled RFQ, complete with the vacuum manifolds and the RF input couplers.

The RFQ has been designed for maximum transmission at 100 mA current, in order to minimise activation when operating CW, and with a constant maximum peak field of 31 MV/m (1.7 kilpatrick), to minimise the risk of breakdowns. These requirements resulted in a design with variable transverse focalisation, where both the voltage and the vane transverse curvature radius change along the RFQ. The main beam dynamics design parameters along the RFQ are shown in Fig. 2.7 (a) and (b). The vane voltage changes from 87 to 122 kV.

The dependence of the multi-pole components in the electromagnetic field from the vane transverse profile has been extensively analysed by means of the PARMTEQM code. The RFQ cavity has been designed with the constraint that the ratio between the dipole component of the field, responsible for the beam de-focalisation, and the main quadrupole mode in the cavity is always kept below 4.5%. In

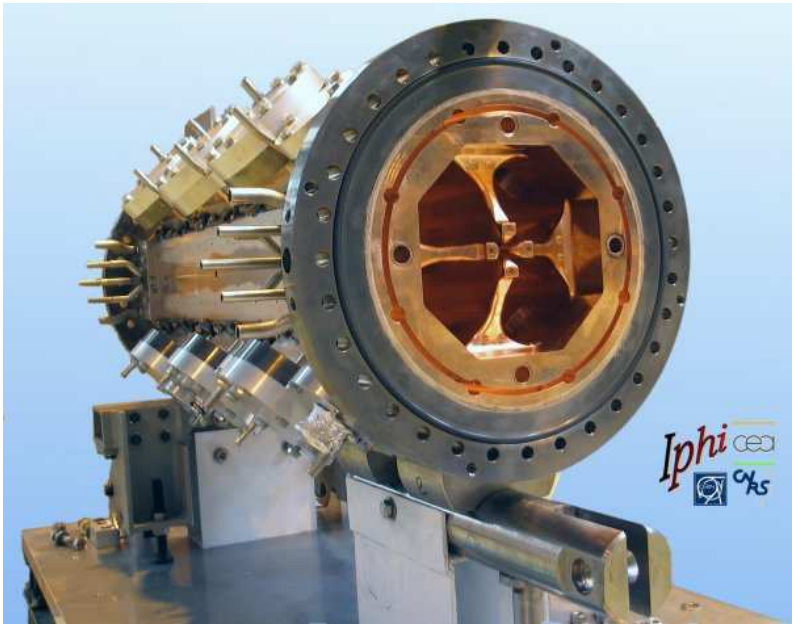

Figure 2.5: Module 1 of the IPHI RFQ after brazing

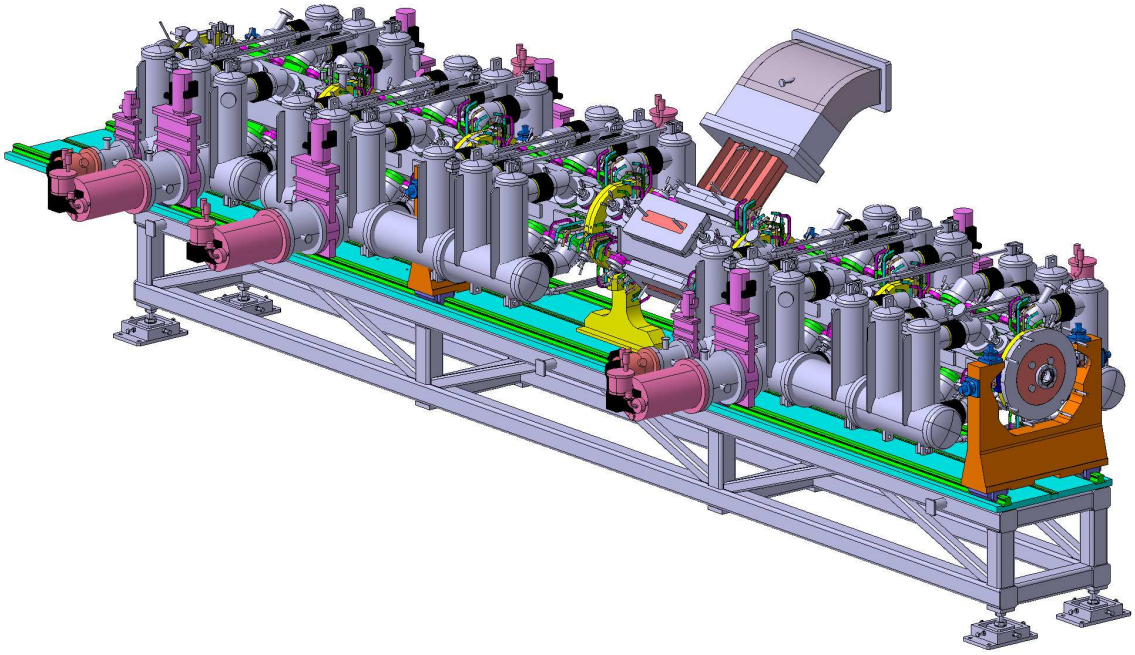

Figure 2.6: View of the assembled RFQ, with vacuum manifold and RF ports

order to obtain 40 mA average pulse current in Linac4 after chopping and scraping, an RFQ current of 70 mA is required, 30% lower than the IPHI design current. Beam dynamics simulations indicate that 99.5% of the beam is transmitted at these values.

The variable voltage law along the RFQ requires a careful control of the local resonating frequency along the cavity, obtained by an appropriate design of the resonator and by a sophisticated tuning procedure developed by CEA Saclay and extensively tested on aluminium models. The final adjustment is obtained by means of a system of tuning pistons, 16 per module, four per quadrant.

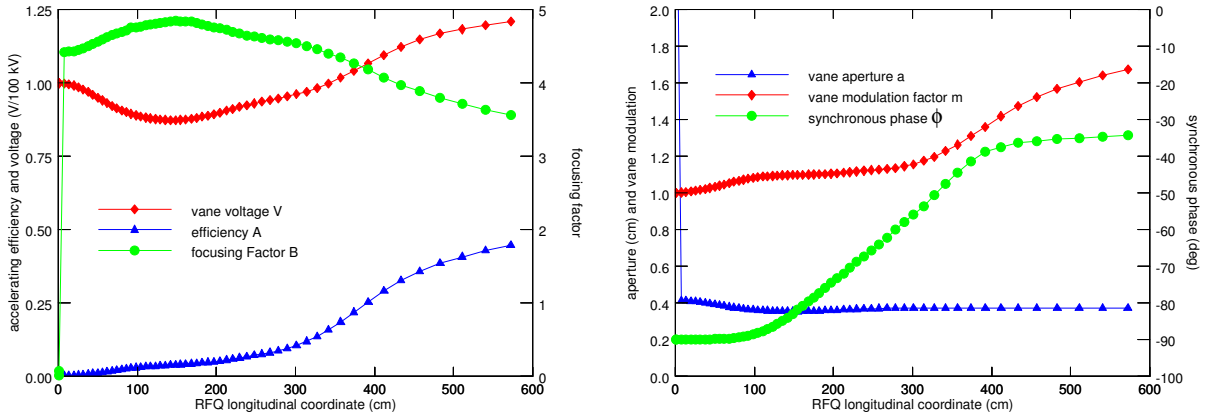

Figure 2.7: (a) Vane voltage, acceleration efficiency, and focusing factor; (b) aperture, vane modulation, and synchronous phase in the IPHI RFQ

From the mechanical point of view, each RFQ segment is made out of 4 copper parts, each comprising a vane and part of the cavity resonator. After high-precision machining, the different components are then shipped to CERN to be brazed. The assembly of each module requires 2 brazing steps. The first one, in horizontal position, is used to assemble the four vanes together to form the cavity resonator, which is also the vacuum vessel. The second brazing is performed in a vertical oven and is used to connect the many different stainless steel flanges to the RFQ.

Four RF input ports are brazed to the RFQ, one per quadrant in module number 4. While at Saclay the RFQ will be fed by 2 LEP type klystrons via 3 RF ports, due to the needs of the 100 mA CW operation; at CERN one 1.3 MW LEP klystron is considered to be sufficient, and only 2 RF ports will be used (the third coupler will be removed from the resonator and replaced with a short-circuit). The RF power is coupled from the WR2300 half-height waveguide via a ridged waveguide connection and a matched coupling iris (Fig. 2.8).

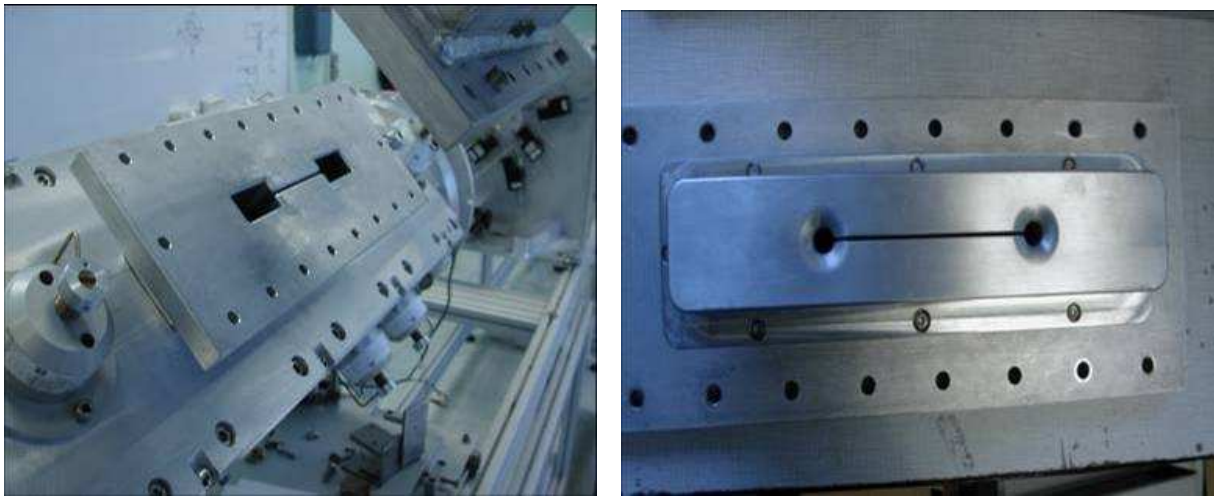

Figure 2.8: Ridged waveguide connection and coupling iris in the RFQ aluminium model

While during high-power CW operation the RFQ tuning control relies on a carefully designed and efficient cooling system, the proper tuning of the RFQ cavity at the Linac4 duty cycle (0.1%) will be achieved by heating the water circulating in two (circuits 2 and 5) of the five existing cooling circuits (Fig. 2.9) and by controlling the temperature difference between the two circuits. A cooling circuit dedicated to the RFQ will control water temperature at the level of 0.1°C. The initial cavity tuning done

in Saclay before the IPHI operation will be performed at a temperature (25°C) corresponding to the operational temperature of the RFQ as Linac4 front end, so that no change of tuning is in principle required when the RFQ will come to CERN. The main RFQ parameters are summarised in Table 2.2.

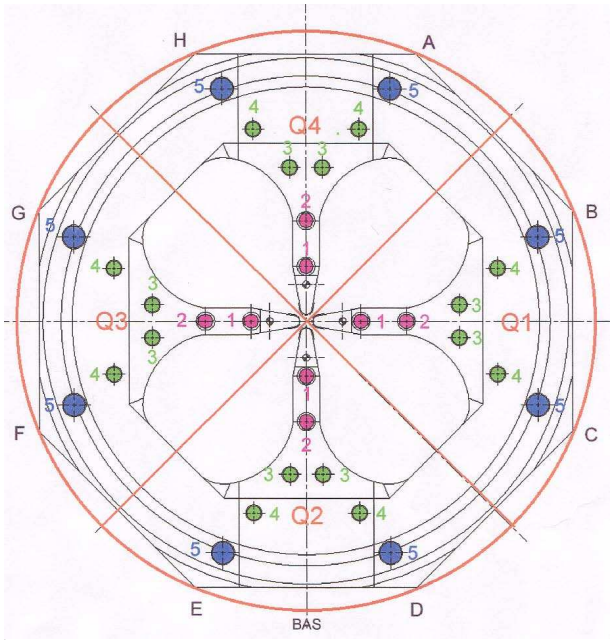

Figure 2.9: The five different cooling circuits of the IPHI RFQ

Table 2.2: Main RFQ parameters

Frequency	352.2 MHz
Total length	5.954 m
Electrical length ($\lambda = 0.85$ m)	7 λ
Number of resonating segments	3
Number of coupling cells	2
Number of cells	560
Aperture radius	3.721–4.129 mm
Modulation	1.00–1.6923 m
r_0	3.69–5.139 mm
Vane voltage	87.32–121.61 kV
Peak electric field	1.7 kilpatrick
Power in copper (SUPERFISH)	674 kW
Beam power	210 kW
Total power expected	1018 kW
Stored energy	3.6 J

2.3 Chopper line

The RFQ is followed by a Medium Energy Beam Transport (MEBT), or "chopper line", containing the beam chopping system, which is an essential component of modern linear accelerators. The system consists of a fast travelling-wave electrostatic beam deflector followed by a dump, which is capable of stopping selected sequences of beam bunches ("micro-pulses"). The purpose of this operation is to avoid

the losses at high energy that occur when injecting linac bunches with typical frequencies in the hundreds of MHz range into ring buckets at frequencies in the MHz range. Linac bunches that would fall in the unstable area of the ring bucket can be removed at the low-energy end, where the induced radiation is minimum. For example, present losses at PS booster injection are about 50%, a significant part of which is caused by the 200 MHz linac bunches falling at the edges of the $\approx$ 1 MHz booster bucket. Activation induced by a similar loss level would be a major concern for the new linac, which has higher energy and current than Linac2. Moreover, the chopper system can also be used to clean the first few tens of μs in the beam pulse which are generally not stable, and finally to create "holes" in the beam pulse timed with the rise-time of the PSB distributor, which switches the incoming linac beam between the four PSB rings.

The natural location for the chopping system is after the RFQ, where the bunch structure is already formed but energy is still low, minimising the voltage and the length of the chopping structure. In addition to the chopping system, the chopper line includes diagnostics elements as well as transverse and longitudinal optical elements, required to transport the beam through the small aperture of the chopper structure and to match the beam out of the RFQ and into the following structure, the Drift Tube Linac (DTL).

In order to avoid partially filled bunches, which could lead to losses at higher energy, the rise-time of the chopper must be smaller than the time separation between two bunches. This constitutes the most severe requirement for the chopper, translating into a maximum rise- and fall-time of 2 ns for 352 MHz bunches (2.84 ns period). The chopping scheme presently envisaged for injection into the PSB consists of removing 133 linac bunches out of the 355 that would fall into one PSB bucket at the injection frequency of 0.99 MHz. The corresponding chopping factor (fraction of beam removed by the chopper) is 37.5%. Moreover, the chopper is also removing 1 μs of beam (357 bunches) every 100 μs to create a gap for the rise-time of the distributor to the 4 PSB rings. The chopping scheme is shown in Fig. 2.10.

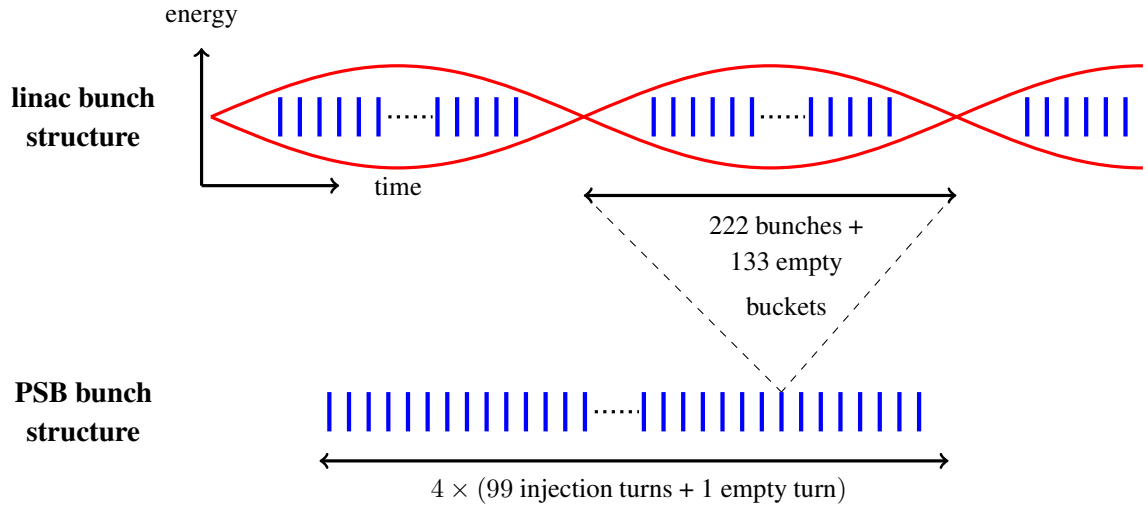

Figure 2.10: Chopping scheme for injection into the PSB assuming the maximum linac pulse length of 0.4 ms

The main chopper deflection parameters (voltage, length and deflection angle) are the result of a compromise between beam dynamics requirements (compact elements, large apertures, high voltage, sufficient separation between chopped and un-chopped beams) and the driver limitations in achieving at the same time short rise-time and high voltage. After a detailed analysis, the design has been based on a minimum effective voltage between the chopper plates of $\pm$400 V, which provides an effective kick of 5.7 mrad with an effective chopper length of 800 mm and a gap between the deflecting plates of 20 mm.

A 3D technical drawing of the chopper line is shown in Fig. 2.11, while Fig. 2.12 shows the beam dynamics layout (elements and beam envelopes in the three planes) of the line. The elements of the complete line are (from left to right, downstream):

- matching section (4 quadrupoles plus buncher cavity),
- beam chopper (2 quadrupoles with chopper plates inside),
- buncher cavity plus quadrupole plus dump (for the chopped beam),
- matching section (4 quadrupoles plus buncher cavity).

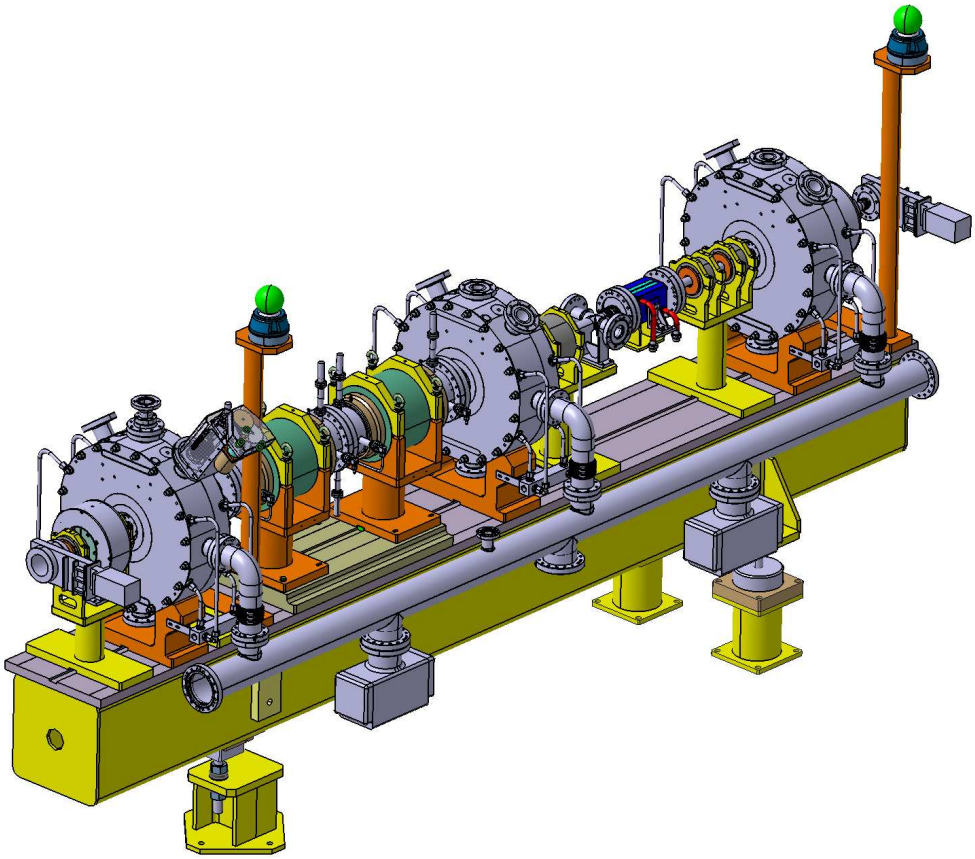

Figure 2.11: Mechanical design of the chopper line on the supporting beam

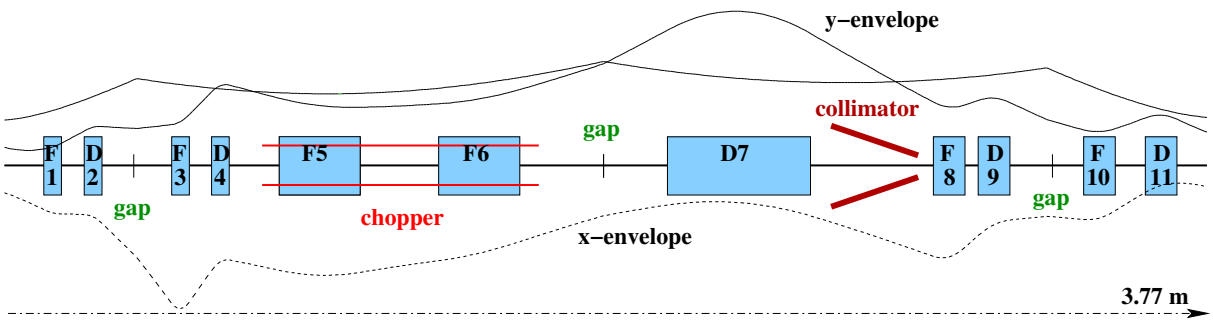

Figure 2.12: Elements of the chopper line with beam envelopes in x, y and z axis

The 11 quadrupoles foreseen in the line will be spare Linac2 quadrupoles, classified according to Linac2 nomenclature [18], each independently powered. A list of quadrupole parameters is given in Table 2.3.

Table 2.3: Magnetic elements in the chopper line

Quadrupole type	**Number**	**Length** [mm]	**Gradient** [T/m]	**Max. gradient** [T/m]
VII	2	255	1.6	2.9*
III	6	56	16-32	60
IV	2	82	13-17	39
IX	1	155	4.5	9

* chopper plates inside

The buncher cavities, resonating at 352 MHz, provide a maximum voltage of 150 kV to the beam. Two out of the three buncher cavities have already been built at CERN and have been tested at both low and high power. The main parameters of the buncher cavities are given in Table 2.4, and Fig. 2.13 shows one of the bunchers open before assembling.

Table 2.4: Main buncher parameters

Buncher type	B30	B40
Number of units	2	1
Aperture diameter [mm]	30.	40.
Inner cavity diameter [mm]	490	467.2
Gap [mm]	12	12
Q value (computed)	23600	22300
Transit time factor	0.581	0.435
Shunt impedance (linac) [MΩ]	3.91	3.35
R/Q [Ω]	27.88	14.18
Nominal voltage [kV]	140	100
Peak dissipated power [kW]	16.0	16.1
Peak electric field on nose cones [MV/m]	25.4	23.8

The beam dynamics design of the line has been optimised to maximise the separation between chopped and unchopped beam at the dump position, keeping the minimum plate voltage. The computed separation at the dump position is shown in Fig. 2.14. A complete description of the beam dynamics in the line will be given in Chapter 3.

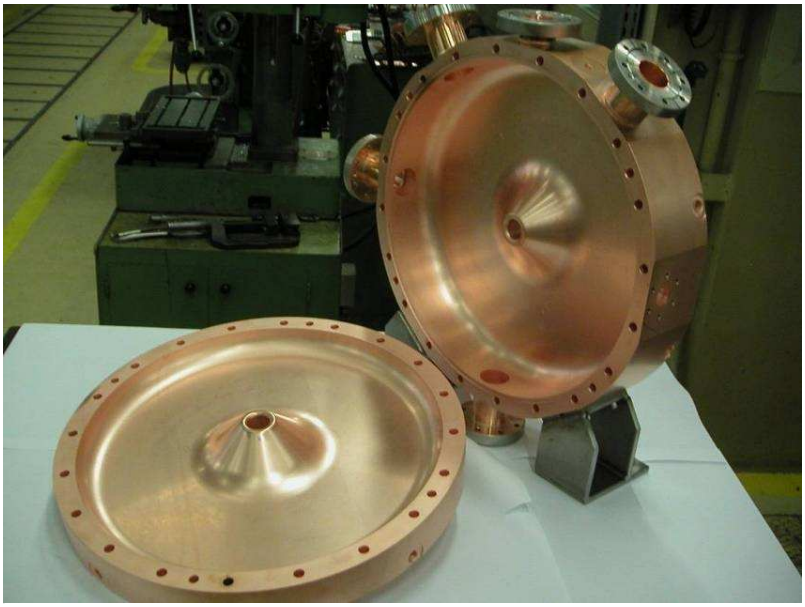

Figure 2.13: Open buncher cavity

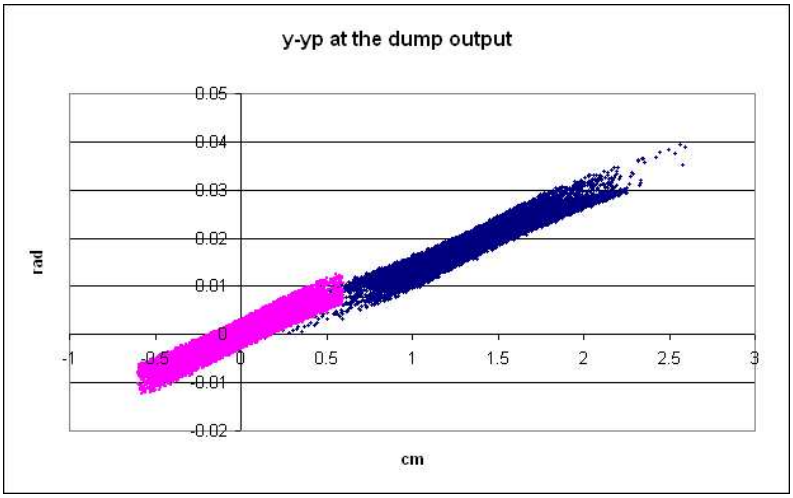

Figure 2.14: Vertical beam emittance at the dump position for unchopped (left) and chopped (right) beam

Chopper structure

Short rise-times in the nanosecond range can be obtained by using travelling-wave strip line structures, where the strip lines are meander-folded in order to match the speed of the travelling-wave to the beam velocity (Fig. 2.15).

In the present design, a section of 1.2 m is foreseen to accommodate two chopper units of 0.5 m, each housing two deflecting plates of 0.4 m length. To minimise the total length of the chopper line, the chopper units are designed to fit into the bore of existing linac quadrupoles (Fig. 2.16). The deflecting plates are driven simultaneously in opposite polarity. The plates are water cooled, in order to remove heating from beam losses as well as from the deflecting RF signal. In Fig. 2.16 are visible the connectors for RF and water input and output.

The travelling-wave structure consists of a double-meander stripline matched to a beam velocity of $\beta = 0.08$. The structure is printed on an alumina substrate of 3 mm thickness. The design is similar to the SNS chopper structure, which is also a printed meander structure [19] but uses notched micro

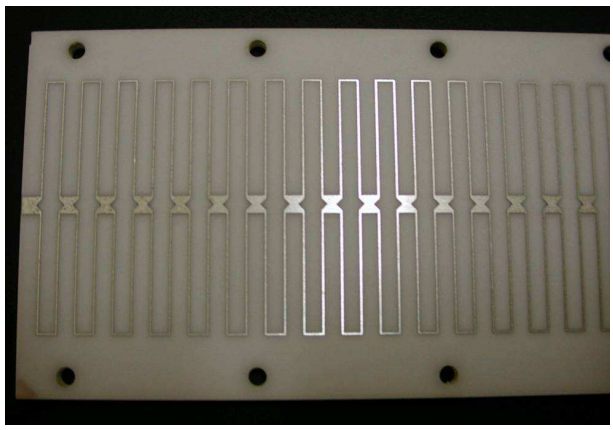

Figure 2.15: Alumina ceramic plates with printed meander structure (MoMn + 30 μm Ag); mounting holes for screws are at the sides

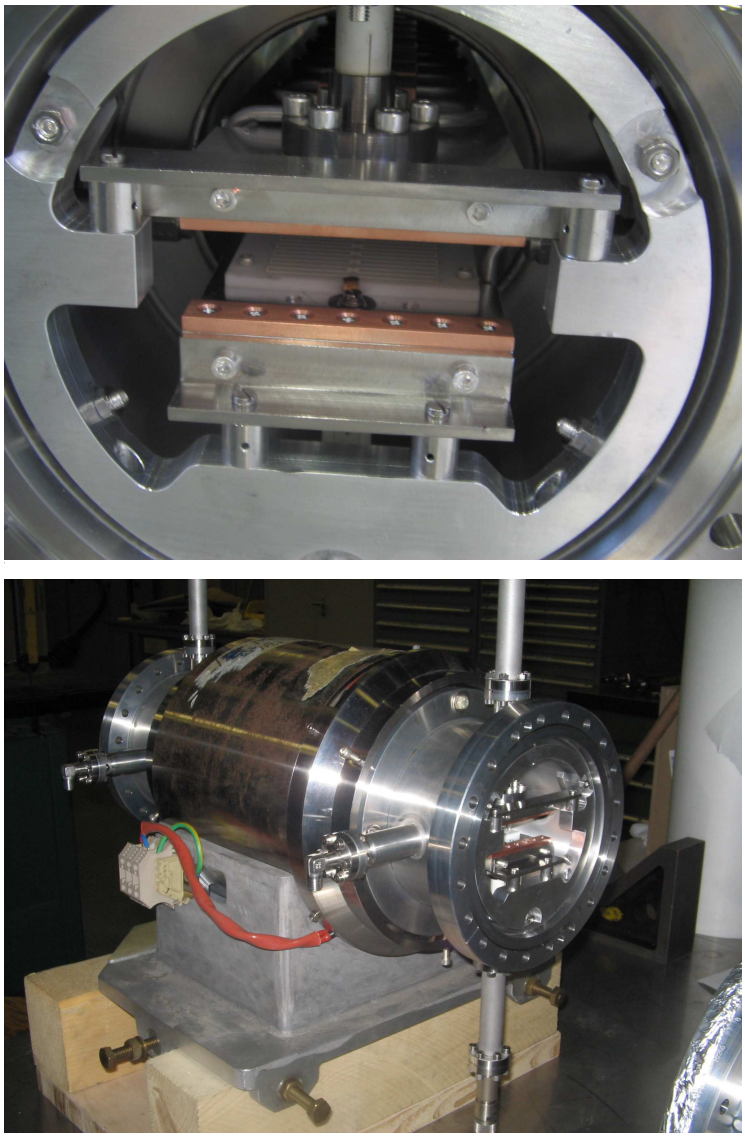

Figure 2.16: The chopper structure inside the quadrupole (top) and a detail of the deflecting plates

strip lines with separating ridges in between. While the SNS structure is printed onto glass micro-fibre PTFE composite material, the CERN chopper adopts an alumina substrate which is considered to be more stable against ionising radiation and which has lower vacuum out-gassing rates as well as higher heat transfer coefficients.

Since the strip lines do not completely cover the deflector plates the applied voltage has to be multiplied by an "effective surface coverage factor" in order to obtain the actual voltage seen by the beam. For this design, this factor amounts to $\approx 80\%$ on axis which means that for a deflection voltage of ± 500 V (i.e. 1 kV in total) the voltage available for the beam is 800 V. In order to confirm the calculated coverage factor a bench measurement test stand has been set up, using a transmission method at low frequency (1 to 10 MHz), which is calibrated by comparison with a flat plate. The result was a measured coverage factor of 78% in the middle of the structure, which goes down to 75% when moving the beam position horizontally off axis, but remaining in the middle plane between deflecting plates.

The electrical length of the printed meander structures can be slightly tuned (i.e. made shorter) by cutting longitudinal grooves over the full length in the metallic support. The tuning range is between 0 and -5% in delay with rather minor and uncritical changes in characteristic impedance and should allow adjusting the electrical delay of both meander plates, different due to production tolerances, to within ± 0.1 ns.

Two plates have already been constructed [20] using a MoMn base layer (fired at $1500\,^{\circ}$C in hydrogen/nitrogen atmosphere) and several layers of other metals added. Its final shape is determined by a chemical etching process. Results of extensive numerical simulations as well as measurements on the rise- and fall-times and the deflecting efficiency have been already presented in [21].

As an alternative to the MoMn process with chemical etching done at CERN a different technique is being proposed by industry. The actual base layer is a silk screen printed silver alloy, normally used for brazing ceramic-metal interfaces. This layer (a few μm thick) is fired at high temperature under vacuum and has an adhesion strength of 100 N/mm^2, which is nearly as good as MoMn. Subsequently by electrochemical deposition the conductor (copper) thickness is increased up to 30 μm, followed by a flash of gold to avoid surface degradation due to contact with air.

Chopper pulse amplifier

The electric field between the two deflector plates has to be established or removed in the time separating two bunches (2 ns). To avoid the displacement of the baseline (0 V for the unchopped beam) across the output pulse mean value, the low-frequency cut-off must be practically DC. To relax the low-frequency requirements and make use of a band-pass amplifier, the bunch removal scheme shown in Fig. 2.17 will be used, where the bunches are dumped using the superposition of two 22 MHz square waves with 50% duty cycle, inverse polarity and shifted by half a period. In this way, the maximum repetition frequency of the chopper driver can be the 44 MHz, as required for a potential use in a Neutrino Factory [6].

The exact number of extracted bunches is obtained adjusting the first and last cycle pulse length and/or a slight change of the square wave frequency. In the above mentioned conditions, to limit the baseline displacement to 2%, the low-frequency cut-off must be set around 140 kHz while the required 2 ns fronts impose a high frequency response extending to above 175 MHz. To achieve such a wide-band response and to manipulate the high required power (5 kW), the pulse amplifier will be based on an ultra-broadband hybrid coupler with a theoretically infinitely high frequency response independent of the electrical length of the transmission lines composing it. Because of the freedom in choosing the line length, the circuit allows the use of any amount of ferrite to shift the low-frequency cut-off to the desired point. Like all hybrid couplers it can be used in sum and difference modes. The latter mode will be used to sum the signal of two identical amplifiers, obtain the polarity inversion required by the scheme and thus achieve DC cancellation. Using the same basic configuration a two-way hybrid and a four-way hybrid have been designed for signal combination. In both cases the -3 dB response goes from

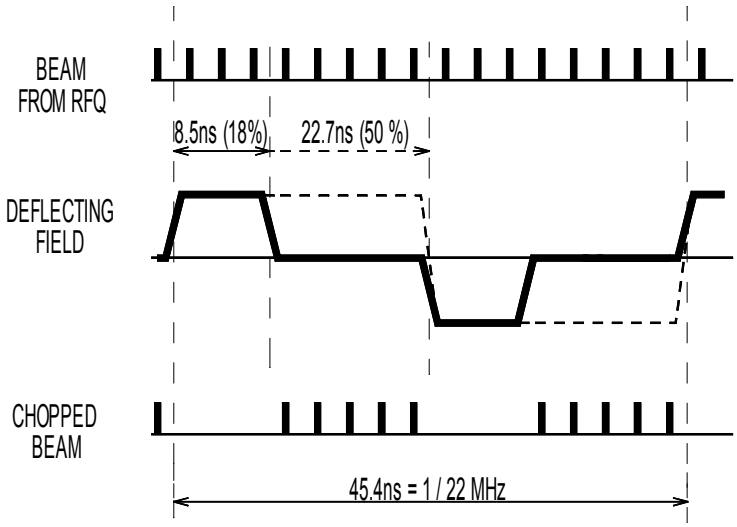

Figure 2.17: Alternate polarity extraction scheme

below 20 kHz to above 500 MHz. The basic amplifier unit shown in Fig. 2.18 is also built around the hybrid coupler but used in sum mode. To limit the number of cascaded stages and to achieve the required bandwidth, MOSFETS with V_{DS}=150 V and low capacitances ($C_{iss} \approx 50$ pF, $C_{rss} \approx 2$ pF, $C_{oss} \approx 20$ pF) have been selected.

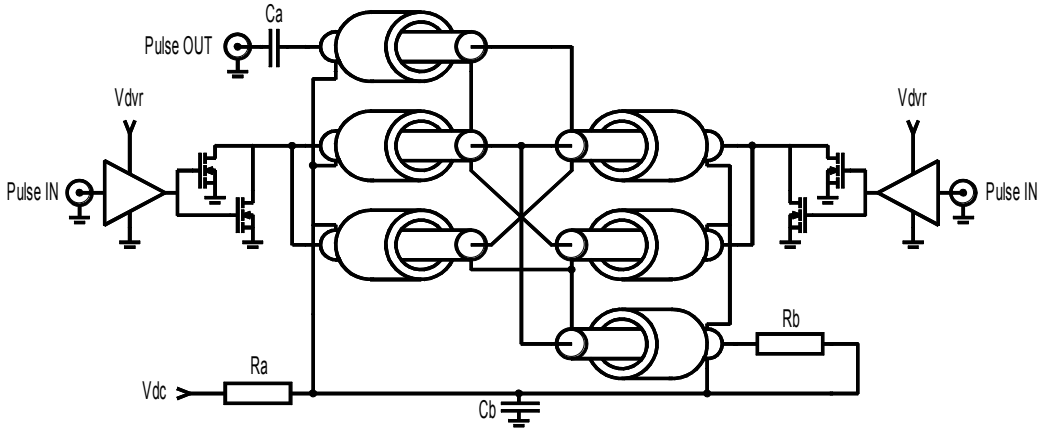

Figure 2.18: Basic amplifier unit, simplified schematic

The drain circuit high-frequency cut-off is above 300 MHz and the transient time about 1.7 ns. With a DC supply of 100 V the nominal output pulse amplitude of the unit is ≈ 150 V on 25 Ω. The gates are driven by commercial drivers requiring TTL levels at the input. To maintain the wide-band response of the circuit the DC supply is fed to the MOSFETS drains via the hybrid itself from a zero RF point. Unfortunately the ferrite used to increase the transmission lines common mode impedance at low frequency is biased by the supply current. This current is basically zero at rest, depends on the output pulse duty cycle and can reach ≈ 8 A so that the low-frequency cut-off sweeps from ≈ 40 kHz to ≈ 120 kHz. Two such units are combined with a two-way hybrid into a 50 Ω, 300 V module. Four modules are then used to achieve 550 V or $\pm$250 V (Figs. 2.19 and 2.20) and 16 modules produce the specified $\pm$500 V [22].

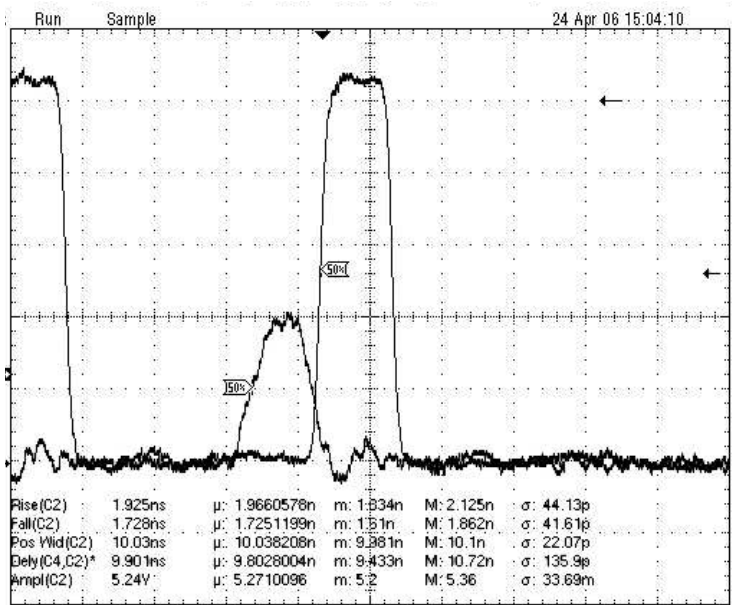

Figure 2.19: 550 V module output signal (100 V/div, 10 ns/div)

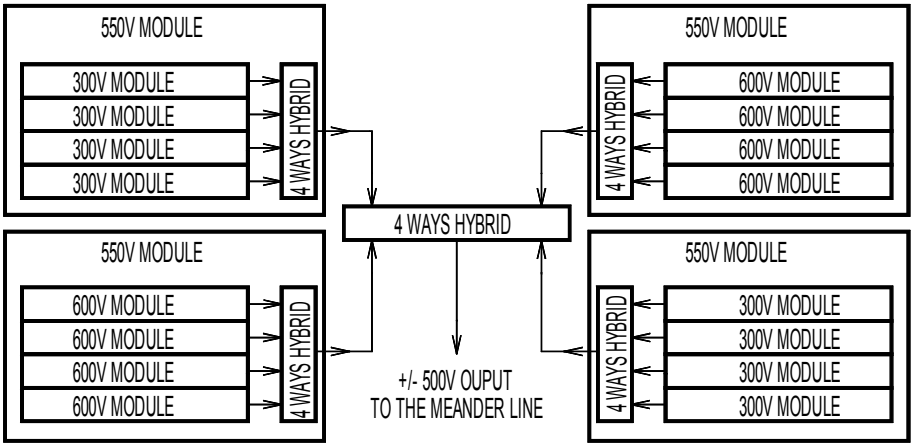

Figure 2.20: Combining scheme

Chopper dump

The beam bunches deflected by the chopper structure are absorbed by an internal dump, placed about 1 m downstream of the second chopper plate. The dump has been designed to stand the high beam power of a high duty-cycle SPL beam ≈ 2.5 kW. For Linac4, the dump will operate with minimum or no cooling as the beam power is of the order of 100 Watts.

The cross-section of the dump is shown in Fig. 2.21. It is made of a conical element (the "dump core") embedded into a thick brick-shaped jacket with 5 hypervapotron circular cooling loops [23]. The inner conical surface of the core is inclined at an angle of 11 deg in order to spread uniformly the deposited power. The minimum bore aperture of the cone is 12 mm, thus limiting the flux of scattered particles at degraded energy as well as the main-beam particles at large radii.

The dump jacket is made of stainless steel, while the core is made of alumina dispersion-strengthened copper Glidcop Al60. A 150 µm thick electrolytic nickel layer is deposited on the inner copper surface, in order to minimise radiation induced by the particle loss on the surfaces. Two dump assemblies have been recently made for the 3 MeV test stand. Figure 2.22 shows the inner core and the assembled jacket.

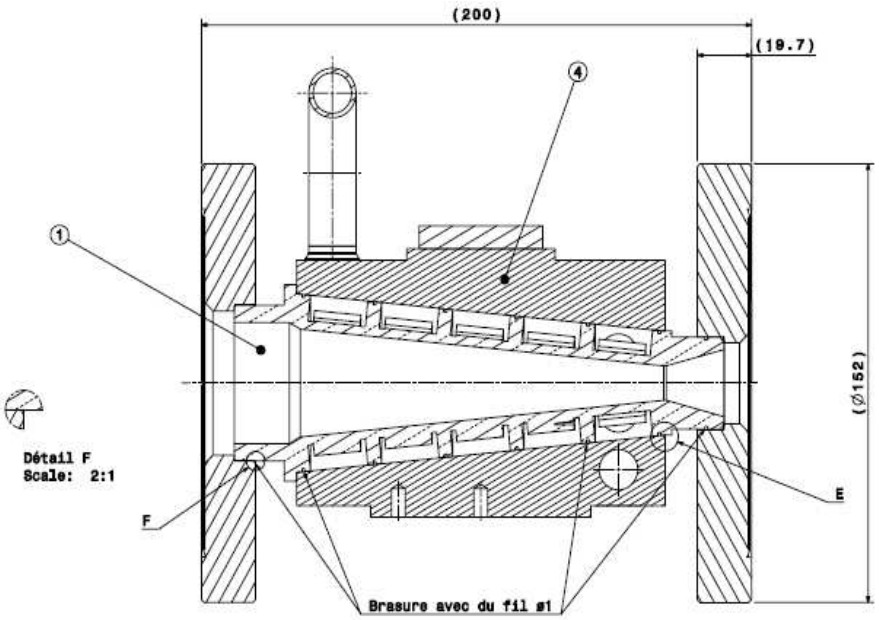

Figure 2.21: Cross-section of the chopper dump

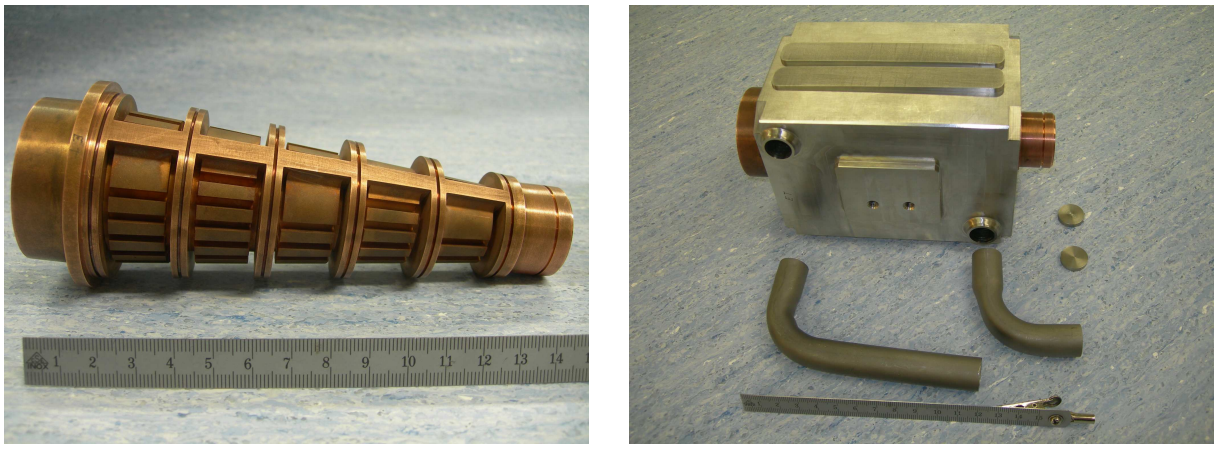

Figure 2.22: Dump core and assembly

2.4 Drift tube linac

The present CERN proton linac (Linac2) [24] consists of three drift tube linac tanks accelerating the beam to 50 MeV. Linac2 has operated from the start at the design current of 150 mA and has been upgraded lately to 180 mA, indicating the validity of the mechanical solutions adopted for construction and alignment of the drift tubes. For this reason, the basic mechanical design concept of Linac2 has been retained for Linac4, although applying the many improvements made possible by the technological advance in the last 25 years, in particular adopting modern and more reliable vacuum seals. With respect to Linac2, an additional design constraint is the requirement to operate at high duty cycle (up to 10%) for a possible future high-intensity facility [6]. Whereas this constraint complicates in some respect the design, imposing a detailed thermal analysis and the design of a sophisticated cooling system, it provides on the other hand some additional safety margins during operation at the Linac4 duty cycle, in particular for cooling and beam loss.

Differently from Linac2, or from the recently installed DTL at SNS [25], there is no field ramp in the first DTL tank, which simplifies considerably its RF tuning. In order to avoid too strong longitudinal

focusing at the beginning of the tank, the first drift tubes were lengthened to reduce the transit time factor. Furthermore the synchronous phase at the tank entrance was raised to -30° (compared with typical values of $\approx -45^\circ$). This procedure also results in more longitudinal space for the first quadrupoles which are housed in the drift tubes. The synchronous phase is then ramped to -20° towards the end of tank 1 and kept constant for the remaining two DTL tanks. The slightly more ambitious value of -20° (compared to the typical value of -25°) has been chosen together with a relatively high accelerating gradient (3.3 MV/m in tank 1 and 3.5 MV/m in tanks 2 and 3) in order to reduce the overall length of the DTL section. It has been verified that the higher synchronous phase has no degrading effect, neither on the r.m.s. emittance growth in case of longitudinal errors, nor on the development of energy and phase jitter due to variations in the klystron output voltage and phase. The choice of a high accelerating gradient, which pushes up the RF power requirement, is economically justified by the availability of the LEP klystrons. The result is a compact DTL design, with the first tank only 2.6 m long, and the overall DTL going from 3 to 40 MeV in 13.4 m, still keeping the peak surface field between 1.4 and 1.7 times the Kilpatrick limit, which is considered safe for reliable operation.

Another choice with a strong impact on the DTL design is the magnet type. In a DTL at low energy the strong space-charge defocusing requires high integrated quadrupole gradients which are in contrast to the short length of the drift tubes and their limited transverse space. While Linac2 adopted conventional electromagnets, the technical difficulties and costs of developing a high-gradient, high duty cycle electromagnet fitting in the small first drift tubes of Linac4 led to the choice of Permanent Magnet Quadrupoles (PMQ) for the Linac4 DTL. Taking into account the increased accuracy of modern beam dynamics simulation codes, it is considered acceptable to rely on a fixed focusing channel in a DTL, which is similar to the fixed focusing channel of the RFQ. Simulations show that matching into the DTL is possible for beam currents ranging from 20 to 65 mA, using the last (electromagnetic) quadrupoles of the chopper line. Long-term stability of the PMQs, especially in a high-radiation environment, has been analysed, and recent experimental data appears to confirm that magnetisation is preserved even in the long term [26]. From the operational point of view the use of PMQs represents a considerable simplification, and their smaller diameter as compared to ElectroMagnetic Quadrupoles (EMQs) allows for smaller drift tubes leading to higher shunt impedance and less RF power.

Starting from the beam dynamics design, the DTL resonator has been designed using both 2D and 3D RF simulation codes. The shunt impedance could be further increased by adopting a variable face angle on the drift tubes. From the RF point of view, the DTL has been divided into 3 tanks, the first being 2.6 m long, whereas the other tanks are made of two mechanical sections with about the same length of tank 1, but connected to form two tanks of about 5.2 m length, in order to minimise the number of transitions. The layout of the Linac4 DTL is presented in Table 2.5.

Precise adjustment of the field in the tanks is provided by fixed tuners (5 for the first tank, 10 for the following tanks). One movable tuner per tank section keeps the tanks on frequency during operation. Post-coupler stabilisation is foreseen in the three tanks, although it is made more difficult by the small drift tube diameter leaving a distance of 1.01 $\lambda/4$ between the tank and the drift tube surface, which is a value considered at the limit for achieving an effective stabilisation. For this reason, a detailed 3D analysis of the post-coupler modes has been performed indicating that, even for the chosen configuration of one post-coupler every three drift tubes in tank 1, stabilisation can be achieved with the length of the post-coupler being adjusted at ± 1 mm.

The RF power will be coupled into the DTL from one single port per section and per klystron, via a coupling iris whose dimension is precisely computed by means of 3D RF codes. Exact matching to the DTL impedance is provided by an adjustable short-circuit placed on the waveguide at $\lambda/4$ from the iris. While tank 1 is fed by one klystron, two klystrons feed each of tank 2 and tank 3, sharing a common driver and low-level RF system.

The mechanical design has to ensure long-term stability and minimise maintenance while providing the tight tolerances in the positioning of the quadrupoles to fulfil the requirements of the beam

Table 2.5: Parameters of the three DTL tanks

	Tank 1	**Tank 2**	**Tank 3**
Output energy [MeV]	9.8	25.0	39.9
Frequency [MHz]	352.2	352.2	352.2
Gradient E_0 [MV/m]	3.3	3.5	3.5
Synchronous phase [deg]	$-30/-20$	-20	-20
Lattice	FOFODODO	FODO	FODO
Aperture radius [mm]	10	10	10
Diameter [m]	0.52	0.52	0.52
No. of modules	1	1	1
Drift tube diameter [mm]	90	90	90
Inter-tank spacing [mm]	122	193	–
Length [m]	2.63	5.20	5.21
Max. surface field [kilp.]	1.6/1.7	1.4/1.6	1.4/1.6
Peak RF power [MW]	0.75	1.57	1.55
N. of klystrons	1	2	2
Quadrupole length [mm]	45	80	80
N. of gaps	28	33	24
No. of post-couplers	9	16	23
Stem diameter [mm]	28	28	28
Post coupler diameter [mm]	20	20	20
N. of tuners	2	2	2
Tuner diameter [mm]	90	90	90
No. of fixed tuners	5	10	10

dynamics. Statistical error analysis indicates a maximum acceptable transverse quadrupole displacement of ± 0.1 mm (maximum displacement for a random uniform error distribution), which in turn translates into a precision of ± 0.05 mm in the positioning of the PMQ magnetic axis inside the drift tube and in another ± 0.05 mm in the positioning of the drift tube with respect to the supporting girder.

For the connection of the drift tube to the tanks a girder system like the one developed for Linac2 has been preferred to simpler solutions (SNS, JPARC) because it does not require O-ring joints, considered as a concern for long-term maintenance. The girder system provides an easy external reference for drift tube alignment, but requires a bellow for the displacement of the drift tube and a complex alignment system for each drift tube.

Because of the lack of engineering support at CERN in the mechanical design of the DTL, the development of the detailed mechanical solutions for the DTL as well as the thermo-mechanical calculations have been done by the VNIIEF Institute in Sarov (Russia), under the sponsorship of the ISTC (International Science and Technology Center) and in collaboration with ITEP (Moscow). Figure 2.23 shows a 3D view of the tank 1 prototype designed by VNIIEF and Fig. 2.24 shows its inner section [27].

The main features of the VNIIEF design are:

– Laser welding of the drift tube covers. Conventional electron beam welding cannot be used to seal the drift tubes, because the PMQ field deflects the electron beam. It may be possible to keep the PMQs in vacuum and avoid the welding, but this solution would considerably increase the surface to be pumped and require a more powerful pumping system and longer pumping times. The alternative that is being studied for Linac4 is laser welding of the drift tube assembly, using powerful enough lasers for a sufficient weld penetration depth.

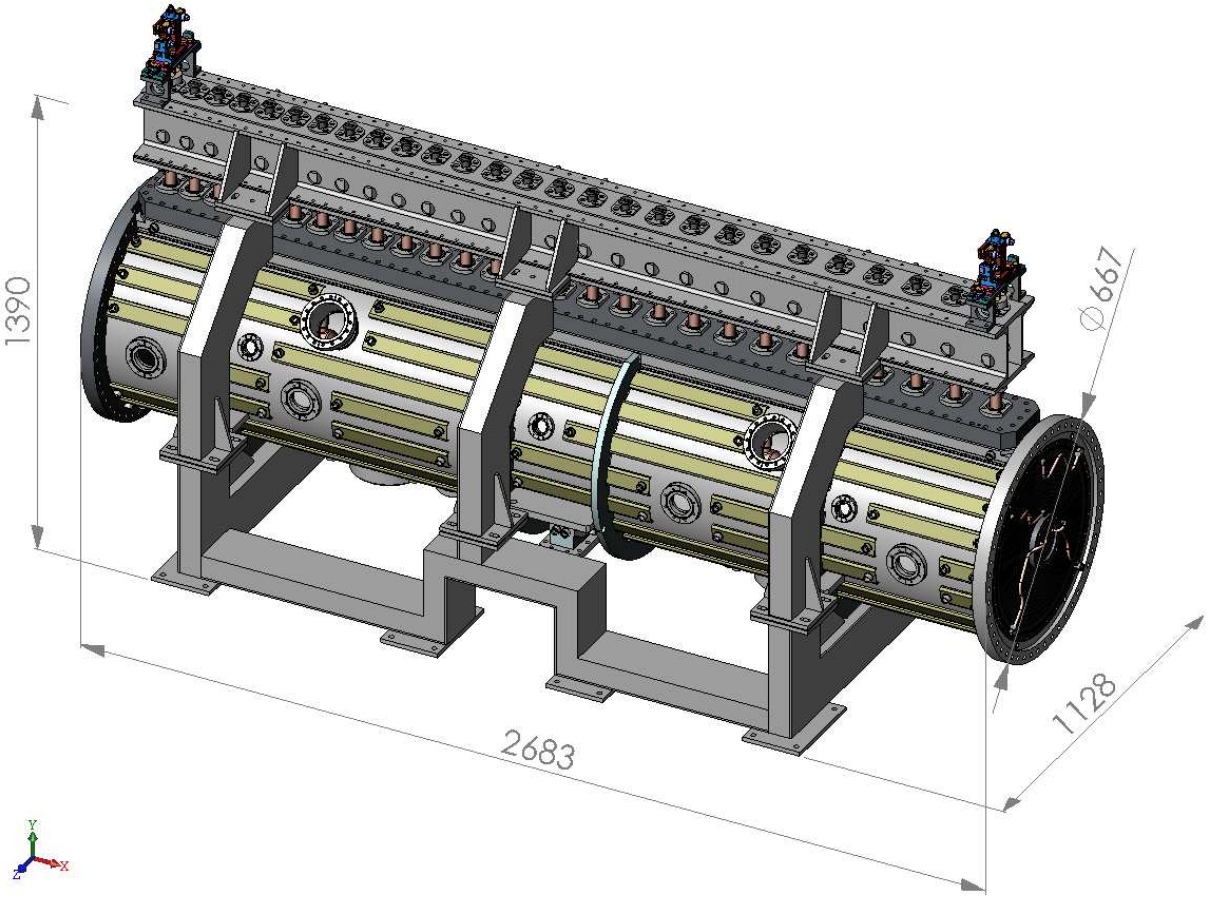

Figure 2.23: 3-D model of DTL tank 1 with girder and support structure

– Precision alignment of drift tubes with a movable mechanism (Fig. 2.25). In order to reduce the number of alignment mechanisms to be produced, the same mechanism can be moved from one drift tube to the other. When the required alignment precision is achieved, the tube is fixed into position by pouring a fixing liquid in a small sink on the top of the drift tube.
– Decoupling of the girder from the tank: the girder is supported by 6 supports (in order to keep inside tolerance the deformation of the girder under vacuum) and aligned independently from the tank. Only 3 supports define the position of the girder, the others are shimmed once the girder is aligned.

The prototype of DTL tank 1 which is being built by the ISTC project will consist of tank, girder, and girder support, and will be equipped with only one complete drift tube, containing a PMQ with rod technology made at ITEP (Moscow) and shown in Fig. 4.12. The other tubes will be aluminium dummies. This prototype will be used to validate the mechanical design and will undergo vacuum and low-power RF testing (tuning and field adjustment). It is foreseen to equip the prototype in a second stage with the complete set of drift tubes, and then proceed with high-power RF testing and eventually with beam tests at the CERN test stand. The general mechanical drawing of the DTL is shown in Fig. 2.26.

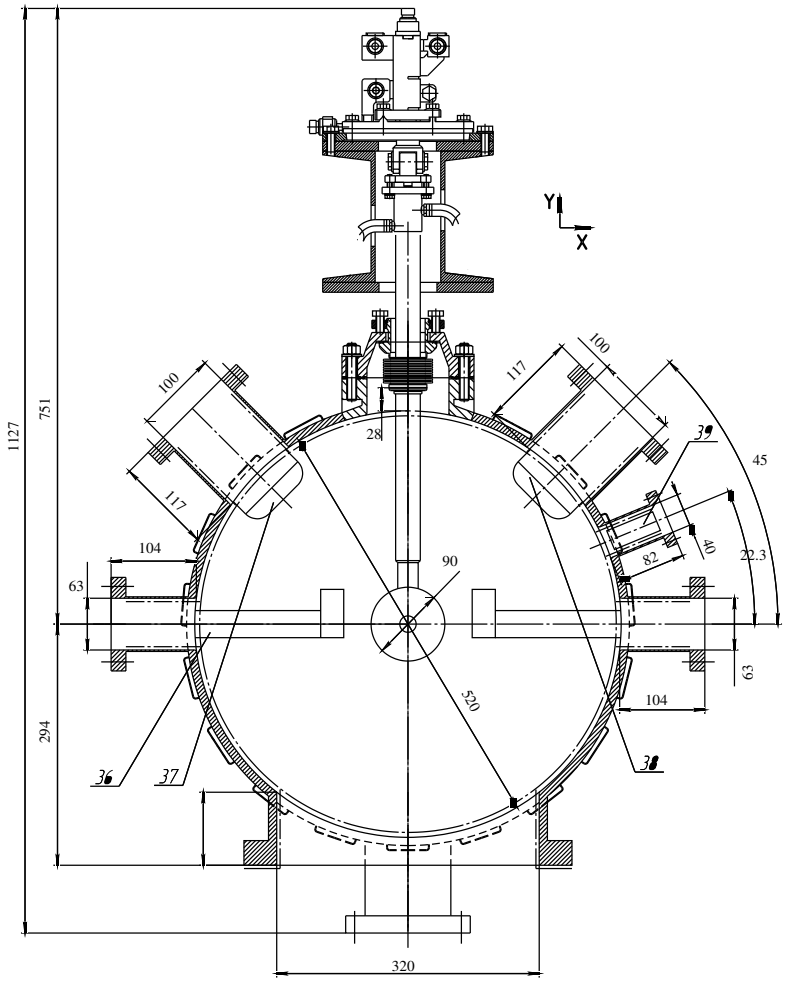

Figure 2.24: DTL cross-section

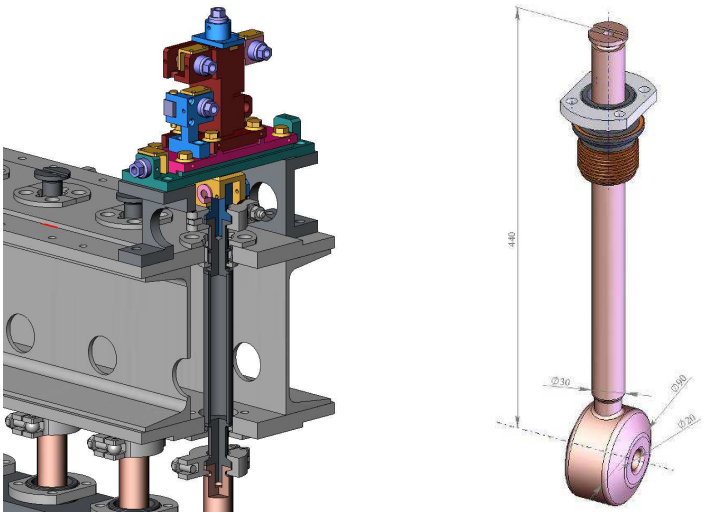

Figure 2.25: Drift tube alignment mechanism (left) and drift tube geometry (right)

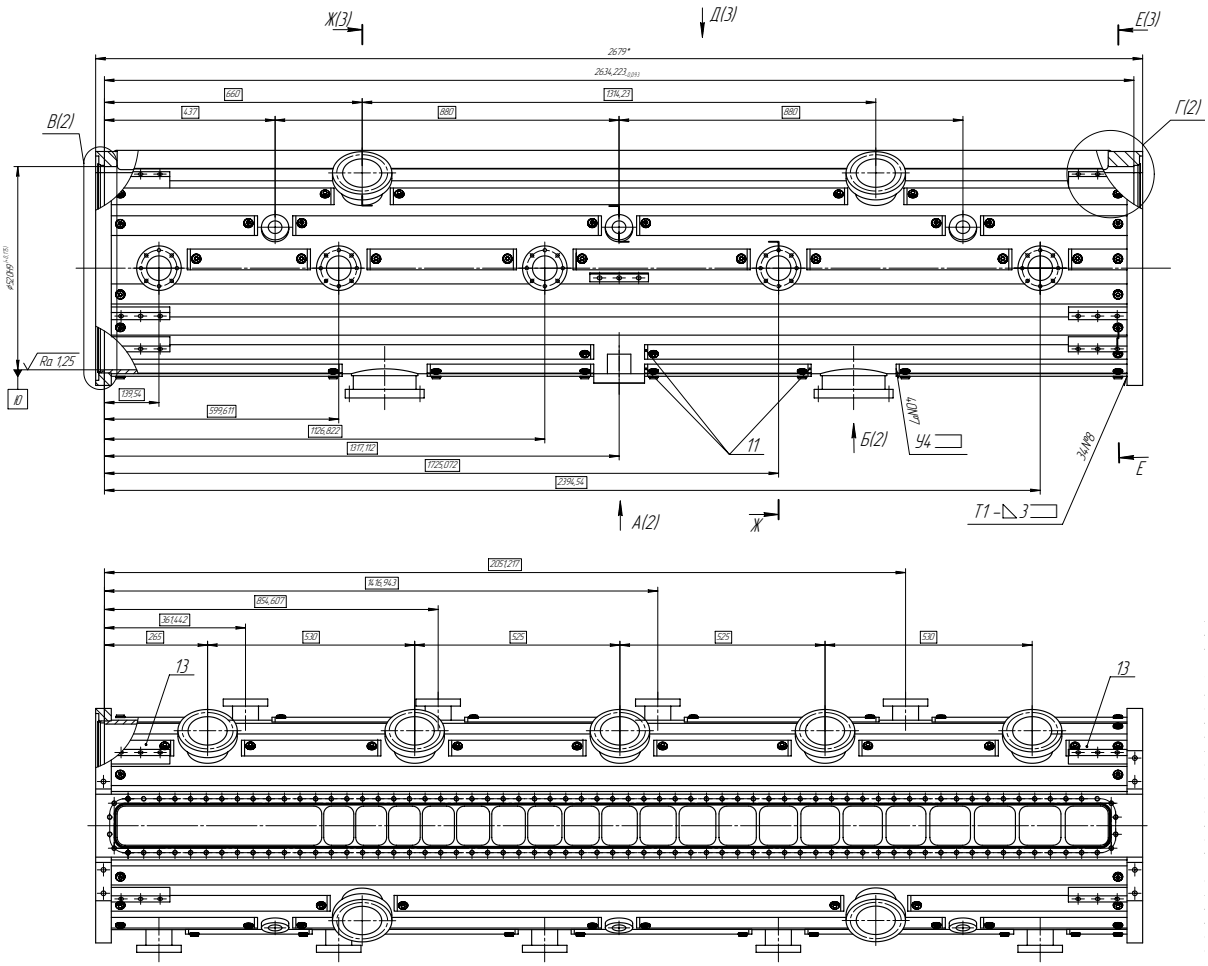

Figure 2.26: Side cut and top view of the DTL prototype tank, constructed at VNIIEF, Sarov

2.5 Cell-coupled drift tube linac

At linac energies above 40 MeV, alternative structures to the conventional drift tube linac can be used, providing comparable efficiency with simpler construction and alignment. Different designs have been considered, all based on short DTL-like tanks containing only few empty drift tubes, with quadrupoles placed externally between tanks. The main advantage of these structures is their lower price per meter as compared to a DTL, whose cost is dominated by the complex construction and alignment of the drift tube-quadrupole assembly and by the machining, handling and plating costs of the long DTL tanks. For structures with external quadrupoles the drift tube alignment tolerances are much less demanding than for the DTL, and thanks to the small drift tube diameter a good shunt impedance can be maintained whilst profiting of the adjustability of electromagnetic quadrupoles. Moreover, the time needed to access and replace the quadrupole in case of problems during operation is minimum. However, placing the quadrupoles outside of the accelerating structure increases the lenght of focusing periods, and the maximum tolerable phase advance per period sets a lower limit to the energy at which these structures can be used.

The structure adopted for Linac4 is shown in Fig. 2.27. This is a particular version of Cell-Coupled Drift Tube Linac (CCDTL) [28] operating at the same RF frequency as the DTL, 352 MHz, in order to make maximum use of the existing LEP klystrons. The accelerating tanks contain two drift tubes, and are connected by coupling cells leaving an inter-tank space for the quadrupole. This layout results in a focusing period of 7 $\beta\lambda$, which beam dynamics simulations show is acceptable above 40 MeV energy. A string of 3 tanks forms a module, directly fed by a 1 MW klystron. From the RF point of view, a module is composed of 5 coupled resonators operating in the $\pi/2$ mode, i.e. at the operating frequency only the accelerating tanks are excited (see Fig. 2.27). Each tank, considered as a stand-alone resonator, operates in the usual DTL 0-mode, i.e. the distance between gaps in a tank is $\beta\lambda$ as for the DTL.

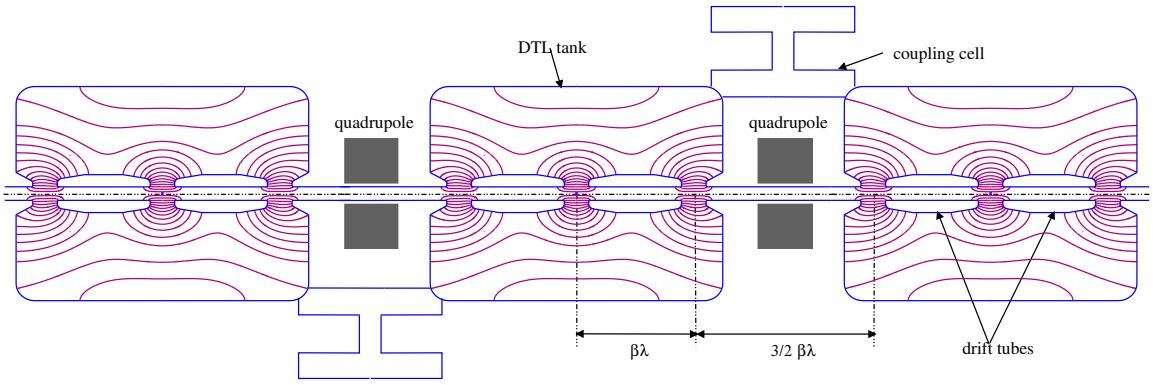

Figure 2.27: Scheme of a CCDTL module showing electric field lines

The advantages of this structure are the easy access, alignment and cooling of the quadrupoles, the simpler construction of the small tanks and the simplified alignment of the drift tubes. While in the case of the DTL the tolerances for drift tube alignment are dictated by the positioning of the quadrupole, for the CCDTL only the symmetry of the RF field is affected by misalignments, leading to tolerances between 5 to 10 times less severe than for the DTL. By using coupling cells between tanks, the module can be directly fed by a klystron, clearly defining the tank phases and amplitudes. Finally, a CCDTL allows for a continuous focusing lattice with adequate space for diagnostics, reducing the risk of beam mismatch at the DTL intertank regions.

Figure 2.28 presents the computed shunt impedance of DTL, CCDTL and of the following structure in Linac4, the SCL. Contrarily to DTL or CCDTL, the SCL is a π-mode structure at twice the basic RF frequency, characterised by a shunt impedance increasing with the energy. In the Linac4 DTL, a high shunt impedance has been achieved by using permanent magnetic quadrupoles (PMQs) instead of elctromagnetic ones, yielding smaller drift tube diameter, lower capacitance and higher shunt impedance.

Operational considerations led to the decision to use EMQ's in the rest of the linac resulting in a 20% reduction in shunt impedance at the transition between DTL and CCDTL. At high energies, the shunt impedance of DTL and CCDTL decreases rapidly because of the increasing length of drift tubes, justifying the transition to another structure like the SCL. In Linac4 this transition has been fixed to 90 MeV, where the still lower SCL shunt impedance is compensated by the reduced cost of the 704 MHz Radio Frequency.

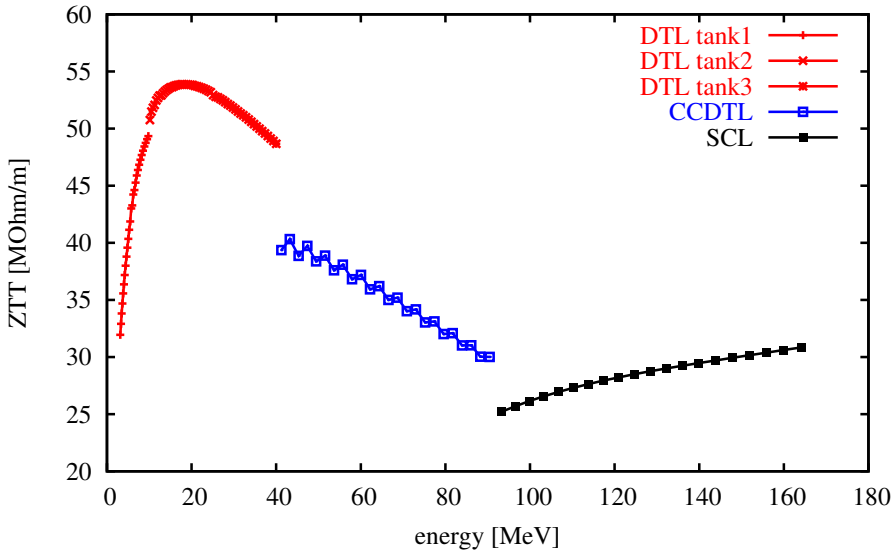

Figure 2.28: Computed structure shunt-impedance (linac definition) for the three Linac4 accelerating structures. The values are multiplied by 0.8 to account for additional losses with respect to simulations and include losses on end walls, stems and coupling slots.

The CCDTL of Linac4 is composed of 8 modules of three 3-gap cavities each, for a total of 24 tanks covering a length of 28 m. The RF input is from an iris-type waveguide coupler identical to the one of the DTL, placed in the central tank. The main design parameters are presented in Table 2.6, a view of a CCDTL module is shown in Fig. 2.29 and the overall CCDTL layout is presented in Fig. 2.30.

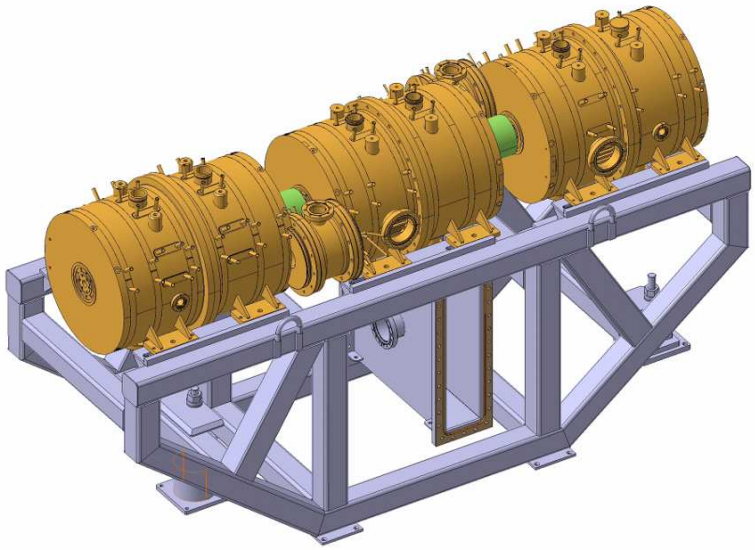

Figure 2.29: 3D view of a CCDTL module with support and waveguide coupler

Table 2.6: Main CCDTL parameters

Input energy	40 MeV
Output energy	91.7 MeV
Frequency	352.2 MHz
Gradient E_0	2.8/3.9 MV/m
Synchronous phase	$-20°$
Lattice	FODO
Aperture radius	14 mm
Diameter	0.52 m
No. of modules	8
Tanks per module	3
Gaps per tank	3
Drift tube diameter	85 mm
Length	25.2 m
Max. surface field	1.4/1.7 kilpatrick
Peak RF power	6.4 MW
No. of klystrons	8
No. of gaps	$3 \times 3 \times 8$
Stem diameter	24 mm

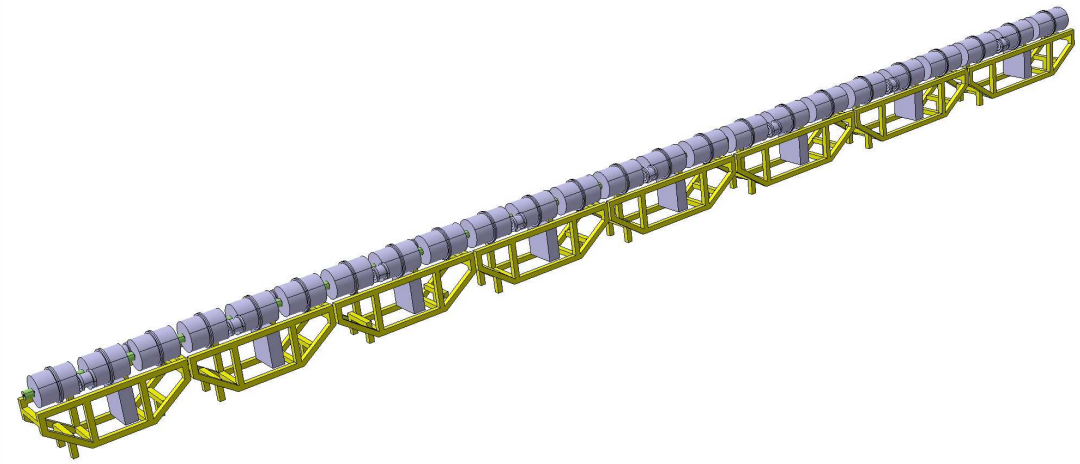

Figure 2.30: complete CCDTL layout

The mechanical and RF design of this CCDTL concept have been studied at CERN since 1997. The mechanical and RF solutions developed during this study have been applied to the construction of a prototype CCDTL structure made of two half-tanks and one coupling cell (Fig. 2.31), which is undergoing high-power RF tests at the SM18 RF test stand [29]. The tanks are made of copper-plated stainless steel. The copper drift tubes are installed inside the tank and then welded in position.

In the frame of an ISTC project with BINP (Novosibirsk) and VNIITF (Snezinsk), the CERN mechanical design has been adapted to the Russian production technologies and a second prototype has been manufactured by VNIITF and is presently under RF tuning and assembly in Novosibirsk (Fig. 2.32). It is expected to be delivered to CERN and undergo high-power RF tests. This second prototype is composed of two full tanks and one coupling cell, and could be completed at a later stage with a third tank, in order to form a complete module.

Figure 2.31: CCDTL prototype 1 (CERN)

Figure 2.32: CCDTL prototype 2 (ISTC - Russia)

2.6 Side-coupled linac

Above $\approx$ 90 MeV the shunt impedance of drift tube based structures like DTL or CCDTL starts to decrease rapidly, and the only option to keep high acceleration efficiency is to pass from structures operating in the 0-mode (0° phase difference between adjacent gaps on the beam axis) to structures operating in π-mode, which present a shunt impedance increasing with energy (Fig. 2.28). At the same time, the reduced bunch length at high energy due to phase damping allows doubling the RF frequency, with a further increase in shunt impedance and the possibility to operate at higher gradients. However, the smaller cell dimensions impose a drastic change in the mechanical construction technique, passing from the bolted units made out of copper-plated stainless steel used at 352 MHz to modules composed of smaller brazed full copper cells. Moreover, at the new frequency one is no longer limited by the power of the LEP klystron, and the new accelerating section can be based on newly built pulsed klystrons at higher power. The consequence is that the number of accelerating cells per resonator increases drastically, and in order to ensure a stable field profile the chain of accelerating cells is doubled by coupling cells placed between accelerating cells, thus creating a long resonator chain which from the RF point of view has to operate in the $\pi/2$ mode. During normal operation, the coupling cells have no fields inside, and only the accelerating cells present their standard electric field pattern. The advantage of $\pi/2$ mode operation is that in presence of mechanical errors that would lead to asymmetries in the electric field distribution the coupling cells get excited and contribute to building up a mode component that preserves the field symmetry, thus stabilising the chain of resonators.

Different types of $\pi/2$ mode structures have been considered for Linac4, and eventually the classical Side-Coupled Linac (SCL) structure, originally developed at Los Alamos in 1967 and then used in most of the high-energy linac projects worldwide, was retained [30]. The SCL for Linac4 is composed of tanks, each containing 11 accelerating cells and 10 coupling cells placed on alternating sides of the accelerating cells (Fig. 2.33). The cells are magnetically coupled by slots at the intersection between accelerating and coupling cells. Electromagnetic quadrupoles are placed between tanks, and in order to form a continuous RF structure the quadrupoles are bridged by off-axis 3-cell bridge coupler units. For a maximum klystron output power of 4 MW, 5 tanks can be connected to form a module of 117 coupled cells fed by a single klystron [31].

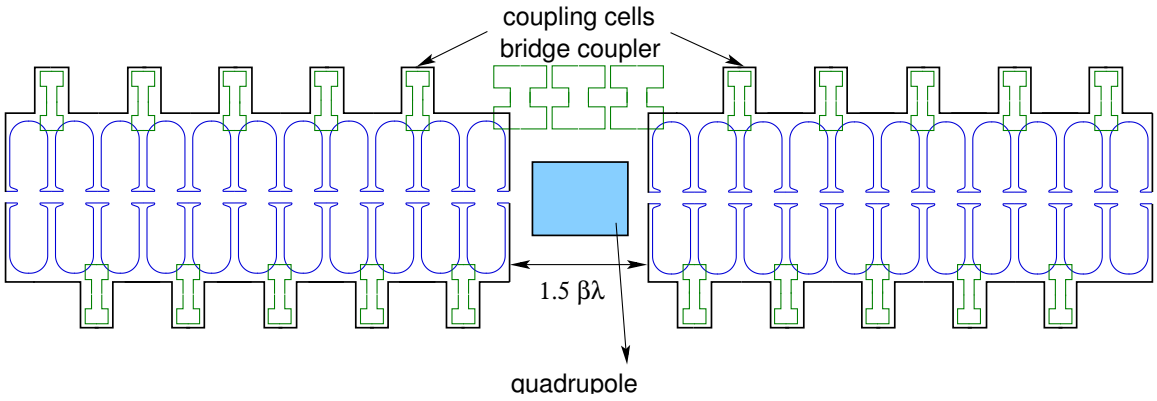

Figure 2.33: Scheme (cross-section) of two SCL tanks with quadrupole and bridge coupler

The cell geometry and the coupling cell positions have been optimised by means of 2D and 3D RF codes, in order to maximise the shunt impedance and to obtain the required 3% coupling factor. Figure 2.34 shows the electric and magnetic field distributions of a simulation model used for GdfidL [32].

Each module is powered at one of the two middle bridge couplers. The feeding leads to a 1.2% decrease of the gap voltages ("power flow droop") towards the longer end of the module (see Fig. 2.35) which is still acceptable from the beam dynamics point of view.

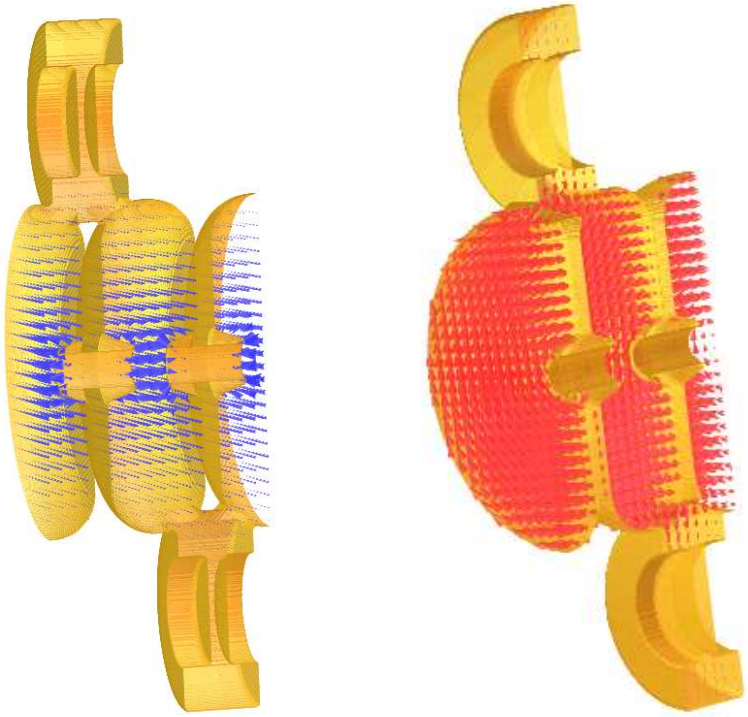

Figure 2.34: The electric (left) and the magnetic (right) field of the operating $\pi/2$-mode in a section of an SCL tank

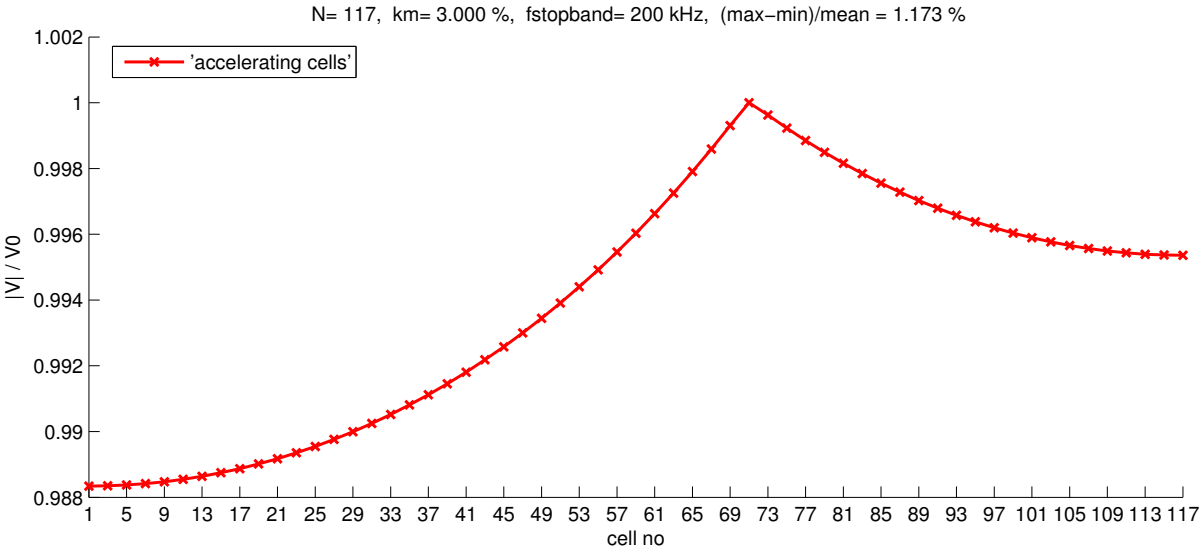

Figure 2.35: The normalised voltages in accelerating cells. The voltages diminish from the fed cell onward due to losses in the cavities.

The construction techniques of the SCL differ from those of DTL and CCDTL because of the higher frequency and smaller size. The SCL cells are machined out of solid copper blocks, and then all cells in a tank are piled up and furnace brazed. RF tuning of the individual cells is required before brazing, and then the complete tank can be tuned to frequency and residual field errors corrected by applying deformation tuning ("dinging") of the cells. This construction and tuning technology is commonly used for this type of structures, and was successfully applied at CERN for the prototype of the LIBO medical accelerator at 3 GHz frequency [33].

The SCL structure for Linac4 is being developed inside the HIPPI Joint Research Activity (JRA), supported by the EU. The LPSC Laboratory of IN2P3 in Grenoble (France) is building a cold model of SCL (Fig. 2.36), in order to study the RF properties and to optimise the tuning strategy. A technological model of the SCL, made of two copper half-cells brazed together, is being built in BINP (Novosibirsk) under the sponsorship of ISTC, in view of a future construction of the complete SCL accelerator. The main parameters of the SCL section are summarised in Table 2.7.

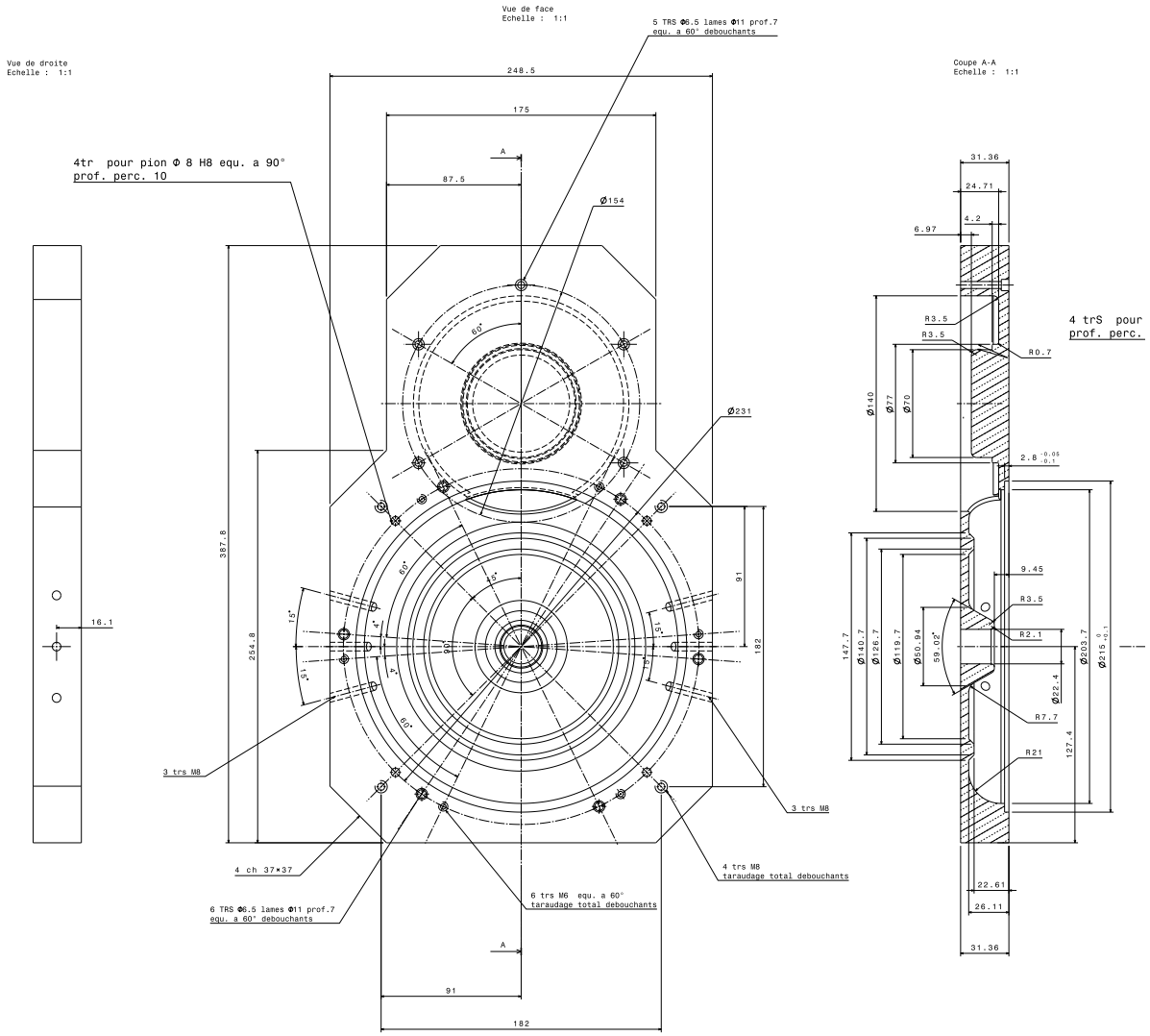

Figure 2.36: Drawing of one cell of the SCL model built by LPSC Grenoble

Table 2.7: Main SCL parameters

Input energy	91.7 MeV
Output energy	160.1 MeV
Frequency	704.4 MHz
Gradient E_0	4 MV/m
Synchronous phase	$-20°$
Lattice	FODO
Aperture radius	16 mm
Cell diameter	0.30/0.31 m
No. of modules	4
Tanks per module	5
Gaps per tank	11
Total length	28.0 m
Max. surface field	1.2/1.2 kilpatrick
Peak RF power	12.5 MW
N. of klystrons	4

2.7 Measurement line and dump

A the end of the linac, between the last SCL module and the LEIR wall, the straight path between the end of the SCL and the LEIR wall is about 13 m long and it will house a permanent diagnostic line as well as a beam dump. The line is also equipped with a quadrupole of the type used in the transfer line to the booster to be able to adjust the optics parameters for an optimised emittance measurement.

A beam transformer, a phase pick-up and a profile monitor are placed after the last SCL quadrupole and the bending that switches the beam towards the booster. After the bending there is a quadrupole, a Feshenko box for the measurement of the 3D beam size and then an emittance measurement device. The line is terminated with a 5 m long dump to collect the beam during commissioning and in the event of bending magnet failure. The dump is dimensioned to collect permanently 50 μs of beam at 2 Hz, as required during the setting-up of the linac. The 95% beam sizes at the diagnostic elements are reported in Table 2.8 for the case of nominal operation, i.e. for nominal SCL quadrupoles settings and the line quadrupole switched off. These values are compatible with the proper functioning of the diagnostic instruments.

Table 2.8: Beam size at the diagnostic tool for nominal optics

	x [mm]	**y** [mm]	**Phase** (at 700 MHz)
Transformer	± 4.5	± 3	$\pm 8°$
Feshenko box	± 3	± 11	$\pm 12°$
Emittance measurement	± 5	± 13	$\pm 15°$
Dump entrance	± 8	± 17	$\pm 20°$

2.8 Transfer line

A new transfer line will transport the beam from the end of Linac4 to the PS Booster: its general parameters are summarised in Table 2.9. The choice of the layout to connect the Linac4 location in the PS South Hall to the existing Linac2 line upstream of the PSB injection has been significantly constrained by the necessity of integration in the existing complex of accelerators and by the rationale of keeping Linac2 in operation for the whole duration of Linac4 commissioning. The schematic path of the transfer line is shown in Fig. 2.37.

Table 2.9: Main transfer line parameters

Total length (to PSB entrance)	193.2 m
Length of new section (to the junction with Linac2 line)	105 m
N. of quads	23
Quadrupole aperture	70 mm
Max. quadrupole integrated gradient	2.25 T
Number of bendings	5
Number of RF cavities (352 MHz)	2

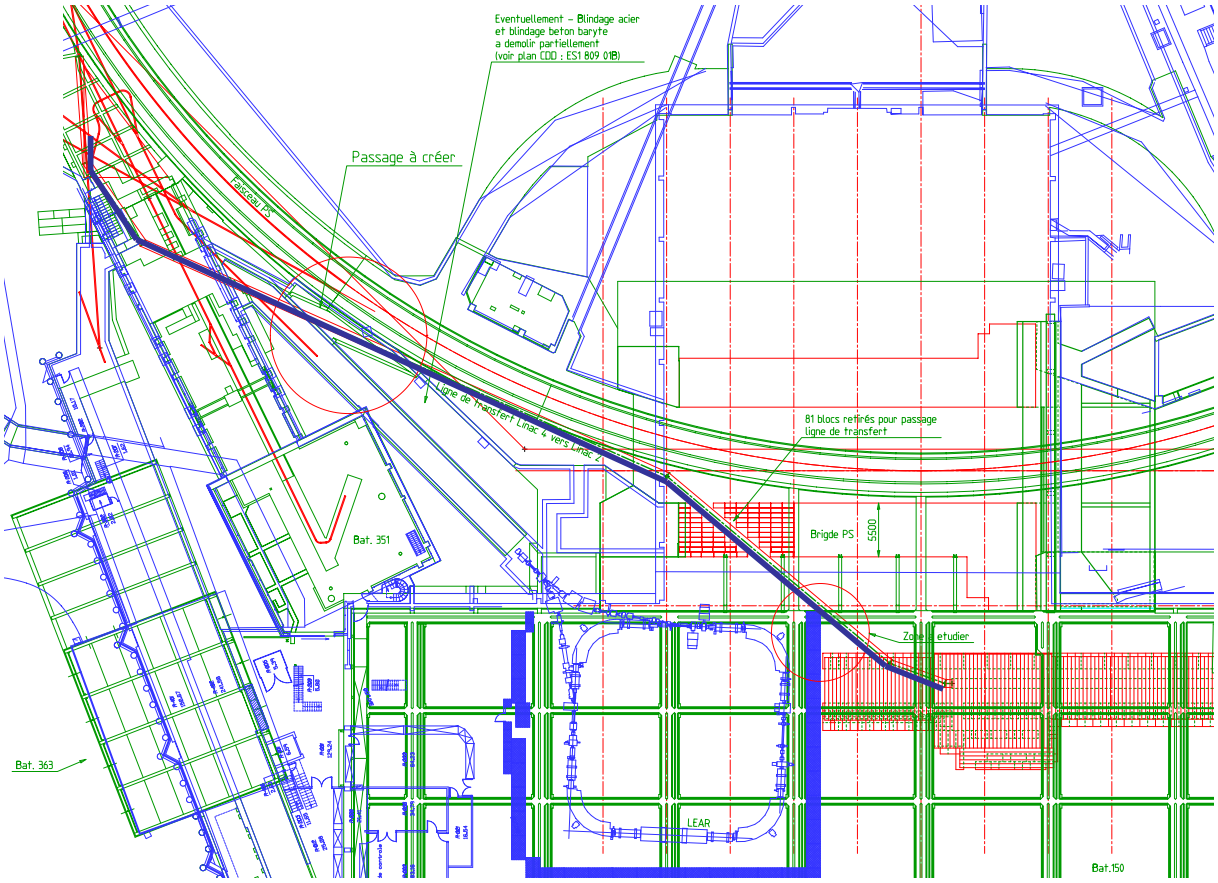

Figure 2.37: Layout of the Linac4 transfer line

Transporting the beam to the Booster with a straight line was clearly not feasible, and bendings had to be introduced to go round the LEIR ring first and then redirect the beam towards the PSB. The line is therefore composed of three straight sections: one short matching line at the Linac4 exit and two doublet channels. The first long straight section passes close to the LEIR wall and then crosses the shielding wall of the PS with a long pipe without magnetic elements. The second straight section passes close to the PS and then crosses the wall of the inflector area, traversing the Linac3-LEIR line and finally joining the existing Linac2 line just upstream of the LT.BHZ30 dipole. The length of the new line, up to the point where it connects with the existing line, is 105 m. A further 88 m separate this point from the PSB injection area, bringing the total length to just over 193 m. Transverse focusing is provided by 23 standard quadrupoles, which are 6 m long and have a 70 mm aperture diameter. They can be coupled in pairs on a same power supply (14 needed in total) and the maximum pole-tip field strength does not exceed 0.26 T. Five dipole magnets are used for bending the line with a magnetic field B=1.0125 T.

After the last bending that joins the existing Linac2 line it is possible to keep the existing equipment (quadrupoles and steerers), though new power supplies will be probably required; only the transverse focusing will have to be readjusted in order to meet the new beam size and orientation requirements for matching into the PSB transverse acceptance.

The line section inside the PS tunnel comes close to the PS magnets, being at only 2.5 m from the PS beam line at the point of closest approach. In order to avoid interferences from the PS magnetic fields, magnetic screening of the Linac4 beam pipe is foreseen. The nature and amount of screening that needs to be applied are currently being studied. Calculations have also shown that, at the value of the magnetic field used, the probability of H^- stripping in the dipoles is less than 0.002% [34].

An RF system is needed to rotate the beam emittance in the longitudinal phase space from the initial upright position (with large energy spread and small phase width) to the final horizontal position, corresponding to a beam almost completely debunched and a minimum energy spread matched to the acceptance of the PS Booster. Studies have shown that two 352 MHz 5-cell cavities with voltages of 1.35 MV and 0.55 MV respectively will be sufficient to control the energy spread of the beam during transport and at injection with no strong sensitivity on possible beam current variations. The position of the first cavity is chosen as a balance between letting the growth in energy spread of the beam under space-charge effects reach saturation and avoiding the introduction of RF non-linearities that occur once the beam phase width is larger than the linear region of the RF slope ($\Delta\phi < 50°$). In the present scheme, a location approximately 20 m downstream of the Linac4 exit has been chosen, at which point the voltage required to completely tilt the beam in phase space is found to be 1.35 MV. One cavity powered at this full voltage would be sufficient for de-bunching, but a second one has been foreseen some 42 m downstream in order to have a larger margin in matching the energy spread of the beam to the acceptance requirements of the PSB. The voltage applied to this second cavity will however be much lower, around 0.55 MV. The required aperture radius for the two cavities (7 times r.m.s. beam size) is 35 mm.

The two debunching cavities have been designed for a maximum voltage of 1.5 MV, while keeping the RF power below 80 kW, in order to use existing RF amplifiers coming from the SPS that can deliver a maximum power of 100 kW in pulsed mode. The relatively high shunt impedance required can be provided by a multi-cell cavity, like the 5-cell π-mode structure shown in Fig. 2.38.

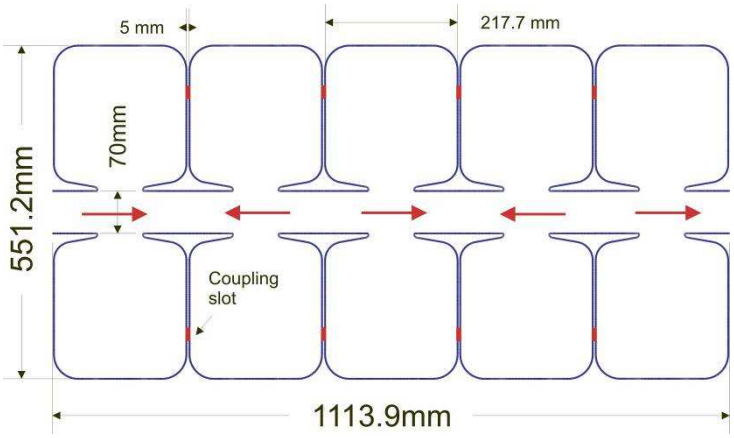

Figure 2.38: Layout of a debunching cavity

This cavity is very similar to the LEP normal-conducting cavities [35] with the simplification that no cooling is required for the small Linac4 duty cycle (these cavities are specific for the PSB injection and will never be used for a high-duty machine). Coupling between cells is provided by slots on the side walls, and a 2% coupling is sufficient to keep total field errors at a tolerable level. The computed RF parameters of the debunching cavities are presented in Table 2.10.

Table 2.10: Geometrical and RF parameters of the debunching cavities

Bore aperture radius	35 mm
Gap	75 mm
Number of cells	5
Cell length	222.8 mm
Septum thickness	5 mm
Diameter	551.2 mm
ZT^2/cell	6.057 MΩ
R/Q (per cell)	235.4 Ω
Q	25730
Transit time factor	0.89
Kilpatrick factor @ 1.5 MV	0.72
Coupling factor	2%
Power @ 1.5 MV	74.3 kW

2.9 Booster injection

The 160 MeV beam from Linac4 will be distributed to the four levels of the PSB by a sequence of a vertical bending magnet (BI.DVT30), a system of five pulsed magnets, the so called proton distributor (BI.DIS), a so called pre-deflector magnet (BI.DVT40) and 3 septum magnets (BI.SMV). The beam will be subsequently injected horizontally into the PSB rings. The Linac4 beam injection line can be built keeping the present layout and positions [36] as shown in Fig. 2.39, by modifying the existing equipment or building new equipment with higher performance. In order to make this possible, the required pulse structure from Linac4 shall consist of 4 individual pulses typically 65-100 μs long, depending on the required number of injected turns per ring, spaced by a 1 μs gap allowing for the BI.DIS rise-time. The BI.DIS timing shall be linked to the linac pulse structure. Furthermore, a general clean-up of the line shall be performed, removing obsolete equipment, such as the ion distributor directly downstream of BI.DVT40.

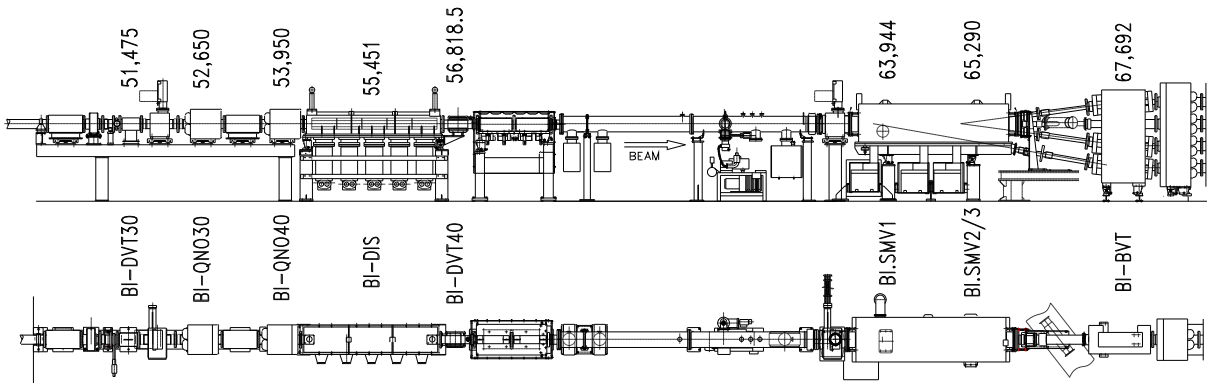

Figure 2.39: PSB Injection Line layout, side view (top) and top view (bottom), giving main components and longitudinal positions in metres

Distributor system

The vertical distribution system [37] in the injection line, as schematically represented in Fig. 2.40, consists of the proton distributor BI.DIS, a system of five pulsed ferrite core magnets, which kicks time resolved slices of the beam to different vertical positions at the vertical septum BI.SMV.

The PSB beam levels are designated counting from the bottom with ring 3 at the PS beam level. The linac beam enters the BI.DIS with a ≈ 5.2 mm vertical offset and is deflected by a fixed field iron magnet (BI.DVT40) into an absorber block, the so called head dump, at level 5. Once the rise time of the linac pulse is over, the BI.DIS deflects the beam sequentially into the different apertures of the BI.SMV, which will further deflect the beam vertically into the four separate BI.BVT magnets to achieve the required PSB beam level separation of 360 mm between each ring. The beam in the fall-time of the linac pulse is deflected to a second absorber block, the so called tail dump, at level 0.

In case of a complete BI.DIS failure or missing trigger, the full linac pulse will be directed to the head dump, which shall be robust enough to withstand a full beam impact at 160 MeV. In case of individual BI.DIS magnet failures, pulses will be directed to other rings depending on which magnets fails. An example would be the deflection of the tail dump pulse to ring 1 in case of a BI.DIS0 failure. These failure cases should be further studied in the context of the PSB H^- injection system.

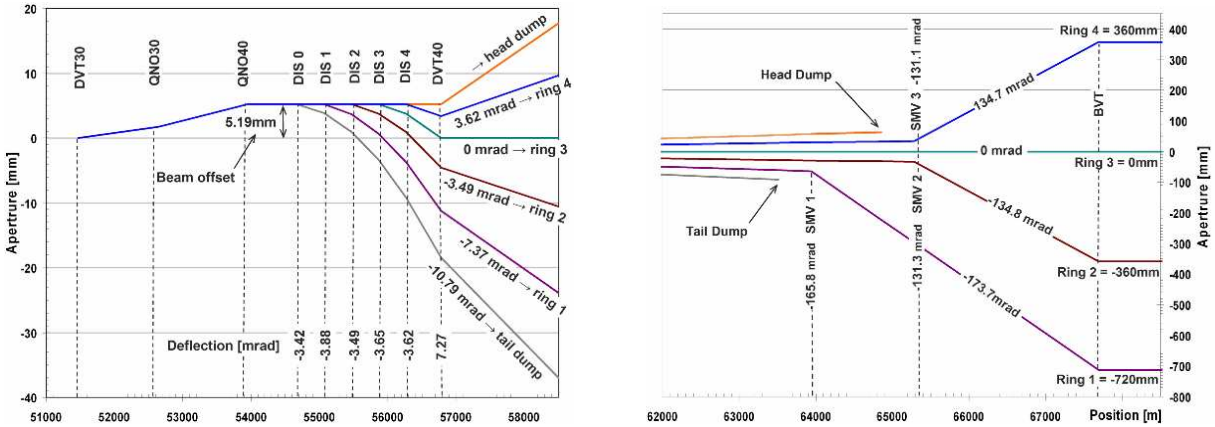

Figure 2.40: Schematic representation of the PSB injection line with the BI.DIS (left) and BI.SMV (right) vertical separation schemes

Linac4 pulse structure

The rise and fall-time of the BI.DIS system will be increased to $\leq 1\,\mu$s. Therefore the Linac4 pulse structure will consist of 4 individual pulses, typically 65-100 μs long (depending on the required number of injected turns per ring) and separated by a 1 μs particle-free gap allowing for the BI.DIS rise-time. In order to keep flexibility, Linac4 pulses and BI.DIS timing can be adjusted (Fig. 2.41) to fit the required number of injection turns from pulse to pulse, or to not fill a ring if needed. Therefore the BI.DIS timing must be linked to the linac chopper, which builds the linac pulse structure. The BI.DIS pulse lengths will be fixed, but different for each magnet.

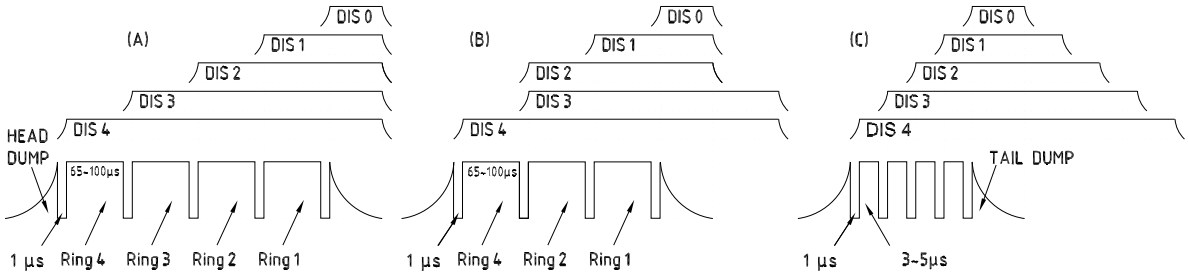

Figure 2.41: Proposed Linac4 pulse structure and BI.DIS timing showing: (A) standard operation with 65-100 injected turns per ring, (B) operation with 0 injected turns for ring 3 and (C) pilot beam with 3-5 injected turns per ring

Distributor BI.DIS

The BI.DIS system, in combination with the BI.DVT30 and BI.DVT40, is designed such that a $\approx$ 3.5 mrad deflection produces a vertical beam separation of 35 mm at the entrance of the BI.SMV septa. In order to achieve these deflection angles at 160 MeV an increase by a factor of ≈ 1.9 in the integrated field $\int B\mathrm{d}l$ is required. This will be possible by modifying the BI.DIS system to provide up to 950 A to the magnet, at a 4.3 mrad design value, compared to 500 A for the current 50 MeV beam. To achieve this, the rise- and fall-time shall be increased from 100 ns to less than 1 μs and the BI.DIS pulse lengths will be fixed but different for each magnet.

Magnetic septa BI.SMV

Time resolved slices of the beam will be kicked by the BI.DIS vertically in the gap of the electromagnetic septa (BI.SMV), as shown on the right of Fig. 2.40, which will then deflect the beam vertically out of the common transfer line vacuum chamber, into the separate PSB rings. The beam then passes through a strong vertical bending magnet, the so-called BI.BTV, to achieve the required position and angle. Three separate BI.SMV magnets will be required to provide the $\approx$ 131 mrad deflection necessary for ring 2 and ring 4, and the ≈ 166 mrad deflection necessary for ring 1. The design of these 3 magnets could be identical. Beam designated for ring 3 will see no magnetic field and shall go straight, between BI.SMV2 and BI.SMV3, towards its required position. In order to obtain the required deflection angles at 160 MeV, again an increase by a factor 1.9 in $\int B\mathrm{d}l$ is required compared to the current situation. In order to achieve this, the BI.SMV horizontal aperture needs to be reduced from 112 mm to 70 mm, matching the aperture assumed for the Linac4 transfer line.

The head and tail dumps will be positioned just upstream of the BI.SMV yokes, allowing for maximum beam separation yet optimum protection of the septa.

Other magnetic systems

In order to achieve a ≈ 5.2 mm beam offset at the entrance of BI.DIS, the BI.DVT30, BI.QNO30 and BI.QNO40 need to be modified to operate at a factor 1.9 higher in $\int B\mathrm{d}l$. Furthermore, the optics in this region needs to be matched and suitable beam sizes need to be obtained. The same applies to the BI.BVT, which needs also to be modified for a 1.9 increase of $\int B\mathrm{d}l$, of up to 0.36 Tm, to deflect the beam, exiting the BI.SMV, to the required horizontal plane of the PSB rings.

H^- injection system

The charge-exchange injection scheme is based on the scenario already conceived in [38]. It assumes that the local orbit of the circulating beam is displaced by up to 65 mm to meet the incoming beam at an angle of 66 mrad, using two independent closed orbit bump systems. In reality, to avoid that the painted intensity distribution has a large peak at zero, the beam should already be injected with an offset of a few mm at the start of the process; however, in the present description the element specifications are derived using a full bump with no offset, to give the limiting numbers for the element strengths.

The first bump, called the injection bump, is made by a set of four new pulsed dipole magnets (BS1 – BS4) located in the injection straight section, and displaces the beam by a constant 38 mm during the injection process. The second bump, called the painting bump, is made using four existing kicker magnets (KSW1 - KSW4) distributed around the ring to produce a closed orbit offset of 27 mm at the injection foil. The amplitude of the painting bump is reduced during the injection, to distribute the injected beam over the horizontal PSB aperture. The optical functions in the PSB in this region, and the closed orbit bump formed by the KSW and BS magnets are shown in Fig. 2.42.

In each of the four PSB rings the L1 injection straight section of 2.564 m is being redesigned to accommodate the injection elements: four new BS magnets, foil holder and handler, the beam dump for unstripped H_0/H^-, and suitable instrumentation for setting up and optimising the injection process. The

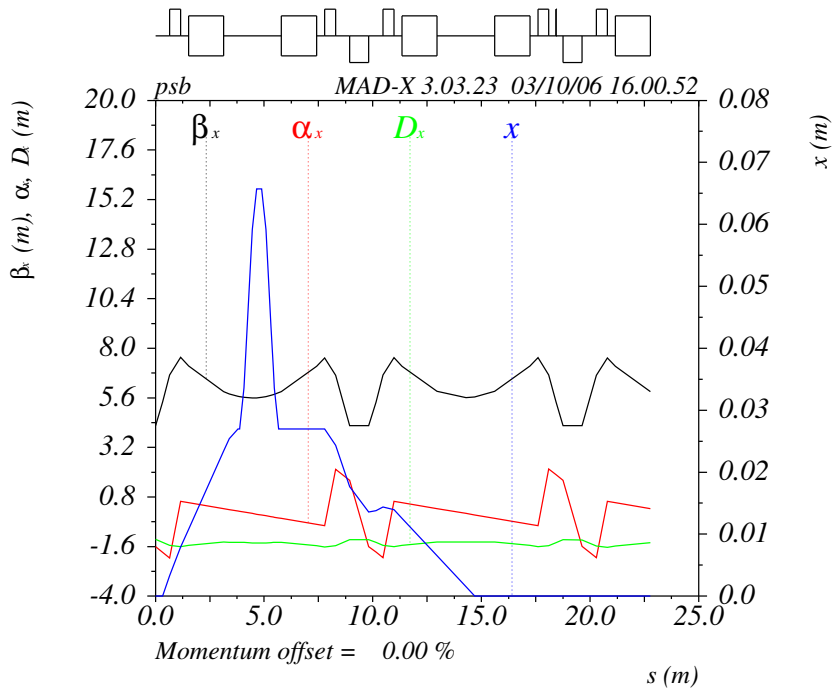

Figure 2.42: H^- injection scheme assuming that the circulating beam is shifted 38 mm by 4 new BS injection dipoles and by a further 27 mm at the start of the injection process using the 4 existing KSW orbit bumpers

existing KSW1L1 magnet located in this section (one per ring) must be displaced to accommodate the new elements, and needs to be re-engineered.

The geometry of the injection region is defined by the BI line, transporting the incoming H^- beam. This line intersects the PSB axis some 2.41 m after the start of the straight L1. The foil edge will be located at about 55-60 mm from the central orbit, with the exact position being a compromise between intercepting the maximum extent of the incoming H^- beam and minimising the number of foil traversals of the circulating proton beam. The preliminary geometry is shown in Fig. 2.43, and the required layout modifications in Fig. 2.44.

The BI line should deliver a beam at the injection point which is small horizontally, to minimise the number of foil hits. However, due to the geometry of the injection region the foil must be located displaced from the centre of the straight section, such that the Twiss parameter α is non-zero. This is not optimum and the optical match at the injection point has to be studied in more detail. A preliminary assessment indicates that the ratio of the vertical to horizontal β-function at the injection point should be as large as possible, with α close to zero, in order to minimise the number of foil traversals per proton. The present optical functions from the BI line at the foil are rather unsuitable, with a horizontal β of over 10 m and α of about -1, and some re-matching of the optics for optimising the injection efficiency will need to be made.

The first BS magnet (BS1) must act as a septum, with a thin element dividing the high-field region of the circulating beam from the field-free region through which the injected H^- beam must pass, (see Fig. 2.45). The positions chosen for the elements are essentially fixed by the space available and the position and angle of the incoming BI line. It has been assumed that at both end2 of each element, 25 mm is required to accommodate the vacuum vessel and flanges. All BS magnets are assumed to have a magnetic length of of 0.2 m. The strengths of the BS and KSW magnets are determined by the 66 mrad injection angle and maximum painting bump amplitude respectively. Assuming the latter is 27 mm, the

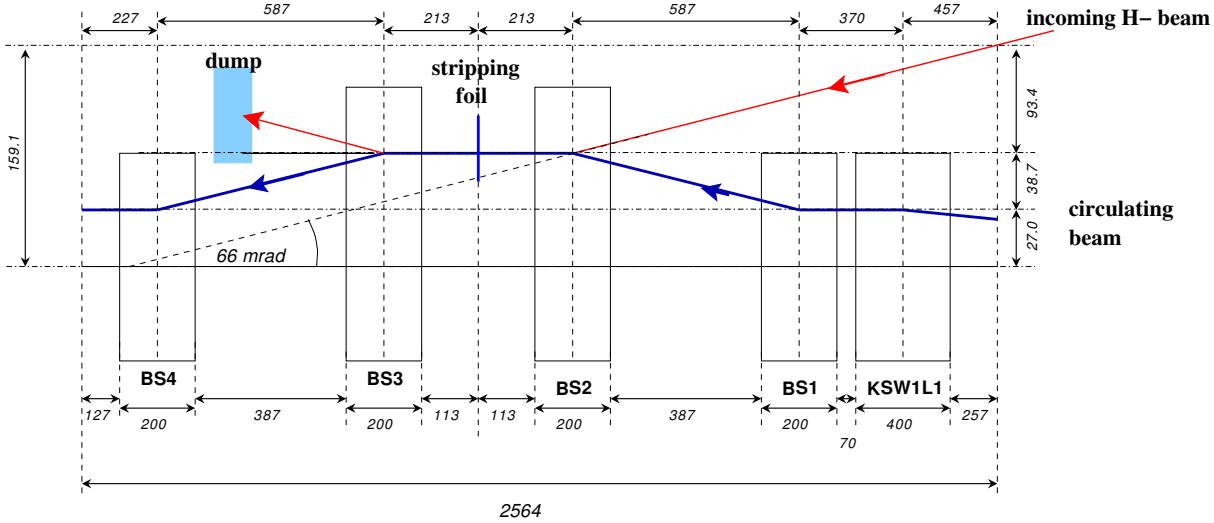

Figure 2.43: Geometry of injected beam and injection region, with all distances given in mm from the start of the L1 straight section

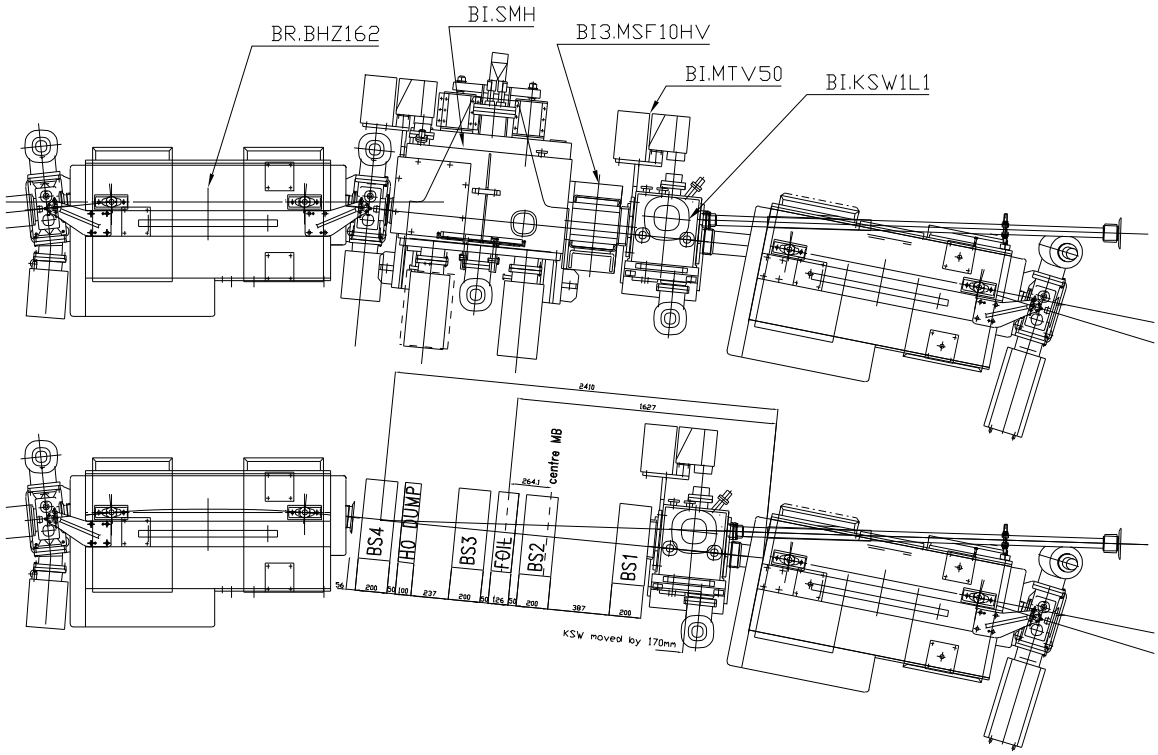

Figure 2.44: Existing (top) L1 injection region and proposed (bottom) new layout, showing lengths of main elements

required deflection angles for the KSW magnets at 160 MeV are such that the $\int Bdl$ can be obtained with the currents presently used for the 50 MeV PSB injection. The BS magnets need to provide a field of about 0.63 T. The assumed position and magnetic/active lengths available for each element are given in table 2.11.

It is assumed that the number of turns for the injection process will be between 20 and 120. This fixes the range for both the BS magnet flat-top and the KSW magnet fall-time to between about 30 and

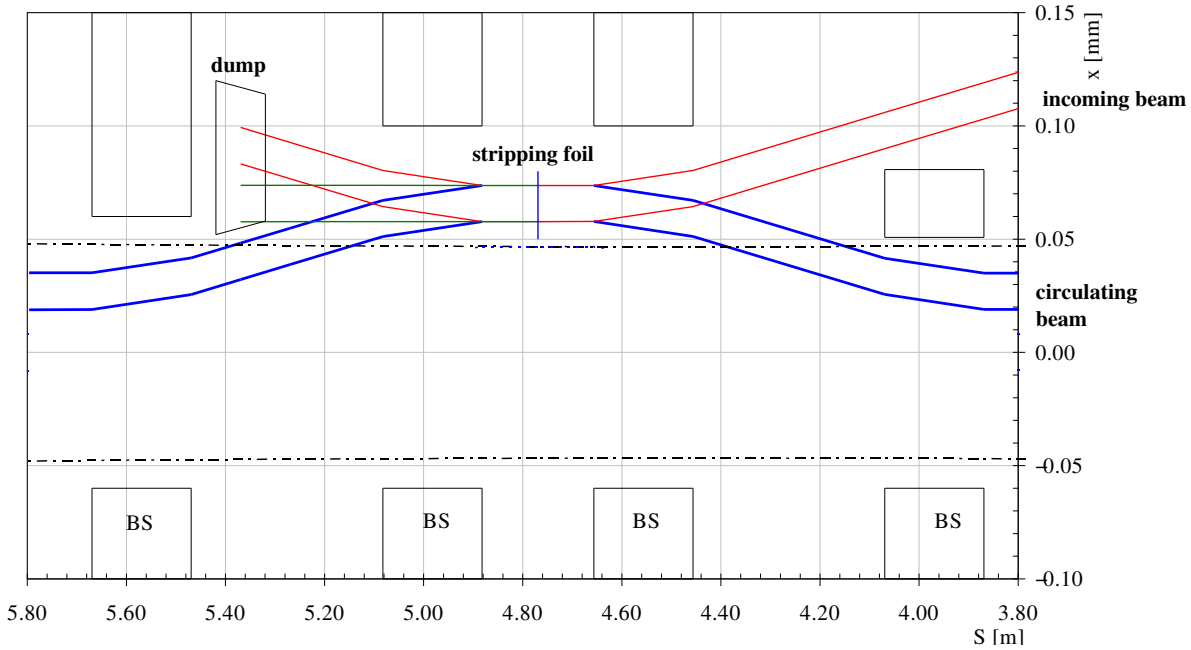

Figure 2.45: Schematic of injection region showing injected and circulating (first-turn) beam envelopes

Table 2.11: Physical lengths, apertures and strengths of KSW and BS injection bumper magnets

Magnet	**Aperture** H×V [mm×mm]	**Length** [mm]	**Peak field** [T]	$\int B\mathrm{d}l$ [T m]	**Deflection** [mrad at 160 MeV]
KSW1L1	120×70	354	0.0467	0.0165	8.7
KSW1L4	132×132	444	0.0073	0.0033	1.8
KSW2L4	132×132	444	0.0242	0.0107	5.6
KSW16L4	132×132	444	0.0582	0.0259	13.6
BS1	110×46	200	0.6300	0.1260	66.0
BS2	160×46	200	0.6300	0.1260	66.0
BS3	160×46	200	0.6300	0.1260	66.0
BS4	180×46	200	0.6300	0.1260	66.0

120 μs. The effects of these durations needs to be studied carefully to ensure that the parameter space coverage is adequate for all the foreseen injection scenarios. The shape of the falling current form is assumed to be linear in a first instance, although in general a more complex non-linear shape can produce more uniform painted distributions and will be investigated. The fall-time of the BS magnets should be of the order of 30 μs, since above this value the number of foil hits per proton begins to increase (see Fig. 2.46). This fall-time is also important for the losses which might occur on the BS1 septum, and so should be kept as short as is reasonably possible. The BS magnet flat-top and fall-time can be constant, with just a shift of the timing of the magnet pulse with respect to the beam injection according to the number of turns to be accumulated.

The ripple at the flat-top of the BS magnets should be below about $\pm 1\%$, and the error between the current in the different magnets during the fall-time should not exceed about $\pm 1\%$. The linearity of the BS magnet falling edge is not at all critical, as long as the magnet currents remain synchronised and the initial current drop at the start of the falling edge is at the rate of about 3% per μs. For the KSW magnets the error between magnets can be $\pm 2\%$; however here the linearity of the fall-time is more important

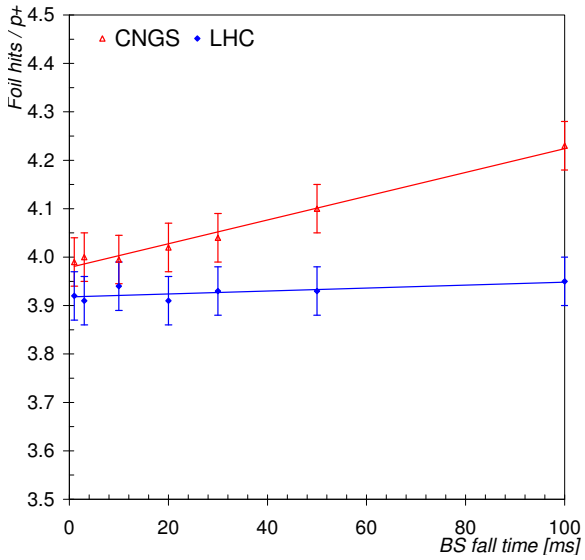

Figure 2.46: Dependence of foil hits per proton with BS magnet fall-time, for CNGS and LHC-type beam injections (no space-charge effects included)

than for the BS magnets and the maximum deviation should be of the order of $\pm 2\%$.

The layout leaves space for instruments between the BS2-3 and the BS3-4 magnets, as shown in Fig. 2.42. The longitudinal space available for each element is 187 mm, including vacuum tank and flanges, and here a BTV screen or SEM-grid able to image the injected and first-turn beams is required. The details of the requirements need to be defined, including the intensity and emittance range, the resolution and the in-beam positions.

The foil is assumed to be between 100 and 200 μg/cm^2 carbon. A relatively thick foil seems justified on the grounds that minimising the amount of unstripped H_0 or H^- is going to be a very important aspect of the injection design, and the benefits of a thicker foil will outweigh the disadvantages of extra foil heating, losses and emittance blow-up. This foil should strip over 99% of the H^- to H^+, leaving less that 1% of H_0 and less than 0.1% of H^- [39] - the optimisation of the foil thickness is an important area for future study. The foil will need to be about 20 mm high and 20 mm wide, and may need a positioning mechanism to allow some adjustment in the x-direction in order to minimise the number of H^- ions which miss it. For operational efficiency, it must be possible to exchange foils remotely. The space available for the foil holder/handler module is only 126 mm long: this is expected to be a difficult item to design mechanically, especially given the need for four such mechanisms stacked on top of each other.

The unstripped ions must be intercepted by a beam dump, which for space reasons will have to be located in the PSB ring. The injection geometry and the very limited space available in the existing L1 straight appear to preclude any extraction of the unstripped ions, as is used or planned for high-power charge-exchange injection systems such as JPARC [40]. The asymmetry of the injection elements and geometry with respect to the centre of L1 means that there is no possibility to add a second foil to strip the remaining ions, and to extract the resulting protons past or via the BS4 magnet. The only possibility for such an extraction-based external dump system would be to increase the angle of the incoming B1 line to at least 100 mrad and to reduce the distance between the BS1-2 and BS3-4 magnets to about 0.3 m. However, this solution would require several changes to the proposed version: it would reduce the space available for the H^- holder/handler unit to only 60 mm, it would require a completely new geometry of the incoming B1 line, it would require stronger BS magnets, with about 1 T field, it would need another foil holder/handler unit and it would need the BS4 magnet to be built as an extraction septum. For these reasons this alternative is presently not under consideration. Instead an internal dump is proposed,

housed in a separate unit just up-stream of BS4. At present 0.15 m longitudinal space is allocated for the dump block, including vacuum tank and flanges - detailed energy deposition simulations are needed to check if this is adequate given the expected peak and integrated beam loading, and also tracking studies need to be made to determine whether the location allows sufficient aperture for the injected beam, while ensuring that all unstripped or partially stripped ions are intercepted.

The peak fields in the BS magnets will be 0.63 T with the present geometry, which should keep the losses due to Lorentz stripping of the incoming H^- beam below the 10^{-7} level.

In the proposed layout, the physical aperture requirements are important to minimise beam loss in this already difficult region. The vertical aperture of the BS magnets has been chosen to remain in the shadow of the main PSB dipoles, scaling with the local β-function. In the horizontal plane, the BS1 septum element will be a critical aperture location. Assuming a septum width of 30 mm is technically possible, the aperture available for the injected and the circulating beam is about 17 mm from the beam axis (note for the circulating beam, this is the clearance from the axis of a beam making one turn, from which the falling edge of the KSW bump must be subtracted). At the proposed beam dump location, the clearance to the first turn of the injected beam is even smaller, at about 15 mm. The effect of the injected beam distribution, injection mismatch, space-charge effects, scattering and other diffusion processes on the expected distribution of the circulating beam needs to be carefully evaluated, to determine the expected loss levels and real aperture requirements at these critical locations.

Chapter 3

Beam dynamics

Beam dynamics considerations have influenced the choice of the structure parameters from the first conception stage. The main guidelines have been the control of losses, the minimisation of the emittance growth as well as the minimisation of the halo development. In order to achieve this, much care has been put in following the constraints of keeping: i) a zero-current phase advance always below 90° , for stability; ii) a longitudinal to transverse phase advance ratio (with current) between 0.5 and 0.8 in order to avoid emittance exchange, and iii) a smooth variation of the transverse and longitudinal phase advance per metre.

The accelerator optimisation has been conducted in sections. An end-to-end simulation has validated the choices and has allowed to smooth transitions wherever needed. Particular care has been put into the matching at each transition point: an initial envelope-type matching has been subsequently refined by a multi-particle-type matching on a cloud of particles generated at the low-energy end.

The starting point of the simulations is the Low Energy Beam Transport (LEBT) between the source and the first stage of RF acceleration. In this section the space-charge electric field of the quasi-DC beams can be compensated by the trapping of positive ions created by ionization of residual gas molecules, and the rapid expulsion from the beam of the free electrons by the electric field. The partial neutralisation of the beam current has an impact on the emittance growth and on the halo development and it can significantly change the beam distribution at the start of the acceleration.

When the simulations from the source were not available we have tracked two different distributions through the accelerator: a 4D waterbag and a Gaussian. The difference in the behaviour of those two distributions can set boundaries to the behaviour of a "real" beam.

Most of the simulations have been run with 50,000 macro-particles, therefore giving to any global quantity reported in this chapter an accuracy of about 0.5%. The figures of merit for the beam dynamics are: the losses, the r.m.s. emittance growth, the ratio of the r.m.s. beam size to the aperture and the sensitivity to errors. A description of the beam dynamics in each accelerator section is given in the following. Calculations have been done with the codes PATH [41], TOUTATIS [42], TRACEWIN [43] and IMPACT [44]. These have been made read/write compatible for the purpose of tracking beam from the low-energy to the high-energy end without regenerating a distribution at any point along the line. All programs agree to within few percent, therefore only one of the results is presented. Further details on code comparison results can be found in [45].

3.1 Front-end: LEBT, RFQ, and chopper line

LEBT (95 keV)

The Low Energy Beam Transport (LEBT) must ensure the matching of the beam from the source to the RFQ, while minimising the emittance growth. The choice has been made to employ magnetic lenses rather than electrostatic ones for the following reasons: i) to avoid the high-tension discharge problems of electrostatic lenses, ii) the possibility of space-charge compensation and iii) the availability of spare pulsed solenoid lenses from Linac2. Furthermore, there is a long experience at CERN in the design and operation of two-solenoid LEBT systems, used in the new RFQ injector at Linac2.

Simulations have been performed of the beam transport in the LEBT with the multi-particle code PATH, using calculated field maps of solenoid magnets. Beam input conditions have been based on measurements of the DESY RF source, and tracked through a post-accelerating system bringing the energy from 35 to 95 keV. The beam is created with a uniform beam distribution in the transverse plane, and the space-charge forces are calculated using the SCHEFF routine, imposing a circular symmetry of

the space-charge field. Calculations use a linear compensation of the beam intensity to simulate the effect of beam space-charge neutralisation. Several groups have reported successful use of this compensation model to explain empirical measurements of beam transport. However, to understand and limit the creation of beam halo will require understanding of the non-linear behaviour of compensation [46].

The simulations have yielded the following information:

- The nominal beam ($\varepsilon = 0.25$ mm mrad, 70 mA) can be transported and matched to the RFQ with no losses.
- With full space-charge, emittance growth can be contained within 25% by limiting the dimension of the beam in the solenoids to avoid lens aberrations, which in turn would lead to a strongly non-linear space-charge field. Such a requirement also leads to shortening the distance between the source and the first solenoid.
- With a space-charge compensation fraction of 90%, the emittance growth can be limited to 2%.
- There is negligible emittance growth due to misalignments of the beam or solenoids (up to 2 mm and 20 mrad respectively). It is required that the beam is steered into the acceptance of the RFQ.

RFQ (95 keV to 3 MeV)

The beam dynamics in the IPHI RFQ has been extensively presented in [17, 47, 48]. The RFQ is capable of accelerating with a $> 99\%$ efficiency a beam of 20 to 100 mA current with limited emittance growth. Simulations show that, even for a perfectly matched beam, halo develops in the RFQ at the level of 10^{-4} and that transverse emittance grows by 8% for a 70 mA beam. The output beam phase space calculated with TOUTATIS is shown in Fig. 3.1 some halo is visible in the x-y plot at the bottom-right corner. The emittance growth happens in the RFQ coupling gaps, placed every two metres along the structure. Figure 3.2 shows very clearly this effect.

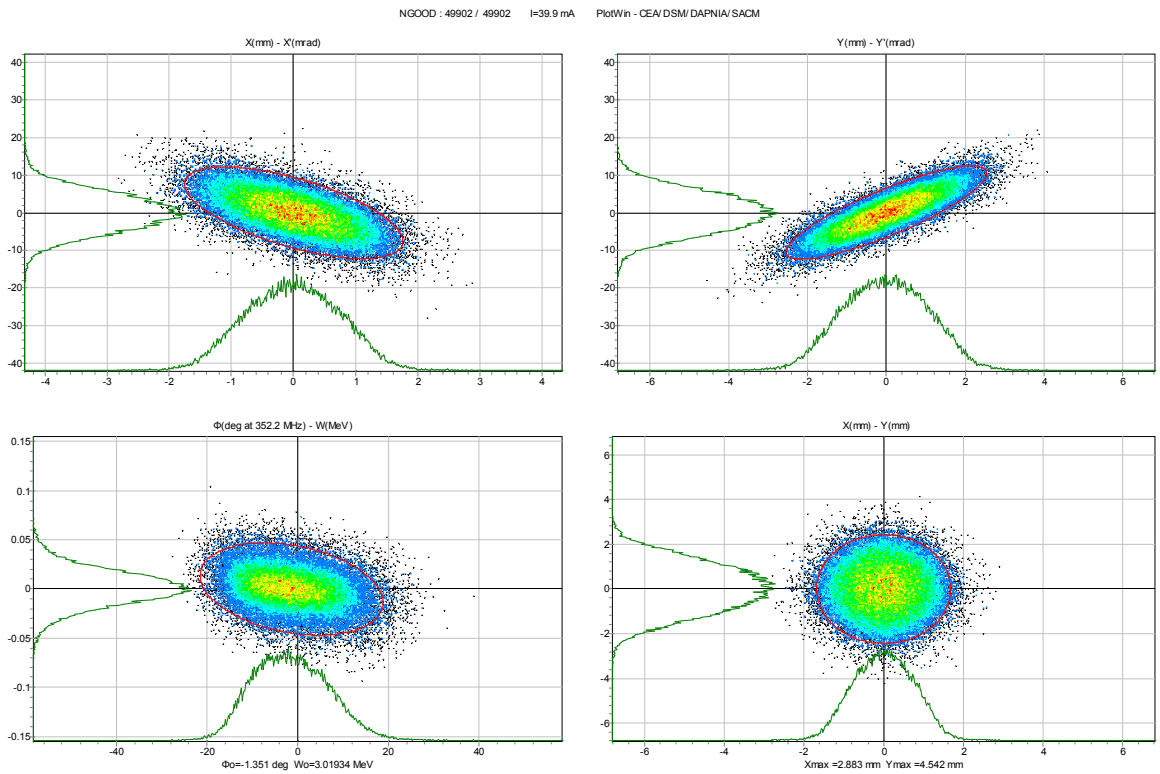

Figure 3.1: Beam phase space portrait at the output of the RFQ for an initially Gaussian distribution (matched)

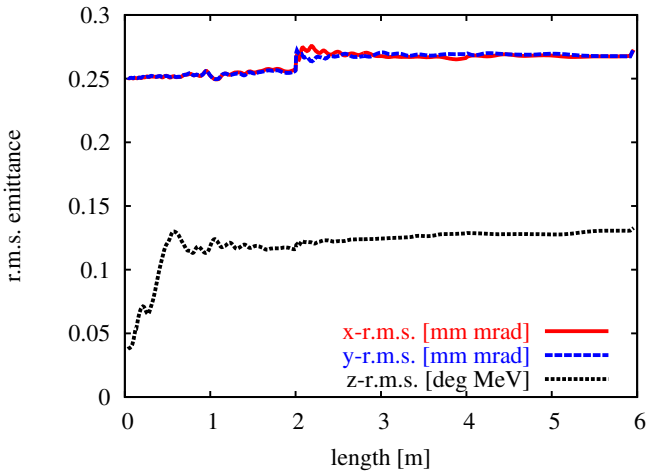

Figure 3.2: Transverse and longitudinal r.m.s. emittance along the IPHI RFQ

Chopper line and matching to the DTL (3 MeV)

The chopper line is intended to house the beam chopper, and to match the beam out of the RFQ and into the DTL. Due to the conflicting needs of high voltage and fast rise-time the chopper is a relatively long object, compared to the speed of the particles: housing it in the beam line implies an abrupt modification of the phase advance per metre. In order to disrupt as little as possible the continuity of the phase advance, the chopper is integrated in a F0D0 period, with a length of 1.6 m. A total of four F0D0 periods assure the matching from the RFQ to the chopper and from the chopper to the DTL. The F0D0 period housing the chopper is also essential for the chopping action, as it amplifies the effective kick of the chopper (5.3 mrad kick for 400 V effective voltage per plate) by the appropriate phase advance for the beam centre (almost 90° from the centre of the chopper to the middle of the dump). With 11 quadrupoles (already existing at CERN) and 3 bunchers, the beam can be chopped with only 0.2% of current left in the empty bunches. After the dump, where the unwanted bunches are eliminated, the beam is matched to the DTL focusing structure, which in the first tank is an FFDD system. Space-charge induced emittance growth is very severe when the beam is compressed back in volume to fit a fast phase advance focusing channel. In our case it amounts to almost 20%. The losses in the main beam are partly on the chopper plates (4%) and partly on the dump (8%). The envelopes of the chopped and un-chopped beams are shown in Fig. 3.3.

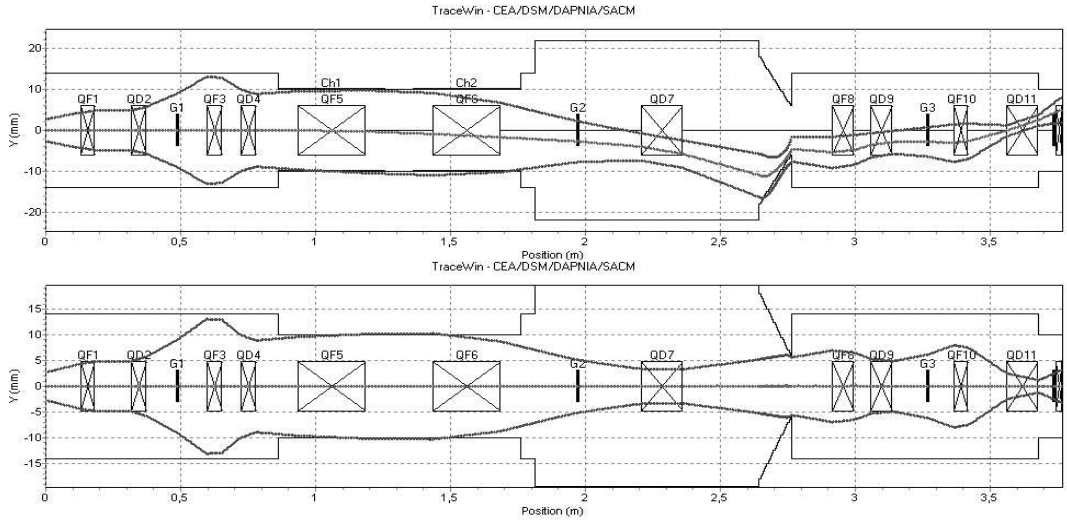

Figure 3.3: Beam envelope in the chopper line: chopped beam (top) and un-chopped beam (bottom)

3.2 Main linac and transfer line

DTL, CCDTL and SCL (3 MeV to 160 MeV)

After chopping, the beam is accelerated to 40 MeV in three DTL tanks equipped with Permanent Magnet Quadrupoles (PMQ). In the first tank the reference focusing scheme is FFDD whereas in the following tanks F0D0 is preferred. The reason for this choice is purely technical as it was not sure whether the higher integrated gradient needed for a F0D0 at 3 MeV and 352 MHz would be reliably achievable. The transition between the two focusing schemes is smooth and no emittance growth is observed provided the matching is done adequately. A scheme with FD configuration everywhere has been studied and it gives some advantages with respect to sensitivity to beam errors: it can be accommodated at any time in the linac design without modification of the tank structure.

The DTL is fully equipped with PMQs, i.e. there is not any possibility of adjustment at a later stage. We have verified that with the chosen quadrupole settings - optimised for 65 mA - currents in the range between 20 mA and 70 mA can be accepted and that the electromagnetic quadrupoles in the chopper line can match the beam for the different current values.

At 40 MeV the beam is energetic enough to allow the transition to a structure which doesn't follow the beam velocity profile cell-by-cell. Acceleration to 90 MeV happens in a CCDTL composed of 3-gap tanks. The average phase in each tank is -20° and the focusing period is 3 $\beta\lambda$. At the transition between tanks and/or structures where one or more gaps are "missing" the phase of the neighbouring cavities is adjusted to cope with the transition and to insure a smooth variation of the longitudinal phase advance. At 90 MeV the structure used is an SCL at twice the basic frequency with 11 cells per tank. The variation of longitudinal phase advance due to the frequency jump is controlled by adjusting the phase in the modules at the transition. The resulting phase advances are varying smoothly and do not give rise to emittance growth.

The transverse and longitudinal (phase) r.m.s. envelope for a matched Gaussian beam generated at the entrance of the DTL are shown in Fig. 3.4.

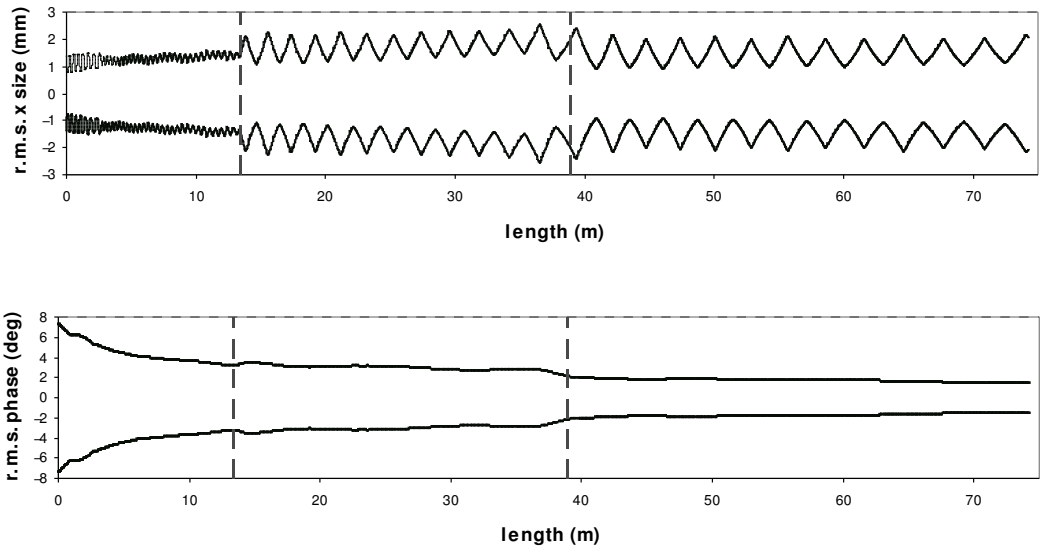

Figure 3.4: Transverse (x) and phase r.m.s. envelope along the DTL-CCDTL-SCL

At all time during the acceleration (except at one point) the ratio of transverse to longitudinal phase advance is chosen to respect Hoffmann's stability criterion [49]; hence the emittance exchange during acceleration is under control. Table 3.1 summarises the emittance growths in each section for Gaussian and uniform input beam distributions.

Table 3.1: Emittance increase between 3 and 160 MeV for a uniform and Gaussian beam

		DTL	CCDTL	SCL	Total
Gaussian	x [%]	5.5	0,1	2.8	8.7
	y [%]	4.3	1.8	2.6	9.0
	z [%]	4.6	1.4	0.3	6.4
Uniform	x [%]	1.4	0.1	0.7	2.2
	y [%]	−1.0	3.3	0.3	2.6
	z [%]	4.0	1.1	0.6	5.7

Transfer line to the PS booster

At 160 MeV the beam (Fig. 3.5) shows some halo, which is very well transmitted throughout the machine, and has an excessive energy spread that must be reduced to match the acceptance of the PS Booster. The main constraint in the design of the transfer line arises from the difficulty of integrating the transfer line in the complex of CERN accelerators. Existing buildings and other accelerators make it necessary to divide the line in three sections with bending magnets in between. The most critical part from the beam dynamics point of view is the initial part, just after the SCL, where the beam has a big energy spread and is very compressed in phase. The combination of dispersion and space-charge effects are difficult to handle without allowing for some emittance growth. The evolution of the emittance along the transfer line is shown in Fig. 3.6 where one can clearly see the emittance growth due to the dispersion which is only partly compensated by the following bending.

3.3 End-to-end beam dynamics and error studies

After an initial phase of optimisation of each individual section of the accelerator, a campaign of end-to-end simulations was launched with the purpose of identifying bottlenecks, weak points, and acceptance limitations, thus allowing for a fine tuning of the layout. The evolution of the r.m.s. emittances in the three planes as calculated with PATH is presented in Fig. 3.6. The transverse emittance growth is much localised and occurs in the LEBT, in the chopper line and in the transfer line to the PSB. There is no visible emittance growth during the main acceleration from 3 to 160 MeV, indicating that the transition between the four focusing schemes and the three accelerating structures has been done smoothly and respecting the phase advance criteria. Some work is still ongoing to further decrease the emittance growth in the LEBT and in the transfer line to the PSB. Some improvement might be possible with a better knowledge of the source output distribution and a better matching from the last acceleration section to the transfer line. Nevertheless, with the present optics the r.m.s. normalised emittance delivered to the PS Booster is half the one delivered by the present Linac2 injector.

A quality factor of the solidity of the design is the ratio of the r.m.s. beam size to the radius of the vacuum chamber. From Fig. 3.7 it is clear that the transverse Linac4 bottlenecks are the chopper and the dump, where the aperture approaches two times the r.m.s. beam size. Losses are localised in this area and the geometry of the chopper defines the minimum transverse acceptance of the whole linac.

Error studies

The sensitivity to alignment and RF errors in Linac4 has been studied by tracking a Gaussian distribution containing 50,000 particles over 1,000 different linacs with random errors uniformly distributed within the values given in Table 3.2. No correction scheme has been implemented; no beam mismatch has been included at the beginning. The longitudinal errors have been divided in two classes: the class referred to as “klystron errors” contains amplitude- and phase-error of the RF power sources (3 for the DTL, 8 for the CCDTL and 5 for the SCL). These errors are applied coherently to all the RF gaps powered by

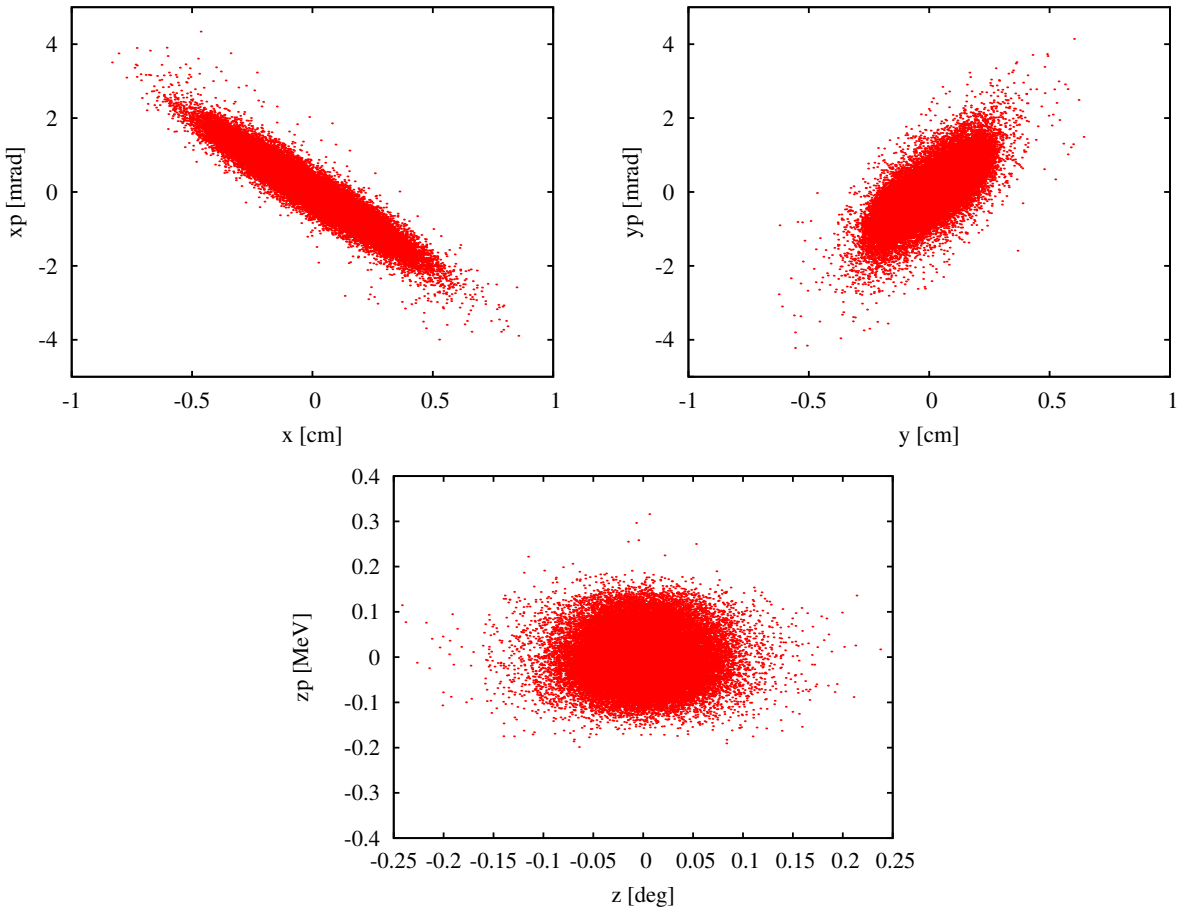

Figure 3.5: Beam phase space at the exit of the SCL: transverse planes (top) and longitudinal plane (bottom)

the same source. The second class, refereed to as "gap errors" contains amplitude- and phase-errors that are applied individually to each accelerating cell and that are uncorrelated between cells. These errors mimic the phase- and amplitude-errors resulting from manufacturing errors in any multi-cell structure. The values assumed in Table 3.2 are the ones foreseen to remain after an accurate tuning procedure.

Table 3.2: Total error amplitudes used for sensitivity studies

Quadrupole gradient [%]	± 0.5
Quadrupole displacement [mm]	± 0.1
Quadrupole rotations (x, y) [deg]	± 0.5
Quadrupole rotations (z) [deg]	± 0.2
Cavity field phase [deg]	± 1.0
Cavity field amplitude [%]	± 1.0

The above errors have been simulated individually and then all together to study how individual sensitivities add up. The results of TRACEWIN calculations, over 500 to 1,000 runs with a Gaussian distribution containing 50,000 particles generated at the beginning of the DTL are reported in Table 3.3 and Table 3.4. The results refer to the end of the SCL at 160 MeV. The error distribution is uniform within the boundaries indicated for each case. Each column in the table indicates respectively: the average emittance growth in the two transverse planes, and the average energy and phase deviations.

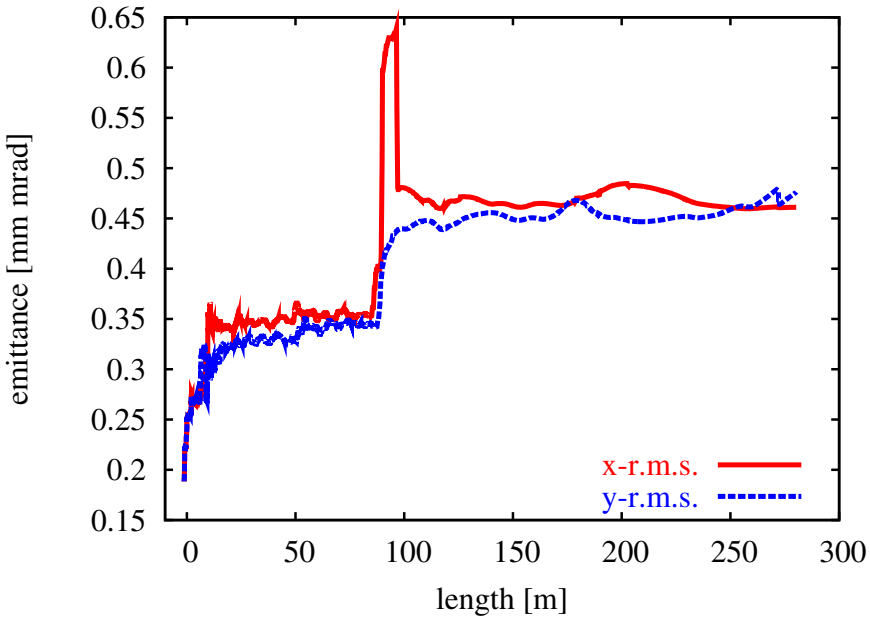

Figure 3.6: Transverse r.m.s. emittance throughout Linac4 and transfer line. Starting point (z=0) is the RFQ input plane, z=10 m is the DTL input plane and z=85 m is the beginning of the transfer line to the booster.

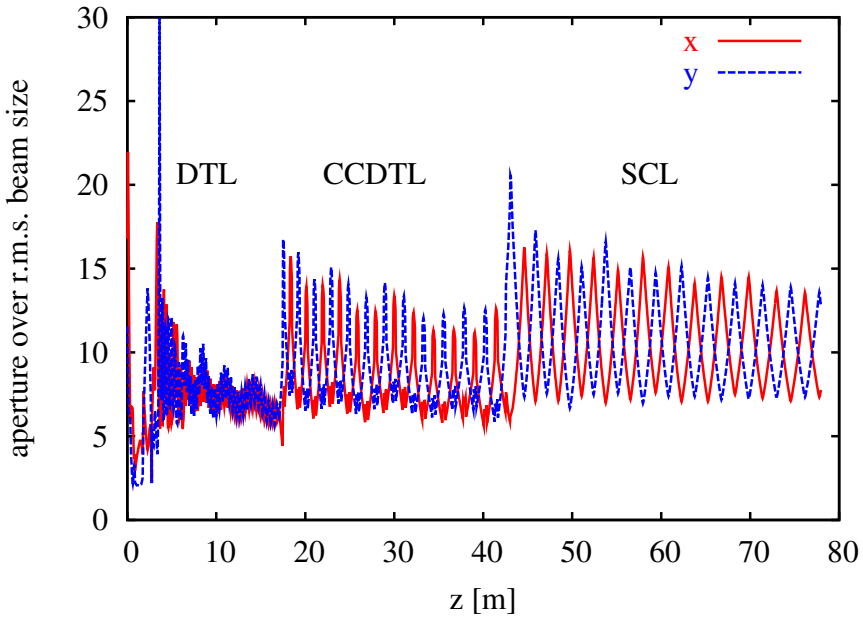

Figure 3.7: Aperture over r.m.s. beam size from chopper to SCL

In the last column an account of the runs showing losses is given. For each of the above quantity the r.m.s. of the output distribution is given, as well as the cumulated probability that the degradation of each quantity due to errors is within 1% or 5%. More details are in [50]. From the last row we can see that all errors combined and uncorrected generate an emittance increase of some 10-15% in all three planes, an energy jitter of 270 keV r.m.s. and a phase jitter of 1.8° (r.m.s.) at the end of the linac. These values are presently acceptable for injection into the booster as the energy jitter will be reduced by the de-bunching cavity in the line to about 65 keV.

Table 3.3: Sensitivity of Linac4 to RF errors

Error	$\Delta\varepsilon_x/\varepsilon_x$ $\pm$ r.m.s. [%] probab. [%]	$\Delta\varepsilon_y/\varepsilon_y$ $\pm$ r.m.s. [%] probab. [%]	$\Delta\varepsilon_z/\varepsilon_z$ $\pm$ r.m.s. [%] probab. [%]	ΔE $\pm$ r.m.s. [keV]	$\Delta\phi$ $\pm$ r.m.s. [deg]	**Lossy runs/ total runs Loss range**
$E_{\text{gap}} = \pm 1\%$	0.45 ± 0.7 $< 1\%$: 79.5 $< 5\%$: 99.8	0.7 ± 1.1 $< 1\%$: 68.4 $< 5\%$: 99.3	0.5 ± 1.3 $< 1\%$: 66.6 $< 5\%$: 99.5	-13.3 ± 71.3	0.0 ± 0.6	0/1000 $< 2 \times 10^{-5}$
$E_{\text{klystron}} = \pm 1\%$	1.9 ± 2.0 $< 1\%$: 39.6 $< 5\%$: 92.4	2.3 ± 2.8 $< 1\%$: 43.3 $< 5\%$: 84.4	3.5 ± 5.0 $< 1\%$: 32.1 $< 5\%$: 75.4	-11.2 ± 211	0.2 ± 1.5	0/1000 $< 2 \times 10^{-5}$
$\phi_{\text{klystron}} = \pm 1^\circ$	1.4 ± 1.4 $< 1\%$: 43.9 $< 5\%$: 97.6	1.8 ± 2.0 $< 1\%$: 41.2 $< 5\%$: 91.9	3.0 ± 3.6 $< 1\%$: 31.9 $< 5\%$: 78.7	-8.6 ± 150	0.1 ± 1.0	0/1000 $< 2 \times 10^{-5}$
All RF errors	3.8 ± 3.5 $< 1\%$: 17.0 $< 5\%$: 75.1	4.8 ± 5.0 $< 1\%$: 17.5 $< 5\%$: 64.5	10.1 ± 15.9 $< 1\%$: 11.8 $< 5\%$: 42.9	-12.9 ± 262	0.2 ± 2.0	0/1000 $< 2 \times 10^{-5}$

Table 3.4: Sensitivity of Linac4 to transverse errors

Error	$\Delta\varepsilon_x/\varepsilon_x$ $\pm$ r.m.s. [%] probab. [%]	$\Delta\varepsilon_y/\varepsilon_y$ $\pm$ r.m.s. [%] probab. [%]	$\Delta\varepsilon_z/\varepsilon_z$ $\pm$ r.m.s. [%] probab. [%]	ΔE $\pm$ r.m.s. [keV]	$\Delta\phi$ $\pm$ r.m.s. [deg]	**Lossy runs/ total runs Loss range**
x displ.	3.9 ± 3.3	1.1 ± 0.7	3.7 ± 2.8	-15.7	2×10^{-3}	0/600
	$< 1\%$: 12.0	$< 1\%$: 51.0	$< 1\%$: 9.4	± 3.2	$\pm 3.3 \times 10^{-2}$	
± 0.1 mm	$< 5\%$: 75.5	$< 5\%$: 99.8	$< 5\%$: 77.3			$< 2 \times 10^{-5}$
x rotat.	0.01 ± 0.05	0.01 ± 0.02	0.03 ± 0.02	-14.1	3×10^{-2}	0/500
	$< 1\%$: 100	$< 1\%$: 100	$< 1\%$: 100	± 0.06	$\pm 3 \times 10^{-4}$	
$\pm 0.5^\circ$	$< 5\%$: 100	$< 5\%$: 100	$< 5\%$: 100			$< 2 \times 10^{-5}$
z rotat.	1.3 ± 1.3	1.7 ± 1.0	0.1 ± 0.1	-14.3	3×10^{-2}	0/1000
	$< 1\%$: 53.1	$< 1\%$: 22.9	$< 1\%$: 100	± 0.2	$\pm 1 \times 10^{-3}$	
$\pm 0.2^\circ$	$< 5\%$: 98.4	$< 5\%$: 99.0	$< 5\%$: 100			$< 2 \times 10^{-5}$
$\Delta G/G$	0.5 ± 0.7	1.2 ± 1.0	0.1 ± 0.2	14.2	3×10^{-2}	0/500
	$< 1\%$: 81.8	$< 1\%$: 49.5	$< 1\%$: 99.8	± 0.4	$\pm 3 \times 10^{-3}$	
$\pm 0.5\%$	$< 5\%$: 99.8	$< 5\%$: 99.0	$< 5\%$: 100			$< 2 \times 10^{-5}$
All errors	10.4 ± 4.8	12.7 ± 6.1	17.3 ± 10.2	-6.4	0.3	10/1000
transverse +	$< 1\%$: 0.0	$< 1\%$: 0.0	$< 1\%$: 0.1	± 271	± 1.8	
longitudinal	$< 5\%$: 7.7	$< 5\%$: 3.9	$< 5\%$: 3.1			$10^{-4}/10^{-5}$

A comparison of error simulations was made for the DTL part of the Linac, benchmarking simulation results of TRACE-WIN with those from IMPACT. The results are given in Table 3.5. In general the results of the two codes agree quite well. Large discrepancies can be observed in the quadrupole gradient errors but here the total emittance growth in both cases is below 0.5%, meaning that the differences can probably be explained by numerical or statistical noise. The other major difference is in relation to the effects of the energy and phase errors of the klystrons which is probably caused by the different RF gap models implemented in IMPACT and TRACE-WIN.

Table 3.5: Comparison between TraceWin (TW) and IMPACT (I) results (500 runs per case with each code)

Error	**Code**	$\Delta\varepsilon_x/\varepsilon_x$ $\pm$ r.m.s. [%]	$\Delta\varepsilon_y/\varepsilon_y$ $\pm$ r.m.s. [%]	$\Delta\varepsilon_z/\varepsilon_z$ $\pm$ r.m.s. [%]	ΔE $\pm$ r.m.s. [keV]	$\Delta\phi$ $\pm$ r.m.s. [deg]
x displ.	TW	2.0 ± 1.6	0.2 ± 0.1	1.6 ± 1.3	–	–
(± 0.1 mm)	I	1.7 ± 1.5	0.02 ± 0.09	1.5 ± 1.3	–	–
z rot.	TW	0.9 ± 0.8	1.0 ± 0.8	0.03 ± 0.04	–	–
($\pm 0.2^\circ$)	I	0.9 ± 0.6	0.8 ± 0.6	0.02 ± 0.05	–	–
$\Delta G/G$	TW	0.2 ± 0.4	0.2 ± 0.3	0.0 ± 0.1	–	–
($\pm 0.2\%$)	I	0.4 ± 1.3	0.4 ± 1.9	0.03 ± 0.3	–	–
ΔE, $\Delta\phi$	TW	0.1 ± 0.6	0.2 ± 0.5	0.7 ± 1.0	-6.9 ± 29	0.0 ± 2.1
($\pm 1\%$, $\pm 1^\circ$)	I	0.3 ± 1.6	-0.1 ± 1.4	2.0 ± 3.7	-2.0 ± 19	0.2 ± 2.2

3.4 Loss management

During normal operation, i.e. excluding equipment failure scenarios, there are three identified causes of uncontrolled beam loss in an H^- linac: i) scraping of part of the beam halo as consequence of alignment errors and/or beam mismatch, which lead to oscillations of beam centre and halo growth; ii) H^- stripping by collision with residual particles in the vacuum chamber; and finally iii) H^- stripping in magnetic fields perpendicular to the direction of motion. A tight loss management is crucial in order to maintain hands-on machine maintenance and to minimise the radiation to the environment, in particular for the South Hall where space for concrete shielding is limited. (see Section 5.1).

The beam losses on the chamber walls are mainly driven by transverse alignment errors in the focusing elements, and can be amplified by gradient errors and beam centroid errors. Longitudinal errors (RF errors) have little if no influence on the transverse losses in the linac itself, but have an effect in the transfer line where dispersive elements (bending magnets) convert energy errors into position errors. In order to calculate the expected beam loss, two types of errors have been considered: static errors, which are constant along the pulse and dynamic errors which can vary from pulse to pulse. For the first type we can limit the effect of the errors by using strategically placed correction dipoles (steerers), for dynamic errors no correction is possible. All alignment errors are considered as static, i.e. with a drift-time of hours or days. In the simulations, only the power-loss distribution above 3 MeV energy has been considered, as this can be assumed as threshold energy for the generation of neutrons in copper.

A series of statistical runs have been performed, assuming quadrupole gradient and alignment errors as defined in Table 3.2 and an initial beam alignment error of 1 mm and 1 mrad (r.m.s.). To correct beam position, the available steerers are used (see Section 4.2) with a maximum integrated field of 2.7 mT m and an accuracy of ±0.5%. The simulation results are reported in Table 3.6. For each section of the accelerator several errors configurations (1000 to 3000 cases) have been simulated and the average losses recorded. Also the worst loss over the section has been recorded, and this number should be regarded as the upper limit of losses in the most pessimistic case. In all cases the integrated beam loss is well below 1 W/m, which is the limit universally accepted for hands-on maintenance in a linear accelerator [77]. No losses have been observed in the transfer line with the expected energy jitter from the linac.

Next step has been to analyse the loss pattern along the machine in order to identify position and loss level of "hot spots", well identified locations along the machine where beam loss can occur, due to possible mismatch between linac sections or aperture restrictions. An example is shown in Fig. 3.8 where the power-loss distribution in the SCL is plotted. Four hot spots are clearly recognisable, corresponding to the location of maximum excursion of the beam centroid under the effect of the uncompensated errors at the steerer's position. Possibly different steering strategies can further reduce these losses, and studies are continuing in this direction. In all cases observed, losses at "hot spots" are well below 1 W.

Table 3.6: Beam loss due to misalignment and gradient errors assuming correction with steerers

Section	Energy	Length	Lossy runs	Average loss over all runs	Average loss over lossy runs	Max. loss p. section	Max. loss
	[MeV]	[m]	[%]	[W]	[W]	[W]	[W/m]
DTL, tank 1	3–10	2.7	24	0.005	0.02	0.06	0.02
DTL, tank 2	10–25	5.4	0.3	0.0001	0.02	0.004	0.001
DTL, tank 3	25–40	5.7	13	0.01	0.1	0.8	0.14
CCDTL, mod. 1,2	40–52	5.4	23	0.1	0.4	2.2	0.41
CCDTL, mod. 3,4	52–65	6.0	17	0.07	0.4	1.9	0.32
CCDTL, mod. 5,6	65–78	6.6	16	0.07	0.4	2.0	0.3
CCDTL, mod. 7,8	78–90	8.0	16	0.1	0.6	3.1	0.39
SCL, mod. 1	90–106	6.4	5	0.01	0.3	0.8	0.13
SCL, mod. 2	106–124	6.8	30	0.19	0.7	2.9	0.43
SCL, mod. 3	124–143	7.2	15	0.1	0.6	4.0	0.56
SCL, mod. 4	143–160	7.6	12	0.05	0.4	1.0	0.13

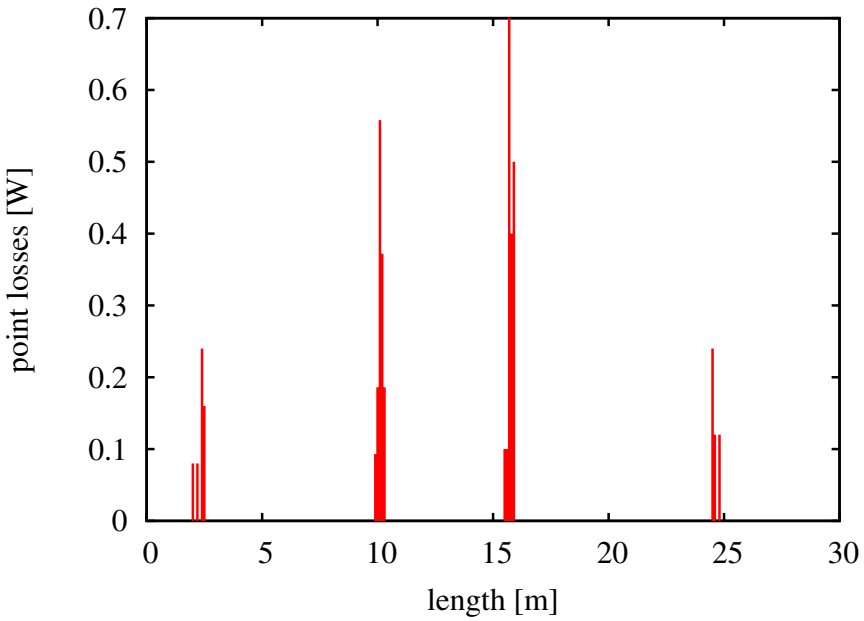

Figure 3.8: Average losses in watts versus length in the SCL assuming: steerers, 40 mA average current, 0.1% duty cycle, 1500 runs with 50000 particles, binning of 10 cm

The losses induced by H^- stripping in vacuum have been estimated using the formulae and cross-section given in [51,52]. The losses are more pronounced at low energy, as the cross-section for electron detachment via collisions decreases with energy. The formula $P = 1 - \exp(-l/\lambda)$ gives the probability of losses in a section of length l, where the mean free path λ equals $kT/\sigma P$, with k being the Boltzmann constant, T the temperature, σ the cross-section and P the vacuum pressure. Using $kT = 4 \times 10^{-21}$ Nm and the cross-section decreasing (with energy) from 10^{-19} to 10^{-21} m^2, we obtain the losses given in Table 3.7 for the different section of the accelerator. As expected, losses due to residual gas stripping are important in the LEBT (4%) but rapidly decrease in the following sections. In all cases loss levels are below 0.1 W/m.

Another loss mechanism is the magnetic H^- stripping in the dipoles of the transfer line. The effect is caused by the electric field seen by a moving particle when passing through the magnetic field of a

Table 3.7: Beam loss due to rest-gas stripping assuming an average current of 40 mA and 0.1% duty cycle

	Pressure [mbar]	**Losses** [%]	**Power** [W/m]
LEBT	1.0×10^{-5}	4.0	
RFQ	1.0×10^{-7}	0.1	
MEBT	1.0×10^{-7}	0.05	
DTL	1.0×10^{-7}	0.003	0.03
CCDTL	1.0×10^{-7}	0.003	0.003
SCL	1.0×10^{-7}	0.0007	0.001
Transfer line	1.0×10^{-7}	0.005	0.002

bending magnet. According to [53] the average lifetime of H^- ions of relativistic parameters (beta) and (gamma) crossing a magnetic field B perpendicular to the direction of motion is:

$$\tau(B) = \frac{7.96 \times 10^{-6}}{\beta\gamma cB} \exp\left(\frac{4.256 \times 10^{9}}{\beta\gamma cB}\right) \tag{3.1}$$

The stripping probability is then given as $P = 1 - \exp(-t/\tau)$ where t is the time it takes the particle to traverse the dipole. For $B = 1\,\mathrm{T}$, $\rho = 2\,\mathrm{m}$, $\varphi = 30\,\mathrm{deg}$ and $\beta\gamma = 0.614$ the losses amount to $< 0.002\%$, or < 0.0001 W/m.

3.5 Beam dynamics in the PS booster

At present Linac2 injects a proton beam of 50 MeV via multi-turn injection into the PSB. The replacement of Linac2 with Linac4 entails a number of changes which will have a substantial impact on the performance of the PSB. With the present 50 MeV injection the intensity per bunch for future LHC beams is limited by the beam brightness that can be achieved out of the PSB. It is clear that the ultimate LHC beam (1.7×10^{11} protons per LHC bunch) cannot be reached even with double batch transfer from the PSB into the PS [54]. Increasing the PSB injection energy from 50 MeV to 160 MeV will yield an increase in the number of particles that can be accumulated and accelerated within the required emittances (see Table 1.1, [54]).

The intensity increase is achieved by the following means:

- The increase in injection energy from 50 MeV to 160 MeV reduces the coherent tune shift induced by the space-charge. This reduction factor is inversely proportional to $\beta\gamma^2$ and amounts to ≈ 2. Assuming one can inject at 160 MeV with the same tune shift as at 50 MeV, it should allow to accumulate and accelerate twice as many particles per booster cycle within the same normalised transverse emittance.
- With the present multi-turn injection scheme the acceptance at injection is determined by the injection septum. Due to the limited aperture, close to 50% of the beam coming from Linac2 is lost already at injection. Changing the injection scheme from multi-turn to H^- injection will remove this limitation and should drastically reduce the injection losses.
- At present every booster ring is filled with a coasting beam which is then bunched afterwards. With Linac4 a low-energy beam chopper is available, which should help to minimise capture losses. Studies of longitudinal painting schemes have started with the aim of obtaining a flat longitudinal profile which is more favourable for the transverse beam dynamics.

Longitudinal aspects of PSB H^- injection

A favourable bunching factor (long bunches with low peak current) is mandatory to minimise the direct space-charge tune shift of high-intensity and high-brilliance beams. Moreover, the beam has to be accelerated as fast as possible to higher energies where space-charge effects become less important. These somehow conflicting requirements can be fulfilled in the following way:

- For a maximum bunch length during acceleration, the synchronous phase must be kept small. Therefore, for a given $\mathrm{d}B/\mathrm{d}t$, the RF voltage must be large since the product of the RF voltage times the sine of the synchronous phase must be proportional to $\mathrm{d}B/\mathrm{d}t$ to achieve synchronous acceleration,
- the resulting large acceptance must be filled, which means that the longitudinal emittance must also be large and adapted to the acceptance,
- a second harmonic RF system can be used to "flatten" the line density of the beam and improve the bunching factor. Uniform longitudinal densities and even slightly hollow bunches and azimuthal symmetry of the density can further improve the situation.

Present PSB proton injection at 50 MeV and extrapolation to H^- at 160 MeV

In the present scheme for 50 MeV protons coming from Linac2, a coasting beam is injected during a few PSB turns and bunched afterwards. Non-adiabaticity due to the relatively fast bunching results in inhomogeneities in the longitudinal phase plane, which lead to a beating of the longitudinal bunch shape and to peak densities increasing the maximum transverse tune shifts and spreads.

With Linac4, the chopped beam will be directly painted in the PSB RF bucket(s), resulting in a more efficient longitudinal capture and less bunch shape oscillations. This is expected to further improve PSB performance beyond what will result from the reduction of the direct space-charge tune shifts and spreads due the higher energy.

For a rough estimate of the performance improvement, using the same working points as today, one may assume that the acceptable direct space-charge tune shifts remain unchanged. Then one obtains:

- *High-brilliance LHC beams*: The normalised transverse emittances must remain unchanged. Thus one expects an increase of the intensity and, in turn, of the transverse brilliance by a factor two.
- *High-intensity beams for the PS*: The normalised transverse emittances must remain unchanged (or even be reduced in order to reduce losses due to the acceptance limitations of the PS). Preliminary investigations of transverse limitations indicate that a vertical tune above the half-integer leads to unacceptably fast blow-up. Thus it is possible that the vertical tune and, in consequence, the maximum vertical tune shift must be reduced with respect to the present 50 MeV proton injection (where the working point for the vertical tune is at 4.55, slightly above the half-integer). This means that the gain in intensity may be smaller than a factor two unless further studies or the actual machine operation show a different behaviour.
- *High-intensity beam delivered from the PSB to experiments*: The beam delivered may have larger normalised emittances provided that the acceptance of the ejection channel is large enough. Thus, an additional gain may be expected to partially or completely compensate the reduction due to a lower working point.

The increase of the injection energy implies that the beam stays slightly longer with a large direct space-charge tune shift and spread (due to a slower increase in $\beta\gamma^2$ if one assumes the same $\mathrm{d}B/\mathrm{d}t$ as presently used). However, this should be counterbalanced by the flexibility offered by transverse and longitudinal painting processes which can be used to shape optimally the distributions of the circulating beam.

Longitudinal painting

Linac4 will be equipped with a longitudinal chopper and thus, elaborate schemes for filling the longitudinal phase space at injection become possible. In most simulations up to now (see next sections) aiming mainly at investigations in the transverse phase space, a chopped long beam with a rather small energy spread has been injected into small low-voltage buckets. Immediately afterwards, the RF voltages are raised within 2.6 ms and the beam blows up and approximately fills the resulting large buckets. This non-adiabatic process still leads to some filamentation in the longitudinal phase space.

Better results can be obtained by painting directly inside a large (about the maximum available RF voltage) stationary bucket. This can be done by modulating the linac beam energy and chopping factor during the pulse. The main aspect and studies to be performed in order to validate the scheme are:

- Detailed investigation of the implications on transverse painting. More specifically, the injection line must be dispersion matched with the PSB lattice.
- Thorough analysis of the longitudinal phase space with direct space-charge forces taken into account. It is planned to use the code ESME [55] for that purpose.
- Since Linac4 will have to deliver an H^- beam with a larger energy spread, the pulse-to-pulse energy jitter will unavoidably increase. Probably a phase loop acting already from an early phase of the injection is mandatory. It has to be verified that the minimum achievable jitter is acceptable.
- The number of foil traversals and the resulting consequences in terms of transverse blow-up and foil heating have to be studied.

Transverse aspects of PSB H^- injection

An increased intensity or beam brilliance out of the PSB can only be achieved if the emittance increase during the acceleration in the PSB is limited. For the LHC "ultimate" beam and the CNGS (single batch) beam, these limits have been defined in terms of normalised r.m.s. emittances at 1.4 GeV injection into the PS (see Table 1.1). One should note that the number of particles that can be delivered within this emittance budget is also dependent on the distribution of the particles within the bunches and it might thus be beneficial to foresee a beam collimation system in the transfer line between the PSB and the PS.

Today it is still beyond the capabilities of available tracking codes and computer systems to reliably simulate a complete PSB cycle. Approximately half a million turns with at least 10^5 macro-particles, (representing 1.25×10^{13} (real) particles in the CNGS case), are needed for this task which corresponds to around one year on a modern PC using ACCSIM [56], the code which has so far been used for the PSB simulations at CERN [57]. Even if there were an ACCSIM version which makes use of massive parallelisation there is still a substantial risk of numerical instabilities which might render the results useless. A second code which is often used for simulations involving high space-charge regimes in circular machines is ORBIT [58]. A comparison of both codes is presently undertaken in collaboration with SNS [59]. A new feature which was recently implemented by the authors of both codes [60, 61] is the adiabatic emittance shrinking due to acceleration, and the results presented here are the first published simulation runs of ACCSIM (using a pre-release version kindly made available to CERN by F. Jones) using this feature.

In order to benchmark the injection modelling with actual PSB performance, we used ACCSIM to model the present 50 MeV multi-turn injection and found a fairly good agreement between the losses predicted by ACCSIM ($\approx 60\%$) and the losses actually observed on the machine ($\approx 50\%$). Machine experiments comparing the ACCSIM simulations with the PSB operation on a 160 MeV plateau are in preparation, even though differences in measured r.m.s. emittance values below 10% will be difficult to discern. For the time being, due to the limitations in the tracking capabilities, it is only possible to make relative comparisons or qualitative studies which is the approach taken in the following.

Transverse painting

Linac bunches are injected using a controlled shift of the horizontal orbit bump as illustrated in Fig. 3.9. For the time being no active vertical painting is used. The injected beam fills a ring in the vertical phase plane, meaning that the particles are only redistributed by space-charge forces over subsequent machine turns. A detailed evaluation of several possible painting schemes should be achieved in future studies.

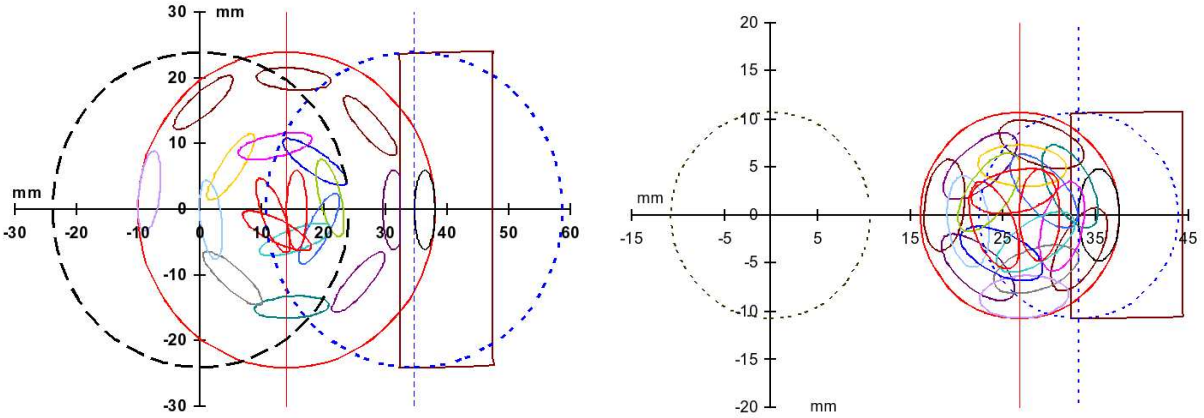

Figure 3.9: Horizontal normalised phase-plane without space-charge for CNGS (left) and LHC (right) beams: ellipse contours on the 1st turn (right circle), the 66th turn (left), 17th (right) (last injection turn, middle circle), and a turn with zero bump amplitude after the injection process (left circle), the x/x' phase plane is normalised to $x_{\mathrm{n}} = x$ and $x'_{\mathrm{n}} = \beta x'$ assuming $\alpha = 0$ at injection

Presently we assume a carbon foil with a thickness of 0.44 μm (100 μg/cm^2). Using the above mentioned painting scheme each particle passes the foil approximately 3 times. The foil traversals are limited to the number of turns that is used for the injection process. Using the foil scattering routines which are built into ACCSIM we found that there is no significant difference in emittance evolution if the scattering routines are used or not. This indicates that there is room for optimisation concerning: i) the thickness of the foil (a thicker foil would reduce the amount of unstripped beam and therefore reduce the activation of the injection area), and ii) the fall-time for the power supplies of the orbit displacement bumpers (a longer fall-time would reduce the cost of these devices).

For the longitudinal capture with ACCSIM we use a quasi-adiabatic scheme [62], raising the voltage from 0.6 kV to 8 kV within 2.65 ms. As mentioned in Section 3.5 this capture scheme is currently being reconsidered and it is likely that a scheme with a higher initial voltage will be used in the future.

Tracking results

After experimenting with different tune settings, the "old" PSB working point of 5.47 (V) and 4.28 (H) was chosen for the ACCSIM simulations with injection at 160 MeV. The "new" working point [4.47 (V) and 4.28 (H)] used in operation since 2004, resulted in an identical emittance evolution. Simulations with different macro-particle numbers showed that $\approx 10^5$ macro-particles on a 151×151 space-charge grid (with 1.0 mm to 1.5 mm grid point spacings) are needed for convergence. Lower matrix grid numbers result in an increased emittance growth. With these settings it takes approximately one week of simulation time for 10,000 to 15,000 turns, corresponding to ≈ 10 – 15 ms in the nominal case considered (i.e. H^- injection at 160 MeV of 1.25×10^{13} particles, quasi adiabatic capture and beginning of acceleration, CNGS scenario). Some attempts have been made to simulate a higher number of turns but these were either terminated by a computer failure or a code crash. The maximum number of turns that was successfully simulated amounted to 40,000, corresponding to approximately one month of simulation time. The simulations in the following are made for the CNGS scenario (see Table 1.1), since this is the case where the beam is subject to the highest space-charge forces ($\approx 30\%$ higher than for the LHC case, and

approximately at the same level with the ISOLDE beam).

In order to estimate the emittance evolution during acceleration to higher energies, the acceleration rate and the dB/dt was artificially increased so that 550 MeV are reached within 18,000 turns, corresponding to 16 ms instead of 260 ms (a full "regular" booster cycle from 160 to 1400 MeV takes $\approx$ 530 ms). This scenario implements the full H^- injection process and the quasi adiabatic RF capture. However, to reduce the mismatch at the PSB injection, the stripping foil is assumed to be located in a region where the betatron function derivatives are zero. Also, no short range orbit bump is involved in the vicinity of the injection point to minimise the optics distortions during the acceleration. Figure 3.10 shows the results of this simulation. The horizontal normalised emittance remains basically constant

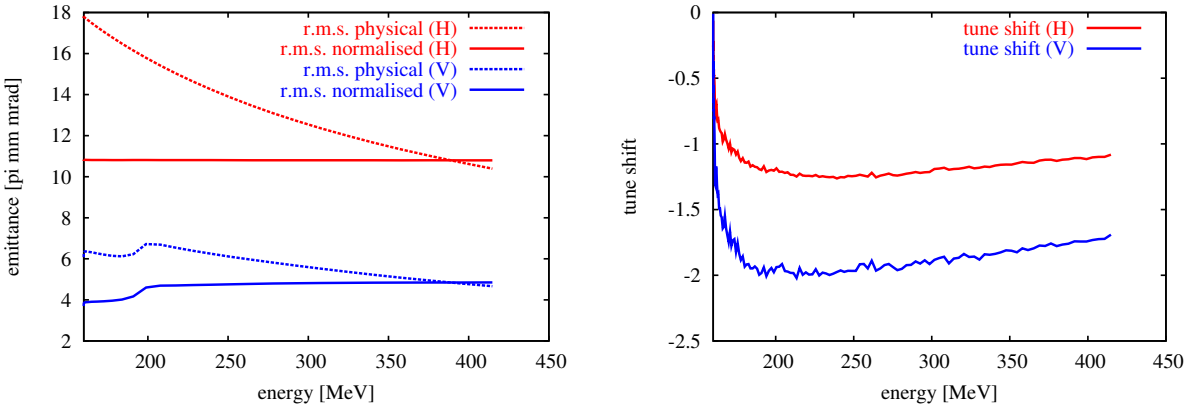

Figure 3.10: (left) emittance evolution and (right) space-charge tune shift for an artificially increased acceleration rate

during the acceleration process but the vertical emittance shows a certain increase around 200 MeV. This increase can be explained by the huge vertical tune shift (right picture in Fig. 3.10). This unrealistically large tune shift is the result of the a longitudinal bunch compression due to the artificially increased accelerating voltage, which was needed to obtain a fast acceleration in the simulation. It can be expected that in the real case with a much lower RF voltage, this increase will not take place, and that a change of the working point will at least reduce the emittance growth.

A further set of simulations was launched using single batch H^+ injection into the PSB, and then keeping the energy at a constant value. This procedure bypasses the complication of H^- injection and makes it easier to start the tracking with a matched beam. In this scenario the RF cavities are used at their maximum voltage (8 kV) and act as buncher cavities. Two cases are considered: i) H^+ injection at 50 MeV with 0.625×10^{13} particles, and ii) H^+ injection at 160 MeV with 1.25×10^{13} particles. Assuming that the maximum number of particles delivered by the PSB within a certain emittance is proportional to $\beta\gamma^2$, then both simulations should show the same emittance evolution. Figure 3.11 shows that indeed the horizontal and vertical tune shifts for both simulations are the same and Fig. 3.12 shows the emittance evolution for both cases over 10 ms.

From Fig. 3.12 we can see that the emittance evolutions for both cases are almost identical. Vertically the emittance growth is limited to 1.5% and horizontally there is a slight emittance decrease, indicating a small vertical to transverse emittance exchange. The average of both transverse emittances (not plotted) shows a small increase at the beginning but remains basically constant after 2 ms. As a result we find that the simple analytic scaling law which says that an increase in injection energy allows to accumulate an increased number of particles (which is $\propto \beta_{\mathrm{new}}\gamma^2_{\mathrm{new}}/\beta_{\mathrm{old}}\gamma^2_{\mathrm{old}}$), is indeed true. The longitudinal emittances remain constant throughout both simulations.

A comparison with ORBIT simulations of the injection on a 160 MeV plateau confirms the results of ACCSIM, provided that the same physics model is used for the longitudinal line density. If both codes use the average longitudinal line density then the space charge forces are equal for all longitudinal

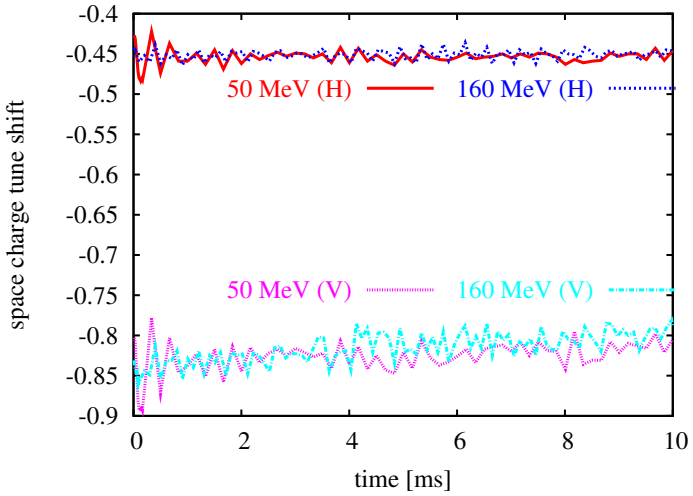

Figure 3.11: Horizontal and vertical tune shift for injection on a constant energy plateau (50 and 160 MeV)

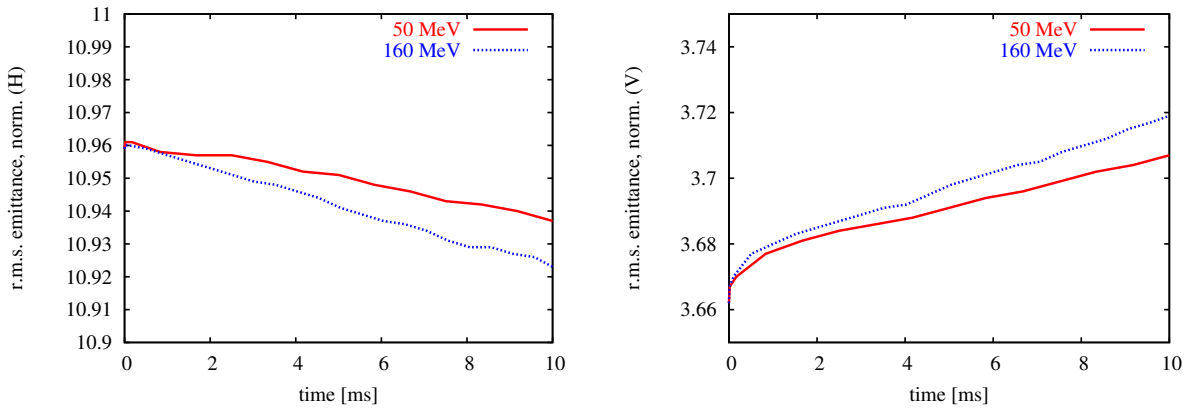

Figure 3.12: Horizontal (left) and vertical (right) normalised r.m.s. emittance evolution for injection on a constant energy plateau (50 and 160 MeV). At 160 MeV twice as many particles are accumulated than at 50 MeV.

beam slices and the simulations agree perfectly. If ORBIT uses the actual line density then the strong longitudinal bunching, caused by using 8 kV to focus the beam longitudinally, results in a significant r.m.s. emittance increase[1]. This means that: i) the presented ACCSIM simulations correspond to a case with a minimum bunching factor, and ii) the voltage profile during acceleration must be optimised such that a minimum bunching is actually achieved, otherwise a considerable r.m.s. emittance blow-up may occur.

The conclusion of the simulations is that we expect the increased PSB injection energy (160 instead of 50 MeV) to double the maximum number of particles that can be accumulated and accelerated within a certain normalised emittance. Whether this maximum can be reached after the installation of Linac4 will depend on optimising: i) the injection layout, ii) the beam parameters of the injected beam, iii) the transverse and longitudinal painting schemes, iv) the choice of the working point, and v) the voltage profile used for the longitudinal capture of the beam.

[1] According to the code author a corresponding simulation with ACCSIM is possible but has not yet been done.

Chapter 4

General services and systems

4.1 Radio frequency

The RF power for the Linac4 accelerating structures will be generated by a combination of 14 klystrons recuperated from the LEP machine (output power 1 MW and 1.3 MW, frequency 352 MHz) and 4 new pulsed klystrons at 704 MHz and 4 MW peak output power. Additionally, three pulsed solid-state amplifiers at 20 kW each will feed the buncher cavities in the chopper line, and two tube amplifiers recuperated from SPS (100 kW peak pulsed power) will feed the two debuncher cavities in the transfer line. The total number of RF chains will therefore be 23, of which 19 are at 352 MHz frequency and 4 are at 704 MHz. A scheme of Linac4 accelerating structures and RF power sources is given in Fig. 4.1.

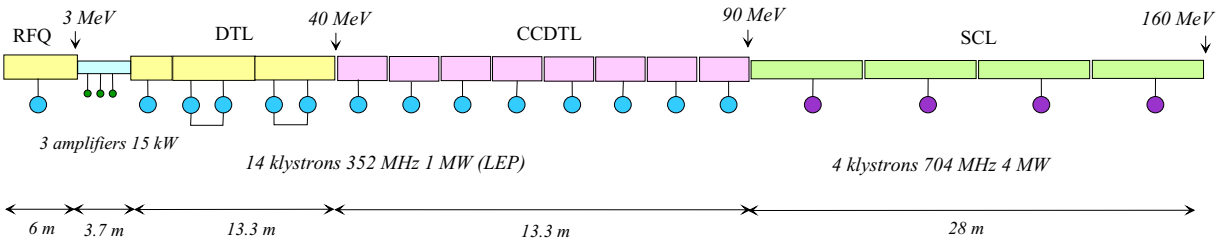

Figure 4.1: Linac4 RF power sources

Each klystron will feed, via a Y-junction circulator and a waveguide line, a single RF port located on one of the accelerating modules. The waveguide size is WR2300 for 352 MHz (most of the components are recuperated from LEP) and WR1150 for the 704 MHz. The average waveguide length will be about 10 m. The klystrons, the circulators and loads, the HV power supplies and the control racks will be located in the South Hall, next to the linac tunnel. The LEP klystrons are horizontal, while the new 704 MHz klystrons will be vertical, for a more efficient use of the space available in the South Hall.

The 352 MHz klystrons, circulators and RF equipment

The DC to RF power conversion for the 352 MHz accelerating structures (RFQ, DTL and CCDTL) will be provided by 14 klystrons recuperated from the LEP RF installation. A total of 20 klystrons have been revised after the dismantling of the LEP RF system and stored in the PS South Hall to be used for Linac4; 14 klystrons will be installed on the machine and 6 kept as spares. The klystrons from LEP come from three different manufacturers (Thales, EEV and Philips) and have an average of 12,000 operation hours. Considering an expected life-time of 35,000 hours per klystron, the LEP klystrons recuperated for Linac4 are at about half of their life expectancy. Some of these klystrons can deliver only 1.1 MW peak power, while most of them are capable of 1.3 MW. The main CW operating parameters for the 1.3 MW klystrons at the rated output power are given in Table 4.1.

The klystrons will be used in pulsed mode, fed by a pulsed HV modulator. The RF duty cycle being very low, only limited cooling will be applied to the collector and to the cavity body. It has been estimated that about 20 l/m water flow will be sufficient for the cooling of the collector and klystron body [63]. The klystron will be protected against reflections by a three-port junction circulator and a fast active reflection interlock, acting within 10-20 μs. To ensure stable tube operation a temperature control system automatically adjusts the circulator's magnetic field to compensate for the ferrite temperature variations keeping optimum input matching and isolation at all forward power levels (see below). The LEP circulators will be used, 20 of them are stored for use in Linac4. The main circulator parameters are given in Table 4.2. They must cope with high peak power levels when feeding the cavities and in case

Table 4.1: Main parameters of the LEP-type klystrons

Output power	1.3 MW
Operating frequency f_0	352 MHz
DC to RF conversion efficiency	$\geq 62\%$
Operating voltage	≤ 100 kV
Maximum beam current	20 A
Gain	≥ 40 dB

of breakdowns in the resonators. These reflected signals, which are in the microsecond range, can cause arcing between the ferrite plates of the circulator. The circulators will be protected against unusually high reflection levels by a fast active reflection interlock as well as arc detectors.

Table 4.2: Main Parameters of the LEP-type circulators

Operating frequency f_0	352 MHz
Type	3-port junction circulator
Ports	WR2300 full height waveguide
Maximum forward power	1.3 MW
Maximum reflected power	1.3 MW, at any phase
Insertion loss at rated forward power	≤ -0.1 dB
Isolation	
a) within frequency range $f_0 \pm 0.25$ MHz	≤ -28 dB
b) within frequency range $f_0 \pm 12$ MHz	≤ -20 dB

It is foreseen to reuse the 300 kW LEP RF water loads, which have an attenuation of only -14 dB. It is not clear yet if they can stand the 1.3 MW peak power; arcing in the load waveguide to coaxial transition risks to damage the Teflon plate which ensures the tightness between waveguide (air) and the load water cooling circuit. The loads will be tested in the test stand presently in preparation (3 MeV test stand), and in case they do not cope with peak power requirements, waveguide ferrite loads with attenuation up to -30 dB must be purchased.

Each klystron and related equipments will be controlled by a Programmable Logic Controller (PLC) containing basic software blocks for each device and a common control sequencer. The design will be based on what has been done for the LHC klystrons, while performances and cost can be further optimised by using new technologies. The PLC will treat and generate "slow" interlocks whereas specially developed interlock modules treat the "fast" interlocks ($\approx 10\,\mu$s). As in the LEP and LHC RF units, there is a first interlock level at which only the RF is switched off, and a second at which the power converter is switched off.

The klystron 200 W drive amplifiers will be recuperated from the LEP RF system, and they will be modified to cope with the new control system specifications. Since all valid LEP focusing-coil power supplies have been reused for LHC, new ones must be purchased.

As for the other klystron ancillary equipment, new arc detectors have to be built, using the LHC design. New power meters have to be designed, the LHC model not being suited for a pulsed system. A circulator Temperature Control Unit (TCU) has to be developed based on the LHC version.

The 704 MHz klystrons

The 4 klystrons at 704 MHz will need to be designed and built for the Linac4 project, although they can be very similar to the 805 MHz, 5 MW klystrons that have been built for the SNS facility. In order to reduce the arcing problems at the klystron output window, for Linac4 the peak power has been limited to 4 MW. The main parameters of the 704 MHz klystrons are reported in Table 4.3.

Table 4.3: Main parameters of the 704 MHz klystrons

Output power	4 MW
Operating frequency f_0	704 MHz
DC to RF conversion efficiency	$\geq 52\%$
Operating voltage	≤ 135 kV
Maximum beam current	70 A
Gain	≥ 50 dB
Maximum duty cycle	10%

The 704 MHz klystrons must be protected against reflections by 704 MHz circulators equipped with proper RF loads, which will have to be designed and built. The 704 MHz klystron control system as well as other ancillary equipment can be similar to the 352 MHz one.

The RF system for the chopper line bunchers

The three debunchers of the chopper line (16 kW maximum power) will be fed by new 20 kW solid state amplifiers; for example, five standard 5 kW units can be combined in one single amplifier. The increased reliability and low cost of solid state technology can be an asset for these units, in particular because the low average power reduces the thermal load on the components and allows to operate without water cooling of the transistor plates. PLC controls and interfaces for these units can be based on the present solid state amplifiers (5 kW) used at Linac2 and Linac3.

The RF system for the debunchers of the transfer line

The high-power tube amplifiers that are presently foreseen for the bunchers of the 3 MeV test stand can be used more effectively for the two debunchers in the transfer line (80 kW maximum power). Five such units have been recuperated in the year 2000 from the SPS, where they were used for lepton acceleration. Their final stage has been designed and built at CERN to use the TH571B tetrode. In the SPS these units were operating at a maximum power of 45 kW in CW mode, but the final tube could reach a peak output power of up to 100 kW in pulsed mode, for an anode voltage of about 13.5 kV. For Linac4, it is foreseen to replace the present tube driver stage with a solid state driver, capable of providing the 5 kW maximum drive power required for a minimum amplifier gain of 13 dB. The solid state drivers could use the same design as the bunchers in the chopper line section.

The low-level RF

For the RFQ, the first DTL tank, the CCDTL and the SCL the RF chains consist of one klystron feeding one accelerator module via a circulator-waveguide system. We refer to this as an "RF line" and propose one accelerator module controller per RF line. The second and third DTL tanks are powered by two klystrons and the cavity controller will be different. It will include two klystron polar loops, one around each klystron, and a single RF feedback loop. Much alike the LHC system, the standard controller includes [64, 65]:

- a tuner loop that keeps the structure on resonance,
- an RF feedback, a feed-forward and a one-repetition period feedback that keeps the accelerating voltage at the desired value in the presence of transient beam loading,
- a klystron polar loop that compensates the variation of klystron gain and phase shift caused by High Voltage (HV) supply fluctuations, both the slow (HV droop) and that caused by the mains ripples (up to $12 \times 50\,\mathrm{Hz} = 600\,\mathrm{Hz}$),
- a conditioning system monitoring the main coupler vacuum while feeding the RF line with frequency modulated bursts of RF power of increasing amplitude,
- a klystron drive limiter that prevents from driving the klystron over the saturation limit during loop transients.

The above electronics contain built-in diagnostics; important signals are stored in two sets of memory. The post-mortem memory acquisition is free-running, and stopped by a single specific machine-wide post-mortem trigger. It is meant to correlate acquisitions in different parts of the machine after a fault. The observation memory acquisition can be piloted by an operator, setting sampling rate and triggering the process. It is meant for monitoring the system during operation. The electronics also include built-in facilities to measure frequency or step responses without having to connect measuring instruments (Baseband Network Analyser). All adjustments can be done remotely. A clock generation system is responsible for all fast clocks plus the repetition rate trigger.

Figure 4.2 shows the proposed servo controller. LLRF modules are identified by a rounded enclosure. Each consists of a single custom-made VME card, except for the tuner loop module that consists of two VME cards attached to a single front panel. RF signals are drawn in blue. The klystron feeds a linac module via a circulator. Four RF signals are input to the LLRF: the cavity field probed by an antenna (V_{cav}), the klystron output forward power ($I_{\mathrm{g,fwd}}$) measured by a directional coupler between the klystron and circulator, the forward and reflected powers at the module input ($I_{\mathrm{c,fwd}}$ and $I_{\mathrm{c,rev}}$) measured on the waveguide before the main input coupler. In return the RF modulator generates the klystron drive and the tuner loop module controls the resonant frequency. The diagram has colour codes identifying both signal types (digital, analog base-band, RF) and technology (analog, Field Programmable Gate Array - FPGA, Digital Signal Processor - DSP). Refer to the caption for details.

The LLRF modules are VME 64 cards, 6 Units (U) high, 220 mm deep. We propose to use the same crates as for the LHC LLRF: out of a total of 19 usable VME slots per crate, the leftmost four are 160 mm deep to house off-the-shelf VME modules, 160 mm being the most popular size. The other 15 slots house the CERN custom modules where the extended 220 mm size gives more space for the electronics. We use Electro-Magnetic Compatibility (EMC) qualified crates that provide enhanced shielding and grounding.

In the 160 mm deep region we use extended VME interfacing (32 data and 32 address lines on the two 3×32 pins connectors J1 and J2). Interfacing to the other slots is done using the top connector J1 only (16 data lines and 24 address lines) thereby freeing the lower J2 connector for key signals. For the LHC a custom backplane has been developed for the J2 connector in the 15 rightmost slots [66]. We will adapt it to Linac4. It contains linear $\pm 6\,\mathrm{V}$ and $\pm 12\,\mathrm{V}$ power supplies reserved for the analog and RF circuitry, JTAG for reprogramming the FPGAs, clocks distribution as differential ECL, the functions distributed serially, interlock lines, 18 pins for digital data exchange between neighbouring modules, and a series of hardware timing lines. For the clocks, the J2 backplane has ECL buffers on all connectors so that presence or absence of one card does not affect the phase for the other users and the clock lines are always matched.

Figure 4.3 shows the VME crate containing one servo controller. Shaded are modules that may not be needed. The trigger distributor forwards the general machine timing onto the J2 backplane. One crate is needed per line.

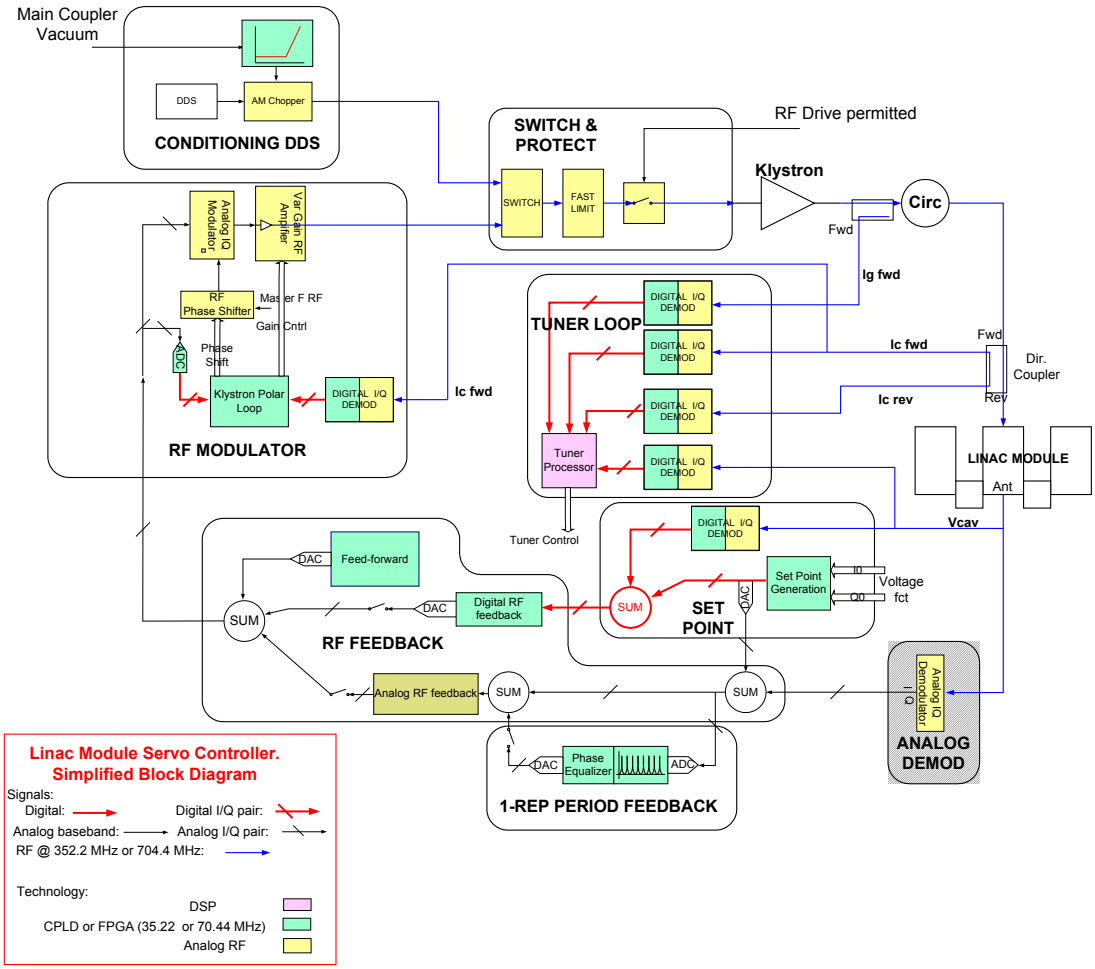

Figure 4.2: Linac4 servo controller

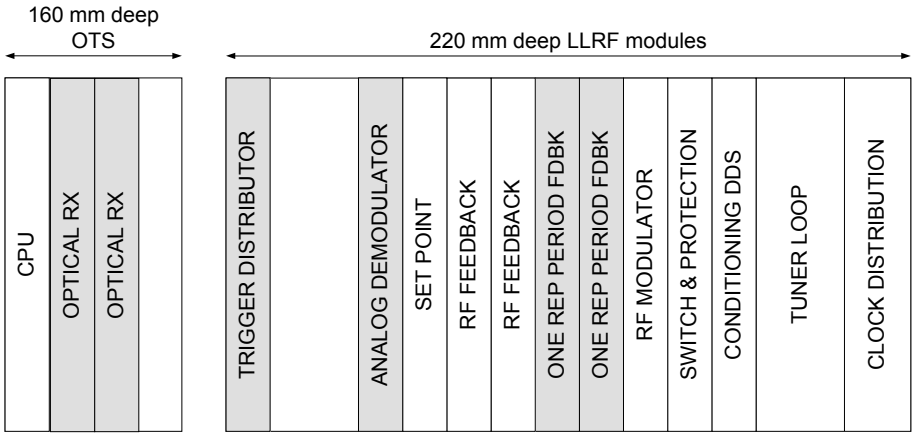

Figure 4.3: Servo controller VME crate

The VME crate is 6 U in height. We must reserve 3 U underneath for cable passage and fan. In addition a Europa mini-crate (3 U plus 2 U for fan) containing a 1 W pre-amplifier for the klystron drive and an antenna attenuator must be placed underneath. An extra 6 U must be reserved for the RF signal manipulation (splitters and couplers) at the bottom of the rack (or at the top if cables arrive at the top). This amounts to a grand total of 20 U in the rack. With an RF feedback, cable delay means higher

impedance. The LLRF rack should be located next to the klystron or on the other side of the linac with respect to the klystron. Reference clock distribution is not discussed in this report. If done via fibers we can use two VME optical receiver modules developed for the LHC to receive the repetition pulse and the RF. In the LHC the corresponding electronics is in an air-conditioned Faraday cage.

The interface to the control system will use the same standard hardware and software components as in the LHC LLRF. The leftmost slot in the 160 mm deep section of the VME crate (slot 0) will house an AB/CO standard PowerPC CPU board. The software running in the CPU will use the CERN Front-End Software Architecture (FESA) framework [67]. FESA allows real-time synchronisation of program actions with timing events from the general machine timing system via a CTR-P receiver board [68], or with interrupts generated inside the VME hardware modules. The framework should allow pulse-by-pulse control and data acquisition at typical linac repetition rates, and its performance will be validated at a repetition rate of 50 Hz during the LHC cavity pulsed conditioning tests in autumn 2006. Device drivers for the VME hardware modules will be developed using the standard AB/CO tools [69]. The similarity to LHC hardware will allow extensive reuse of code, both in drivers and at the FESA level. Once installed, the front-end hardware and software will be managed via the CERN controls configuration system [70], and will be accessible from application programs over the controls middleware [71].

4.2 Beam instrumentation

The Linac4 diagnostics can be divided into two main categories, the diagnostics for the commissioning stage and the one required for standard operation. The first type of instruments will be used for the initial machine setting-up and to analyse beam quality and machine performance. The latter will consist mainly of instruments that will control the machine and will allow fine tuning and fault finding.

Commissioning of source, LEBT, RFQ and chopper line

For the source commissioning, beam intensity will be measured with a retractable Faraday cup, which must be designed to suppress electron emission, and remove any parasitic free electrons from the source. A beam current transformer is also required as a non-destructive intensity measurement. The beam profile and emittance will be measured with a scanning slit and Secondary Electron emission grid (SEM-grid) device. Measurements will be done at different stages: after the source, after the first solenoid and at the RFQ input (matching into the RFQ). The emittance measurement system must be well aligned in order to be used to commission the steering of the beam to the RFQ. The emittance measurements will also be used to quantify the effect of space-charge compensation, and the commissioning of the pre-chopper. For these measurements, time resolution of the emittance instrument is required. The beam energy spread must be determined, and can be measured with a temporary installation of a slit, spectrometer magnet and a SEM-grid. The readout of the SEM-grid must be time resolved to distinguish time dependent variation in beam energy. The same SEM-grid can later be integrated into the LEBT for operational measurements. An additional fixed Faraday cup can be installed after the spectrometer and SEM-grid, to ensure the absence of any impurities in the H^- beam.

For the RFQ and chopping line a dedicated diagnostic line provided by the French IPHI collaboration will be installed downstream of the chopper. This diagnostic line includes a time-of-flight energy measurement, wire scanners, pick-ups and a spectrometer dipole. The measurements will comprise transverse and longitudinal emittance as well as beam energy and energy spread. For the commissioning of the chopper, a dedicated Beam Shape and Halo Monitor (BSHM) has been developed [72]. The chopper line includes two beam current transformers to monitor the transmission. A movable Beam Loss Monitor (BLM) will be used to perform the survey of the showers created by the lost particles.

Commissioning of DTL, CCDTL, SCL and transfer line

In the commissioning phase, the beam at the exit of the different sections of the linac must be characterised in terms of transmission, transverse and longitudinal emittance, energy and energy spread, in order to set RF phase and voltage and quadrupole gradients. This set of measurements should be done after each tank of the DTL, followed by the fully installed CCDTL and SCL. For the three DTL tanks (beam energy up to 40 MeV), we propose to use a movable diagnostic bench. It comprises a moving slit device for emittance measurement, energy degrader combined with a Faraday Cup to set the RF phase and time-of-flight energy measurement as well as a bunch length monitor [73]. Alternatively, components of the existing Linac Beam Spectrometer (LBS) line can be used at this point for energy measurements. At higher energy (CCDTL and SCL sections), it will be necessary to transport the beam to the end of the linac and characterise it in a permanently installed measurement line. Once it is possible to measure the beam energy and phase after any accelerator module, the technique of the characteristic curves, already used in Linac2, can be applied to set the individual amplitudes and phases.

Operation

During operation the retractable Faraday cup, beam current transformer and SEM-grid will remain installed in the LEBT. An additional beam current transformer will be installed at the entrance of the RFQ. Two beam current transformers are installed upstream and downstream of the chopper line to monitor the transmission, and up to three slow wire scanners will be used in the chopper line to check beam size and position before the chopper plates and before the beam dump.

Measurement of beam current and position is mandatory after tanks 1, 2 and 3 of the DTL, after each of the 8 modules of the CCDTL and after each of the 4 modules of the SCL. We propose the use of a combined position and phase pick-up, which also provides a measurement of the beam current. Complementary to this beam current measurement, we require a number of beam loss monitors along the linac and transfer line. Both beam current monitors and beam loss monitors will be used to optimise the transmission and to trigger the interlock in case of beam loss. In addition we plan to install beam current transformers after the DTL, CCDTL and SCL section as well as in the High Energy Beam Transfer line (HEBT). Beam profile measurements with SEM-grids are planned after tank 3 of the DTL, after modules 4 and 8 of the CCDTL as well as after modules 2 and 4 of the SCL. A measurement line will be permanently installed in the straight line between the end of the linac and the dump. It will include an energy spectrometer, a bunch length monitor and a transverse emittance diagnostic (moving slit and SEM-grid).

Instrumentation hardware

A dedicated Beam Shape and Halo Monitor (BSHM) has been developed to monitor the correct functioning of the chopper structure and, at the same time, provide a transverse image of the beam [72] (see Fig. 4.4. As this device has an extremely high dynamic range of 10^6, it can measure an intensity of down to 10^3 ions in the vicinity of a bunch populated with 10^8 ions and can hence verify if a bunch has been successfully chopped. In the transverse plane, the high dynamic range allows to measure the beam halo, populated with 10^3 ions, and at the same time the beam core populated with 10^8 ions.

Standard beam current transformers will be used to measure the absolute beam intensity (see Fig. 4.5. These devices must not only be capable of measuring the total beam current through the linac but also the part of the beam pulse injected into each of the PS booster rings. This requires additional timing signals indicating the start and the end of the beam pulse going to a defined ring. The Linac2 current transformers solved this problem by fast ADC (Analog Digital Converter) sampling (10 MHz) with subsequent numerical integration. The timing pulses for the booster distributor are sampled synchronously with the transformer signal.

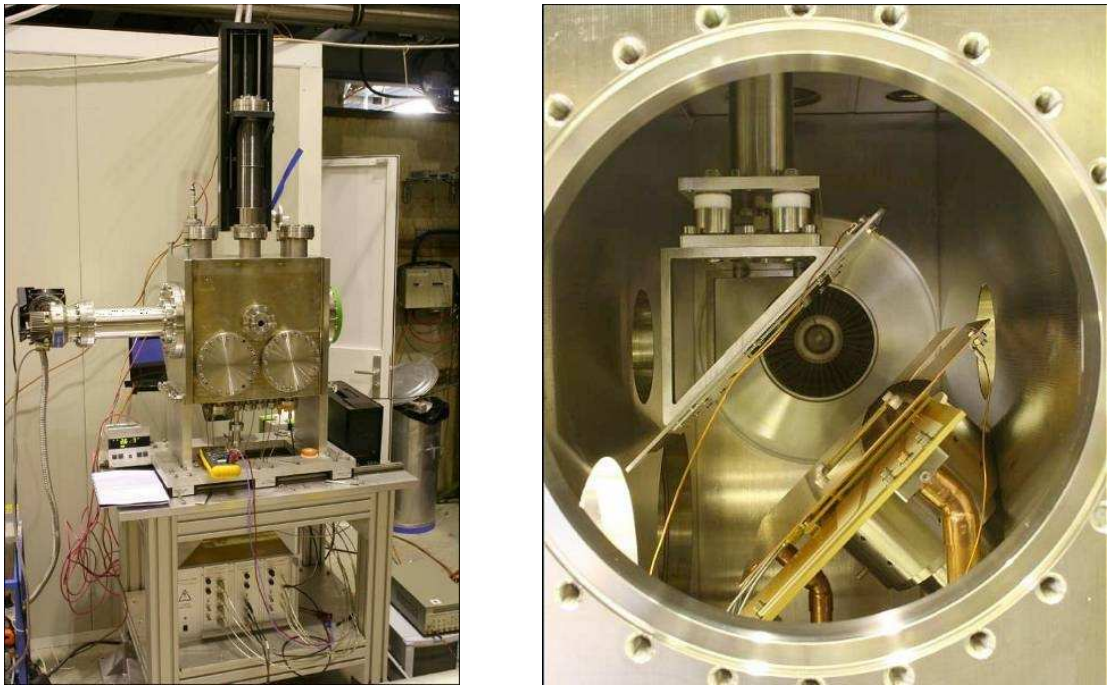

Figure 4.4: Beam shape and halo monitor constructed at CERN. Left: overall view. Right: inside view of the monitor showing target foil and grids.

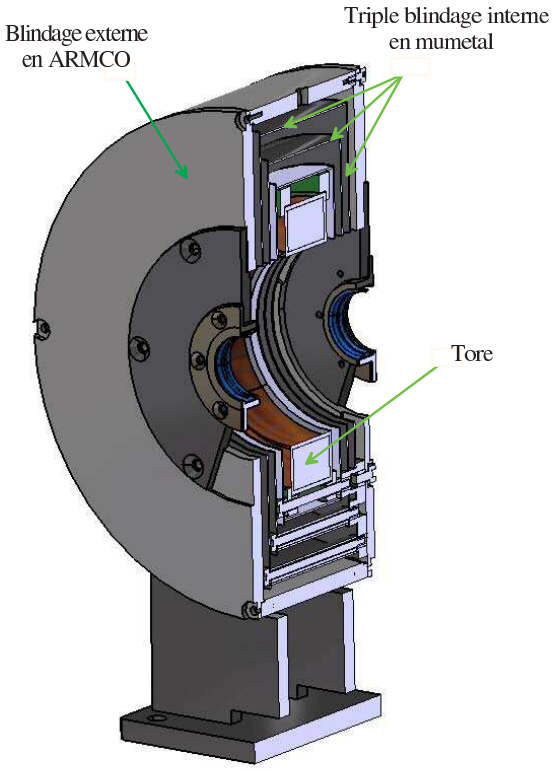

Figure 4.5: Beam current transformer including magnetic shielding under construction at CERN for the 3 MeV chopper line

SEM-grids are the first choice for profile measurements in linear accelerators with low duty cycle because they are capable of measuring the beam in a single beam shot. Actually, time resolved measurements are possible along the full 0.4 ms beam pulse. However, SEM-grids are intercepting devices and high-energy deposition in the wires may cause the wires to break. The maximum beam density seen by a single wire must therefore be limited. SEM-grids are also rather expensive devices because they require an in/out mechanism and an amplification and conversion chain per wire is needed. The expected beam spot requires 24 wires with a wire spacing of 0.8 mm.

A bunch shape monitor [74, 75] suited for linear accelerators has been proposed by Russian physicists from INR in Moscow and successfully used on many installations in the world. CERN has 2 variants of the device, the Linac3 BLVD (Bunch Length and Velocity Detector) and the Linac2 3D-BSM (3D Bunch Shape Monitor). The device uses a wire which is hit by the primary beam and creates secondary electrons. These electrons are accelerated by a polarisation field applied to the wire and later deflected through an RF deflector whose deflecting field is synchronous to the linac accelerating RF. The time structure of the analysed beam is thus converted into a spatial distribution which can be measured with a profile measurement device. In the case of the BLVD the wire can be moved precisely along the beam axis and a Time Of Flight (TOF) measurement allows determining the mean particle velocity and therefore the mean beam energy. In the 3D-BSM case the wire can be moved transversely and slits in front of the wire allow selecting a beam slice in the orthogonal transverse direction. Due to the dependency on the accelerating frequency which is different between Linac2 or 3 and Linac4, 2 new devices must be built for Linac4.

For phase, position and current pick-ups and for TOF measurements, it is foreseen to use dual plane, shorted strip-line pick-ups in order to measure beam position and beam phase in the very limited space between the RF tanks. The sum signal from the pick-ups will also be used for relative beam current measurements. The 4 electrode signals, with bunch frequencies of 352 MHz, will be band pass filtered and down mixed. They are followed by analog to digital conversion and digital I/Q demodulation. I/Q demodulation enables direct and precise beam phase calculation and thus a time of flight measurement between two pick-ups. It is important that both the local oscillator and ADC clock are synchronised to the cavity RF reference signal.

For a dynamic range of 20 dB it is expected a phase resolution $< 0.5^\circ$ and an absolute precision within a few degrees. For the position measurements the goal is a resolution of $< 1\%$ of the half aperture and a precision in the order of 0.3 mm. For the relative current measurement the precision of 1% between two consecutive pick-ups should be possible, as well as an average resolution in the order of 10 μA.

The beam loss along the linac could be monitored with an ionization chamber based measurement system like it is done for the SNS linac. At the SNS monitors with a nitrogen gas volume of 0.1 l at 1.1 bar and an ion collection time of 72 μs are installed every two metres. The LHC type of ionization chamber has a nitrogen gas volume of 1.5 l at 1.1 bar and an ion collection time of 80 μs. The larger chamber volume will result in a 15 times higher loss sensitivity. Adopting the electronics developed for the LHC will allow the use of the whole dynamic range of the ionization chambers. To adapt the integration time requirements of the chamber signals for the application in the linac, the program of the reconfigurable FPGA could be changed.

In Table 4.4 are listed all the devices needed for the linac and the transfer line at the commissioning and operation stage, while Fig. 4.6 shows a diagram of the linac and of the proposed diagnostic elements.

Table 4.4: Summary of the diagnostic instrumentation foreseen for Linac4 (MB = Movable Bench, CL = Chopper Line, ML = Measurement Line, BI = Booster Injection)

System	Position	Quantity
Time of flight	linac/MB	1/1
BPM (pick-up)	DTL/CCDTL/SCL/HEBT/MB	3/8/8/12/1
Phase pick-up	DTL/CCDTL/SCL/HEBT/MB	3/8/8/12/1
Energy spectrometer	LEBT/ML/BI	1/1/1
Beam transformer	LEBT/CL/DTL/CCDTL/SCL/HEBT/MB	2/2/1/1/1/7/1
Beam profile monitor	LEBT/CL/DTL/CCDTL/SCL/HEBT/BI/MB	1/3/1/2/2/6/8/1
Phase space scanner	LEBT/ML/HEBT/MB	1/1/1/1
Bunch length monitor	ML/MB	1/1
Faraday cup	LEBT/MB	2/1
Beam loss monitor	linac/HEBT/MB	8/17/1
Beam halo monitor	CL	1

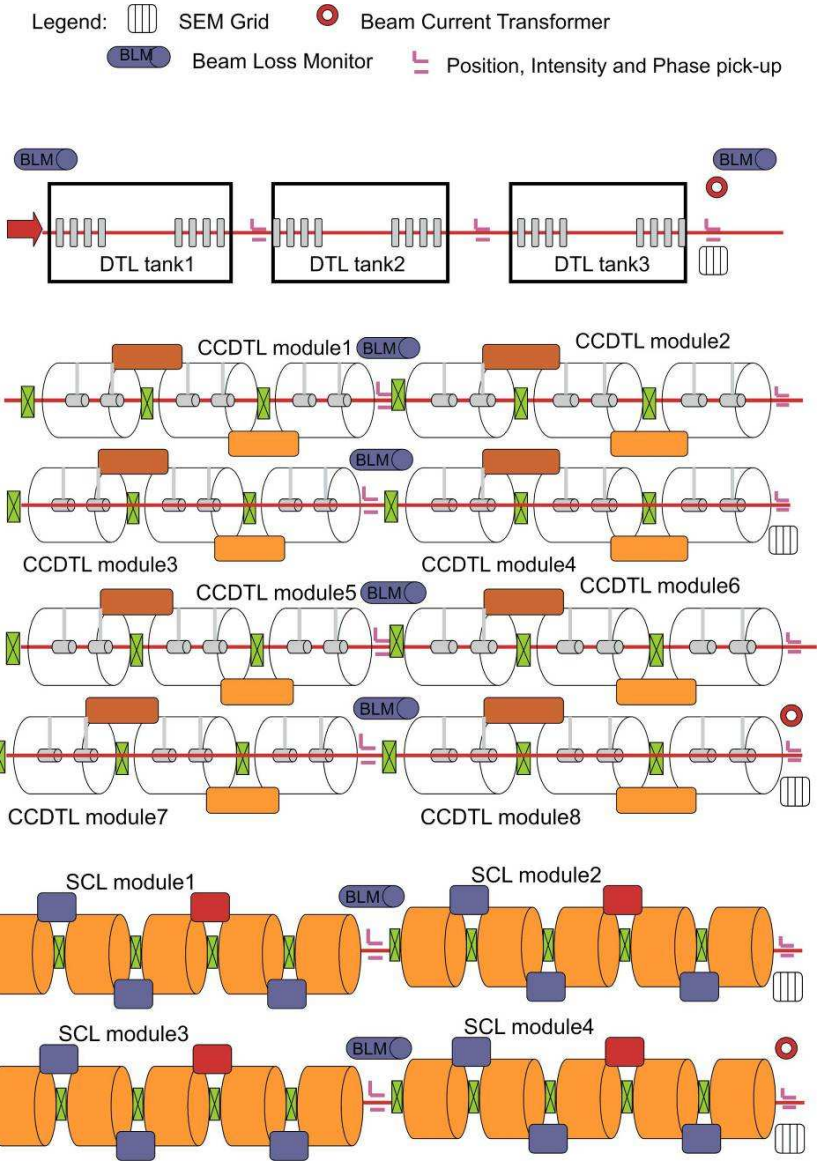

Figure 4.6: Scheme of Linac4 with the proposed diagnostic elements

4.3 Magnets

In total nearly 100 new electro-magnets are needed for the Linac4 project. These include 24 quadrupoles for the Cell-Coupled Drift Tube Linac (CCDTL), 20 quadrupoles for the Side-Coupled Linac (SCL), 14 steering magnets in total for Drift Tube Linac (DTL), CCDTL and SCL. For the new Transfer Line (TL) from Linac4 to the PS Booster (PSB) 23 quadrupoles, 5 bending magnets and 12 steering magnets are required. These numbers do not include any spare magnets. In addition 85 Permanent Magnet Quadrupoles (PMQs) are required for the DTL.

Electromagnets

The magnet parameters like aperture, integrated magnetic field respectively integrated magnet gradient and required field quality are determined by beam optics considerations.

The geometrical boundary conditions are derived from the layout of the accelerating structures; the space between the tanks limits the maximum overall length of the magnets. Further restrictions stem from the space required for installation of other equipment e.g. beam instrumentation, which also needs to be located between the tanks.

Apart from the requirements and restrictions given by the beam optics and mechanical layout, two other issues determine the magnet design: powering the magnets in pulsed or continuous mode and cooling the magnets by water or air.

As mentioned in Section 5.6, either standard commercial solutions or power converters of the same type as already used at CERN are preferred wherever possible. Considering also power converter aspects, preference was given to pulsed magnets. This minimises r.m.s.-power consumption and allows using air instead of water cooling for most of the magnets, which consequently cuts the installation and operation cost for a cooling water system. In addition, an air-cooled magnet design permits reduction of the overall magnet dimensions helping to cope with the limited available space.

The use of commercially available pulsed power converters puts constraints on the design of magnets and coils by limiting the electrical parameters (i.e. the pulse rise-time ($\mathrm{d}I/\mathrm{d}t$) and the maximum current) to a certain range.

Another aspect influencing the design of the magnets for the Linac4 section (quadrupoles and steering magnets) is the demand to use these magnets not only in Linac4 but possibly also in a future Superconducting Proton Linac (SPL) [6]. This means that these magnets have to operate not only at a 2 Hz repetition rate as requested for Linac4, but also at 50 Hz for the SPL. This option assumes that the power converters provide cycles with short rise- and fall-time ($< 200\,\mu$s) and a flat top duration of 700 μs at a repetition rate of 50 Hz to limit the r.m.s. current.

Following a detailed analysis of the requirements and restrictions, several magnet designs have been studied and are presented in this Section. It should be noted that the presented designs are preliminary and will need further optimisation.

CCDTL & SCL quadrupoles

24 quadrupoles are needed for the CCDTL and 20 for the SCL (see Fig. 4.7). The required gradients vary between 11.1 T/m and 17.7 T/m whereas the aperture radius for both types is 17 mm. The gradient homogeneity ($\Delta \int G / \int G_0$) shall be smaller than 1% inside the defined good field region defined as 75% of the mechanical aperture, i.e. 12.7 mm.

As already mentioned the total length of the magnets is restricted by the available space between the drift tube tanks and has to be below 120 mm. The coupling cells in the SCL set another limit for the transverse dimensions of the magnet. Therefore, the outer magnet diameter must not exceed 220 mm.

In order to reduce the costs for design, procurement and manufacturing and to decrease the number of required spare magnets, a common design for both types (CCDTL & SCL) is recommended.

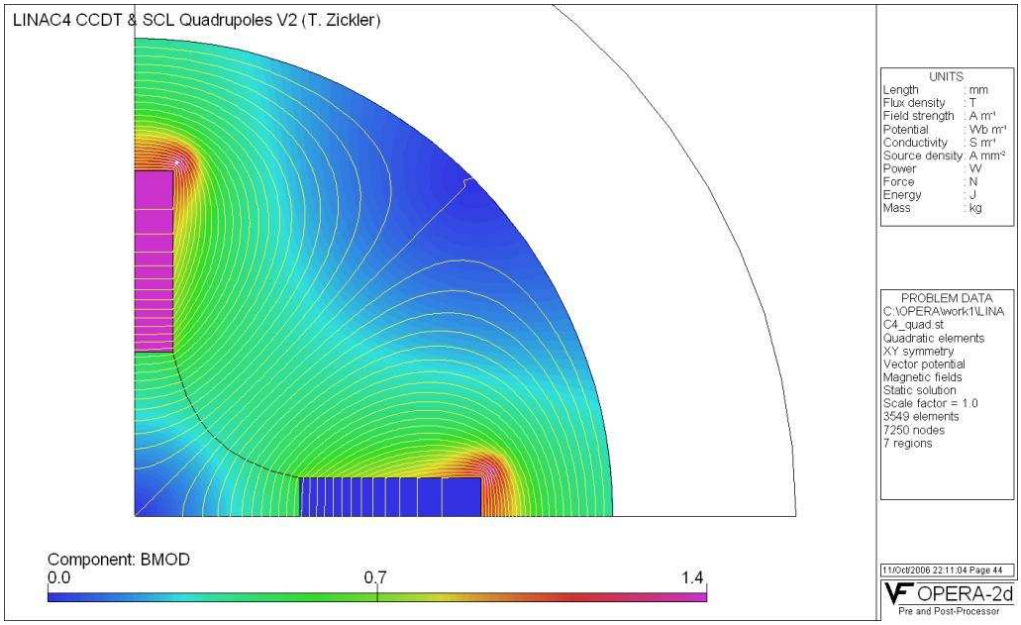

Figure 4.7: CCDTL & SCL quadrupole – two-dimensional magnetic field computation (OPERA 2D)

The yoke design is based on an existing quadrupole (Linac2 type V), but the pole contour has been modified from a straight shape to a hyperbolic shape to improve the field quality. The proposed design is shown in Fig. 4.7 (only one quadrant has been modelled). To optimise further the gradient homogeneity and the integrated field quality, 3D Finite Element (FE) computations of the pole shape will be necessary.

The magnet yoke is laminated using low-carbon steel sheets of 0.3 mm thickness glued together. The coils shall be made of round or squared enamelled solid copper wire. After assembly, the coils and the magnet yoke are vacuum impregnated using radiation resistant charged epoxy resin. Since the coils are air cooled, only pulsed operation is possible. The detailed parameters are shown in Table 4.5.

The proposed design can also be used at 50 Hz repetition rate as required for SPL operation, but an optimisation of the coil design has to be considered.

Steering magnets for DTL, CCDTL, SCL, and TL

Fourteen steering magnets are needed for the DTL, CCDTL, and SCL sections. The deflection angle at the beam energy of 160 MeV shall be at least 2 mrad. The free magnet aperture is 70 mm $\times$ 70 mm. A common design for all correctors in the entire Linac4 is proposed to reduce the costs and the number of spare magnets.

The maximum length of the magnets is again dictated by the available space between the drift tube tanks in the DTL and has to stay below 110 mm. Although more space is available in the following CCDTL and SCL sections, all correctors have the same length since only one type of magnet is considered at present. It is, however, not excluded to build two or more magnet families if this turns out to be more convenient.

The proposed design is a combined horizontal and vertical window frame corrector. A 2-dimensional Finite Element (FE) model showing the magnetic field distribution is presented in Fig. 4.8 (only one coil pair is powered). The magnet yoke is laminated using low-carbon steel sheets of 0.3 mm thickness glued together. The coil wound directly around the yoke shall be made of round or squared enamelled solid copper wire. The mass insulation shall be made of glass fibre tape impregnated with epoxy resin. Since the coils are air cooled, only pulsed operation is possible. A detailed parameter list is shown in Table 4.6. The presented design can also be used in the SPL at 50 Hz repetition rate.

Table 4.5: CCDTL and SCL quadrupole characteristics

Number of magnets	44 + 4
Cooling	air
Magnet characteristics	
Gradient	18.0 T/m
Aperture radius	17.0 mm
Iron length	95.0 mm
Effective length	108.6 mm
$\int G\mathrm{d}l$	1.95 Tm/m
Field quality $\Delta G/G_0$	$< 1\%$
Good field region	12.75 mm
Dimensions	
Total magnet length	111 mm
Outer diameter	145 mm
Total magnet weight	11.1 kg
Electrical parameters	
Max. current	100 A
Duty cycle ($I_{\mathrm{max}}/I_{\mathrm{rms}}$)	4.4%
R.m.s. current	4.4 A
Magnet resistance at 20 C°	101.8 mΩ
Inductance	1.9 mH
Max. voltage	398 V
Max. dissipated power (pulsed)	2.0 W

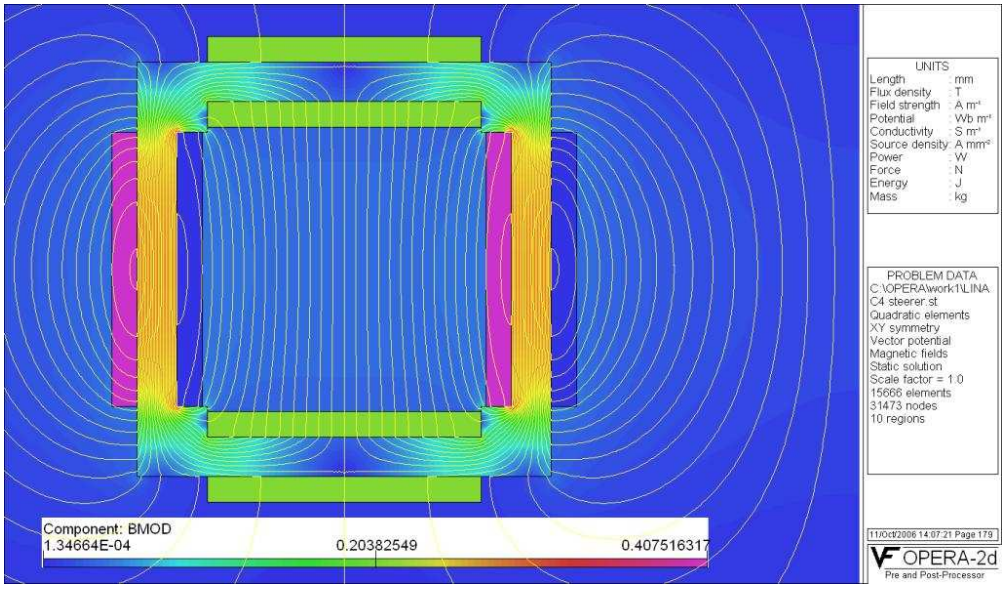

Figure 4.8: CCDTL and SCL steering magnet – two-dimensional magnetic field computation (OPERA 2D)

For the Linac4 transfer line 12 steering magnets are needed. To reduce the number of different magnet types to a minimum, it is foreseen to use the same type of steering magnet as for the DTL, CCDTL and SCL.

Quadrupoles for the Linac4 – PSB transfer line

23 quadrupoles are needed for the new transfer line from the Linac4 to the existing LT (Linac Transfer) transfer line which directs the beam towards the PS booster. The required maximum integrated gradient is 2.2 Tm/m and the aperture radius is 35 mm. The gradient homogeneity shall be better than 1% within the defined good field region (75% of the mechanical aperture).

Table 4.6: Linac steering magnet characteristics

Number of magnets	26 + 2
Cooling	air
Magnet characteristics	
Magnet field	27.0 mT
Gap height	70.0 mm
Gap width	70.0 mm
Iron length	80.0 mm
Effective length	147.2 mm
$\int B\mathrm{d}l$	4.0 mTm
Deflection angle	2.1 mrad
Dimensions	
Total magnet weight	4.2 kg
Total magnet length	103 mm
Total magnet width	116 mm
Total magnet height	116 mm
Electrical parameters	
Max. current	20 A
Duty cycle ($I_{\mathrm{max}}/I_{\mathrm{rms}}$)	11.2%
R.m.s. current	2.2 A
Magnet resistance (hot)	401.3 mΩ
Max. dissipated power (pulsed)	2.0 W
Inductance	4.5 mH

Table 4.7: Quadrupole characteristics (transfer line)

Number of magnets	23 + 3
Cooling	air
Magnet characteristics	
Gradient	8.0 T/m
Aperture radius	35.0 mm
Iron length	250.0 mm
Effective length	278.0 mm
$\int G\mathrm{d}l$	2.22 Tm/m
Field quality ($\Delta G/G_0$)	$< 1\%$
Good field region	26.25 mm
Dimensions	
Total magnet weight	97.1 kg
Total magnet length	277 mm
Outer diameter	270 mm
Electrical parameters	
Max. current	200 A
Duty cycle ($I_{\mathrm{max}}/I_{\mathrm{rms}}$)	5.0%
R.m.s. current	10.1 A
Magnet resistance at 20 C°	89.3 mΩ
Max. dissipated power (pulsed)	9.1 W
Inductance	3.6 mH
Max. voltage	741 V

There are no special restrictions for the overall dimensions of the magnet, but a compact design was made in order to reduce manufacturing costs and to improve the field quality.

The magnet yoke is laminated using low-carbon steel sheets of 0.5 to 1 mm thickness glued together. The coils shall be made of round or squared enamelled solid copper wire. The mass insulation shall be made of glass fibre tape and the coils shall be vacuum impregnated using radiation resistant charged epoxy resin. Since the coils are air cooled, only pulsed operation is possible. The detailed parameters are given in Table 4.7.

Bending magnets for the Linac4 – PSB transfer line

Five bending magnets are needed for the new Linac4 transfer line. There are two magnets with an integrated field of 0.66 Tm, one magnet with 0.53 Tm and two magnets with 1.03 Tm. The gap height for all types is 70 mm and the pole width is 150 mm. Again, in order to reduce costs and to save on spare magnets, it is proposed to reduce the number of magnet types to two: type A with an iron length of 0.6 m and type B with an iron length of 1 m. Both types are H-shaped magnets and have an identical cross-section layout to minimise the tooling costs. A possible design is shown in Fig. 4.9 (only one quadrant has been modelled). To further optimise the field homogeneity and the integrated field quality, 3D FE computations of the pole shape are needed.

The magnet yoke is laminated using low-carbon steel sheets of 1 mm thickness glued together. The coils shall be made of square hollow copper conductor, type OFE (Oxygen Free Electronic) with a circular cooling duct. The mass insulation and inter-turn insulation shall be made of glass fibre tape and the coils shall be vacuum impregnated using radiation resistant epoxy resin. The coils are water cooled, but nevertheless the magnets shall be operated in pulsed mode with a duty cycle of about 30% or lower, although they can be powered in continuous mode with an enhanced cooling performance. The parameters for both types are quoted in Table 4.8 and the magnetic field distribution is presented in Fig. 4.9.

Table 4.8: Characteristics of the bending magnets in the transfer line

	type A	**type B**
Number of magnets	3 + 1	2 + 1
Cooling	water	water
Magnet characteristics		
Magnet field [T]	1.0	1.0
Gap height [mm]	70	70
Iron length [mm]	600	1000
Effective length [mm]	677	1077
$\int B\mathrm{d}l$ [Tm]	0.677	1.077
Deflection angle [mrad]	357	573
Dimensions		
Total magnet weight [kg]	805	1329
Total magnet length [mm]	788	1188
Total magnet width [mm]	530	530
Electrical parameters		
Max. current [A]	1000	1000
Duty cycle ($I_{\mathrm{max}}/I_{\mathrm{rms}}$) [%]	29	34
R.m.s. current [A]	294	337
Magnet resistance (hot) [mΩ]	24.3	35.7
Max. dissipated power (pulsed) [kW]	2.1	4.0
Inductance [mH]	8.2	13.1
Cooling parameters		
Pressure drop [bar]	1.0	3.0
Temperature rise [K]	11	14
Total cooling flow [l/min]	2.7	4.1

Existing magnets in the LT, LTB and BI transfer lines

Coming from the new Linac4 transfer line, the 160 MeV proton beam will be deflected into the existing LT line upstream of the LT.BHZ30 bending magnet. This line is basically designed for 50 MeV proton operation. Using the line at 160 MeV energy means an increase of beam rigidity and bending strength by a factor 2. The power requirements for the steering magnets and the quadrupoles are however determined by the future beam optics layout.

All existing magnets in LT (Linac Transfer), LTB (Linac Transfer Booster) and BI (Booster Injection) transfer lines were examined to understand if their performance is adequate to transport a 160 MeV proton beam towards the PS booster. Special attention was given to the magnetic field (gradient) strength and the field (gradient) quality. Whenever the present performance turned out to be insufficient for

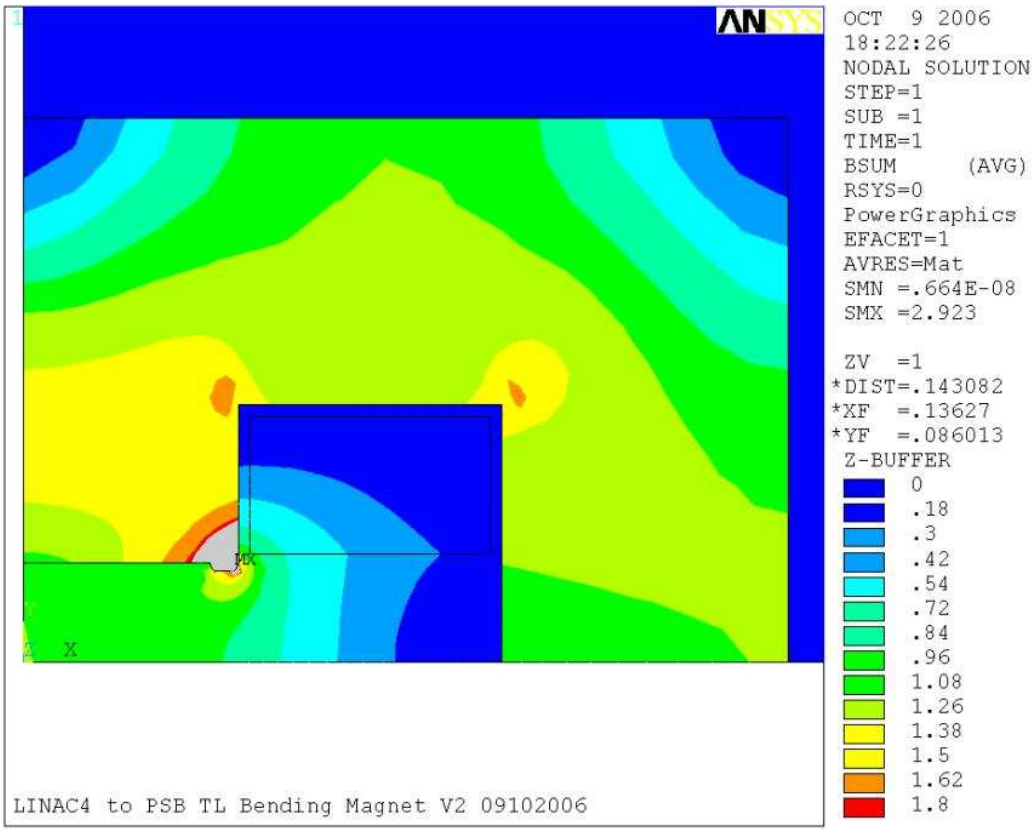

Figure 4.9: New Linac4 TL bending magnet – two-dimensional magnetic field computation (ANSYS)

160 MeV operation, it was studied whether the magnet can be upgraded to meet the future requirements by either changing from continuous operation to pulsed operation mode or by increasing the cooling performance to allow higher r.m.s. currents.

When it was not possible to upgrade the magnet, a replacement of the concerned magnet is proposed, either by an existing magnet available at CERN or by new a magnet to be designed and built.

Table 4.9 gives an overview of all magnetic elements under the responsibility of AT/MEL that are presently installed in the concerned transfer lines. Magnet type, cooling mode (air or water) and operation mode (pulsed or continuous) are specified. The magnetic field respectively gradient requirements and the corresponding current for operation at 160 MeV is compared with the maximum current allowed for all magnets.

In the following we analyse each single magnet and its potential recuperation for Linac4. For those magnets that cannot be reused, replacement magnets with enhanced performances are discussed. Figures 10 and 11 show the layout of the LTB and BI transfer line: magnets marked with a green dot can be reused for Linac4 without modifications; magnets with a yellow dot can be reused, but only with modifications; magnet which are marked in red have to be replaced.

A first analysis confirms that all steering magnets in the LT and LTB line can be reused for Linac4 without any modifications.

Also the quadrupoles, LT.QFW70, LTQDN75, LTB.QDN10, LTB.QFN20, which are either of type SMIT air-cooled or type LINAC VII are suitable for an operation at 160 MeV. The excitation current has to be adapted to the new beam optics requirements, but is well below the maximum permitted current.

In 1997, four new air cooled quadrupoles (LTB.QDW30, LTBQFW40, LTB.QFW50, LTB.QDW60)

type TRIUMF were installed in the LTB line. The maximum continuous current is limited to 17.7 A, but needs to be increased to at least 24 A for future Linac4 operation. These magnets are actually powered in continuous mode, but since they are laminated they could also be operated in pulsed mode to keep the r.m.s. current below the limits. In this case appropriate power converters have to be made available.

The bending magnet LT.BHZ30 (IB1 type) has been equipped with new water-cooled coils in 2004. It is presently pulsed at 260 A for 50 MeV proton beam operation. To achieve the necessary factor two in bending force, the magnet needs to be powered with twice the nominal current (520 A). Since it is operated in pulsed mode, there is no particular problem in view of total dissipated power and cooling.

When sending beam directly to the PSB, the bending magnet LTB.BHZ40 (IB2 type with indirect water-cooling) is not switched on. Only when using the LBE/LBS lines for measurement and diagnostic reasons, the magnet is powered to deflect the proton beam into the LBE/LBS lines. The bending LTB.BHZ40 and all other magnets in the LBE/LBS lines are not discussed any further in this report, but their performance for a 160 MeV operation has to be reviewed.

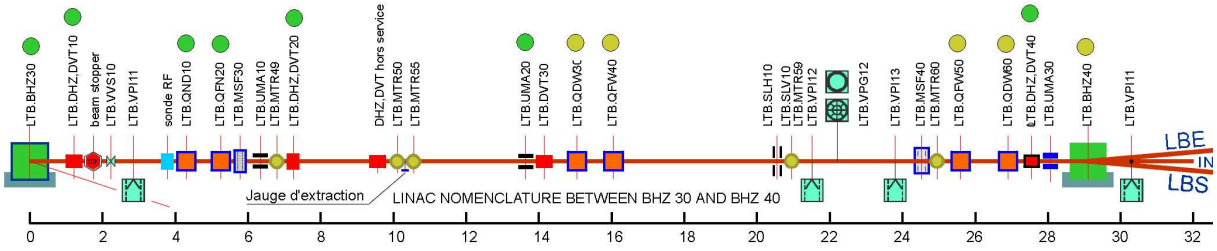

Figure 4.10: Overview of magnetic elements in the existing LTB transfer line

As for the BI line, all steering magnets can be reused without any modifications.

The maximum current of the quadrupoles BI.QNO10, BI.QNO20, BI.QNO30, BI.QNO40 is 24 A. They are of type SMIT, air-cooled, with a massive yoke, hence they cannot be operated in pulsed mode neither can their cooling performance be enhanced. For Linac4 they are required to run at almost 30 A, which is not achievable with the actual magnets. Consequently these four magnet need to be replaced.

One option is to install new quadrupoles of type TRIUMF, which are laminated and air-cooled and allow pulsed operation. An alternative could be to replace the SMIT air-cooled quadrupoles by existing old SMIT water-cooled quadrupoles. Because of their massive yokes it will not be possible to use them in pulsed mode. In addition, cooling water supply has to be foreseen for these magnets.

The BI.BVT vertical bending magnet presently installed after the distribution septum bends the four separated beams back into the horizontal plane. To handle the augmented beam rigidity, the integrated bending strength has to be increase up to 0.36 Tm. This 4-gap magnet has a massive yoke and 3 water cooled coil pairs. The operation current is limited to 220 A and cannot be further increased to the required 430 A without upgrading. Assuming that the magnet yoke can be reused, 3 new coils with an improved cooling performance will have to be manufactured and installed. This solution has the advantage to keep the overall dimensions of the magnet unchanged – only the total magnet length could increase by a maximum of 10% due to the more sophisticated cooling circuit.

The two quadrupoles, BI.QNO50 and BI.QNO60 (type SMIT water-cooled) can be reused without any modifications. The foreseen future operation current is clearly below the allowed limits.

Permanent magnet quadrupoles

Transverse focusing in all the DTL sections is provided by Permanent Magnet Quadrupoles (PMQ). With respect to electromagnetic quadrupoles, they allow higher gradients and their compactness leads to a higher RF efficiency.

Table 4.9: Characteristics of magnets installed in the actual LT, LTB and BI line to be reused for Linac4

Steering magnet	**Comment**	**Cooling**	**Operation mode**	**Type**			**Maximum current** [A]	**Maximum B-field** [T]	**Maximum** $\int B\mathrm{d}l$ [Tm]	**B-field ampere** [T/A]	**Resist.** [Ω]	**Induct.** [mH]
LT.DHZ/DVT 50	ok	air	pulsed	9af			10	1.36×10^{-3}	5.30×10^{-3}	1.36×10^{-4}	9.7	7
LTB.DHZ/DVT 10	ok	air	pulsed	10af			10	9.32×10^{-4}	3.60×10^{-3}	9.23×10^{-5}	3.5	11.3
LTB.DHZ/DVT 20	ok	air	pulsed	10af			10	9.32×10^{-4}	3.60×10^{-3}	9.23×10^{-5}	3.5	11.3
LTB.DHZ/DVT 30	ok	air	pulsed	10af			10	9.32×10^{-4}	3.60×10^{-3}	9.23×10^{-5}	3.5	11.3
LTB.DHZ/DVT 40	ok	air	pulsed	10af			10	9.32×10^{-4}	3.60×10^{-3}	9.23×10^{-5}	3.5	11.3
BI.DHZ/DVT 10	ok	air	pulsed	10af			10	9.32×10^{-4}	3.60×10^{-3}	9.23×10^{-5}	3.5	11.3
BI.DHZ/DVT 20	ok	air	pulsed	10af			10	9.32×10^{-4}	3.60×10^{-3}	9.23×10^{-5}	3.5	11.3
BI.DHZ/DVT 30	ok	air	pulsed	10af			10	9.32×10^{-4}	3.60×10^{-3}	9.23×10^{-5}	3.5	11.3
BI.DHZ/DVT 40	ok	air	pulsed	1			20	3.74×10^{-2}	1.57×10^{-2}	1.87×10^{-3}	3.3	320
BI.DHZ/DVT 50	ok	air	pulsed	10af			10	9.23×10^{-4}	3.60×10^{-3}	9.23×10^{-5}	3.5	11.3
BI.DHZ/DVT 70	ok	air	pulsed	9af			10	1.36×10^{-3}	5.30×10^{-3}	1.36×10^{-4}	9.7	7
Quadrupoles magnet	**Comment**	**Cooling**	**Operation mode**	**Type**	**Req. gradient** [T]	**Req. current** [A]	**Maximum current** [A]	**Maximum gradient** [T/m]	**Maximum** $\int G\mathrm{d}l$ [T]	**Gradient ampere** [T/m/A]	**Resist.** [Ω]	**Induct.** [mH]
LT.QFW 70	ok	air	cw	SMIT	−0.25	−3.53	24	1.70	0.78	7.08×10^{-2}	0.93	310
LT.QDN 75	ok	air	pulsed	LINAC VII	0.24	15.47	250	3.95	0.75	1.58×10^{-2}		
LTB.QND 10	ok	air	pulsed	LINAC VII	−2.66	−168.04	250	3.95	0.75	1.58×10^{-2}		
LTB.QFN 20	ok	air	pulsed	LINAC VII	0.45	28.67	250	3.95	0.75	1.58×10^{-2}		
LTB.QDW 30	ch. to pulsed	air	cw	TRIUMF	1.68	**23.38**	17.7	1.27	0.58	7.18×10^{-2}		
LTB.QFW 40	ch. to pulsed	air	cw	TRIUMF	−1.81	−25.17	17.7	1.27	0.58	7.18×10^{-2}		
LTB.QFW 50	ch. to pulsed	air	cw	TRIUMF	1.01	14.10	17.7	1.27	0.58	7.18×10^{-2}		
LTB.QDW 60	ch. to pulsed	air	cw	TRIUMF	−1.13	−15.77	17.7	1.27	0.58	7.18×10^{-2}		
BI.QNO 10	replace	air	cw	SMIT	1.41	19.91	24	1.70	0.78	7.08×10^{-2}	0.93	310
BI.QNO 20	replace	air	cw	SMIT	−2.05	−28.94	24	1.70	0.78	7.08×10^{-2}	0.93	310
BI.QNO 30	replace	air	cw	SMIT	1.54	21.80	24	1.70	0.78	7.08×10^{-2}	0.93	310
BI.QNO 40	replace	air	cw	SMIT	−1.70	−24.03	24	1.70	0.78	7.08×10^{-2}	0.93	310
BI.QNO 50	ok	water	cw	SMIT	−1.64	−66.15	300	7.45	3.43	2.48×10^{-2}	0.18	40
BI.QNO 60	ok	water	cw	SMIT	1.79	71.94	300	7.45	3.43	2.48×10^{-2}	0.18	40
Bending magnet	**Comment**	**Cooling**	**Operation mode**	**Type**	**Req. B-field** [T]	**Req. current** [A]	**Maximum current** [A]	**Maximum B-field** [T]	**Maximum** $\int B\mathrm{d}l$ [Tm]	**B-field ampere** [T/A]	**Resist.** [Ω]	**Induct.** [mH]
LT.BHZ 30	ok	water	pulsed	IBH1	0.74	521	210	0.30	0.31	1.42×10^{-3}	62	95
LTB.BHZ 40	to be checked	water (ind)	pulsed	IBH2	0	0	88	0.09	0.10	9.77×10^{-4}	43	64
BI.BVT	replace	water	cw	I_BH2	0.40	440	220	0.20	0.17	9.09×10^{-4}	0.16	

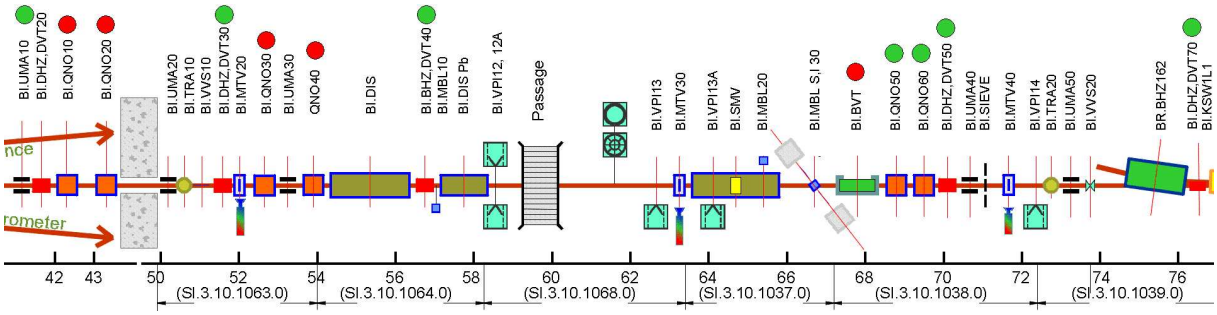

Figure 4.11: Overview of elements in the existing BI transfer line

A prototype magnet has been built by ITEP (Moscow) in the frame of a collaboration with CERN funded by the ISTC Organisation. The magnet design is based on identical $SmCo_5$ rods homogeneously magnetised orthogonally to their axis. The angles of rod magnetisation follow the $2\ \psi$ law first derived by Halbach [76], to produce a quadrupole. The rods are adjusted inside holes drilled in two concentric aluminium cylinders, forming a two-layer structure. The required orientations are obtained by a system of key-ways. Key-ways are machined longitudinally at the required angles with respect to the rod magnetisation which is measured by means of a Hall probe. The main magnet parameters and tolerances are listed Table 4.10, and the prototype PMQ is shown in Fig. 4.12.

Table 4.10: Main parameters of the PMQ's for the Linac4 DTL

Specifications	
Integrated gradient	2 to 2.5 Tesla
Geometrical length	> 40 mm
Inner diameter	22 mm
Outer diameter	60 mm final, 61 mm for correcting errors
Tolerances	
Integrated gradient error	$\pm 0.5\%$
Field linearity	$\Delta B/B \leq 0.01$ at 75% beam aperture
Harmonic content	$< 1\%$ of the main field at 75% of aperture
Magnetic axis w.r.t. geometric axis:	0.1 mm
Yaw/pitch/roll	1 mrad
Field direction	1 mrad

In order to verify that tolerances on integrated field strength, field quality, magnetic axis and roll angle are met, the prototype and the series magnets will be measured at CERN with a dedicated bench. The measurement is done by means of the rotating coil technique, and it provides the magnetic axis and angle in a reference frame defined by mechanical surfaces machined on the magnet. The magnets are measured horizontally, on a V-shaped support. The measuring coil is mounted on a ceramic shaft, and the signals are conveyed to the integrators by slip ring contacts. To stay well within the allocated error budget of 0.1 mm for the magnetic axis, the specified tolerance on the reference surfaces is of 10 μm. The global uncertainty on the magnetic axis measurement is of about 15 μm, and of 0.6 mrad on the field direction. After measurement, the positioning of the PMQ in the drift tube will be done by means of pins, and at this stage it is envisaged to correct for the axis and angle errors.

4.4 Booster injection equipment

In order to distribute the 160 MeV beam from Linac4 to the four levels of the PSB, new distributor magnets (BI.DIS) and magnetic septa (BI.SMV) need to be built. The proposed distribution scheme also

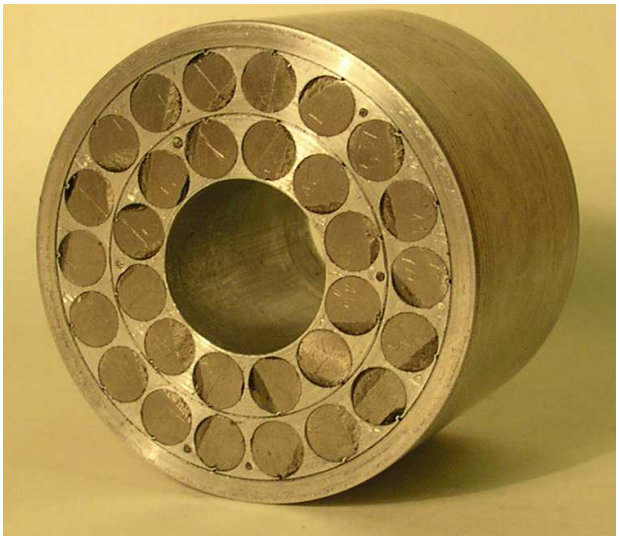

Figure 4.12: First PMQ prototype from ITEP

requires the construction of new pulse generators (PFN) to double the magnitude of the BI.DIS field pulse and increase the duration of the pulse from 100 μs to a maximum of 0.42 ms.

Distributor magnet BI.DIS

New distributor magnets are required in the booster injection line for the separation of the beam towards the BI.SMV septa in the direction of the four booster rings. The main parameters of the distributor magnets, for a 160 MeV beam from Linac4, are given in Table 4.11.

Table 4.11: Main BI.DIS kicker system parameters

	DIS0	**DIS1**	**DIS2**	**DIS4**	**DIS5**
Deflection angle [mrad]	3.42	3.88	3.49	3.65	3.62
Integrated field ($\int B\mathrm{d}l$) [mTm]	6.5	7.4	6.6	6.9	6.9
Gap field [mT]	18.4	20.9	18.8	19.6	19.5
Gap width [mm]	50	50	50	50	50
Gap height [mm]	98	98	98	98	98
Length (magnetic) [mm]	354	354	354	354	354
Length (Ferrite) [mm]	400	400	400	400	400
Conductor thickness [mm]	1	1	1	1	1
No. of conductor turns	1	1	1	1	1
Peak current [A]	731	830	746	781	774
Pulse length [ms]	0.42	0.32	0.22	0.12	0.02
Repetition rate [Hz]	2	2	2	2	2
Magnet inductance [μH]	0.9	0.9	0.9	0.9	0.9
Magnet resistance [mΩ]	0.03	0.03	0.03	0.03	0.03
Maximum voltage [kV]	28	28	28	28	28
Maximum field rise-time [μs]	≤ 1.0	≤ 1.0	≤ 1.0	≤ 1.0	≤ 1.0
PFN impedance [Ω]	12.5	12.5	12.5	12.5	12.5
PFN charging voltage [kV]	21.5 (30 maximum)				

The required field strength allows the use of ferrite yokes. It should be verified whether the present magnets can sustain the required voltage. Furthermore, it needs to be tested whether the magnets are fast enough to provide the required field strength and homogeneity and whether they can cope with the increased r.m.s. current. If these conditions are met the magnets can be recovered and installed in a newly designed vacuum vessel. If new magnets are needed, a new design, based on the existing magnets, using a modified ferrite core and coil geometry needs to be made.

The vacuum design will be based on standard PS equipment, such as vacuum seals, flanges and vacuum pumps. A vacuum in the 10^{-9} mbar range is expected. No bake-out system is foreseen, except for heating jackets on the ion pumps. The magnets will be built into one vacuum tank as a modular plug-in unit, such that it can be exchanged within one day in the event of a failure.

Magnetic septa BI.SMV

New magnetic septa are required for the separation of the beam towards the four booster rings. The main parameters of the septa, for a 160 MeV beam from Linac4, are given in Table 4.12.

Table 4.12: Main BI.SMV magnet parameters

	SMV1	**SMV2**	**SMV3**
Deflection angle [mrad]	165.8	131.3	131.1
Integrated field ($\int B\mathrm{d}l$) [Tm]	0.315	0.250	0.250
Gap field [T]	0.329	0.260	0.260
Gap width [mm]	70	70	70
Length (magnetic) [mm]	960	960	960
Septum thickness [mm]	4.5	4.5	4.5
No. of conductor turns	1	1	1
Peak current [kA]	18.3	14.5	14.5
Half sine pulse width [ms]	≈ 4	≈ 4	≈ 4
Repetition rate [Hz]	2	2	2
Magnet inductance [μH]	1.3	1.3	1.3
Magnet resistance [mΩ]	0.1	0.1	0.1

The required field strength in the gap imposes the use of a laminated steel yoke. To reduce the heat load on the magnets they will be individually powered from a capacitor discharge power supply. Each magnet will be equipped with its proper high-current feed-through. The magnets will be used in the same layout as the present BI.SMV. In order to cope with the increased beam rigidity and to allow for increased deflection angles, the horizontal aperture will need to be reduced to 70 mm matching the aperture assumed for the Linac4 transfer line, while the vertical beam acceptance of the layout will be kept the same. The fringe field at 15 mm from the septum is expected to be below 0.5% of the integrated gap field.

It will be necessary to build curved magnets and subsequently curved coils, to minimise the magnet cross-section, which will allow beam 1 at the exit of SMV1 to pass under SMV2 and to reduce the vacuum exposed surface of the magnets. A new magnet design is thus required (it should be noted that currently no experience in curved, under-vacuum, laminated steel septa magnets is available at CERN).

New head and tail dumps need to be developed, which will be able to cope with the increased repetition rate and beam energy. The head dump shall be robust enough to withstand a full beam impact at 160 MeV. The possible need of water cooling for the internal dumps, to limit the vacuum gas load, needs to be studied.

Scrapers shall be installed, just upstream of all septum conductors, to define the aperture and to

Table 4.13: Proposed nominal BI.DIS generator parameters

Characteristic impedance	12.5 Ω
Two-way delay (FWHM)	460 μs
Maximum current	1200 A
Nominal current	860 A
PFN maximum charging voltage	30 kV
PFN nominal charging voltage	21.5 kV
Total inductance	2.9 mH
Total capacitance	18.6 μH
Number of cells	33
Central cell inductance (L)	88 μH
Central cell capacitance (C)	563 nF
Central cell resistance ($R_{\mathrm{p}} = R_{\mathrm{p2}}$)	150 Ω
Thyratron end cell inductance (L_1)	114 μH
Thyratron end cell capacitance (C_1)	605 nF
Thyratron end cell resistance (R_{p1})	64 Ω
Front cell resistance (R_{front})	15 Ω
Front cell capacitance (C_{front})	400 nF

limit the heat load and the activation of these fragile conductors.

As for the BI.DIS system, the vacuum design will be based on standard PS equipment, such as vacuum seals, flanges and vacuum pumps. Furthermore, an under-vacuum bake-out system will be included to achieve the expected vacuum level in the 10^{-9} mbar range after a 5-day bake out period, including 24 hours at 200 °C for the magnet cores. The magnet will be built as a modular plug-in unit, such that it can be exchanged within one day in the event of a failure.

Three 400 V, 3 phases, 32 A r.m.s. power supplies will be required in order to pulse the magnets. Ten l/min demineralised water (ΔT <2 K) are required to evacuate the estimated 0.35 kW of heat generated per magnet.

BI.DIS pulse generator

The proposed BI.DIS scheme requires that the BI.DIS timing is linked to the Linac4 pulse structure and that the BI.DIS pulse lengths will be fixed, but different for each magnet, with a maximum of 0.42 ms pulse length. To reach the required current, the impedance of the PFN and the terminating resistor will be reduced from 25 Ω to 12.5 Ω and the PFN will be designed for up to 30 kV in voltage, which will allow a maximum pulse current of 1200 A to be delivered to the magnet.

In order to economically obtain the required maximum 0.42 ms pulse flat-top length without excessive droop of the field pulse, the PFN will be a lumped element device of 12.5 Ω impedance and 33 LC cells. Each PFN cell will be approximately 88 μH and 563 nF, as shown in Table 4.13. PSpice simulations have shown that a reduction of the number of cells could be possible, at the expense of an increased duration of the flat-top field ripple; however, each cell would require a larger value of inductance and capacitance.

A front cell, connected at the thyratron end of the PFN, as shown in Fig. 4.13, will be used to obtain the required field rise-time of 1 μs (1% to 99%). Mutual inductance between adjacent PFN cells helps to control the magnitude of the flat-top ripple. A resistor will be connected in parallel with each PFN inductor to provide further damping of the ripple. In order to maintain a constant mutual inductance between adjacent cells it is desirable to arrange the PFN coil to be straight and continuous.

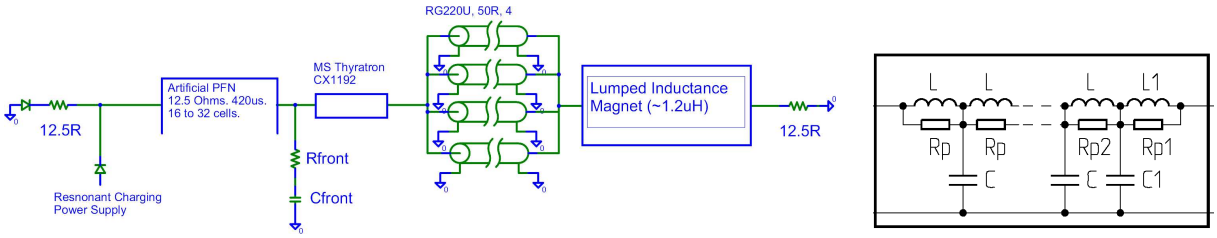

Figure 4.13: Schematic circuit diagram of kicker system (left) and proposed PFN cells (right)

For a 33 cell PFN, with parameters as listed in Table 4.14, the predicted field pulse of the BI.DIS magnet is as shown in Fig. 4.14. The 1% to 99% rise-time is ≈ 200 ns with a field overshoot of approximately 1%, about 12 μs from the start of the flat-top field.

The size of the proposed PFN system, for a 0.42 ms flat-top pulse assuming a single PFN line, is presented in Table 4.14. The size of the PFN systems for a flat-top pulse with shorter duration can be reduced correspondingly. It is important to note that the large physical size of the PFN's will require additional floor space to be found in or close to the booster equipment room.

Table 4.14: Assumed PFN sizes using a single PFN line

Coil diameter	0.19 m
Coil shield diameter	0.40 m
Capacitor length[1]	0.35 m
Capacitor diameter[2]	0.30 m
Overall length	5.00 m
Overall width	0.50 m
Tank height	0.90 m

[1] based on 80 V/μm gradient [2] larger than assumed cell spacing of 125 mm, thus an alternative to a cylindrical shape needs to be considered.

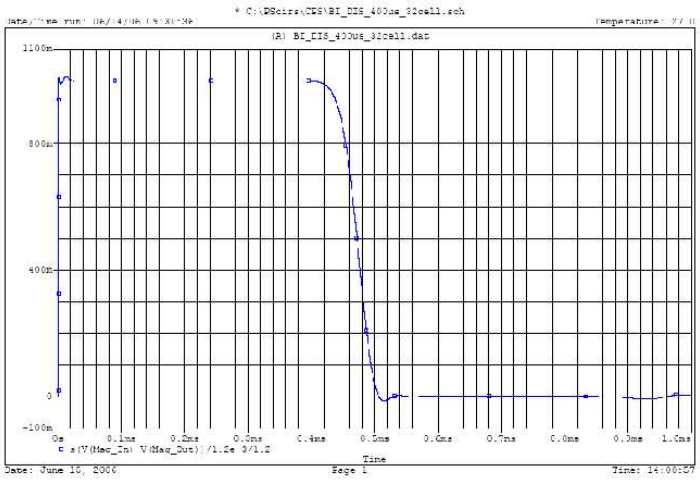

Figure 4.14: Simulated field pulse for a 33-cell PFN

4.5 Controls

The control system architecture for Linac4 will be largely based on that used for the LHC. Figure 4.15 shows the different blocks involved to service all controls requirements. A given application will only use a subset of these services.

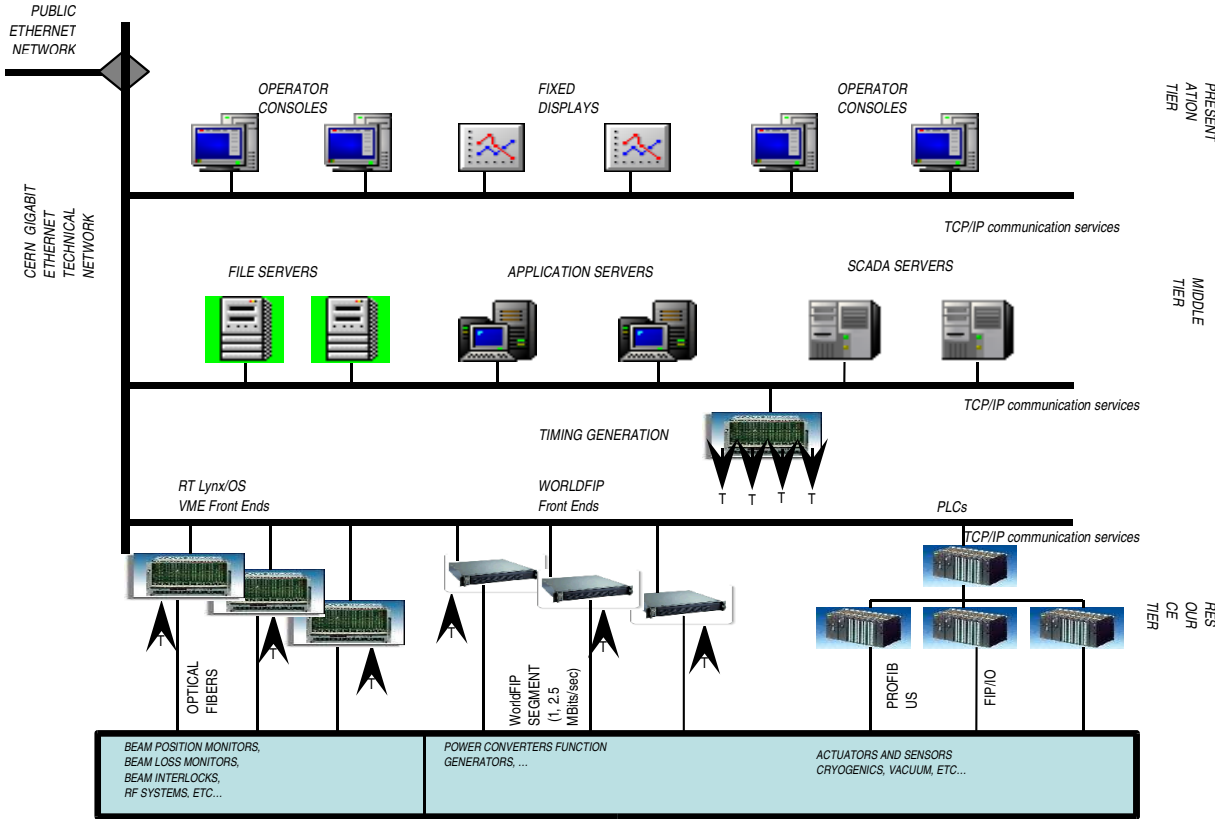

Figure 4.15: Overall control system architecture for Linac4

Graphical application programs run on operator consoles (Linux or Windows PCs) on what is called the presentation-tier. For a two-tier application, these programs send control values and receive status information to/from the front-end computers sitting in the resource-tier.

Front-end computers can be Programmable Logic Controllers (PLCs), PCs (running Linux or LynxOS) or VME PowerPC processors running LynxOS (a real-time Unix-like operating system). Linux and LynxOS front ends typically use CERN's Front-End Software Architecture (FESA) framework, which provides a set of basic functionalities such as persistence of data, synchronisation with the timing system, communication with the upper layers using Controls Middleware (CMW) and a rapid application development environment for real-time tasks. Front-end computers also act as gateways between the ethernet-based technical network and field buses such as MIL1553, Worldfip and Profibus. A typical two-tier application is the control of power converters for magnets using either MIL1553 or Worldfip.

For some applications, it is interesting to have a computer in the so-called middle-tier to centralise requests from several presentation-tier Java applications and service them via appropriate access to front ends. This middle-tier software is typically programmed in Java and provides services such as access to databases, data logging for off-line analysis and arbitration for competing requests to access hardware. One example of a three-tier application is the Open Analog Signals Information System (OASIS), which lets users view analog signals from front ends in virtual oscilloscope screens on an operator console. The signals can be very distant geographically, but OASIS handles network communication and trigger synchronisation all over CERN to give the user the illusion of having local access to hundreds of signals.

Fully industrial control systems, such as the one used in the LHC for cryogenics, are also supported through the use of PVSS, a Supervisory Control and Data Acquisition (SCADA) system standardised at CERN. PVSS provides a rapid application development environment for graphical applications running in operator consoles, as well as convenient methods to communicate with front-end PLCs through the network.

Databases using Oracle technology are extensively used to document hardware and software installed in the front ends and to automatically generate generic software from this information. Other uses of databases in the control system include asset management, physical layout descriptions, logging for off-line analysis and persistence for settings management.

CERN's General Machine Timing (GMT) system will be used for the coordination in time among different pieces of equipment (in the same or different accelerators), as well as for real-time tasks synchronisation. This system consists of a master module (per accelerator) driving an RS-422 multi-drop network with messages signalling different events. At the receiving side, electronic modules in VME, PCI and PMC formats can be installed in front-end computers and programmed to react to a given event by producing either a TTL pulse (for hardware synchronisation) or an interrupt to the front-end processor (for real-time software tasks). The GMT master's clock is driven by a Rubidium-based GPS receiver and all the events generated on the timing cable are UTC-related. To synchronise with the beam, there are external clock inputs in the timing receiver cards. All pulses output by these cards are UTC time tagged with a precision of around 25 ns, a very useful feature for diagnostics.

4.6 Power converters

The proposed power converter topologies make use of the most advanced technology in the power conversion domain, taking benefit from the most recent advancements in the field of high- and low-voltage semiconductors, commercial power supplies, switch-mode techniques and control electronics.

After analysis of the requirements for the Linac4 klystron and magnet power supply systems, a pulsed solution was adopted for all power converters, except for the ones of the RF amplifier tubes (3 units, approximately 700 W each). By this strategy, the r.m.s. power consumption at the grid is significantly reduced; forced air cooling is possible instead of water cooling in the power converters and volume and costs are minimised. Only the bending magnet power converters (6 units) are water cooled. Furthermore, the majority of the magnets may be natural air cooled and the klystron water-cooling circuits are reduced to the minimum.

Whenever possible, either a commercial standard solution was found or power converters of the same type as others already used at CERN were selected, in order to reduce development and procurement time and to facilitate maintenance and spare parts management. Only two types of power converters need to be developed: i) the high-voltage klystron pulsed modulators (prototype already undergoing development) and ii) the pulsed high-current power converters for the septa magnets.

Pulsed modulators for the LEP and new 704 MHz klystrons

The cathode terminal of the klystrons will be supplied by a high-voltage pulse generated externally, using an electronic solid state pulse modulator. The main ratings of this pulse modulator are presented in Table 4.15. The simplified circuit schematics and main waveforms are shown in Fig. 4.16. The cathode pulse generator is composed by a medium-voltage commercial capacitor bank charger (PS1) which charges the capacitor bank up to 12 kV during the relief period between two consecutive pulses. To generate the pulse, the capacitor bank is discharged into the primary winding of a pulse transformer, via the solid state medium-voltage electronic main switch. The pulse transformer increases the voltage at the secondary winding by a factor of 10 and directly feeds the klystron. The undershoot network (diode, capacitor, resistor and MOV in parallel with the primary winding) absorbs the energy stored in the pulse transformer and secondary-side high-voltage cables in case of klystron internal arcing, protecting

it with no need for additional costly and bulky high-voltage crowbars (like thyratron based). A droop compensation system, using a high-frequency switch-mode power converter (PS3), will be implemented to precisely control the flatness of the pulse in closed loop.

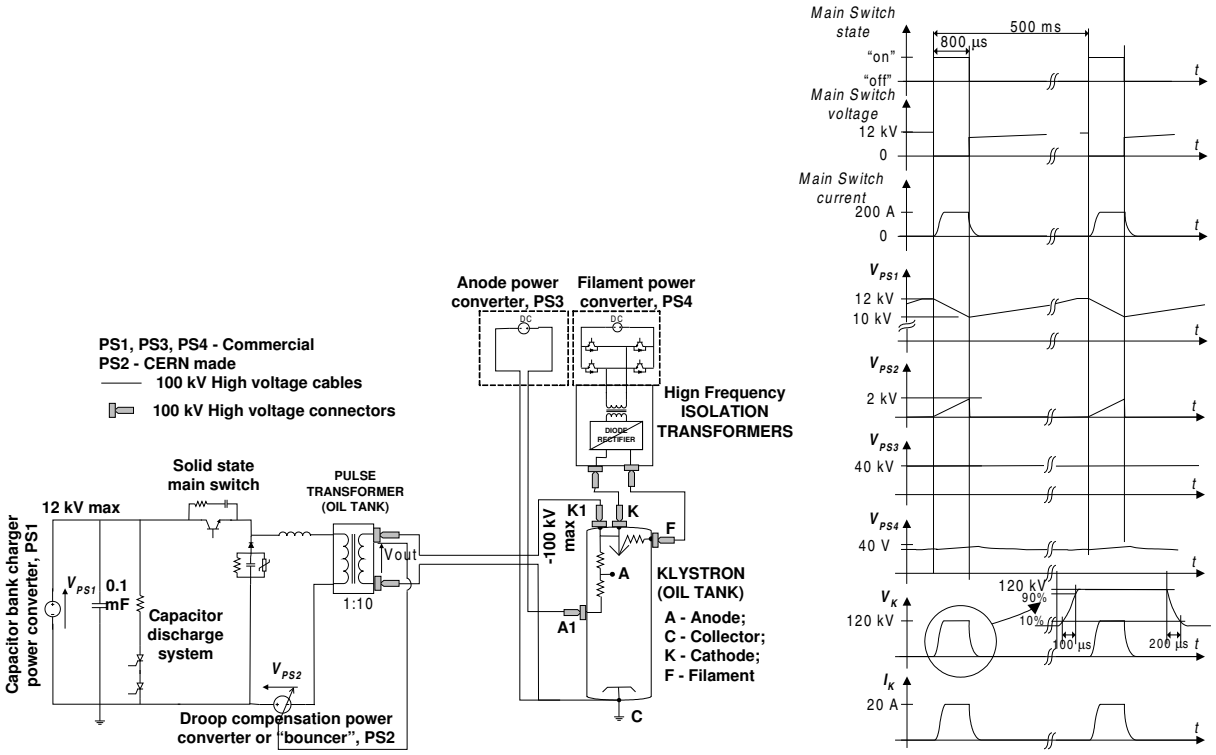

Figure 4.16: Pulsed modulators for the klystrons: (left) circuit schematics and (right) waveforms

The LEP klystrons were designed for operation in CW mode and are equipped with a modulating anode. In pulsed mode, this terminal is useless and will be polarised with a constant (however configurable) voltage. The anode voltage is derived from the cathode voltage via a resistive divider and can be varied in a specific range by adjusting the PS3 high-voltage power converter (commercial standard type).

The filament heater power converter (PS4) is based on a switch-mode topology, using a special high-frequency transformer for floating output capability and closed loop feedback for precise heating current control.

The development of a prototype of the solid state pulse modulator rated for 100 kV, 20 A (peak), 0.80 ms pulse width and 2 Hz pulse repetition rate was already launched to probe further this new high-level technology concept.

In principle, each klystron is foreseen to be supplied by a dedicated pulse modulator. However, for reasons of cost and standardisation, the supply of two klystrons in parallel by one pulse modulator may be considered, although this strategy requires further studies.

Each klystron pulse modulator may be installed in a single cabinet formed by 4 to 5 assembled racks, each: 19" width, 2.2 m height, 8 m depth. An electrical AC feeder (3 phase+N, 400 V, 32 A) will be required per klystron pulse modulator.

DC high-voltage power converters for RF amplifier tubes

The main characteristics of these DC high-voltage power converters are shown in Table 4.16.

They will be selected amongst any suited commercial type available in the market. An interface system for remote control will be developed and/or installed, according to the control standard adopted

Table 4.15: Operational characteristics of pulsed solid state modulators for klystrons

Application	LEP klystron	704 MHz klystron
Output characteristics		
Voltage amplitude [kV]	100	140
Current amplitude [A]	30	60
Rise-time [ms]	0.10	0.10
Fall-time [ms]	0.15	0.15
Flat-top duration [ms]	0.60	0.60
Repetition rate [Hz]	2	2
Flat-top voltage ripple [%]	0.1	0.1
Flat-top voltage droop [%]	1	1
Input characteristics		
Electricity	3-phase, 400 V, 50 Hz	
Cooling	air	air
Power consumption per converter, nom. operation [kW]	5.8	15
No. of converters	14	4
No. of spare converters (cabled from AC side)	1	1
Total no. of converters	15	5
Total power consumption, nom. operation [kW]	81.2	60

Table 4.16: Operational characteristics of HV-DC power converters with output crowbar for RF amplifier tubes

Application	RF amplifier tubes
Output characteristics	
DC voltage	15 kV
DC current	30 mA
Voltage ripple	0.1%
Voltage droop (due to RF pulse)	1%
Input characteristics	
Electricity	mono-phase, 400 V, 50 Hz
Cooling	air
Power consumption per converter, nom. operation	0.7 kW
No. converters	3
No. spare converters (cabled from AC side)	1
Total no. converters	4
Total power consumption, nom. operation	2.1 kW

later on (see point). The typical size of each power converter chassis, without control interface system, is 19" width $\times$ 5 Units (U) height $\times$ 0.8 m depth. All these power converters may be installed in one rack: 19" width, 2.2 m height, 0.8 m depth.

An electrical AC feeder (3 phase+N, 400 V, 32 A) will be required per rack. A distribution network will be installed inside the rack to supply each power converter with one single power line protected by a dedicated circuit breaker.

Pulsed power converters for quadrupoles (CCDTL & SCL)

These power converters are of the MaxiDiscap type, already used for supplying magnets in pulsed mode in other linear accelerators, like Linac2. The simplified electrical schematics and mechanical assembly

layout are shown in Fig. 4.17.

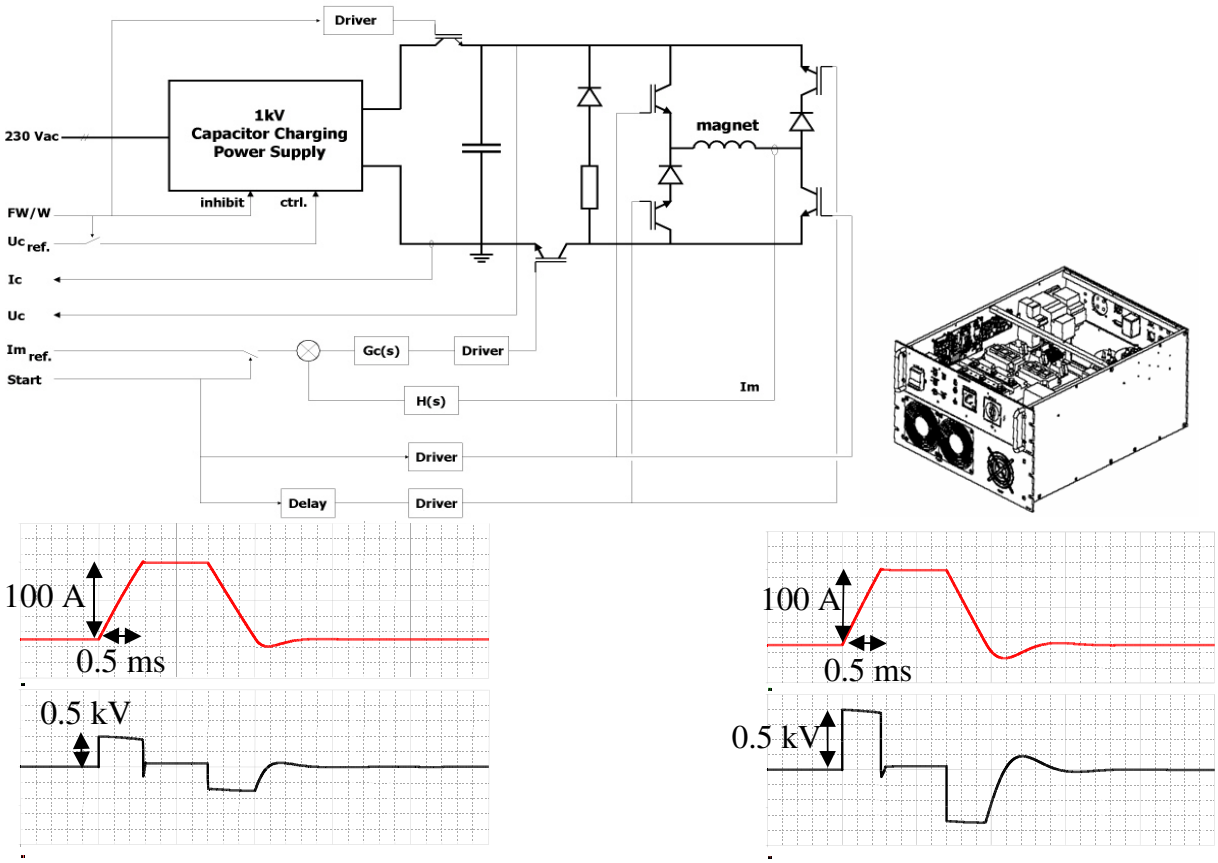

Figure 4.17: Pulsed MaxiDiscap power converters: - circuit schematics, mechanical view and pulse waveforms: (left) one magnet per converter, (right) two magnets in series per converter

A commercial capacitor charging power supply charges a capacitor bank to 1 kV. The capacitor bank is discharged into the magnet by the 4 IGBT H-bridge arrangement. A fifth IGBT, placed in series with the capacitor bank and H-bridge, is activated in active mode for closed loop current regulation during the flat-top. Some power converters will supply a load formed by two quadrupoles in series, but 8 of them will supply a single magnet. The load current pulse waveform has trapezoidal shape (Fig. 4.17). The main characteristics and parameters, corresponding to operation of this family of power converters with their loads, are listed in Table 4.17.

The typical size of each power converter chassis, including the power part and control electronics with remote interface system, is 19" width $\times$ 9 U height $\times$ 0.6 m depth. Three power converters may be installed in one rack: 19" width, 2. m height, 0.8 m depth.

An electrical AC feeder (3 phase+N, 400 V, 10 A) will be required per rack. A distribution network will be installed inside the rack to supply each power converter with one single-phase power line protected by a dedicated circuit breaker. In order to distribute homogeneously the power consumption amongst the three phases, each phase will supply one converter.

Pulsed power converters for the steering magnets

The power converters selected for this application are of the MiniDiscap type, already installed in Linac2. The simplified electrical schematics and photograph is shown in Fig. 4.18.

A switch-mode step-up booster with PFC functionality (Power Factor Correction) charges a capacitor bank up-to 700 V. Thanks to the PFC, the line current is nearly sinusoidal and with unitary power

Table 4.17: Operational characteristics of pulsed MaxiDiscap power converters for CCDTL and SCL quadrupoles

Application	**Linac quadrupoles**
Output characteristics	
Current amplitude	100 A
Rise-time	0.5 ms
Fall-time	0.6 ms
Flat-top	0.6 ms
Repetition rate	2 Hz
Flat-top precision (current)	5×10^{-4}
Input characteristics	
Electricity	mono-phase, 220 V, 50 Hz
Cooling	air
Power consumption per converter, nom. operation	300 W
No. of converters	26
No. of spare converters (not cabled from AC, DC)	3
Total no. of converters	29
Total power, nom. operation	7.8 kW

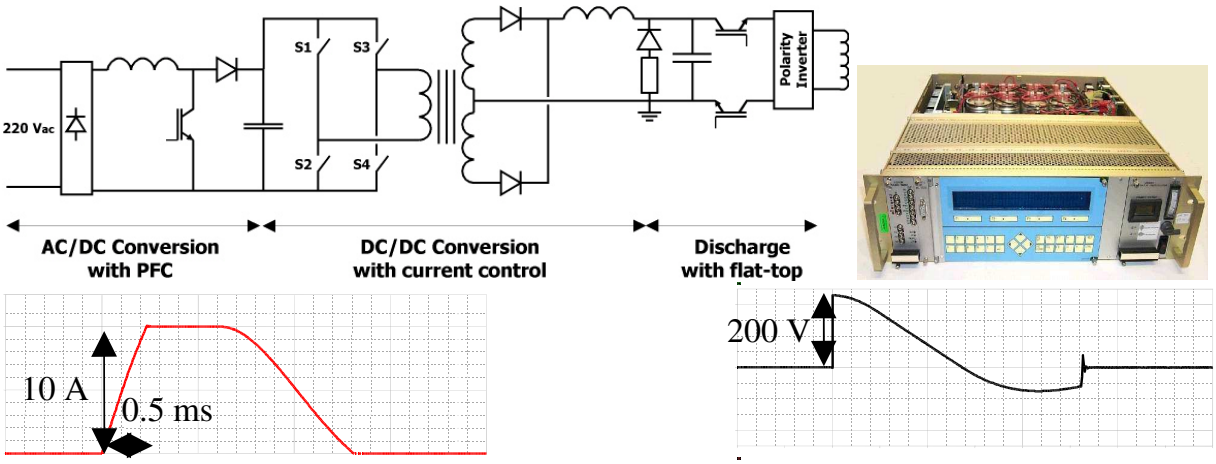

Figure 4.18: Pulsed MiniDiscap power converters: circuit schematics, mechanical view and pulse waveform

factor. An H-bridge inverter feeds a high-frequency transformer. The magnet supply voltage is then generated by rectification of the output transformer voltage. Two IGBT's, operating in active mode, assure the specified pulse flatness.

Each power converter will supply a single magnet. The magnet current pulse waveform is composed by a linear rise period, a flat-top and an exponential fall period (Fig. 4.18). The main characteristics and parameters, corresponding to operation of this family of power converters with their real loads, are listed in Table 4.18.

The typical size of each power converter chassis, including the power part and control electronics with remote interface system, is 19" width $\times$ 3 U height $\times$ 0.55 m depth. Up to 6 power converters may be installed in one rack: 19" width, 2.2 m height, 0.8 m depth.

An electrical AC feeder (3 phase+N, 400 V, 4 A) will be required per rack. A distribution network will be installed inside the rack to supply each power converter with one single-phase power line protected by a dedicated circuit breaker. In order to distribute homogeneously the power consumption amongst the three phases, each phase will supply 2 converters.

Table 4.18: Operational characteristics of pulsed MiniDiscap power converters for steerers

Application	**Steerers**
Output characteristics	
Current amplitude	20 A
Rise-time	0.5 ms
Fall-time	2 ms
Flat-top	0.6 ms
Repetition rate	2 Hz
Flat-top precision (current)	5×10^{-4}
Input characteristics	
Electricity	mono-phase, 220 V, 50 Hz
Cooling	air
Power consumption per converter, nom. operation	200 W
No. of converters	24
No. of spare converters (not cabled from AC, DC)	3
Total no. of converters	27
Total power consumption, nom. operation	4.8 kW

Pulsed power converters for quadrupoles of the transfer line

The power converters for the quadrupoles of the transfer line are of the MaxiDiscap type, shown in Fig. 4.17. Each power converter will supply a load composed by a single magnet. The characteristics and parameters corresponding to the operation with this load are specified in Table 4.19.

Table 4.19: Operational characteristics of pulsed MaxiDiscap power converters for TL quadrupoles

Application	**TL quadrupoles**
Output characteristics	
Current amplitude	200 A
Rise-time	1.3 ms
Fall-time	1.5 ms
Flat-top	0.6 ms
Repetition rate	2 Hz
Flat-top precision (current)	5×10^{-4}
Input characteristics	
Electricity	mono-phase, 220 V, 50 Hz
Cooling	air
Power consumption per converter, nom. operation	300 W
No. of converters	23
No. of spare converters (not cabled from AC, DC)	3
Total no. of converters	26
Total power consumption, nom. operation	6.9 kW

The same mechanical assembling principle into 19" racks and electrical AC feeder requirements adopted for the machine quadrupoles are extended to this application (see quadrupoles for CCDTL and SCL).

Pulsed power converters for bending magnets type A and B

The topology adopted for this application is similar to the one adopted for the new PS Pole Face Winding (PFW) new power converters developed in the framework of the PS consolidation program. It is based on a switch-mode current-regulated converter where the regulation is permanently activated during the whole cycle length (see Fig. 4.19). Unlike the cases presented above, an arbitrary reference function shall be generated as input for the controller with the same waveform as the desired one for the load current pulse.

The AC mains voltage from the grid is adapted to the load requirements by the three-phase transformer. A DC-link bus is generated by rectification of the transformer output voltage by means of a diode bridge and filtered by a LC filter. A switch-mode 4-quadrant DC/DC converter formed by an IGBT H-bridge converts the fixed DC-link voltage to an adjustable DC voltage with high harmonic contents. These high-frequency harmonics, undesirable for the load, will be filtered by a second LC high-frequency filter. A brake-chopper is installed in the DC-link to absorb the energy from the magnets during the phases of current reversal. An output bidirectional crowbar protects the load in case of over-voltage.

Each power converter will supply one bending magnet. The main parameters of operation of these power converters with their loads are listed in Table 4.20.

These power converters require demineralised water cooling.

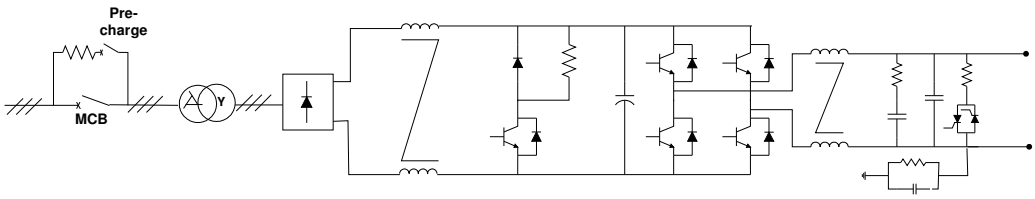

Figure 4.19: Pulsed, current-regulated 4-quadrants switch-mode power converters: circuit schematics

Table 4.20: Operational characteristics of switch-mode current-regulated power converters for bending magnets

Application	**bending magnets**	
Output characteristics	**Type A**	**Type B**
Current amplitude [kA]	1	1
Rise-time [ms]	35	55
Fall-time [ms]	35	55
Flat-top [ms]	20	20
Repetition rate [Hz]	2	2
Flat-top precision (current)	1×10^{-4}	1×10^{-4}
Input characteristics		
Electricity	three-phase, 400 V, 50 Hz	
Cooling	demineralised water, 10 l/min	
Power consumption per converter, nom. operation [kW]	3.5	6.5
No. of converters	3	2
No. of spare converters (cabled from AC side)	1	0
Total no. of converters	4	2
Total power consumption, nom. operation [kW]	10.5	13.0

Pulsed power converters for injection septa magnets

The septa magnet power converters are designed in general to produce pulse currents up to several kA, requiring typically several hundred volts. The parameters of the required power converters, for this particular application, are listed in Table 4.21.

Table 4.21: Operational characteristics of high-current pulsed power converters for BI septa

Application	**BI septa**	
Output characteristics	**SMV1**	**SMV2, SMV3**
Current amplitude [kA]	18.3	18.3
Rise-time [ms]	3	3
Fall-time [ms]	3	3
Flat-top [ms]	0.6	0.6
Repetition rate [Hz]	2	2
Flat-top precision (current)	5×10^{-4}	5×10^{-4}
Input characteristics		
Electricity	three-phase, 400 V, 50 Hz	
Cooling	air	air
Power consumption per converter, nom. operation [kW]	10	10
No. of converters	1	2
No. of spare converters	1	0
Total no. of converters	2	2
Total power consumption, nom. operation [kW]	10	20

In the existing CERN applications, these converters are of capacitor discharge type with integrated active filters in closed loop control for pulse flatness improvement. This type of converter design is more than 20 years old and is not optimised in terms of volume and cost, taking no benefit from the latest developments in power converter semiconductors and associated topologies. The existing power converters for the booster septa injection magnets, of this traditional technology, are not adapted to the new load requirements, have about 20 years of operation and some of the spare parts are obsolete. No other exploitable converters of this type are available at CERN.

In this context, a new design is proposed for this application and future similar ones at CERN. A feasibility study, including the analysis of several modern circuit alternatives, the selection and dimensioning of the best suited topology that shall privilege adoption of modern semiconductors and switching techniques should be carried out.

A unique model of this type of power converters, rated for a pulse magnitude of 20 kA, will be developed and will cover the three applications SMV1, SMV2, SMV3.

Remote control system

The remote control system to be adopted for the power converters is under evaluation. A traditional solution in the PS complex is today based on the MIL 1553 with G64 for the field-bus, GFAS for the current reference generation, TG8 timing system and optional OASIS for current acquisition and monitoring.

Although this traditional solution could be adopted, investigations on a new standard for general power converters controls in the PS complex have been launched and consequently a new standard could be selected, based on a modern standard field-bus.

A unique remote control system shall be used for all the power converters in Linac4.

Table 4.22: Power converter maximum ratings

Application	Converter type	I_{nominal}	V_{nominal}	Parameters	Quantity
LEP klystron	Pulsed klystron modulator	30 A	100 kV	Rise-time: 0.10 ms Fall-time: 0.15 ms Flat-top: 0.60 ms Rep.-rate: 2 Hz ΔV: 1%	15
704 MHz klystron	Pulsed klystron modulator	60 A	140 kV	Rise-time: 0.10 ms Fall-time: 0.15 ms Flat-top: 0.60 ms Rep.-rate: 2 Hz ΔV: 1%	4
Transfer line and linac quadrupoles	Pulsed MaxiDiscap	200 A	1 kV	Rise-time: 2 ms Fall-time: 2 ms Flat-top: 1 ms Rep.-rate: 2 Hz ΔI: 5×10^{-4}	55
Steering magnets	MiniDiscap	20 A	700 V	Rise-time: 2 ms Fall-time: 15 ms Flat-top: 1 ms Rep.-rate: 2 Hz ΔI: 5×10^{-4}	27
RF amplifier tubes	DC HV	30 mA	15 kV	ΔV: 1%	
Transfer line bending magnets Type A & B	Pulsed current-regulated during all pulse phases	1 kA	250 V	Rise-time: 55 ms Fall-time: 55 ms Flat-top: 20 ms Rep.-rate: 2 Hz ΔI: 1×10^{-4}	4 6
Booster injection	Pulsed septa	20 kA	300 V	Rise-time: 2 ms Fall-time: 15 ms Flat-top: 1 ms Rep.-rate: 2 Hz ΔI: 5×10^{-4}	4

Table 4.23: Full list of power converters for the 3 MeV test stand

Application	Converter type	I_{nominal}	V_{nominal}	Parameters	Quantity
LEP klystron	Pulsed klystron modulator	20 A	100 kV	Rise-time: < 0.10 ms Fall-time: < 0.15 ms Flat-top: < 0.60 ms Rep.-rate: 2 Hz ΔV: 1%	1
Chopper line quadrupoles	Pulsed MaxiDiscap	300 A	700 V	Rise-time: < 2 ms Fall-time: < 2 ms Flat-top: < 1 ms Rep.-rate: 2 Hz ΔI: 5×10^{-4}	11
Chopper line LPSS Steerer	DC current-regulated	20 A	35 V	ΔI: 1×10^{-4}	2
H^- source platform 1 potential rise	DC HV	10 mA	35 kV	ΔV: 0.05%	1
H^- source platform 2 potential rise	DC HV	2 mA	65 kV	ΔV: 0.05%	1
H^- source power amplifier screen bias	DC HV	1 A	2 kV	ΔV: 0.05%	1
H^- source power amplifier grid bias	DC HV	0.5 A	0.5 kV	ΔV: 0.05%	1
H^- source power amplifier anode bias	DC HV	80 mA (DC) 20 A (pulse)	20 kV	ΔV: 0.05%	2
LEBT solenoids	Pulsed capacitor discharge	1200 A	1 kV	Rise-time: < 5 ms Fall-time: < 5 ms Flat-top: 0.6 ms Rep.-rate: 2 Hz ΔI: 5×10^{-4}	2
LEBT LPSS for steerer	DC current-regulated bipolar w. inv. switch	10 A	70 V	ΔI: 1×10^{-4}	4
LEBT LPS2 for bending	DC current-regulated bipolar w. inv. switch	50 A	35 V	ΔI: 1×10^{-4}	1

4.7 Vacuum

The vacuum system of Linac4, which has an overall length of about 183 m, can be divided into nine warm vacuum sectors: the proton source with the Low Energy Beam Transfer (LEBT), the RFQ section, the chopper line (MEBT), the Drift Tube Linac (DTL), the Cell-Coupled Drift Tube Linac (CCDTL), the Side-Coupled Linac (SCL), and the Transfer Line (TL).

Owing to the short time that the protons spend in the accelerator, the pressure requirements given by the life-time considerations are between 10^{-5} mbar (source/LEBT) and 10^{-7} mbar (rest of the linac). The different machine components will have complex vacuum vessels and probably little space available for pumps, which will require for some parts pumping manifolds as already designed for the chopper line. The apertures (diameters) of the beam tube vary along the linac between 4 mm and 147 mm.

The linac pumping system must be compatible with the vacuum equipment typically used in CERN accelerators. The evacuation of the vacuum system from atmospheric pressure will be done with pumping groups (primary and turbo molecular pumps) and lumped sputter ion pumps; standard Penning/Pirani gauges will be distributed for pressure logging during operation. The whole vacuum system must be metal-sealed using either Conflat™ (all vacuum equipment) or Helicoflex™ seals (joints between tanks), O-rings being excluded. The vacuum control of all machine equipment has to be compatible with the existing CERN installations.

Differential pumping in the LEBT should be as efficient as possible aiming at a pressure lower than 10^{-6} mbar at the exit of the LEBT.

An evaluation of the necessary vacuum equipment for each part of the linac is summarised in Table 4.24. It can only be considered as a rough approximation as long as the linac design is not finished and approved.

Table 4.24: Overview of vacuum equipment needed for each part of Linac4

	Source + LEBT	**RFQ**	**Chopper**	**DTL tanks**			**CCDTL**	**SCL**	**TL**
				1	**2**	**3**			
Vacuum sector	1	2	3	4	4	4	5	6	7,8,9
Length [m]	0.50 + 1.80	5.95	3.72	2.63	5.20	5.20	25.2	28.0	105
Modules	–	1	–	1	1	1	8	4	–
Tanks p. module	–	–	–	–	–	–	3	5	–
Aperture diam. [mm]	to be defined	3.6 – 4	26 – 147	20	20	20	28	32	70
Vacuum [mbar]	$10^{-5}/10^{-6}$	10^{-7}	10^{-7}	10^{-7}	10^{-7}	10^{-7}	10^{-7}	10^{-7}	10^{-7}
Sector valves	1	1	1	–	–	1	1	1	3
Pumping manifold	-	1	1	-	-	-	-	1	-
Pumping groups	2 + 1	1	1	–	1	–	2	4	2
Ion pumps	–	4	2	1	2	2	8	20	10
Gauges	1	1	1	1	1	1	4	4	4

4.8 Survey

The Linac4 project requires the precise alignment, in both the horizontal and vertical planes, of elements along approximately 200 m beam line ($\approx$ 80 m in the linac and $\approx$ 110 m in the transfer line) from the source to the PS booster.

Based upon the results from simulations maximum error budgets have been fixed for the displacement of the linac quadrupoles (see tables below). These error budgets are applicable to either the radial or vertical position of a quadrupole relative to the average beam line in the linac. They include mechanical, construction and alignment errors.

The most difficult elements to align are considered to be the quadrupoles of the DTL which are positioned inside a tank and are not visible at the time of alignment. For the alignment of the DTL tanks, the errors associated with the 6 activities listed in Table 4.25 below should be taken into account. It is assumed that these are random errors, which are normally distributed and can be added quadratically to meet the overall error budget.

The first four sources of error derive from the fabrication and production of these tanks. The quality control of these activities should be handled during this production. The last two activities will be controlled by the survey group.

Table 4.25: Errors associated with the alignment of the DTL tanks

Error source - DTL tank alignment	**Maximum error**
Determination of quadrupole magnetic field axis with respect to the mechanical axis Positioning of quadrupole inside the drift tube Linear alignment of drift tubes Determination of external mechanical references with respect to the drift tubes	± 0.10 mm
Determination of survey reference targets with respect to external mechanical references	±0.15 mm
Positioning of DTL tank with respect to theoretical beam line	±0.15 mm

For the CCDTL and SCL modules, the alignment errors associated with the 5 activities listed in Table 4.26 below should be taken into account. The maximum error budget for the first 3 activities is ±0.1 mm. Assuming that the errors are random, normally distributed and can be added quadratically, the error budget has been broken down as shown.

Table 4.26: Errors associated with the alignment of the CCDTL& SCL modules

Error source – CCDTL & SCL module alignment	**Maximum error**
Determination of quadrupole magnetic field axis with respect to the mechanical axis Fiducialisation of the quadrupoles, tanks and BPM	± 0.08 mm
Linear alignment of the quadrupoles, tanks and BPM on the module support	±0.06 mm
Determination of survey reference targets on the module support with respect to the aligned elements on the support	±0.15 mm
Positioning of module support with respect to theoretical beam line	±0.15 mm

In this case only the last three activities will be the responsibility of the survey group and controlled by them.

The values found in Tables 4.25 and 4.26 are maximum errors and require a tight control of both the mechanical manufacturing of the elements and the measurement and alignment procedures. If we

consider the error to be normally distributed with standard error, σ, they should represent errors at the $\approx 3\sigma$ level.

The standard error for the final relative radial or vertical positioning of the DTL tanks, the CCDTL and the SCL modules is therefore taken to be 0.05 mm. This demands extremely precise alignment using traditional techniques. It is therefore proposed to develop a mobile wire positioning system based upon existing technology (such as that used in the LHC) in order to meet these requirements. This will require a permanent hydrostatic levelling system along the linac. It is essential that a dedicated space be defined and kept clear for this survey instrumentation and the measurements, and this free space will be clearly shown and maintained in the plans and 3D models of the machine layout.

The stringent alignment requirement also imposes demanding requirements on the support and alignment reference systems to be used. The support positioning systems classically used to date for small light components would no longer give sufficient control over the small movements required by the final alignment. The survey group will be included in the approval list for the support positioning system design.

It is noted that to achieve and maintain this level of alignment precision, several factors must be taken onto account: the stability of the zone in which the machine is to be installed; the rigidity of module supports; and the thermal expansion of the supports and the elements themselves linked to changes in the ambient temperature. It is understood that these factors will all be considered and that their effect on the alignment of the machine will be negligible in comparison to the maximum error budgets outlined above.

A significantly lower precision is required for the alignment of the quadrupole magnets with respect to its neighbouring dipole magnets in the transfer line, equivalent to that imposed for the other transfer lines of the PS complex. More traditional methods will therefore be used for these elements.

Support and alignment reference systems

A geodetic reference network will be established along the linac and the transfer line to the PS booster. New points, in the form of permanent pillars equipped with the CERN standard survey reference sockets will be added alongside the linac and where they are necessary for the transfer line. This network will be measured using a total station, nylon wire offsets, and direct levelling. The network will be determined relative to the existing networks of the PS complex. It will serve as a reference to maintain the overall geometry of the machine and the relative positions of the Linac4 machine and the PS booster.

As already mentioned a new form of support / positioning system will be required for the elements to be aligned, and will provide the means to change the position of the elements with a precision $\leq$ 0.01 mm. The systems should disassociate the movements in the horizontal and vertical planes to this same level of precision. The survey group will help to define the systems and will be included in the approval list for the final designs.

All elements to be aligned are to be equipped with survey reference points (or fiducials) and a means to establish the tilt of the element. This could be achieved by two appropriately positioned fiducials and a flat surface to measure the tilt, or three appropriately positioned fiducials. The survey group will help with the definition and placement of these fiducials and will be included in the approval list for the final designs.

To enable the necessary survey and alignment measurements, the fiducials used for the radial and vertical alignment of all elements along the linac must lie along the same spatial line. Space around that line must be kept completely clear and will be included in the plans of the machine layout.

Geometrical quality control measurements

For all the elements of the linac, and the transfer line to the PS booster, the geometrical quality control measurements of the mechanical construction will be performed before any intervention by the survey group.

Fiducialisation measurements

The fiducials and reference surfaces on each element to be aligned will be defined with respect to the mechanical / magnetic axis of the element in question and the "horizontal" plane of the element. This will be done before their alignment by the survey group.

The survey group will be provided with the position of the external reference marks on the DTL tanks relative to the internal alignment of the quadrupoles, and will subsequently determine the position of the survey fiducials relative to these marks and hence the same internal alignment.

The quadrupoles, tanks, and beam position monitors of the CCDTL and SCL modules will be positioned on their module supports along a straight line using a laser tracker, and direct levelling. The positions of the module's fiducials and reference surfaces relative to the line defined by the module's elements will be determined at the same time.

Local reference networks will be established as necessary in the areas where this work is carried out.

Theoretical data

The MAD file defining the beam line elements and the layout plans for the machine will be provided to the survey group prior to any survey or alignment work being carried out in area where the accelerator is to be installed. The MAD file will be inserted into the SURVEY database.

Plans for each of the elements to be aligned (including those to be aligned on a module support) will also be provided to the survey group prior to any survey or alignment work along with the parameters of the survey reference targets for each element. This data will also be entered into the SURVEY database.

Marking out

The marking out of the beam line and the supports of the elements to be alignment will be carried out using a total station. The geodetic reference network will be used and the data previously entered into the SURVEY database.

Positioning & smoothing

The initial positioning of the beam line elements will be carried out using a total station and direct levelling from the geodetic reference network and nylon offsets on the elements themselves. In the transfer line the dipoles will be aligned from the network and the quadrupoles and other elements aligned relative to the two nearest dipoles either side of them.

A final smoothing to achieve the desired relative alignment of the modules and other elements along the linac will be carried out using a mobile Wire Positioning System (WPS) that would be implemented using existing technology. Use of such a system will require the installation of a Permanent Hydrostatic Levelling system (HLS) along the full length of the linac comprising of 5 sensors. This HLS will be used to characterise the curve of the WPS wire so that it can also be used for smoothing in the vertical plane.

A smoothing of the transfer line will also be carried out using a total station, nylon wire offsets, and direct levelling on the elements themselves. If nylon wire offsets are not feasible for the transfer line, the use of a laser tracker to establish the final smoothed radial position will be considered.

Chapter 5

Radiation protection and safety

5.1 Radiation protection

In terms of radiation exposure the PS South Hall and its extension (buildings 150 and 152) will be classified as supervised area according to the new version of the CERN radiation safety code, while the nearby office buildings will be non-designated areas (see Table 5.1). The machine tunnel will be a separate part of the supervised area, where access during beam-on conditions will be prevented by the interlock and access systems. In access mode the tunnel will be classified as either supervised or controlled area according to the residual dose rates. Table 5.1 lists for the three types of radiation areas defined in the new safety code the maximum effective dose admitted in a consecutive 12-month period for a person under normal working conditions, the corresponding dose equivalent rate assumed as guideline and the access requirements. The maximum dose rate is calculated under the conservative assumption of a maximum occupation time of the various areas equal to 2000 hours per year.

Non-designated areas are monitored by installed detectors or passive dosimeters but wearing of a personal dosimeter is not required. For persons working on the CERN site but who are not exposed to ionising radiation in the exercise of their profession an effective dose of up to 100 μSv per working year from the operation of accelerators and experiments is considered as justified by the safety code and further optimisation is not necessary once this value is respected. For members of the general public this limit is reduced to 10 μSv per year. In the case of a full beam loss the shielding and the accelerator interlock must be such as to limit the integrated dose received by an individual to a small value. Here a guideline value of 10 μSv has been chosen.

Table 5.1: Designation of radiation areas

Type of area	**Max. yearly effective dose** [mSv]	**Max. ambient dose equivalent rate** [μSv/h]	**Requirements**
Non-designated	1	0.5	None
Supervised	6	3	Personal dosimeter
Controlled	20	10	Personal dosimeter + individual dosimeter with alarm function

Routine operation, normal beam losses

In the design of modern linear accelerators, it is generally assumed that the maximum beam loss level should be ≈ 1 W/m, considered as the threshold for hands-on maintenance on the machine [77]. Linac4 has been designed to become the injector for the future SPL, and the beam dynamics design as well as the apertures have been optimised to keep losses below 1 W/m at the SPL beam duty cycle of 4%. In the shielding calculations for the Linac4 case, the loss level of 1 W/m has been assumed as guideline, corresponding to a safety factor of 40 (ratio of SPL and Linac4 duty cycles). Therefore, the present shielding calculation should be considered as particularly conservative from the machine loss point of view.

In a realistic scenario, beam losses will not be equally distributed along the machine, but concentrated in few "hot spots", usually following a transition between structures and focusing periods or a frequency jump. Losses will occur in the aperture restrictions, typically inside quadrupoles. Other critical spots are the bending sections of the transfer line, where particles outside the energy acceptance

of the bending will be lost on the vacuum chamber. In order to have a realistic loss configuration, in the following it is assumed that constant losses at the level of 10 W occur at selected points along the machine. For the shielding requirements this loss distribution is approximately equivalent to a uniform loss of 1 W/m.

Eight representative loss points along the accelerator were considered, at energies ranging from 20 to 160 MeV. The lost protons were assumed to strike a thick copper target to mimic losses in a magnet coil or yoke. Copper was chosen as element representative of other materials with similar density (e.g., iron and stainless steel). The radiation attenuation that can be provided by the quadrupole yoke was not taken into account in the shielding calculations. The ambient dose equivalent rate at one metre distance from the 10 W loss points ranges from 100 mSv/h to 1.3 Sv/h, according to the beam energy. These values are in agreement with results of FLUKA [78, 79] simulations performed for the previous 120 MeV version of Linac4 [80].

The ambient dose equivalent rate H past the lateral shield for a point source can be approximately calculated as:

$$H = \frac{H_{\pi/2}\, e^{-d/\lambda}}{r^2} \tag{5.1}$$

where r is the distance from the radiation source to the exposure point of interest, $H_{\pi/2}$ is the source term for 90º emission, d is the shield thickness and λ is the attenuation length of the shielding material (concrete in this case). The parameter r was assigned a value of 4 m, which corresponds to a maximum distance of one metre from the outer wall of the shield. All results of the shielding calculations refer to this representative point. Given the distance between the loss points, the dose equivalent rate at a given location outside the shield only depends on the facing loss point (i.e., upstream and downstream loss points do not contribute to the dose rate). For a given shielding material, the attenuation length λ depends on the proton energy and on the target thickness. In particular, two models may be used to estimate λ, for thin and for thick target. As for the source terms, in the following the thick target model was used. Table 5.2 shows the shielding parameters used in the calculation and the resulting minimum shield thickness required to keep the dose rate in the representative points at 0.5 μSv/h (non-designated area), 3 μSv/h (supervised area) or 10 μSv/h (controlled area) for a beam loss of 10 W. A safety factor of 3 in the shielding attenuation was added to the minimum thickness, given by an additional 1.1 λ. For the South Hall the shielding requirement for a supervised area must be considered. More details are given in [81].

Figure 5.1 shows a detailed view of the preliminary shielding design which would reduce the prompt radiation along the accelerator to a level compatible with a supervised area. The left shielding wall increases from 0.8 m at the low energy end of the linac up to a maximum of 2.8 m at the high energy end. Whilst the left wall shields areas that are always accessible by personnel, the right wall runs along the main PS shielding wall, where access should normally not be required. The right wall is 0.8 m thick in the RFQ section (as the left wall), 1.3 m thick along the first 8 m of the DTL section (almost the same as the left wall), 1.5 m thick at the downstream end of the DTL, and 1.6 m further downstream. Access to the stairs taking to the so-called “PS bridge” at the beginning of the PS wall should be closed during operation of Linac4, as well as the passages on the ground floor and on the first floor between the linac shielding and the PS wall.

Measurements at the planned 3 MeV test stand will allow assessing the radiation level of the Linac4 front-end. If the radiation level is below the limit for a supervised area, it is foreseen to shield the beam line locally between the chopper line and the DTL and to modify the shielding allowing access to the 3 MeV section during operation.

Table 5.2: Source terms for 10 W proton losses, attenuation length in concrete (2.4 g cm^{-3} density) and shielding required to obtain a dose equivalent rate of 0.5 μSv/h, 3 μSv/h or 10 μSv/h at 4 m distance from the beam line, corresponding to a non-designated, supervised or controlled area, respectively. The South Hall is a supervised area.

Proton energy [MeV]	H [mSv/h]	**Attenuation length** [cm]	**Concrete thickness in** [cm] **for Non-designated area**	**Supervised area**	**Controlled area**
20	112	12.1	115	95	80
40	268	12.5	130	110	95
60	449	13.8	150	125	110
80	632	16.5	185	155	135
100	804	19.2	220	185	165
120	969	21.0	245	210	185
140	1140	23.0	275	230	205
160	1290	24.9	300	255	225

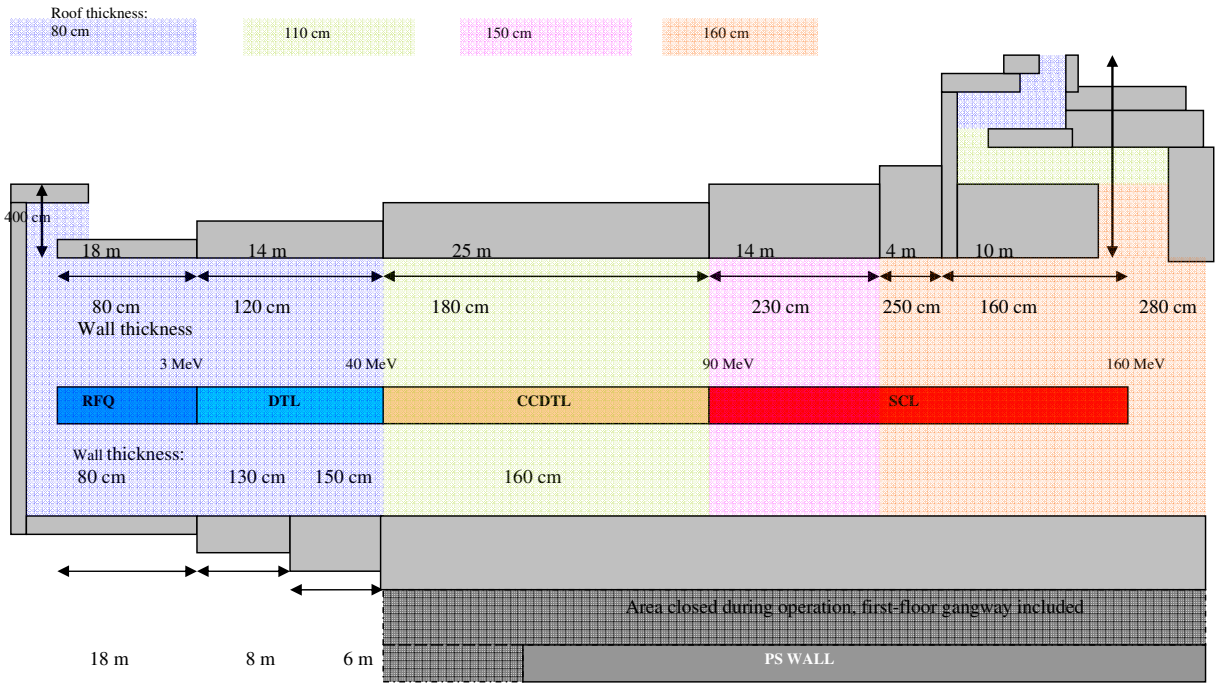

Figure 5.1: Schematic layout of Linac4 shielding

Accident scenario, full beam loss

The dose rate in case of a full beam loss can be calculated by scaling the value relative to a 10 W loss at the point of interest to the total beam power at the same point. The total beam power, for the nominal Linac4 current is approximately given by $P[\mathrm{W}] = 30 \cdot E[\mathrm{MeV}]$, where E is the beam energy (Table 5.3). The maximum instantaneous dose rate with the proposed shielding is 0.57 mSv/h. As stated above, the maximum acceptable accumulated dose caused by one full beam loss is 10 μSv. This implies that the beam must be switched off within one minute in case of the worst loss scenario, a condition easily met by the linac interlock system.

A more detailed study was made on the radiation hazard caused by a full beam loss for a previous Linac4 design at 120 MeV energy. Quadrupoles, copper drift tubes and iron supports were implemented

Table 5.3: Dose rates outside the proposed shielding at selected energies for a full beam loss

E [MeV]	20	40	60	80	100	120	140	160
Beam power [W]	600	1200	1800	2400	3000	3600	4200	4800
H*(10) [μSv/h]	21	136	11	173	95	382	570	504

in FLUKA in full details and four representative loss positions along the accelerator were evaluated (60, 70, 85 and 100 MeV). In spite of the completely different approach of the two methods, the results between the present estimates and the FLUKA simulations are in good agreement.

Roof shield

As for the lateral shielding, the thickness of the tunnel roof should vary along the accelerator according to the beam energy and to the intensity of the beam losses (Fig. 5.1). During linac operation, access to the tunnel roof will be forbidden and the crane driver must not be allowed to work above the linac tunnel. In order to evaluate the minimum required thickness of the top shield, dedicated simulations were run with a model of the South Hall [82]. The case of a 1.2 m thick top shield was compared to the case of a 1.6 m shield. Only losses at 160 MeV were simulated, because this case requires thicker shielding than at lower energies and represents the worst case assumption.

With a maximum top shield concrete thickness of 1.2 m, the dose rate in the South Hall would be around 1 μSv/h on the ground floor and on the gangway running along the first floor of the hall opposite to Linac4. This is not acceptable for the latter as the gangway is a non-designated area. A 1.6 m thick top shield would keep the dose rate below the limit of 0.5 μSv/h with a reasonable safety margin. However, the dose rate in the offices of nearby buildings might lead to an annual dose higher than 100 μSv for people who should not be exposed to ionising radiation in the exercise of their profession. This further constraint, which becomes critical in the buildings 249 and 354, may require improvement of both the roof and lateral shielding of Linac4. It should be borne in mind that the PS operation also generates stray radiation in the hall, which adds to the contribution from Linac4. The roof shielding might need to provide a further attenuation of about a factor of 3 at 80 MeV and of about a factor of 10 at 160 MeV, which can be achieved by adding an additional 0.2 m and 0.6 m of concrete, respectively [83]. This issue will need specific attention at the time of the final shielding design, according to the foreseen occupation of the buildings in the future years. A combination of iron + concrete can also be considered in order to improve the attenuation properties of the roof without increasing its thickness.

Access labyrinths

Access to the accelerator will be granted via two labyrinths, one at its low-energy end and the other at its high-energy end. The design of the former requires 0.4 m thick concrete walls. The labyrinth at the high-energy end of the tunnel has five legs and it is designed to keep the dose rate behind the shielding below 3 μSv/h during operation under the assumption of a 10 W beam loss in front of the maze mouth (which corresponds to a dose rate exceeding 1 Sv/h inside the linac tunnel), and within the required limit in case of accident. The design of the labyrinth can possibly still be optimised in order to reduce its size. If the shielding were to be continued downstream of the labyrinth, the concrete wall should be 2.8 m thick. Table 5.4 gives the dimensions and the transmission factor (the ratio between the dose rate at the end and at the beginning of the leg) for each leg of the labyrinth. With this design the labyrinth is large enough to allow access of large objects (with length of up to 2 m) into the tunnel.

Table 5.4: Dimensions (L=length, W=width; height = 3 m) and attenuation factors of the five legs of the waveguide labyrinth at the high-energy end of Linac4

Leg		1st	2nd	3rd	4th	5th
Dimensions	L [m]	3.4	8.5	2.4	4.4	2.0
	W [m]	2.4	1.6	2.4	1.6	2.4
Transmission factor		0.33	0.007	0.09	0.03	0.1

Beam dump

A preliminary estimate has been made of a dump to be placed at the end of the linac and capable of absorbing the full beam for pulse lengths up to 100 μs, the length required for beam setting-up [84]. An interlock system will prevent from sending longer pulses to the dump. The inner core of the dump should be made of graphite and should be surrounded by an inert gas to avoid ignition. A more complete thermal study is required to assess the need of active cooling, but this will most likely be unavoidable. If the maximum beam allowed on the dump does not exceed 10% of the nominal beam, water cooling may not be necessary.

Beam transfer line

The shielding of the beam transfer line from Linac4 to the PSB will depend on beam losses during operation and on the classification of nearby areas (non-designated, supervised or controlled). In a first approximation losses are assumed to be uniformly distributed along the line. Independently from the previous parameters, the accident scenario sets a minimum value to the thickness of the shielding wall of 1.8 m, which guarantees a maximum integrated dose of 10 μSv if the beam is switched off within one second. Every 0.2 m reduction of the shield thickness would lead to an increase by a factor of 2.3 of the integrated dose. The integrated dose is also directly proportional to the time needed to stop the beam. With 2 Hz operation, a reaction time of 1 s is a realistic assumption. The above minimum thickness will still guarantee a maximum integral dose of 100 μSv in case, for any reason, the accelerator is switched off in 10 s rather than in 1 s.

Under the assumption of a continuous loss uniformly distributed along the transfer line, the shield thickness for 160 MeV protons as a function of the dose rate limits given in Table 5.1 and of the intensity of the beam loss (1 W/m, 0.1 W/m or 0.05 W/m) is given by the expression:

$$t = 23.406 \ln\left(\frac{0.05265P}{H_{\text{lim}}}\right) \tag{5.2}$$

where t is the shield thickness (cm), H_{lim} is the dose rate limit (Sv/h) and P is the beam loss (W/m). The minimum wall thickness required for shielding a non-designated, supervised or controlled area are given in Table 5.5. It must be underlined that here no extra-λ, i.e. no additional safety factor, has been added, as in principle the operation of a beam transfer line is much less subject to uncertainties than the operation of an accelerator.

Induced radioactivity and dose rates

Preliminary Monte Carlo simulations were performed to obtain a first idea of the induced radioactivity to be expected in the accelerator structures and in the tunnel walls [82]. The induced radioactivity in magnets, beam pipes, water and concrete was calculated for point losses of 10 W at 160 MeV and, for quadrupoles only, of 1 W at 40 MeV. It was assumed that 10 W of protons at 160 MeV (i.e., 3.9×10^{11} protons per second) are lost every ten metres.

Table 5.5: Thickness of the concrete shield required around the beam transfer line for different loss scenarios

Beam loss [W/m]	**1**	**0.1**	**0.05**
Shielding thickness for			
Non designated area [m]	2.7	2.2	2.0
Supervised area [m]	2.3	1.8* (1.75)	1.8* (1.60)
Controlled area [m]	2.0	1.8* (1.5)	1.8* (1.3)

* Minimum thickness determined by the accident scenario (full loss, 4.8 kW beam power). If the shielding requirements for the accident scenario are changed, the shield should not be thinner than the value indicated in brackets.

The estimation of the induced radioactivity in the accelerator components is particularly important for maintenance interventions (e.g., dose planning) and final disposal of radioactive waste. The highest levels of radioactivity are obviously expected in the elements that are directly hit by the beam. The produced radioactive nuclides depend on the exact chemical compositions of the irradiated materials, which are not known at the present state of the project. To obtain a preliminary estimate of the dose rate in the high-energy part of the accelerator, two sets of simulations were run with a 160 MeV beam hitting a 0.125 m^3 target of copper and iron. The inventory of radioactive nuclides obtained with FLUKA was used to calculate the ambient dose equivalent rate, H*(10), at one metre distance from an irradiated element. Figure 5.2 shows values of H*(10) after 7 month irradiation and different waiting times, assuming a point loss of 10 W with 160 MeV proton energy.

Due to the relatively high dose rate expected in the tunnel, maintenance must be carefully planned, especially near the magnets in the SCL section of the linac. All elements of the SCL section that are directly exposed to the beam halo will have to be disposed of as radioactive waste at the moment of decommissioning.

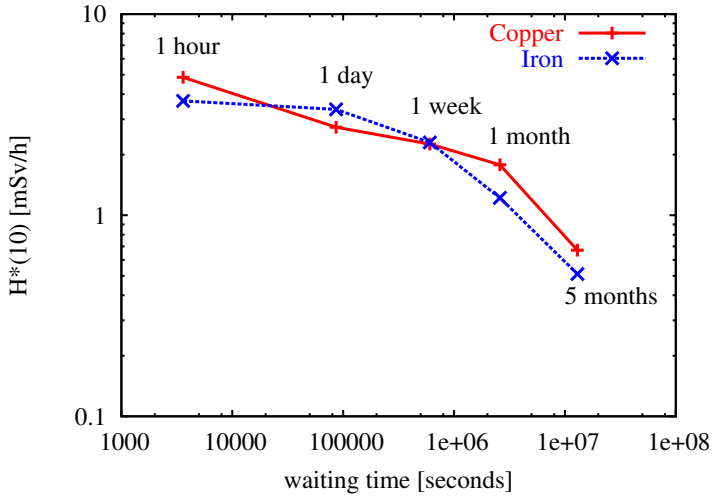

Figure 5.2: Ambient dose equivalent rate at one metre distance from irradiated elements (copper and iron). Values refer to 160 MeV protons, 10 W beam loss and 7 month continuous irradiation.

Further studies

The impact of a large technical gallery running under the South Hall and of various ducts traversing the hall floor on radiation streaming have not yet been assessed. For the final shielding design the radiation streaming through the various passages must be determined by Monte Carlo simulations and proper

countermeasures will have to be taken. The design of the labyrinth can possibly still be optimised. In particular, if access of equipment can be made at the low-energy end of the linac tunnel, the labyrinth at the high-energy end will only be used as emergency exit and can probably be reduced in size.

The design of the dump at the end of the linac and of the additional shielding which may be required will depend on the maximum beam intensity which will be allowed to be dumped. A detailed study is required.

Injection of the H^- beam into the PS booster by charge-exchange will create four neutral beams (due to non-fully stripped H^- ions at injection into the four booster rings) which will have to be absorbed by dumps located in the booster hall. Due to the energy (160 MeV) and power (≤ 25 W) of the neutral beams, apart from the dump themselves the magnets and the shielding wall surrounding the dumps will become radioactive if the dumps are not properly shielded. FLUKA simulations have provided a preliminary estimate of the induced radioactivity and the dose rate to be expected during maintenance in the vicinity of the dumps. The results show that maintenance interventions should be carefully planned even several months after ceasing operation. A possible solution to mitigate the problem is to install the dumps inside the shielding wall, in order to properly shield the secondary radiation and minimise activation of nearby equipment of the booster.

A more detailed assessment of the induced radioactivity in accelerator structures and surrounding equipment and walls is needed, in order to properly plan maintenance interventions. A complete radionuclide inventory will have to be established before decommissioning, in order to decide on disposal pathways. The activation induced in air during accelerator operation must also be assessed. The ventilation system must be designed in such a way to avoid release of radioactive air in the South Hall. The air vented in the atmosphere must be monitored as done for all releases from CERN beam areas.

5.2 Access control

Linac4 will be equipped with standard access control system (PACS, PS Access Control System), in order to ensure personal and equipment protection (PASS, PS Access Safety System). A general overview of the access control and machine interlock safety systems is given here, while the precise layout will be defined once the project is completely defined.

The Linac4 infrastructure will be considered as a primary beam area. For access control (PACS) it is proposed to use the same equipment as for LHC access control, i.e.:

- a SAS personal traffic (MAD),
- a SAS material traffic (PAD),
- a cards reader (Milfer) and a biometric reader,
- a keys distributor,
- a panel signalling the access mode,
- an audio and video supervision equipment,
- a fire door exit, and
- two doors technical gallery.

The personal protection (PASS) is ensured by a PLC (MIS). In access mode, a VETO signal hampers any activation of the specific machine equipment called (ISC), in particular:

- beam stopper,
- source,
- HT modulators,
- RF modulators,
- etc.

5.3 General safety

Safety concepts will be integrated into the Linac4 layout from the design stage. The main potential risks concerning the Linac4 environment are:

- ionising radiation,
- electrical risks,
- isolation of workers in the linac tunnel.

Other usual risks are absent in the case of Linac4, as no cryogenic liquids will be used, no gases (flammable or not) are present in the machine tunnel or in the South Hall, no lasers are used, and finally no combustible materials are present.

The strategy for protection against ionising radiation is extensively discussed in Section 5.1. Electrical risks are mainly related to standard HV supplies, which will be treated applying the usual safety procedures. An additional concern is given by the presence of many MW of installed RF power, however the very low duty cycle (0.1%) allowed by the power supplies will prevent reaching the threshold for personnel hazard even in case of a serious RF accident. The long (100 m) linac tunnel will have two access doors, at either end, to allow safe evacuation in case of an accident in a linac section. The tunnel will be equipped with standard fire detectors.

One or two beam stoppers at low energy (between source and RFQ) and a bending magnet in the transfer line will be part of the Linac4 safety chain. In case of an access to the PS, two elements will prevent the linac beam from being sent to the PS area.

5.4 Machine and personnel protection

The machine (MPS) and personnel protection system (PPS) will follow the established CERN safety rules.

The fastest element to switch off the beam is the H^- ion source. However, stops of several minutes or hours will destabilise the source and long start-up times may be required for a re-start. The down-time of the source can be reduced to 1–2 s if a beam stopper is used in the LEBT, which needs approximately 1 s to be inserted into the beam line. In order to have a redundant safety system, a second beam stopper should be foreseen in the LEBT. In addition, a watchdog programme for machine protection will read the values of the beam transformers and will switch off the source in case of abnormal beam loss between two subsequent transformers.

The area downstream of the linac will be protected by switching off the first bending magnet in the transfer line. At the same time a beam stopper will be inserted in the transfer line while the beam is collected in the dump at the end of the linac.

Chapter 6

Civil engineering and infrastructure

6.1 Layout

The main criteria for selecting the Linac4 location were as follows:

- installation of Linac4 close to the injection point into the PS Booster,
- design allowing for possible later dismantlement and re-installation as front-end of the future Superconducting Proton Linac (SPL),
- maximum use of existing buildings and infrastructure in the PS area.

Three solutions satisfying the above criteria have been identified:

1. Installation of Linac4 in buildings 150 and 152 (PS "South Hall"): this implies the conversion and rehabilitation of these buildings which are currently used for storage and the construction with concrete blocks of a bunker enclosing the machine inside the hall. The connection with the present Linac2 line is made via the PS tunnel.
2. Installation of Linac4 in a dedicated underground tunnel to be built underneath the "Mont Citron" (area between building 363, the present Linac2 location, and the Rutherford Road): this solution implies the construction of a new tunnel and of a surface equipment building. The new tunnel could be easily connected to the last section of Linac2.
3. Installation of Linac4 in the Linac2 tunnel, extended towards the low-energy side: this implies the construction of an extension for about 40 m to the low-energy end of the Linac2 tunnel to reach the length required by the Linac4 machine plus a new equipment building on the surface.

Solution 1 ("South Hall") retains the largest potential for an economic construction and for an easy dismantling of the linac in case it has to be moved to the SPL location. However, the connection to the existing Linac2 to PSB line can be done only through the PS tunnel, for a length of about 100 m. This solution has been proposed since the start of the project and is extensively analysed in the following sections. For the moment, it is considered as the nominal solution, to which the other options have to be compared for cost and benefits.

Solution 2 is potentially expensive, but presents the advantage that the induced radioactivity from the linac has the minimum impact on existing buildings and offices. Connection to the existing Linac2 transfer line is easy and full commissioning of Linac4 is possible while Linac2 is operating.

Solution 3 has been proposed more recently, and is described in some detail at the end of this section. New construction is limited and connexion to the existing transfer line is straightforward. However, the upgrade of the existing Linac2 shielding is a concern, and the need to combine the dismantling of Linac2 with the installation and commissioning of the high-energy part of Linac4 during a shut-down period would require a challenging and very precise planning.

For the needs of the present report, the nominal solution is analysed in detail, and an overview of the third solution is presented for completeness. The final decision on the Linac4 location will depend on many factors and will be taken at the official start of the project.

Linac4 layout in the PS South Hall

Buildings 150 and 152 would have to be converted to house the Linac4 machine components and auxiliary equipment (klystrons, electronic racks, etc.). Building 150, one of CERN's oldest buildings, already contains the LEIR machine. An extension (building 152) was built in 1960. An area about 100 m long

is available for the new Linac, located between the end of building 152 and the LEIR shielding in building 150. The floor area available is approximately 2000 m^2 in building 150 and 1100 m^2 in building 152. These buildings are currently used for storing items such as the RF components recovered from the LEP machine that will be used for Linac4.

Figure 6.1 shows a schematic view of the planned layout of the various components of Linac4 in buildings 150 and 152.

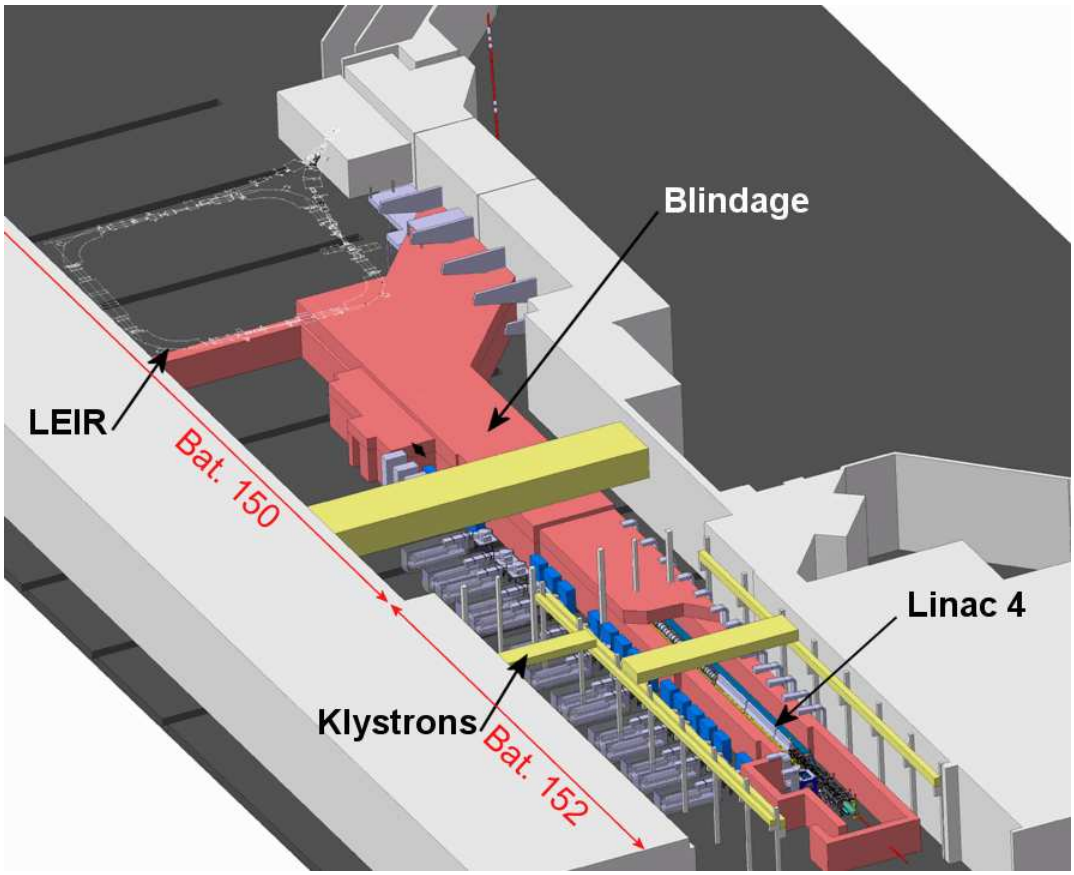

Figure 6.1: Linac4 layout in the PS South Hall (shielding on top of the low-energy part removed to show position of the machine)

Linac4 would start at the entrance of hall 152 and run up to the LEIR shielding wall. This would be the starting point for a transfer line that would penetrate the PS shielding and run into the PS tunnel, following the latter for a few metres before crossing over into the LEIR tunnel via a new underground connection structure. It would then carry on until connecting with the Linac2 transfer line at the PS booster.

The Linac4 shielding would be a stack of pre-cast concrete blocks, whose thickness is determined by radiation protection. This shielding design allows for an easy installation and maintenance of the linac and transfer line components by the simple removal of blocks and, in case Linac4 becomes the front-end of the SPL at another location, the dismantlement of the whole structure.

The klystrons and their electrical power supplies would be positioned on the ground, parallel to the machine and connected to it by waveguides passing over to the opposite side of the shielding. Figure 6.2 shows the positioning of the klystrons and the power supplies for the RF structures.

Buildings 150 and 152 are equipped with travelling cranes, and this is an advantage for the transfer line and shielding assembly as well as for subsequent maintenance operations.

The modifications to buildings 150 and 152 would be minimal, consisting essentially of:

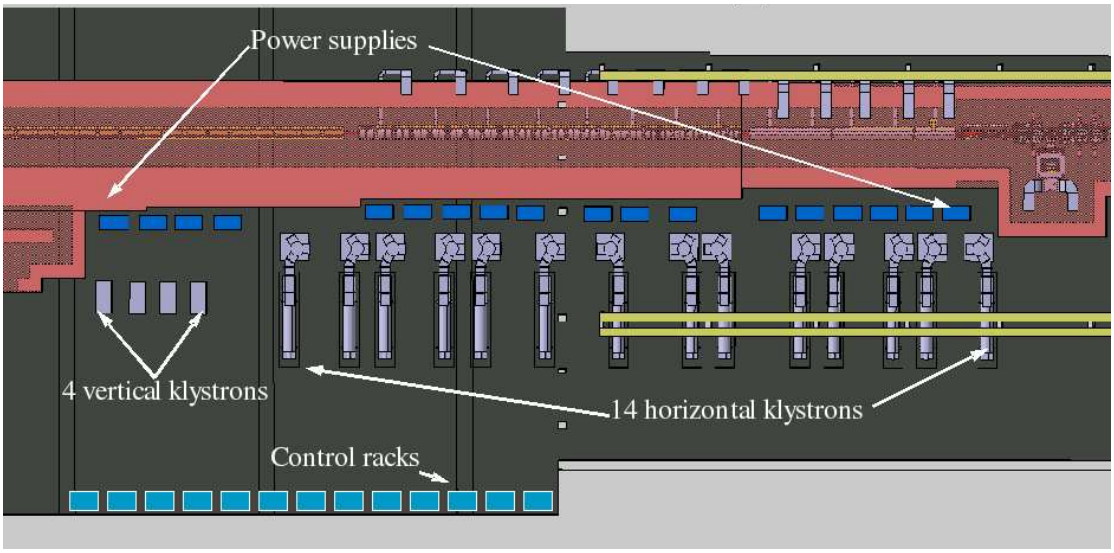

Figure 6.2: View of the hall with position of Linac4 and of the RF klystrons

- a new passage through to building 355 for the removal of PS equipment. Since Linac4 will block the current PS exit through building 152, a new passage will have to be built in building 355, as shown (orange) in Fig. 6.3. The precise details of this intervention will be worked out later, but it might be necessary to cut through some of the roof girders and to reinforce the slab. In this case, the passageway would be somewhat smaller than at present, but it would still be large enough to allow passage for the material that is usually brought into the PS through this access door.
- a passage through the wall between buildings 150 and 152 for the installation of the shielding (red on Fig. 6.3);
- a modification of the travelling crane in building 150; the crane's control booth will have to be dismantled, as it interferes with the shielding in the high-energy part of the linac. Indeed to allow for the handling of the concrete blocks, it will be necessary to reduce the total height of the shielding in the operating area of the travelling crane by some 0.5 m, from the nominal height of 3 m. This reduction can be envisaged by replacing part of the concrete shielding with iron plates.
- filling of the trenches in the area covered by the linac to satisfy radiation protection requirements. It is proposed to fill the trenches with sand so that when Linac4 is dismantled, they can be recovered in their present condition;
- a modification of the technical gallery under the wall separating buildings 150 and 152 (in blue on Fig. 6.2). An in-depth radiation protection study will have to be performed on this gallery, which passes underneath Linac4. It will likely have to be completely shut down and interlocked when the machine is operating.

In addition to these alterations, it will be necessary to provide for the evacuation of all materials stored in building 150, the dismantlement of the steel platforms and the removal of all offices in building 152. When these operations are realised, it will be necessary to take account of the presence of asbestos in certain premises and facilities to be dismantled.

Moreover, given the age of buildings 150 and 152 (built in 1956 and 1960 respectively), it will probably be necessary to schedule some infrastructure consolidation work. This could relate to the roof, the travelling cranes and a general re-painting of the buildings.

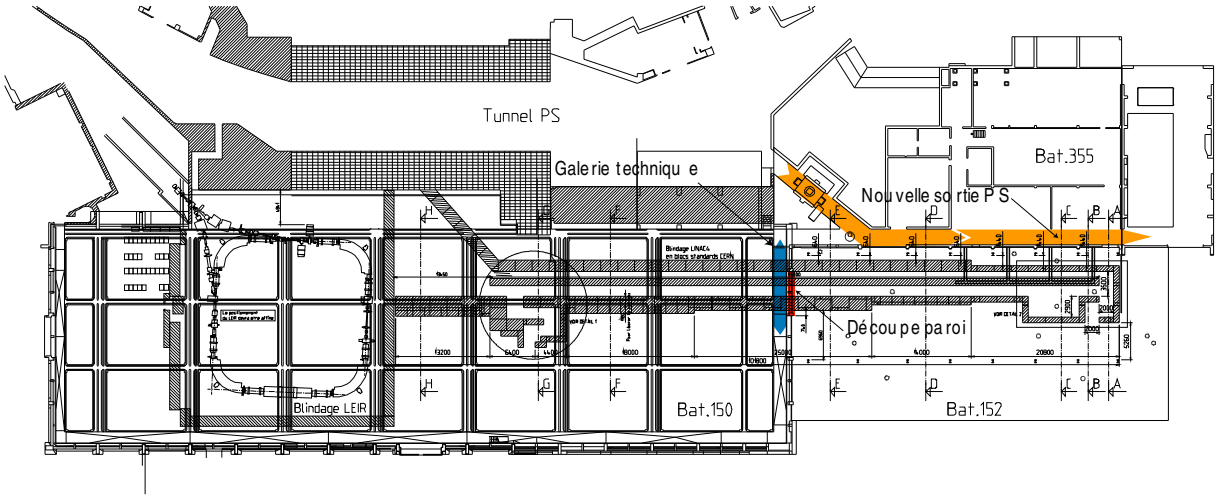

Figure 6.3: Layout of buildings 150 and 152

Transfer line

At the location of the LEIR shielding wall, part of the PS shielding wall will have to be dismantled to allow passage of the Linac4 transfer line (Fig. 6.4). After passing through the wall and continuing along the PS tunnel, the transfer line will cross over the space separating the PS from the LEIR injection line tunnel and will finally be connected to the line from Linac2 to the PS booster.

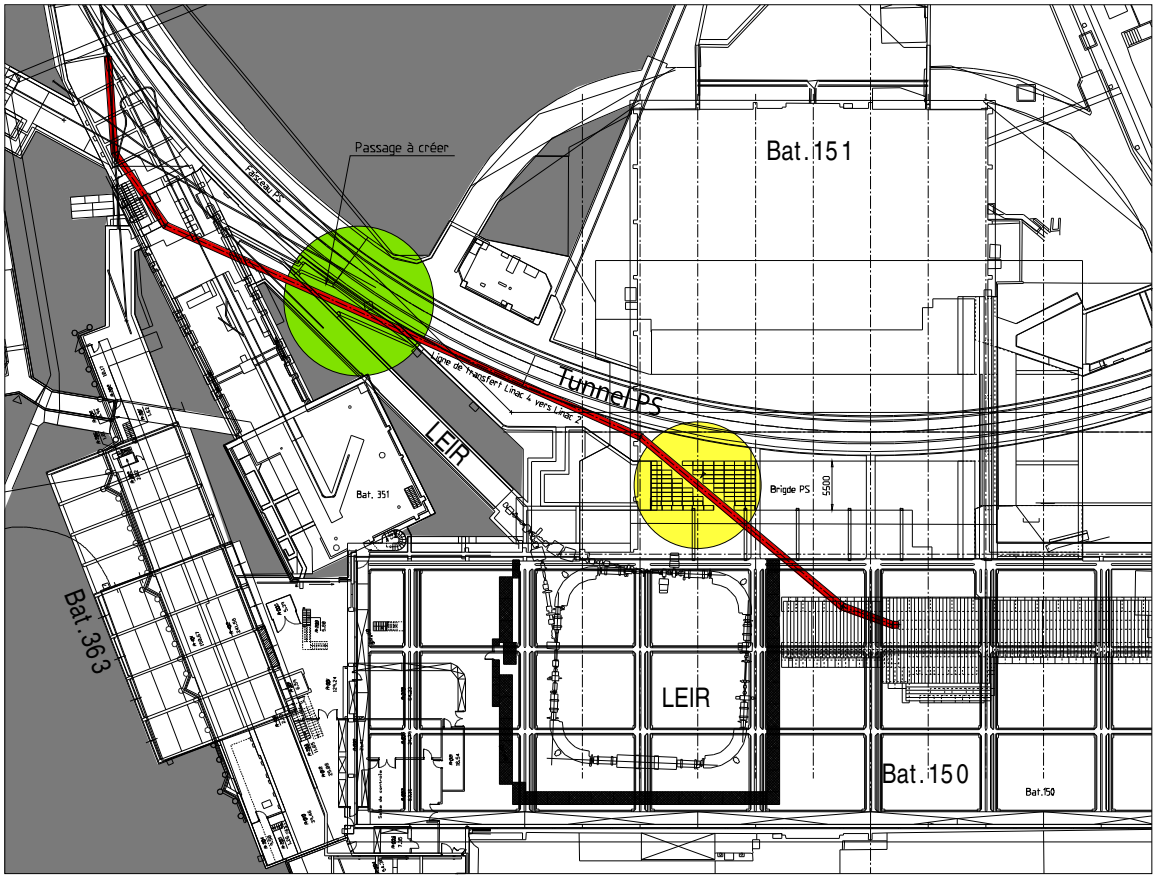

Figure 6.4: Transfer line Linac4 – PS Booster

From the civil engineering point of view, apart from making a few holes in the concrete walls, which will be studied at a later date, the only large-scale structure required would be the connection between the PS and the LEIR tunnel (green in Fig. 6.4). The connecting section would be approximately 15 m long, 3 m wide and 2.5 m high, built from the ground up-wards to reduce any impact on the line equipment in the vicinity of the PS and LEIR (in green on Fig. 6.5) to a minimum. An open-air excavation, with shoring, is foreseen.

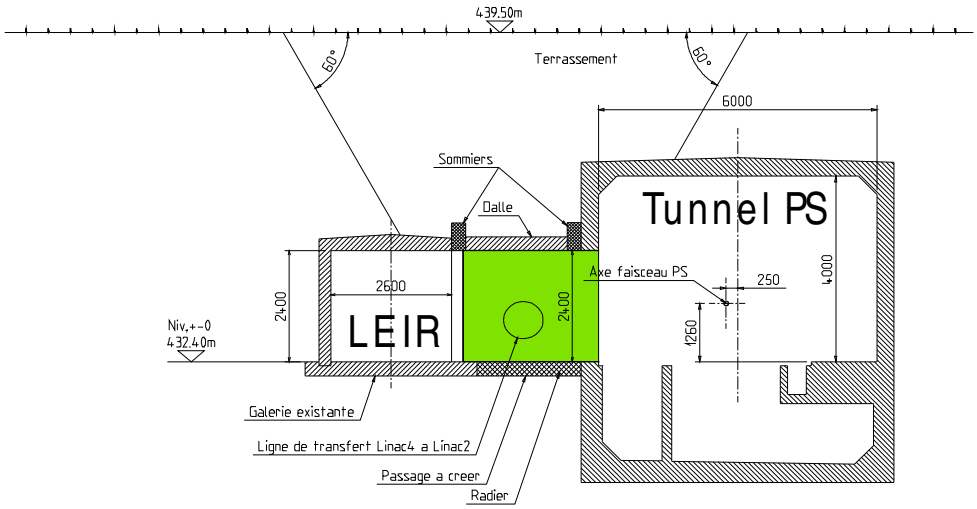

Figure 6.5: Connecting structure between the PS and LEIR

Linac4 in a extended Linac2 building

The alternative solution, which is still under consideration, is shown in Fig. 6.6. It consists in building an approximate 40 m long extension to the Linac2 tunnel in the direction of the Bloch Road, and in the construction of a new surface building approximately 15 m wide, 15 m long and 4 m high, connected to the existing building 363.

Once these structures have been built, the low-energy part of Linac4 could be installed and tested in the tunnel extension and the klystrons housed in the new building, so as not to disturb the operation of Linac2. The machine components of the Linac2 would then be completely dismantled and replaced by those of the high-energy part of the Linac4 during one of the Linac2 annual shut-downs.

This alternative solution is presently being studied from the radio-protection point of view. If it is confirmed that the Linac2 shielding can be upgraded to the Linac4 requirements, this solution would allow the Linac2 and the present transfer line to be effectively reused.

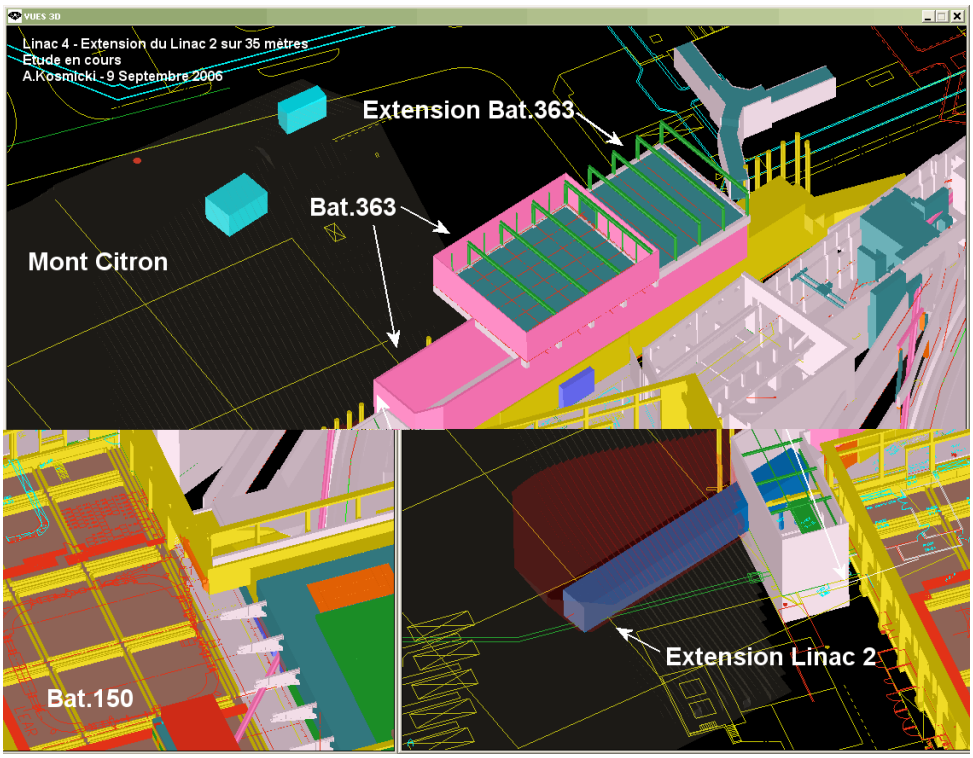

Figure 6.6: Building layout for the alternative solution - Linac2 extension

6.2 Electrical infrastructure

The existing electrical infrastructure in the South Hall (building 150 and 152) is more than 30 years old and does not comply anymore with current technical standards and safety regulations. A certain quantity of oil-filled low-voltage cables is still present in the cable galleries and ducts of the hall, representing a considerable risk in case of fire. General services installations in the hall have also reached the end of their lifetime.

For the Linac4 project it is therefore required a dismantling of the existing electrical installations in the South Hall, including a thorough cable dismantling campaign in the existing galleries.

As for the general services covering the electrical infrastructure of the South Hall, which mainly consists of lighting and power socket boxes, a detailed study for the renovation will be required, but most likely the total power consumption remains similar to the existing installations.

For Linac4, the power estimation obtained adding up the foreseen consumption from the different equipment and then applying a reasonable safety margin comes to about 1.1 MVA. Together with the 3 MeV test stand in the South Hall extension, the power consumption will not exceed 1.6 MVA. The following technical design proposal is valid for a maximum power consumption of up to 1.6 MVA for the total of Linac4 and the 3 MeV installation.

High voltage installations

Based on a total load of 1.6 MVA, one single transformer 18/0.4 kV 2 MVA will supply the Linac4, including its 3 MeV Front-end. The power distribution system will have a thermal rating of 2 MVA. The transformer will be of the cast-resin type and will thus be suitable for indoor installation.

The transformer 18/0.4 kV 2 MVA will be supplied from the Meyrin 18 kV distribution network, most likely from the existing ME6 substation which is also supplying the PS machine.

Alternatively, an extension of the 18 kV substation ME7 in building 250 could be taken into con-

sideration. Currently, there is no space available for the extension of an existing HV switchboard. An extension of the HV switchboard would be possible, if an existing steel support for the building structure could be moved to another place. Obviously, the implications for building stability and civil engineering need to be investigated.

The supply of Linac4 via one single transformer would facilitate the localised switch-off of the entire machine in case of emergency (equipment stop), via red buttons installed close to the equipment. The equipment stop system is not part of a regular test program of TS-EL.

In addition, the zone will be integrated into the standard CERN emergency stop system which cuts all sources of energy entering the South Hall building. In case of emergency stop operation all electricity sources of the South Hall will be switched off, including general services and Un-interruptible Power Supply (UPS) circuits, as well as the machine networks for LEIR, PS and Linac4. The emergency stop system is annually tested by TS-EL.

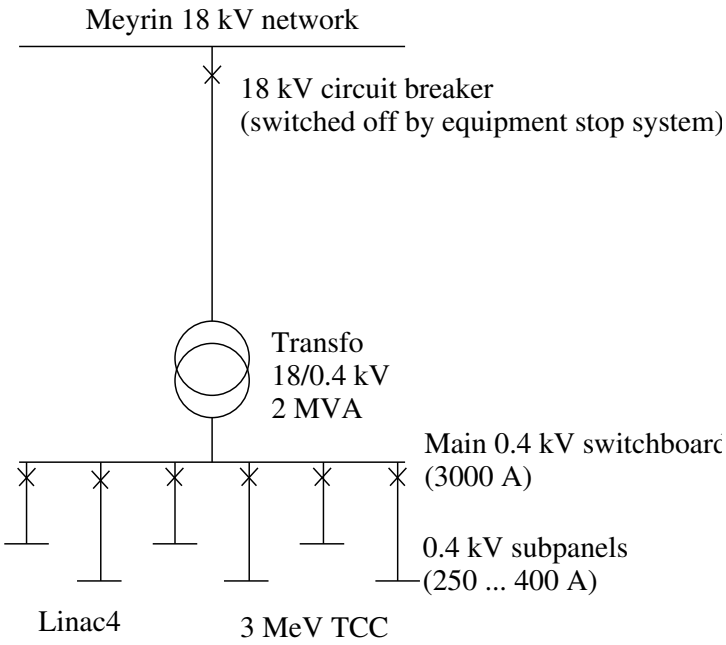

Figure 6.7: General concept for the electricity distribution for Linac4

Low voltage installations

On the low-voltage (LV) side of the 18/0.4 kV transformer there will be a major LV switchboard 3000 A. From there, several smaller sub-panels will be supplied, which should be installed in the vicinity of individual machine sub-systems or 19" racks of the individual users. The sub-panels have ratings between 250 A and 400 A.

To connect the linac and the 3 MeV front-end to the same transformer, the feeding cables for the existing switchboards supplying the 3 MeV Test Stand should then be transferred to the 3000 A switchboard.

To facilitate the high-voltage and low-voltage cabling close to the HV and LV switchboards, a false floor would be installed in this zone. From there, several parallel cable ladders will be required which could be either wall-mounted or be installed on supports fixed on the floor.

Most likely, the supply of uninterrupted power is required for the machine controls as well as for safety critical systems. The existing UPS system of the ME6 substation has ample power reserves but the renovation of the EOD switchboard is essential for this project.

To simplify the cabling, the transformer should preferably be installed indoors, in the vicinity of the main LV switchboard. The electrical installations ideally require a separate room, greatly limiting the risk in case of fire. The space required in the main LV switchboard and the transformer will be about 15 m × 6 m. Additional space will be required in the South Hall for cable ladders and a number of smaller switchboards and racks.

6.3 Cooling and ventilation

Water cooling

The cooling system for Linac4 will be connected to existing demineralised water cooling stations. The loads located in the South Hall will be connected to the ED-52 station whereas the "centre anneau" station will provide the cooling in the PS tunnel.

In spite of the available cooling power of the ED-52 station, the existing demineralised water pumps will not be able to provide Linac4 with the requested water flow rate. The motor-pump sets and their frequency converters will have to be replaced.

Due to the constraining temperature regulation requirements, a new dedicated station is foreseen for the RFQ cooling and will be built already for the 3 MeV Test Stand. This station will provide demineralised water with an adjustable set point and an accurate temperature control (±0.2 K).

The tables below summarise the cooling needs and the parameters defining the circuits.

Table 6.1: Water cooling needs for Linac4

Circuit	**Fluid**	**Power** [kW]	ΔP_{max} [bar]	**Flow rate** [m³/h]
South Hall	Demineralised water	250	15	65
PS tunnel	Demineralised water	10	15	3

Table 6.2: Cooling needs for RFQ

Item	**Fluid**	**Power** [kW]	**Temperature range**	**Accuracy** [°K]
IPHI RFQ	Demineralised water	2	20°C -35°C	0.2

Air-conditioning (HVAC)

Four new AHUs will be distributed along the tunnel. Air conditioning will be in closed circuit, i.e., air is extracted from and returned back to the tunnel without any intake of fresh air. Two openings per ventilation units through the shielding are required for the passage of the ducts (supply and return).

Two additional AHUs will be installed for the supply and extraction of fresh air in the tunnel. The air supply AHU will be fitted with a chilled water coil and an electrical heater in order to blow the air at the desired temperature. The extraction system will also serve as cold smoke extraction.

All the AHUs will be located outside the tunnel in the South Hall.

No control of humidity or specific filtration is required. There are no particular radiation risks, therefore the AHU will be of the industrial type. Neither absolute filters, specific radiation modes, nor pressure control will be considered in the design of the HVAC system.

Certain pieces of equipment requiring a stable room temperature, in particular the low-level RF system, will need to be housed in an appropriate new enclosure provided with a dedicated air conditioning system.

The existing ventilation systems of the South hall and the PS tunnel will remain unchanged.

The table below summarises the cooling needs and the parameters defining the HVAC systems.

Table 6.3: Indoor conditions and internal loads

Building	**Winter** [°C]	**Summer** [°C]	**Load** [kW]	**Remarks**
Tunnel	26°C ±1	26°C ±1	30	Including external heat transfer
Control room	22°C ±1	24°C ±1	20	
South Hall	17°C ±2	*	100[1]	*No air conditioning. The temperature depends on the outside conditions and can exceed 32°C
PS tunnel	20°C ±2	20°C ±2	20	

[1] loads in addition to those existing in the building

Chapter 7

Commissioning and planning

7.1 The 3 MeV test stand

The technology and the beam dynamics issues at the low-energy end are critical for the performance of Linac4, especially in its potential role of first part of a high-intensity high-energy linac (SPL). The halo formation mechanism has to be accurately studied and the techniques for chopping the beam with the appropriate time structure have to be validated. For all these reasons, and with the aim of developing the most critical components of the first part of the Linac4, a 3 MeV test stand has been proposed and its realisation is presently under way.

It consists of the initial 15 metres of the Linac4 accelerator, followed by a diagnostic line that is partly specifically developed for this test stand and partly borrowed from the IPHI experiment at Saclay (see also Section 2.2).

Layout

The 3 MeV test stand layout has been defined in view of the future installation of the Linac4 in the PS South Hall, in such a way that the linac can be built as continuation of the test stand beam line. This choice will minimise the modifications needed for the installation of the rest of the machine and will provide the opportunity to study from the beginning issues like the alignment strategy, whose solution will be implemented as it is on the new accelerator. A 3D drawing of the different components in the 3 MeV test stand is shown in Fig. 7.1.

The source, LEBT, RFQ and chopper line that will be installed in the 3 MeV test stand have been already described in Chapter 2. A LEP klystron will be installed, fed by a prototype power supply.

The diagnostics line has been developed to completely characterise the beam at the chopper line output. It will include the BSHM (Beam Shape and Halo Monitor) described in Chapter 5 and part of the IPHI measurement line [85], which is used for energy and energy spread measurements and for characterising the beam emittance at the output of the chopper line. Energy and energy spread will be measured with the IPHI spectrometer, consisting of a dipole magnet and of two slits, the image slit that is installed in the straight part of the line and the object slit that is at the dipole output, in the bent part of the line. A time of flight energy measurement is also possible since dedicated pick-up probes have been foreseen in the line, with 10^{-3} accuracy in beam energy measurement. The transverse beam emittance is measured by means of a wire scanner that acquires the beam profiles and by changing the field intensity of the upstream quadrupoles.

The IPHI line is also equipped with six beam position monitors and with beam current monitors.

Measurement programme

The purpose of the test stand is threefold. The primary goal is to validate the whole 3 MeV injector, including the chopper system, the second is to study the beam dynamics in the line and verify the simulation codes, and the third is to measure the real beam parameters at 3 MeV so that the design of the downstream accelerator can be optimised. After a series of "routine" measurements (transmission, energy and energy spread) during setting up, the measurements will concentrate on characterising the chopper and the matching to the DTL.

The chopper system is composed of three elements: the chopper itself, which provides a transverse kick to the beam; the quadrupole after the chopper structure, which magnifies the kick; and the dump which collects the deviated beam. Each component will be tested individually. The effective kick received by the beam will be measured on a screen downstream, with a pencil beam and the quadrupole

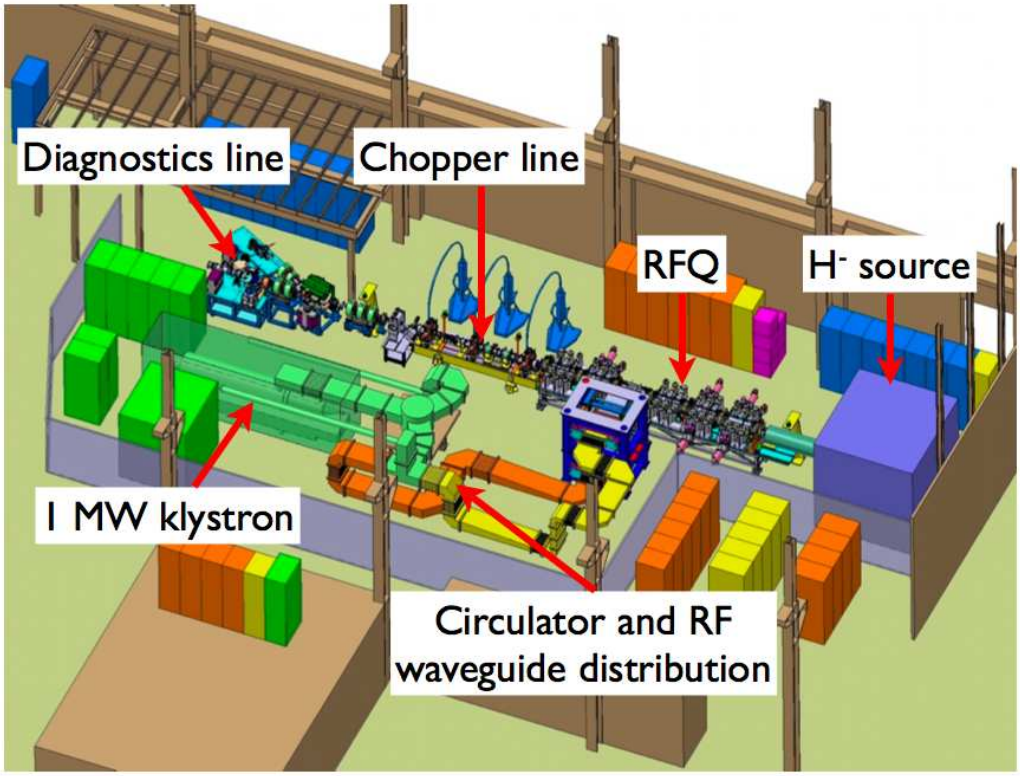

Figure 7.1: Layout of the 3 MeV test stand

switched off. Two spots will be observed, corresponding to the main and the chopped beams. In the absence of quadrupole, the distance between them is proportional to the effective chopper voltage. The current in the quadrupole will then be progressively increased until the second spot on the screen disappears; in this condition one can be sure that the centre of the chopped beam is on the dump and that the main beam goes through the line. The rise and fall times of the chopper will then be estimated with the BSHM, both for the pencil beam and for the full beam. At the end of that series of measurements, the chopper line itself as well as all its components will be fully characterised.

The transverse emittance will be estimated from a series of profile measurements at varying quadrupole strength and the longitudinal emittance will be derived from energy spread measurements at varying buncher voltages. This method should be carefully applied in the presence of space charge. In our case [86], we can achieve accuracy of the order of 10%. This method will also provide a good estimate of the flexibility of the line to meet different requirements for matching at the entrance of the next accelerator. After having assessed the envelope properties of the beam, the 2D readout system of the BSHM will be used to study the halo. The halo will be measured (shape and intensity) for various settings of the source, the RFQ and the line, and the results will be compared to simulations. Finally these parameters will be used to optimise the performance of the collimation system.

Test stand schedule

The preparation of the test stand started already in 2004 and has progressed very slowly because of the limited amount of resources available during the LHC construction. The first two years were spent integrating the different contributions into a single coherent project and defining the standards to be used.

In 2006 the technical infrastructure has been designed and installation has started. The main components of the beam line are now designed and most of them built. The greatest contribution is expected from the IPHI collaboration, that is building the 3 MeV RFQ. Some delay has been accumulated in this respect, however it is still expected that the RFQ will be assembled in Saclay during 2007. The overall test stand project schedule is presented in Fig. 7.2.

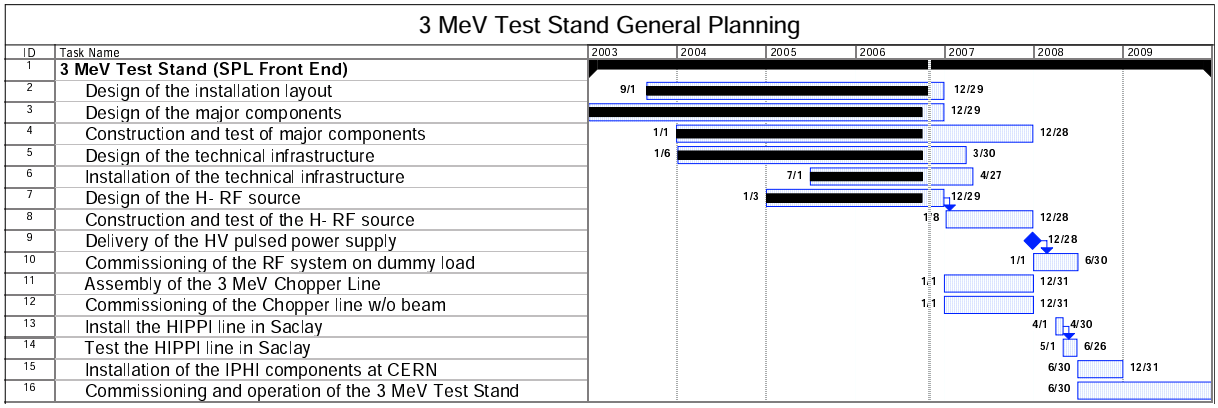

Figure 7.2: Schedule of the 3 MeV test stand

7.2 Commissioning strategy

The commissioning of Linac4 will be done in steps, in order to find for subsequent sections of the machine a table of parameter settings that allows to run the machine with maximum transmission while complying with all safety requirements. During each of the commissioning steps the beam current intensity will be slowly increased up to the source design value of 80 mA.

The commissioning of the low-energy front-end (source, RFQ and chopper line) will take place at a very preliminary stage, in order to leave enough time for optimising the performance of this section, considered as the most critical of the entire linac, and also to modify the design parameters of subsequent elements, on the basis of actual beam measurements out of the front-end.

For the accelerating sections, a removable measurement bench will be installed at the end of each section in order to measure beam parameters. It is foreseen to commission the structures in the following sequence:

1. DTL tank 1,
2. DTL tanks 2 and 3,
3. CCDTL (8 modules), and
4. SCL (4 modules).

While for the DTL commissioning the measurement bench will be used, it is not yet decided whether CCDTL commissioning will be done with the temporary bench or transporting the beam up to the measurement line at the end of the linac. The commissioning of the SCL section will be done using the final measurement line at the linac end.

For each section, after setting the quadrupoles at their nominal values, a low-current beam will be used to find amplitude and phase for the different accelerating modules. It is foreseen to use the phase scan technique, which has been already successfully applied to the three DTL tanks of Linac2, and more recently for the commissioning of the SNS linear accelerator [87]. For each of the accelerating units, the phase and amplitudes are slowly varied and the resulting beam energy evolution is compared to theoretical curves. Fitting of the measured values to the theoretical curves allows finding the nominal

amplitude and phase within the required 1% and 1° accuracy. At a later stage, the quadrupole settings have to be optimised, aiming at maximum transmission and minimum emittance growth. Finally, the current can be ramped up to the nominal value, probably requiring, at least for the low-energy sections, a repetition of the entire parameter optimisation process for the increased space charge.

In particular for the DTL section, where the focusing is provided by permanent quadrupoles, a measurement of the Twiss parameters has to be done as precisely as possible in order to minimise the mismatch at the transition to the CCDTL.

For the commissioning of the long transfer line between Linac4 and PSB, the beam parameters (energy, energy spread and transverse emittance) will be measured in the existing measurement line at the PSB entrance (LBE and LBS), which has to be upgraded for 160 MeV energy. Transporting a low-current beam up to the measurement line will be the first goal, followed by a long optimisation process, mainly to centre the beam inside the large vacuum chamber and then to optimise the quadrupole settings in order to minimise emittance growth. The optimum setting of the two debunching cavities will also need to be defined, relying upon the energy spread measurements at the PSB entrance.

7.3 Tentative project schedule

A tentative schedule for the Linac4 project is presented in Fig. 7.3. The overall duration of the project will be four years. The construction of the accelerating structures will take place during three years, the first one for preparation of execution drawings and for defining the construction strategy, and the rest for the actual fabrication of the accelerator components. In this scheme, based on an early construction of the first DTL tank, commissioning of the first DTL unit will take place already during the first year, while commissioning of the other accelerator elements will cover the whole of the fourth year. Beam commissioning in the PSB will require a long shut-down at the end of the fourth project year.

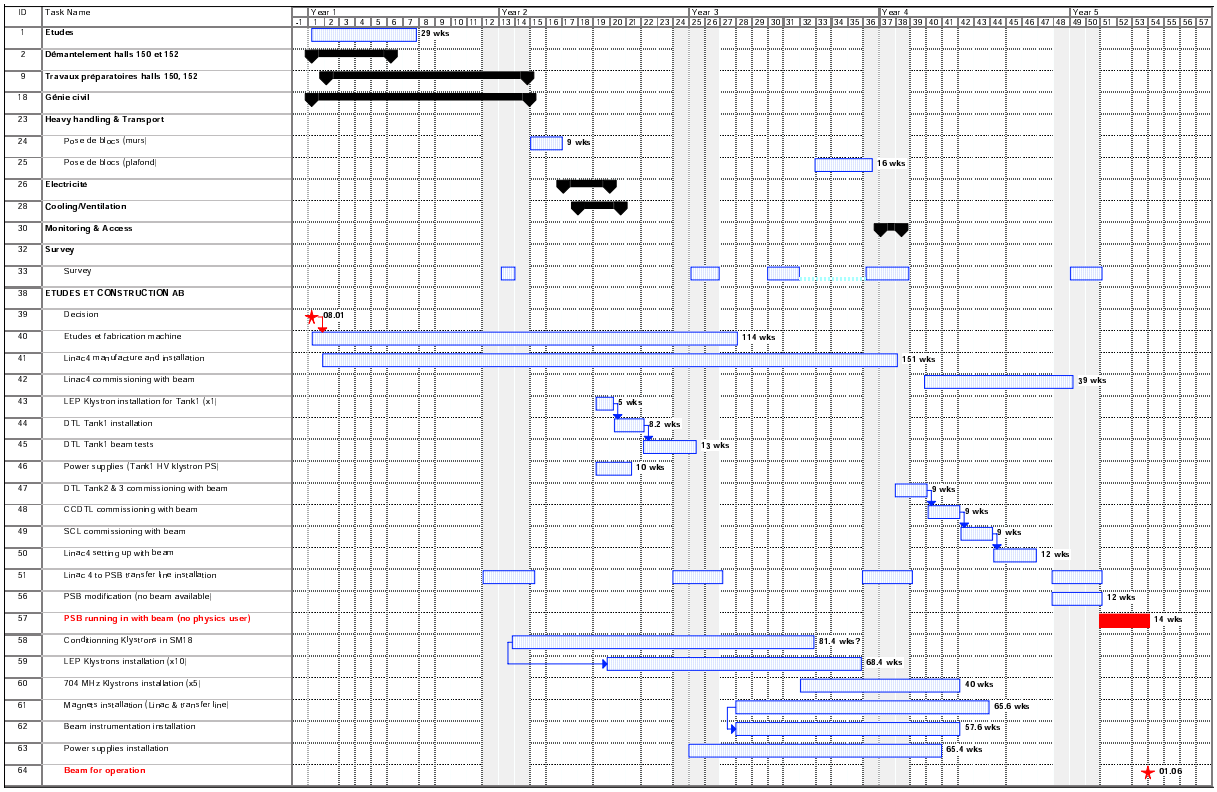

Figure 7.3: Tentative Linac4 construction, installation and commissioning schedule

Acknowledgements

The SPL Study Group has provided the fertile scientific ground on which the Linac4 project has developed, and we are deeply indebted to the many people who, over the years, have contributed to the SPL work.

The preparation of this report has received much support from many collaborators from CERN, and from outside. All fifty authors contributed portions of the text or fundamental calculations, which relied on many more specialists for information. We wish to express thanks to all of them on behalf of the authors. A particular thanks goes to D. Uriot (CEA) and F. Jones (TRIUMF) for having provided essential software for the Linac4 simulations and to H. Schönauer for many stimulating discussions.

Many teams from outside CERN have contributed in different ways to the Linac4 hardware, and we acknowledge the quality and the importance of their contribution. In particular, the IPHI team from CEA and IN2P3 (P.Y. Beauvais, M. Desmons, M. Painchault, P. Ausset) has been working with us for many years and has made great efforts to adapt the IPHI RFQ to the Linac4 needs. Under the patronage of the ISTC, collaborators from Russia have actively participated to the definition of the Linac4 accelerating structures. We wish to thank in particular V. Punin, N. Zavyalov, A. Telnov (VNIIEF Sarov), B. Sharkov, S. Plotnikov, V. Skatchkov, S. Minaev (ITEP Moscow), S. Ivanov, O. Byelaiev (IHEP Protvino), M. Naumenko (VNIITF Snezinsk) and A. Tribendis (BINP Novossibirsk).

Our colleagues of the HIPPI collaboration have provided the fruitful discussion background for the development of many ideas presented in this paper and have participated in the development of critical Linac4 components. We are indebted in particular to J.M. De Conto (LPSC), P.E. Bernaudin (CEA), M. Clarke-Gayther (RAL), C. Prior (RAL), I. Hofmann (GSI), L. Groening (GSI) and U. Ratzinger (IAP-Frankfurt). Finally, the External Scientific Advisory Committee of HIPPI (J. Stovall, Y. Yamazaki, A. Pisent) has provided us with information and advice in many occasions.

Last but not least, we acknowledge the support of the European Community-Research Infrastructure Activity under the FP6 "Structuring the European Research Area" programme (CARE, contract number RII3-CT-2003-506395).

References

[1] D.J. Warner (Ed.), Project study for a new 50 MeV linear accelerator for the CPS, CERN/MPS/LINP 73-1, 1973. [http://cdsweb.cern.ch/record/414071]

[2] LHC Design Report, Volume III, The LHC Injector Chain, CERN-2004-003. [http://cdsweb.cern.ch/record/823808]

[3] D. Boussard, E. Chiaveri, G. Geschonke and J. Tückmantel, Preliminary parameters of a proton linac using the LEP2 RF system when decommissioned, SL-RF Technical Note 96-4.

[4] R. Garoby and M. Vretenar, Proposal for a 2 GeV linac injector for the CERN PS, PS/RF/Note 96-27.

[5] M. Vretenar (Ed.), Conceptual design of the SPL, a high-power superconducting H^- linac at CERN, CERN 2000-012. [http://cdsweb.cern.ch/record/489425]

[6] F. Gerigk (Ed.), The SPL Study Group, Conceptual design of the SPL II a high power superconducting H^- linac at CERN, CERN 2006-006 (2006). [http://cdsweb.cern.ch/record/975366]

[7] M. Vretenar, R. Garoby, K. Hanke, A.M. Lombardi, C. Rossi and F. Gerigk, Design of Linac4, a new injector for the CERN booster, Proc. International Linear Accelerator Conf., Lübek, Germany, 2004. [http://cdsweb.cern.ch/record/806551]

[8] R. Garoby *et al.*, Linac4, a new injector for the CERN PS booster, Proc. 10th European Particle Accelerator Conf., Edinburgh, UK, 2006. [http://cdsweb.cern.ch/record/971752]

[9] M. Benedikt, K. Cornelis, R. Garoby, E. Métral, F. Ruggiero and M. Vretenar, Report of the High Intensity Protons Working Group, CERN-AB-2004-022 OP/RF (2004). [http://cdsweb.cern.ch/record/734636]

[10] J. Peters, Negative ion sources for high energy accelerators, *Rev. Sci. Instrum.* **71** (1999) 1069.

[11] R. Scrivens, Proton and ion sources for high intensity accelerators, Proc. 9th European Particle Accelerator Conf., Lucerne, Switzerland, 2004, [CERN-AB-2004-075]. [http://cdsweb.cern.ch/record/793626]

[12] J. Peters, New developments in RF-driven multicusp H^- ion sources, Proc. International Conf. on Ion Sources, Caen, France, 2005 [to be published in *Rev. Sci. Instrum.*].

[13] J. Peters, The HERA volume H^- source, Proc. International Particle Accelerator Conf., Knoxville, United States, 2005 (IEEE, Piscataway, NY, 2005), p. 788. [http://cdsweb.cern.ch/record/927080]

[14] D. Warner (Ed.), CERN Heavy Ion Facility Design Report, CERN 93-01, (1993). [http://cdsweb.cern.ch/record/249000]

[15] I.A. Soloshenko, Problems of intense negative ion beam transport, *Rev. Sci. Instrum.* **75** (2004) 1694.

[16] C.F. Barnett, Collisions of H, H(2), He and Li Atoms and Ions with Atoms and Molecules, Oak Ridge National Laboratory Report ORNL-6086, Atomic Data for Fusion, **1**, July, 1990. [http://www-amdis.iaea.org/ALADDIN/]

[17] P.-Y. Beauvais, Recent evolutions in the design of the French high intensity proton injector (IPHI), Proc. 9th European Particle Accelerator Conf., Lucerne, Switzerland, 2004. [http://cdsweb.cern.ch/record/822865]

[18] K.R. Littlewood, Magnetic properties of the new linac quadrupoles, PS/SM/Note 77-5.

[19] S.S. Kurennoy and J.F. Power, Development of meander-line current structure for SNS fast 2.5 MeV beam chopper, Proc. 7th European Particle Accelerator Conf., Vienna, Austria, 2000. [http://cdsweb.cern.ch/record/505148]

[20] F. Caspers, Y. Cuvet, J. Genest, M. Haase, M. Paoluzzi and A. Teixeira, The CERN-SPL chopper

concept and final layout, Proc. 9th European Particle Accelerator Conf., Lucerne, Switzerland, 2004. [http://cdsweb.cern.ch/record/790647]

[21] F. Caspers, A. Mostacci and S. Kurennoy, Fast chopper structure for the CERN Superconducting Proton Linac, Proc. 8th European Accelerator Conf., Paris, France, 2002, [CERN-PS-2002-027-RF]. [http://cdsweb.cern.ch/record/562006]

[22] M. Paoluzzi, Status of CERN chopper driver and the solid state alternative, CARE/HIPPI Document-2005-003 (2005) [CERN-AB-Note-2005-031].
[http://cdsweb.cern.ch/record/854660]

[23] Frédéric Escourbiac, J. Schlosser, M. Merola and I.B. Vastra, Experimental optimisation of a hypervapotron concept for ITER plasma facing components, *Fusion Eng. and Design* **66-68** (2003) 301-304.

[24] D.J. Warner, Accelerating structure of the CERN new 50 MeV Linac, Proc. Proton Linear Accelerator Conf., Chalk River, Canada, 1976. [http://cdsweb.cern.ch/record/873818]

[25] Spallation Neutron Source home page, http://www.sns.gov.

[26] R. Hardekopf, Permanent magnet radiation resistance in the SNS linac, SNS Technical Note, 2001.

[27] D.A. Kashinsky *et al.*, First section of a 352 MHz prototype Alvarez DTL tank for the CERN SPL, Proc. 10th European Particle Accelerator Conf., Edinburgh, United Kingdom, 2006. [http://accelconf.web.cern.ch/AccelConf/e06/PAPERS/TUPLS055.PDF]

[28] J. Billen, F. Krawczyk, R. Wood and L. Young, A new RF structure for intermediate-velocity particles, Proc. 17th International Linac Conf., Tsukuba, Japan, 1994.

[29] M. Vretenar, Y. Cuvet, J. Genest, G. Gerigk and C. Völlinger, Development of a 352 MHz cell-coupled drift tube linac prototype, Proc. 22nd International Linear Accelerator Conf., Lübeck, Germany, 2004 [CERN-AB-2004-103]. [http://cdsweb.cern.ch/record/806550]

[30] E.A. Knapp, B.C. Knapp and J.M. Potter, Standing wave high energy linear accelerator structures, *Rev. Sci. Instr.* **39**, 7 (1968), 979.

[31] M. Vretenar, N. Alharbi, F. Gerigk, M. Pasini and R. Wegner, Design and development of RF structures for Linac4, Proc. 23rd International Linear Accelerator Conf., Knoxville, United States, 2006 [CERN-AB-2006-082]. [http://cdsweb.cern.ch/record/989081]

[32] W. Bruns, GdfidL: a finite difference program with reduced memory and CPU usage, Proc. International Particle Accelerator Conf., Vancouver, Canada, 1997. [http://cdsweb.cern.ch/record/910098]

[33] P. Berra *et al.*, Study, construction and test of a 3 GHz Linac-booster (LIBO) for cancer therapy, Proc. 7th European Particle Accelerator Conf., Vienna, Austria, 2000. [http://cdsweb.cern.ch/record/508450]

[34] G.M. Stinson *et al.,* Electric dissociation of H^- ions by magnetic fields, *Nucl. Instrum. Methods*, **74** (1969) 333.

[35] I. Wilson and H. Henke, The LEP main ring accelerating structure, CERN 89-09,1989. [http://cdsweb.cern.ch/record/202932]

[36] L. Petty, PSB injection line, EDMS/CDD PSBIHENS0032 [https://edms.cern.ch/document/219861/AD]

[37] P. Bossard and F. Voelker, A pulsed ferrite magnet system with rise and fall time below 100 ns, Proc. International Conf. on Magnet Technology, Frascati, Italy, 1975.

[38] E. Troyanov and K. Schindl, H^- injection (for p) and betatron stacking (for heavy ions) in the PS booster: a possible "ppm" scheme, PS/HI Note 91-1, 1991.

[39] R.C. Webber and C. Hojvat, Measurement of the electron loss cross sections for negative hydrogen ions on carbon at 200 MeV, *IEEE Trans. Nucl. Sci.* **NS-26** (1979) 4012.

[40] T. Watanabe, M. Babzien, K. Kushce and V. Yakimenko, H^- painting injection system for the

J-PARC 3-GeV high intensity proton synchrotron, Proc. International Particle Accelerator Conf., Knoxville, United States, 2003. [http://cdsweb.cern.ch/record/748840]

[41] A. Perrin and J.F. Amand, Travel v4.06, user manual, CERN (2003).

[42] R. Duperrier, Toutatis, a radio-frequency quadrupole code, *Phys. Rev., ST Accel. & Beams*, **3** (2000) 124201. [http://prst-ab.aps.org/abstract/PRSTAB/v3/i12/e124201]

[43] R. Duperrier, N. Pichoff and D. Uriot, CEA Saclay codes review, Proc. International Conf. on Computational Science, Amsterdam, The Netherlands, 2002.

[44] J. Qiang, R.D. Ryne, S. Habib and V. Decyk, An object-oriented parallel particle-in-cell code for beam dynamics simulation in linear accelerators, *J. Comp. Phys.* **163** (2000) 1-18.

[45] J.B. Lallement, S. Lanzone, A. Lombardi, E. Sargsyan, End-to-end simulations of LINAC4, AB-Note-2006-033 ABP, 2006. [http://cdsweb.cern.ch/record/978354]

[46] A. B. Ismaïl, R. Duperrier, D. Uriot and N. Pichoff, Space charge compensation in low energy proton beams, Proc. 22nd International Linear Accelerator Conf., Lübeck, Germany, 2004. [http://cdsweb.cern.ch/record/844680]

[47] R. Ferdinand *et al.*, Status report on the 5 MeV IPHI RFQ, Proc. 20th International Linear Accelerator Conf., Montery, United States, 2000. [http://cdsweb.cern.ch/record/453393]

[48] R. Ferdinand, P. Mattei and R. Duperrier, Le RFQ du projet IPHI, DSM/DAPNIA/SEA/IPHI 99/62 (1999).

[49] I. Hofmann, Stability of anisotropic beams with space charge, *Phys. Rev.* **E 57** (1998) 4713. [http://prola.aps.org/pdf/PRE/v57/i4/p4713_1]

[50] M. Baylac, Error study of Linac4 using transport code TraceWin, Proc. 39th ICFA Advanced Beam Dynamics Workshop on High-Intensity High-Brightness Hadron Beams, Tsukuba, Japan, 2006.

[51] J. Heinemeier, P. Hvelplund and F.R. Simpson, Collisional detachment cross sections for H^- and He^-- at high energies, *J. Phys. B: Atom. Molec. Phys.* **9**, 15, (1979), 2669.

[52] G.H. Gillespie, High energy cross sections for H^- ions incident on intermediate and high Z atoms, *Phys. Rev. A*, **16**, 3, 1977.

[53] R. Thomas, H^- stripping in the booster proton injection line, AD Booster Technical note 79, BNL, 1987

[54] M. Benedikt (Ed.), R. Garoby (Ed.), K. Cornelis, E. Metral, F. Ruggiero, M. Vretenar, Report of the high intensity protons working group, CERN-AB-2004-022 OP/RF, 2004. [http://cdsweb.cern.ch/record/734636]

[55] J.A. MacLachlan, J.F. Ostiguy, User's guide to ESME 2001, FERMILAB-TM-2132. [http://cdsweb.cern.ch/record/480577]

[56] F. Jones, Development of the ACCSIM tracking and simulation code, Proc. International Particle Accelerator Conf., Vancouver, Canada, 1997. [http://cdsweb.cern.ch/record/910082]

[57] M. Martini and C.R. Prior, High-intensity and high-density charge-exchange injection studies into the CERN PS booster at intermediate energies, Proc. 9th European Particle Accelerator Conf., Lucerne, Switzerland, 2004 [CERN-AB-2004-069]. [http://cdsweb.cern.ch/record/791846]

[58] J.A. Holmes *et al.*, ORBIT simulations of the SNS accumulator ring, Proc. 9th European Particle Accelerator Conf., Lucerne, Switzerland 2004. [http://cdsweb.cern.ch/record/822948]

[59] S. Cousineau, private communication

[60] J.A. Holmes, private communication

[61] F. Jones, private communication

[62] R. Garoby, RF gymnastics in a synchrotron, in *Handbook of Accelerator Physics and Engineering*, Editors: W. Chao, M. Tigner 1999.

[63] Thales Electron Tubes, private communication.

[64] P. Baudrenghien *et al.*, The LHC low level RF, Proc. 10th European Particle Accelerator Conf., Edinburgh, United Kingdom, 2006 [LHC-PROJECT-Report-906]. [http://cdsweb.cern.ch/record/971742]

[65] J. Molendijk *et al.*, Digital design of the LHC low level RF: the tuning system for the superconducting cavities, Proc. 10th European Particle Accelerator Conf., Edinburgh, United Kingdom, 2006 [LHC-PROJECT-Report-906]. [http://cdsweb.cern.ch/record/971770]

[66] J. Molendijk, The RF low level backplane specification, CERN EDMS 603466, [http://edms.cern.ch/document/603466/]

[67] M. Arruat, S. Jackson, J.-L. Nougaret and M. Peryt, Equipment software modelling for accelerator controls, Proc. 10th International Conf. on Accelerator and Large Experimental Physics Control Systems, Geneva, Switzerland, 2005.

[68] J. Serrano, P. Alvarez, D. Dominguez and J. Lewis, Nanosecond level UTC timing generation and stamping in CERN's LHC, Proc. 9th International Conf. on Accelerator and Large Experimental Physics Control Systems, Gyeongju, Korea, 2003. [http://cdsweb.cern.ch/record/693175]

[69] A. Gagnaire and Y. Georgievskiy, Driver generation tools, talk at CERN, Geneva, Switzerland, 2003. [http://ab-co-fc.web.cern.ch/ab-co-fc/drivers/Presentation-MoulinetteDEvelopement-26092003.ppt]

[70] AB/CO Configuration Data Browser. [https://cs-ccr-oas3.cern.ch/config-databrowser/db/configdb/browser/index.html]

[71] K. Kostro, J. Andersson, F. Di Maio, S. Jensen and N. Trofimov, The controls middleware (CMW) at CERN, status and usage, Proc. 9th International Conf. on Accelerator and Large Experimental Physics Control Systems, Gyeongju, Korea, 2003. [http://cdsweb.cern.ch/record/693152]

[72] K. Hanke and M. Hori, Design and construction of a beam shape and halo monitor for the CERN SPL, CARE/HIPPI Document 2005-005 [CERN AB-Note-2005-033 OP], 2005. [http://cdsweb.cern.ch/record/860947]

[73] M.A. Plüm, R.W. Garnett, R. Meyer Sr. and R.E. Shafer, Diagnostic plate for SNS linac commissioning, Proc. International Particle Accelerator Conf., Chicago, United States. [http://cdsweb.cern.ch/record/556148]

[74] A. Feschenko *et al.*, The first result of bunch shape measurements in the SNS linac, Proc. International Linear Accelerator Conf., Lübeck, Germany, 2004. [http://cdsweb.cern.ch/record/925531]

[75] A. Feschenko, Methods and instrumentation for bunch shape measurement, Proc. International Particle Accelerator Conf., Chicago, United States, 2001. [http://cdsweb.cern.ch/record/555691]

[76] K. Halbach, Design of permanent multipole magnets with oriented rare earth cobalt materials, *Nucl. Instr. Meth.* **169** (1980) 1-10.

[77] N.V. Mokhov and W. Chou (Eds.), Beam halo and scraping, Proc. 7th ICFA mini-workshop on high intensity and high brightness hadron beams, Interlaken resort, Wisconsin, United States, 1999.

[78] A. Fasso, A. Ferrari, J. Ranft and P.R. Sala, FLUKA: a multi-particle transport code, CERN-2005-10 (2005), [INFN/TC_05/11, SLAC-R-773]. [http://cdsweb.cern.ch/record/898301]

[79] A. Fasso *et al.*, The physics models of FLUKA: status and recent developments, Proc. Computing in High Energy and Nuclear Physics 2003 Conf. (CHEP2003), La Jolla, CA, USA, 2003, eConf C0303241 (2003) [arXiv:hep-ph/0306267].

[80] M. Silari and H. Vincke, Shielding proposal for the SPL front end, Technical Note CERN-TIS-2003-002-RP-TN (2003).

[81] M. Magistris and M. Silari, Preliminary shielding design of Linac4, Technical Note CERN-SC-2005-011-RP-TN (2005).

[82] M. Magistris and M. Silari, Preliminary shielding design of Linac4, Top shielding and induced radioactivity, Technical Note CERN-SC-2005-050-RP-TN (2005).

[83] T. Otto, Annual effective doses in offices near the proposed Linac4, Technical Note CERN-SC-2005-133-RP-TN (2006).

[84] M. Magistris and M. Silari, Radiological considerations on the 160 MeV neutral dump at injection in the PS booster, Technical Note CERN-SC-2005-142-RP-TN (2006).

[85] P. Ausset *et al.*, Beam diagnostics instrumentation for the high energy beam transfer line of I.P.H.I., 7th European Workshop on Beam Diagnostics and Instrumentation for Particle Accelerators (DIPAC 05), Lyon, France (2005). [http://cdsweb.cern.ch/record/924175]

[86] E. Sargsyan, K. Hanke and A.M. Lombardi, Simulations of the beam diagnostics line for the SPL 3 MeV chopper line, AB-Note-2004-053 (2004). [http://cdsweb.cern.ch/record/746299]

[87] K. Crandall, D.O. Jeon, R. Shafer and J. Stovall, Longitudinal tune-up of SNS normal-conducting linac, Proc. 21st International Linear Accelerator Conf., Gyongju, Korea (2002). [http://cdsweb.cern.ch/record/728999]

Appendix: Linac4 parameter list

Parameter	Value	Comment
General linac parameters		*Section 1.4*
Ion species	H^-	
Overall linac length	80 m	
Output energy	160 MeV	
Bunch frequency	352.2 MHz	
Max. repetition rate	2 Hz	
Beam pulse length	0.4 ms	
Max. beam duty cycle	0.08%	
Chopper beam-on factor	62%	
Source current	80 mA	
RFQ output current	70 mA	
Linac current	40 mA	
Average current	0.032 mA	
Max. beam power	5.1 kW	
Number of particles per pulse	1.0×10^{14}	
Number of particles per bunch	1.14×10^{9}	
Error amplitudes		Maximum, uniform distribution
Quadrupole gradient	$\pm 0.5\%$	
Quadrupole displacement	± 0.1 mm	
Quadrupole rotation (x,y)	± 0.5 deg	
Quadrupole rotation (z)	± 0.2 deg	
Cavity field phase	± 1 deg	
Cavity field amplitude	$\pm 1\%$	
Ion source and LEBT		*Section 2.1*
Ion species	H^-	
Source current	80 mA	
Extraction voltage	95 kV	
Source length	1 m	
LEBT focusing type	solenoid	
LEBT length	1.8 m	
Transverse output emittance	$0.2\,\pi$ mm mrad	(r.m.s., normalised)
Vacuum	10^{-5} mbar	
RFQ		*Section 2.2*
Input energy	0.095 MeV	
Output energy	3.0 MeV	
RF frequency	352.2 MHz	
Peak current	70 mA	
Average pulse current	70 mA	
Design current	100 mA	CW
Design duty cycle	100%	
Voltage	87–122 kV	
Modulation factor	1.0–1.7	
Maximum surface field	1.7 kilpatrick	
RF beam power	210 kW	(70 mA)

table continued on next page

Parameter	Value	Comment
RF peak power (superfish)	674 kW	
RF peak power (expected)	1020 kW	
Number of klystrons	1	
Number of cells	560	
Length	5.95 m	
Beam aperture	3.7–4.1 mm	
Transverse output emittance	0.28 π mm mrad	r.m.s., normalised
Longitudinal output emittance	0.15 π deg MeV	At 352.2 MHz
	0.38 π mm mrad	r.m.s., normalised
Vacuum	10^{-7} mbar	
MEBT (chopper line)		*Section 2.3*
Beam energy	3 MeV	
Peak current	70/64 mA	Input/output
Average pulse current	70/40 mA	Input/output
Effective chopper plate voltage	400 V	Seen by beam
Chopper plate voltage	500 V	
Chopper rise/fall time	< 2 ns	10–90%
Chopper repetition rate	1–50 Hz	
Maximum chopping factor	40%	
Chopper deflection angle	5.3 mrad	
RF frequency buncher cavities	352.2 MHz	
Maximum buncher voltage	150 kV	
RF peak power per buncher	16–18 kW	
Number of buncher cavities	3	At 352.2 MHz
Number of chopper structures	2	Inside quadrupoles
Number of quadrupoles	11	
Length of chopper plates	400 mm	
Chopper plate distance	20 mm	
Length	3.7 m	
Beam collimation	$\approx 9\%$	
Transverse output emittance	0.32 π mm mrad	r.m.s., norm., collimated
Longitudinal output emittance	0.17 π deg MeV	At 352.2 MHz
	0.43 π mm mrad	r.m.s., normalised
Vacuum	10^{-7} mbar	
DTL		*Section 2.4*
Input energy	3 MeV	
Output energy	40 MeV	
RF frequency	352.2 MHz	
Peak current	64 mA	
Average pulse current	40 mA	
Design RF duty cycle	10%	
Gradient E_0	3.3/3.5 MV/m	1st / (2nd,3rd) tank
Maximum surface field	1.4–1.7 kilpatrick	
Synchrotron phase	$-30 \rightarrow -20/-20$ deg	1st / (2nd,3rd) tank
RF beam power	1.5 MW	
RF peak power per tank	0.75/1.57/1.55 MW	1st/2nd/3rd tank
RF peak power	3.9 MW	

table continued on next page

Parameter	Value	Comment
Number of klystrons	1/2/2	1st/2nd/3rd tank
Cells per tank	28/33/24	1st/2nd/3rd tank
Number of tanks	3	
Focusing tank 1	FOFODODO	
Focusing tank 2/3	FODO	
Length per tank	2.63/5.2/5.0 m	1st/2nd/3rd tank
Total length	13.4 m	
Transition to CCDTL	0.25 m	
Beam aperture	20 mm	
Quadrupole type	PMQ	
Quadrupole length	45/80 mm	1st / (2nd,3rd) tank
Number of quadrupoles	81	
Outer drift tube diameter	90 mm	
Inner quadr. diameter	22 mm	
Transverse output emittance	0.34 π mm mrad	r.m.s., normalised
Longitudinal output emittance	0.19 π deg MeV	At 352.2 MHz
	0.49 π mm mrad	r.m.s., normalised
Vacuum	10^{-7} mbar	
CCDTL		*Section 2.5*
Input energy	40 MeV	
Output energy	89.7 MeV	
RF frequency	352.2 MHz	
Peak current	64 mA	
Average pulse current	40 mA	
Design RF duty cycle	14%	
Gradient E_0	2.8–3.9 MV/m	
Maximum surface field	1.4–1.7 kilpatrick	
Synchr. phase	-20 deg	
RF beam power	2 MW	
RF power per module	0.8 MW	
RF peak power	6.4 MW	
Number of klystrons	8	
Cells per cavity	3	
Cavities per module	3	
Number of cavities	24	
Number of modules	8	
Number of quadrupoles	24	
Focusing	FODO	
Length	25.2 m	
Transition to SCL	0.25 m	
Beam aperture	28 mm	
Transverse output emittance	0.35 π mm mrad	r.m.s., normalised
Longitudinal output emittance	0.19 π deg MeV	At 352.2 MHz
	0.4 π mm mrad	r.m.s., normalised
Vacuum	10^{-7} mbar	
SCL		*Section 2.6*
Input energy	89.7 MeV	

table continued on next page

Parameter	Value	Comment
Output energy	160 MeV	
RF frequency	704.4 MHz	
Peak current (at 704.4 MHz)	128 mA	Every 2nd RF bucket filled
Average pulse current	40 mA	
Design RF duty cycle	10%	
Gradient E_0	4 MV/m	
Maximum surface field	1.1–1.2 kilpatrick	
Synchrotron phase	-20 deg	
RF beam power	2.8 MW	
RF peak power	12.5 MW	
Number of klystrons	4	
Cells per cavity	11	
Cavities per module	4–5	
Number of cavities	20	
Number of quadrupoles	20	
Focusing	FODO	
Length	28 m	
Beam aperture	32 mm	
Transverse output emittance	0.36 π mm mrad	r.m.s., normalised
Longitudinal output emittance	0.19 π deg MeV	At 352.2 MHz
	0.48 π mm mrad	r.m.s., normalised
Vacuum	10^{-7} mbar	
Transfer line to PSB		*Section 2.8*
Input energy	160 MeV	
Output energy	160 MeV	
Total length	193.2 m	to PSB entrance
Length of new section	105 m	to junction with Linac2 line
Number of RF cavities	2	5-cell π-mode cavities at 352 MHz
Power per cavity	74.3 kW	
Number of quadrupoles	23	
Quadrupole aperture	70 mm	
Number of bendings	5	
Transverse output emittance	0.43/0.36 π mm mrad	(x/y) r.m.s., normalised
Vacuum	10^{-7} mbar	
PSB injection		*Section 2.9*
RF frequency	992.06 kHz	at injection
RF harmonic number	1	
Injection turns	4×100	
Linac beam energy spread	20 keV	r.m.s.
Linac beam energy jitter	67 keV	r.m.s.